NANO-STRUCTURED CARBON MATERIALS FOR ENERGY GENERATION AND STORAGE

PHAM KIEN CUONG

(B.Eng. (Hons.), NATIONAL UNIVERSITY OF SINGAPORE)

A THESIS SUBMITTED

FOR THE DEGREE OF DOCTOR OF PHILOSOPHY

NUS GRADUATE SCHOOL FOR INTEGRATIVE SCIENCES AND ENGINEERING

NATIONAL UNIVERSITY OF SINGAPORE

&

DEPARTMENT OF MATERIALS

IMPERIAL COLLEGE LONDON

2015

Declaration

I hereby declare that this thesis is my original work and it has been written by me in its entirety. I have duly acknowledged all the sources of information which have been used in the thesis.

This thesis has also not been submitted for any degree in any university previously.

The copyright of this thesis rests with the author and is made available under a Creative Commons Attribution Non-Commercial No Derivatives licence. Researchers are free to copy, distribute or transmit the thesis on the condition that they attribute it, that they do not use it for commercial purposes and that they do not alter, transform or build upon it. For any reuse or redistribution, researchers must make clear to others the licence terms of this work.



_____

Pham Kien Cuong

25th December 2015

Dedicated to my beloved family...

Acknowledgements

First and foremost, I would like to express my sincerest gratitude towards my supervisors, Assoc. Prof. Daniel H. C. Chua, Prof. Andrew T. S. Wee, Prof. David S. McPhail, and Dr. Cecilia Mattevi, for their invaluable support and guidance throughout my study in the past four years. Without their support, this work would not have been possible. I would like to thank Prof. Sow Chorng Haur for his useful feedback and discussions in my thesis advisory committee meetings.

I would like to thank Mr. Wong How Kwong, Mr. Chen Gin Seng (NUS), Dr. Richard Chater, Dr. Sarah Fearn, Dr. Mahmoud Ardakani, Mrs. Ecaterina Ware, Dr. Sergio Bertazzo, and Dr. Masashi Kishimoto (Imperial College London) for their help and meaningful discussions.

I would also like to thank my colleagues and friends, Hu Yan, Tang Zhe, Wang Hongyu, Tamie Loh Ai Jia, Chang Yung Huang, Zheng Minrui, Tan Kuan Khoon Royston, Koh Ting Ting Angel, Lim Su Ru, and Chen Ting, for their constant support. A special thanks is given to Chang Ci'En Sharon for her generous advice and help throughout my joint degree program.

Last but not least, a special thanks goes to my loving family, for being my endless source of love, support, encouragement, and inspiration throughout all the years of my life. This journey would not have been possible without their selfless love and support. This thesis is specially dedicated to my family.

Table of Contents

Acknowledgements i

Table of Contents ii

Summary viii

List of Publications x

List of Tables xi

List of Figures xii

List of Abbreviations xix

Chapter 1 : Introduction 1

1.1. The role of renewable energy and energy storage/conversion technologies in the future global energy landscape 1

1.2. Introduction to Proton Exchange Membrane Fuel Cells (PEMFCs) 6

1.2.1. Main types of fuel cells 6

1.2.2. PEMFC structure and components 8

1.2.3. PEMFC operation and electrochemistry 11

1.2.4. Challenges of PEMFCs 15

1.2.5. Design of carbon support for PEMFCs 16

1.3. Introduction to Hydrogen Evolution Reaction (HER) 21

1.3.1. Hydrogen Evolution Reaction (HER) 21

1.3.2. Molybdenum Sulfide catalysts for HER 24

1.3.3. Graphene-Carbon Nanotube hybrids as catalyst support for amorphous Molybdenum Sulfide in HER applications 29

1.4. Introduction to supercapacitors 31
1.4.1. Operating principle of supercapacitors 31
1.4.2. Amorphous molybdenum sulfide (MoS_x) as a supercapacitor electrode material 33
1.4.3. Graphene-Carbon Nanotube hybrids as support materials for amorphous Molybdenum Sulfide in supercapacitor applications 35
1.5. Research objectives 35
1.6. Thesis structure 39
Chapter 2 : Experimental methodology 41
2.1. Sample preparation methods 41
2.1.1. Carbon support fabrication methods 41
2.1.2. PEMFC electrode fabrication methods 46
2.1.3. Amorphous molybdenum sulfide electrodeposition methods 49
2.2. *Ex situ* material characterization methods 51
2.2.1. Secondary Electron Microscopy (SEM) 51
2.2.2. Transmission Electron Microscopy (TEM) 51
2.2.3. Raman spectroscopy 54
2.2.4. X-ray Photoelectron Spectroscopy (XPS) 54
2.2.5. X-ray diffraction (XRD) 55
2.2.6. Brunauer–Emmett–Teller (BET) surface area and porosity analysis 55
2.2.7. 3D reconstruction of porous nanostructures using a FIB-SEM dual beam technique 56

2.3. Electrochemical evaluation methods 60

2.3.1. PEMFC characterization methods 60

2.3.2. HER characterization methods 65

2.3.3. Supercapacitor electrode characterization methods 67

Chapter 3 : Growth of nanostructured carbon supports 69

3.1. Growth of Carbon Nanotubes on carbon paper 69

3.1.1. Growth of CNTs by the thermal CVD method 69

3.1.2. Effect of growth conditions on the deposition of CNTs on carbon paper 70

3.1.3. Physical characterization of the as-grown CNTs 81

3.2. Growth of free-standing graphene 83

3.2.1. Growth of free-standing graphene by the RF-PECVD method . 83

3.2.2. Effect of growth conditions on the deposition of free-standing graphene 84

3.2.3. Physical characterization of the as-grown free-standing graphene 89

3.3. Growth of Graphene-Carbon Nanotube hybrids on carbon paper 93

3.3.1. Growth of Graphene-Carbon Nanotube hybrids using a two-step growth method 93

3.3.2. Physical characterization of the GCNT hybrids 94

3.3.3. Growth mechanism of the GCNT hybrids 98

3.4. Summary 102

Chapter 4 : Graphene-Carbon Nanotube hybrids as catalyst supports in Proton Exchange Membrane Fuel Cells 104

4.1. Introduction 104
4.2. Physical characterization of the Pt/GCNT catalysts 106
4.3. Electrochemical evaluations for the catalytic activity and electrochemical stability of the Pt/GCNT catalysts 110
4.3.1. The degradation of device performance from a polarization perspective 112
4.3.2. Deconvolution of polarization losses using Electrochemical Impedance Spectroscopy 114
4.3.3. Pt electrochemical surface area loss and carbon corrosion caused by the accelerated degradation test (ADT) 121
4.3.4. Electrode structural study with transmission electron microscopy (TEM) 127
4.4. Summary 130
Chapter 5 : Amorphous Molybdenum Sulfide on Graphene-Carbon Nanotube hybrids as highly active Hydrogen Evolution Reaction catalysts 132
5.1. Introduction 132
5.2. Deposition and activation of MoS_x on carbon supports 133
5.2.1. Deposition of MoS_x catalyst 134
5.2.2. Reductive activation of MoS_x catalyst 137
5.3. Physical characterization of the MoS_x/GCNT hybrids 138
5.3.1. Morphological characterization 138
5.3.2. Chemical state analysis 140
5.3.3. Crystallinity analysis 142

5.4. Electrochemical evaluations of the MoS_x/GCNT hybrids as HER catalyst materials 144
5.4.1. Total electrode catalytic activity 144
5.4.2. Intrinsic catalytic activity 152
5.4.3. Electrochemical stability of the MoS_x/GCNT/CP electrode 156
5.4.4. Understanding of MoS_x active sites through XPS characterization 157
5.4.5. Electrochemical evaluations of the MoS_x/CNT/CP electrodes . 162
5.5. Summary 167
Chapter 6 : Amorphous Molybdenum Sulfide on Graphene-Carbon Nanotube hybrids as supercapacitor electrode materials 168
6.1. Introduction 168
6.2. Electrochemical evaluations of the MoS_x/GCNT hybrids as supercapacitor electrode materials 169
6.2.1. Specific capacitance evaluation with cyclic voltammetry 170
6.2.2. Specific capacitance evaluation with galvanostatic charge/discharge 174
6.2.3. Electrochemical Impedance Spectroscopy measurement 179
6.2.4. Electrochemical stability evaluation 180
6.3. Electrochemical evaluations of the MoS_x/CNT/CP electrode 181
6.3.1. Specific capacitance evaluation with cyclic voltammetry 181
6.3.2. Specific capacitance evaluation with galvanostatic charge/discharge 184
6.3.3. Electrochemical Impedance Spectroscopy measurement 186

6.3.4. Electrochemical stability evaluation 189

6.4. Summary 190

Chapter 7 : 3D reconstruction of porous carbon electrode nanostructures using a FIB-SEM dual beam technique 191

7.1. Introduction 191

7.2. 3D reconstruction of PEMFC cathode catalyst layer nanostructures using the FIB-SEM dual beam technique 195

7.2.1. Effect of silicone resin infiltration and EsB imaging mode on the acquired SEM image quality 196

7.2.2. Image processing 200

7.2.3. Reconstructed nanostructures of PEMFC cathodes 202

7.2.4. Quantification of electrode nanostructures using 3D reconstructed images 205

7.3. Summary 207

Chapter 8 : Conclusions & Future work 209

8.1. Conclusions 209

8.2. Recommendations for future work 214

Bibliography 219

Summary

In this thesis, we investigate nano-structured carbon materials and their applications in electrochemical energy conversion and storage devices. We identify a common need in electrochemical devices for a high surface area, porous and highly crystalline graphitic carbon support with high density of exposed graphitic edges. To this end, we propose and develop a novel nano-structured carbon material referred to as Graphene-Carbon Nanotube hybrid (GCNT), grown directly on carbon paper. The hybrid is grown using a two-step chemical vapor deposition method. The resulting hybrid material combines the advantageous properties of constituent materials, including an ultra-high density of graphitic edges of graphene and a porous structure of CNTs. The GCNT-on-carbon paper possesses an integrated all-carbon hierarchical structure where CNTs are grown directly on carbon paper and graphene is densely grown on CNTs. The hierarchical structure offers direct electrical conducting pathways from graphene to carbon paper. The hybrid also possesses high chemical purity, high crystallinity and high specific surface area. The hybrid is subsequently investigated for its applications in electrochemical devices.

When the GCNT hybrid is used as a carbon support for Pt catalysts in Proton Exchange Membrane Fuel Cell cathodes, the Pt/GCNT catalyst exhibits high intrinsic catalytic activity and superior electrochemical stability compared to a commercial carbon black supported Pt catalyst. The enhanced intrinsic catalytic activity of the Pt/GCNT catalyst is attributed to the high density of graphitic edges present in the hybrid. The superior electrochemical stability of the Pt/GCNT catalyst

is attributed to the high crystallinity of the GCNT support. The superior stability is expressed by a lower loss in polarization performance, a smaller increase in charge transfer resistance, a lower loss in the active Pt electrochemical surface area, a lower rate of carbon corrosion, and a more stable catalyst microstructure.

When the GCNT hybrid is used as a carbon support for amorphous molybdenum sulfide (MoS_x) in hydrogen evolution reaction (HER) catalyst and supercapacitor electrode material applications, the integrated, porous, high surface area and conductive nanostructure of GCNT/carbon paper provides efficient electron transport and mass transport pathways towards the active sites of MoS_x. The enhanced electron transport and mass transport play a crucial role in the enhancement of MoS_x catalytic activity towards HER and its supercapacitive performance. With this strategy, we develop one of the most active molybdenum sulfide-based HER catalysts reported to date. With a catalyst loading of 3 mg cm^{-2}, an overpotential of 141 mV is required to obtain a current density of 10 mA cm^{-2}. A Tafel slope of 41 mV $decade^{-1}$ is demonstrated. The MoS_x-deposited GCNT hybrid also shows high specific capacitances (up to 414 F g^{-1}) even at high discharge rates.

Lastly, an FIB-SEM dual-beam method is also developed to visually reconstruct the porous 3D nanostructure of carbon electrodes commonly used in electrochemical devices. A combination of silicone resin infiltration, energy selective backscattering SEM imaging mode and low primary electron energy proves to be highly effective in unambiguously distinguishing carbon materials, porous channels, and other active phases present in the electrode structures.

List of Publications

Refereed Journal articles

[1] **Pham, K.-C.**, Kishimoto, M., Bertazzo, S., McPhail, D. S., Brandon, N. P., Wee, A. T. S. & Chua, D. H. C. Three-Dimensional Reconstruction of Porous Carbon Electrode Nanostructures Using FIB–SEM Tomography. (*Submitted*)

[2] **Pham, K.-C.**, McPhail, D. S., Wee, A. T. S. & Chua, D. H. C. Amorphous Molybdenum Sulfide on Graphene–Carbon Nanotube Hybrids as Supercapacitor Electrode Materials. (*Submitted*)

[3] **Pham, K.-C.**, Chang, Y.-H., McPhail, D. S., Mattevi, C., Wee, A. T. S. & Chua, D. H. C. Amorphous Molybdenum Sulfide on Graphene–Carbon Nanotube Hybrids as Highly Active Hydrogen Evolution Reaction Catalysts. *ACS Applied Materials & Interfaces* **8**, 5961-5971, (2016).

[4] **Pham, K.-C.**, McPhail, D. S., Mattevi, C., Wee, A. T. S. & Chua, D. H. C. Graphene-Carbon Nanotube Hybrids as Robust Catalyst Supports in Proton Exchange Membrane Fuel Cells. *Journal of The Electrochemical Society* **163**, F255-F263, (2016).

[5] **Pham, K.-C.**, Chua, D. H. C., McPhail, D. S. & Wee, A. T. S. The Direct Growth of Graphene-Carbon Nanotube Hybrids as Catalyst Support for High-Performance PEM Fuel Cells. *ECS Electrochemistry Letters* **3**, F37-F40, (2014).

Conference proceeding and oral presentation

[1] **Pham, K.-C.**, Chua, D. H. C., McPhail, D. S. & Wee, A. T. S. Graphene nanoflakes carbon nanotubes hybrid as highly robust catalyst support in proton exchange membrane fuel cells. *Abstracts of Papers of the American Chemical Society* **246**, (2013).

List of Tables

Table 1-1. A comparison of key characteristics of the main fuel cell types. (Adapted with permission from ref. [14] Copyright © 2003 John Wiley and Sons, and ref. [15] Copyright © 2009 Elsevier Ltd.)..... 7

Table 3-1. Summary of experimental conditions for CNT growth optimization. 71

Table 3-2. Summary of experimental conditions for free-standing graphene growth optimization. 84

Table 4-1. Mathematical expressions of the circuit elements used in the EIS fittings. 118

Table 4-2. Equivalent circuit element fitting parameters. 120

Table 5-1. The BET specific surface area and roughness factor of carbon paper and GCNT/CP electrodes..... 136

Table 5-2. Extracted parameters from the HER polarization curves and Tafel plots.147

Table 5-3. A comparison of the overpotential at $|j| = 10$ mA cm^{-2} with the state of the art molybdenum sulfide catalysts. (Adapted with permission from ref. [60] Copyright © 2014, American Chemical Society)..... 147

Table 5-4. Equivalent circuit fitting parameters for MoS_x catalysts..... 152

Table 5-5. Detailed stoichiometry analysis of the present chemical states in the MoS_x/GCNT/CP electrode after various stages of electrochemical evaluation. 160

Table 5-6. Extracted parameters from the HER polarization curves and Tafel plots for MoS_x/CNT/CP electrodes..... 164

Table 6-1. Comparison for the specific capacitance of the MoS_x/GCNT/CP against the reported literature..... 178

Table 6-2. Equivalent circuit fitting parameters for EIS spectra of the MoS_x/GCNT/CP, MoS_x/CNT/CP, and MoS_x/CP electrodes..... 188

Table 7-1. Quantification of the 3D reconstructed nanostructures..... 205

List of Figures

Figure 1-1. Simplified Ragone plot comparisons between different electrochemical energy conversion and storage systems. (Reprinted with permission from ref. [6] Copyright © 2012 Elsevier Ltd.)..... 5

Figure 1-2. An illustration of the PEM fuel cell stack, a single cell, and the structure of a membrane electrode assembly. [5,16-19] (Adapted with permission from ref. [16] Copyright © 2002 Elsevier Science B.V., ref. [5] Copyright © 2010 Elsevier Ltd., and ref. [18] *"Electrochemistry Encyclopedia"* (http://knowledge.electrochem.org/encycl/) on 14/12/2015)..... 9

Figure 1-3. A schematic illustration of the MEA structure and the electrochemical processes in PEMFCs. 12

Figure 1-4. A schematic illustration of the proposed GCNT structure. 19

Figure 1-5. Dependence of exchange current density on hydrogen adsorption free energy for various HER catalyst materials. (Reprinted with permission from ref. [62] Copyright © 2007, American Association for the Advancement of Science) 22

Figure 1-6. Calculated free energy diagram for hydrogen evolution reaction at standard hydrogen electrode potential and pH = 0 for various materials. (Reprinted with permission from ref. [63] Copyright © 2005, American Chemical Society)..... 25

Figure 1-7. Representative optimization approaches for crystalline MoS_2 nanomaterials for HER. (a) MoS_2/MoO_{3-x} nanowires, [64] (b) vertically aligned MoS_2 and $MoSe_2$, [65] (c) defect-rich MoS_2 nanosheets, [66] (d) MoS_2 nanoparticles on graphene, [67] and (e) MoS_2 double-gyroid mesoporous structure. [68] (Adapted with permission from ref. [64] Copyright © 2011, American Chemical Society, ref. [65] Copyright © 2013, American Chemical Society, ref. [66] Copyright © 2013 WILEY-VCH Verlag GmbH & Co. KGaA, Weinheim, ref. [67] Copyright © 2011, American Chemical Society, and ref. [68] Copyright © 2012, Nature Publishing Group) 27

Figure 1-8. Amorphous MoS_x as HER catalyst materials. (Reprinted with permission from ref. [12] Copyright © 2014, American Chemical Society) 29

Figure 1-9. Schematic illustrations of charge storage process of (a) electrochemical double-layer capacitance, and (b) *pseudo*-capacitance. (Reprinted with permission from ref. [79] Copyright © 2011, Materials Research Society)..... 32

Figure 2-1. A schematic illustration of the magnetron sputtering deposition process. 42

Figure 2-2. A schematic illustration of the thermal CVD setup used for the CNT growth. 44

Figure 2-3. A schematic illustration of the PECVD setup used for free-standing graphene and GCNT hybrid growth. 46

Figure 2-4. A schematic illustration of the three-electrode electrochemical cell setups used for the electrochemical deposition of MoS_x on carbon substrates. 50

Figure 2-5. TEM sample preparation method using the FIB-SEM technique. (a) chamber configuration, (b) deposition of Pt protection mask on the sample surface, (c) ion-milling trenches around the sample, (d) attachment of the sample lamella to the lift-out probe, (e) sample lamella lift-out, (f) attachment of the lamella to the Omniprobe lift-out TEM grid, (g) initial thinning of the lamella, and final thinning of the TEM-ready lamella from (h) side view and (i) top view. 53

Figure 2-6. An illustration of the FIB-SEM dual beam 3D reconstruction method. Experimental setup from (a) a side view and (b) a top-down view from SEM column. (c) A micrograph of the trench, Pt protective mask and alignment markers. (d) An SEM micrograph of the freshly milled sample cross-section, taken with Energy Selective Backscattered (EsB) electrons imaging mode. (e) An illustrative alignments of consecutive "slices". (f) Processed and reconstructed 3D structure of the electrode. 57

Figure 2-7. Experimental setup used for PEMFC electrochemical characterization. .. 60

Figure 2-8. A schematic illustration of the three-electrode electrochemical cells setup used for HER electrochemical evaluations. 66

Figure 2-9. A schematic illustration of the three-electrode electrochemical cells setup used for supercapacitor electrochemical evaluations. 68

Figure 3-1. SEM micrographs of CNTs grown on carbon paper at (a) 650 °C, (b) 750 °C and (c) 850 °C. 72

Figure 3-2. SEM micrographs of CNTs grown on carbon paper at C_2H_4 flow rates of (a) 20 sccm, (b) 30 sccm, and (c) 40 sccm. 73

Figure 3-3. SEM micrographs of CNTs grown on (a, a') Fe-deposited carbon papers after 1 hr CNT deposition time; and Al/Fe-deposited carbon papers after (b, b') 1 hr and (c, c') 30 min CNT deposition time. 75

Figure 3-4. SEM micrographs of the as-grown CNTs on carbon paper with different Al buffer layer thicknesses using thermal CVD growth method. Post-CVD growth micrographs of (a, a') plain carbon paper, (b, b') carbon paper with 25 nm Al deposited, (c, c') carbon paper with 10 nm Fe deposited, (d, d') carbon paper with 5 nm Al/10 nm Fe deposited, (e, e') carbon paper with 15 nm Al/10 nm Fe deposited, and (f, f') carbon paper with 25 nm Al/10 nm Fe deposited. 76

Figure 3-5. Cross-sectional SEM micrographs of the as-grown CNTs on carbon paper with different Al buffer layer thicknesses using thermal CVD growth method. Post-CVD growth micrographs of (a, a') plain carbon paper, (b, b') carbon paper with 25 nm Al deposited, (c, c') carbon paper with 10 nm Fe deposited, (d, d') carbon paper with 5 nm Al/10 nm Fe deposited, and (e, e', e'', e''') carbon paper with 25 nm Al/10 nm Fe deposited. 78

Figure 3-6. SEM micrographs of the annealed catalysts on carbon paper with different Al buffer layer thicknesses. Morphology of the annealed (a, a') plain carbon paper, (b, b') carbon paper with 25 nm Al deposited, (c, c') carbon paper with 10 nm Fe deposited, (d, d') carbon paper with 5 nm Al/10 nm Fe deposited, (e, e') carbon paper with 15 nm Al/10 nm Fe deposited, and (f, f') carbon paper with 25 nm Al/10 nm Fe deposited. 79

Figure 3-7. TEM micrograph of the as-grown CNTs on carbon paper. 81

Figure 3-8. Spectroscopic characterization of the as-grown CNTs on carbon paper. (a) Raman spectroscopy, (b) XPS survey scan and (c) C 1s high resolution scan of the as-grown CNTs on carbon paper..... 82

Figure 3-9. Effect of precursor gas composition on the PECVD growth of free-standing graphene. SEM images of the as-grown free-standing graphene with 60 sccm H_2 and a C_2H_2 flow rate of (a) 60 sccm, (b) 40 sccm, (c) 30 sccm, (d) 20 sccm, and (e) 10 sccm..... 85

Figure 3-10. Effect of deposition temperature on the PECVD growth of free-standing graphene. SEM images of free-standing graphene grown on Al/Fe-deposited carbon papers at (a) 700 °C and (b) 600 °C, and on plain carbon papers at (c) 700 °C and (d) 600 °C. 87

Figure 3-11. Effect of growth time on the deposition of graphene. SEM micrographs of the as-grown graphene on carbon paper after (a) 1 hr and (b) 2 hrs of deposition. 88

Figure 3-12. Electron microscopy characterization of the free-standing graphene grown on Silicon wafer. (a) SEM micrograph of the top surface with (inset) a line profile of the as-grown graphene in the location marked by the green dashed line, and (b) TEM cross-sectional micrograph of the free-standing graphene grown on Silicon wafer, with outlines of graphene sheets marked in red and blue. 90

Figure 3-13. Spectroscopic characterization of the free-standing graphene grown on Silicon wafer. (a) Raman spectra of the free-standing graphene grown on Silicon wafer and of a reference Silicon wafer. (b) XPS survey spectrum and (c) C 1s high resolution scan of the free-standing graphene grown on Silicon wafer. 92

Figure 3-14. Morphological characterization of the GCNT hybrids on carbon paper. SEM micrographs of the hybrids at (a) medium magnification, (b) lower magnification and (c) higher magnification. 94

Figure 3-15. Microscopic and spectroscopic characterization of the GCNT hybrids. (a) Bright field TEM micrograph of the hybrids; (b) HR-TEM micrograph of the GCNT in the region outlined by the black-colored square in figure (a); (c) Background-corrected Raman spectrum (red curve) with Lorentzian peak fittings (blue curves) of the hybrids; (d) Survey scan XPS spectrum and (inset) high resolution scan of C 1s peaks of the hybrids. 96

Figure 3-16. Proposed growth mechanism of the GCNT hybrids. (a) Original CNT scaffold, (b) nucleation of graphene, (c) lateral growth of graphene islands and additional nucleation, (d) buckling of graphene edges upon the collision of a growing graphene island with its neighboring graphene islands, and (e) free-standing graphene continues to grow from the curled graphene edges. 101

Figure 4-1. Schematic illustration of the Pt/GCNT cathode fabrication process and (inset) the structural comparison of the Pt/GCNT cathode and the conventional carbon black-based cathode. 105

Figure 4-2. Electron microscopic characterization of the Pt/GCNT hybrids. (a) FE-SEM micrograph of the Pt/GCNT hybrids; (b) Bright field TEM micrograph of the Pt/GCNT hybrids and (c) HR-TEM micrograph of the Pt/GCNT hybrids in the region outlined by the black-colored square in figure (b). 106

Figure 4-3. XPS characterization of the Pt/GCNT hybrids. (a) XPS survey spectrum and (b) Pt 4f high resolution scan of the Pt/GCNT hybrids. 108

Figure 4-4. Electron microscopic characterization of the Pt/CNT electrode. (a) FE-SEM micrograph of the Pt/CNT electrode; (b) Bright field TEM micrograph of the Pt/CNT electrode with (inset) HR-TEM micrograph of the CNT multi-wall, and (c) HR-TEM micrograph of the Pt/CNT electrode in the region outlined by the black-colored square in figure (b). 109

Figure 4-5. Polarization curves of the Pt/GCNT, Pt/VXC72 and Pt/CNT cathodes (a) before and (b) after the accelerated degradation test. 113

Figure 4-6. Electrochemical impedance spectroscopy and equivalent circuit fitting of the Pt/GCNT, Pt/VXC72 and Pt/CNT cathodes. The EIS spectrum presented in (a) Nyquist plot and (b) Bode plots of the Pt/GCNT cathode obtained at 0.6 V before the degradation test. (c) equivalent circuit model used for the EIS data fitting. EIS spectra of (d) Pt/GCNT, (e) Pt/VXC72 and (f) Pt/CNT measured at 0.7 V, 0.6 V and 0.5 V, before the degradation test. 116

Figure 4-7. EIS spectra of the Pt/GCNT, Pt/VXC72 and Pt/CNT cathodes measured at 0.6 V, before and after the accelerated degradation test. 119

Figure 4-8. Cyclic voltammetry study of the Pt/GCNT, Pt/VXC72 and Pt/CNT cathodes during the accelerated degradation test. Cyclic voltammograms of the (a) Pt/GCNT, (b) Pt/VXC72 and (c) Pt/CNT cathodes measured before ADT and after 10, 20, 50, 100 cycles of oxidative potential cycling. The degradation of Pt electrochemical

surface area of the Pt/GCNT, Pt/VXC72 and Pt/CNT cathodes during ADT, plotted in (d) absolute specific surface area and (e) relative surface area with respect to the fresh electrodes. (f) carbon corrosion of the Pt/GCNT, Pt/VXC72 and Pt/CNT cathodes during ADT, expressed in term of relative changes in double layer capacitance..... 124

Figure 4-9. Electrode structural study using transmission electron microscopy. TEM micrographs of the Pt/VXC72 cathode (a) before and (b) after ADT, with (c) and (d) magnified views of the re-deposited Pt nanoparticles inside Nafion membrane. TEM micrographs of the Pt/GCNT cathode (e) before and (f) after ADT. 128

Figure 5-1. MoS_x-based catalysts preparation process. (a) Deposition current profile during the electrodeposition of MoS_x on conductive supports, with (inset) a magnified representation of the first five minutes of deposition, and (b) polarization curves during the reductive activation process of the 3 mg cm^{-2} MoS_x/GCNT/CP electrode reported on iR-corrected potential and (inset) non-iR-corrected potential scales. 135

Figure 5-2. Morphological characterization with FE-SEM of (a, b) the GCNT/CP support, and (c) the MoS_x/GCNT/CP electrode. (d) A schematic illustration of the GCNT/CP support and the MoS_x/GCNT/CP electrode. 139

Figure 5-3. Chemical analysis with XPS of the activated MoS_x/GCNT/CP electrode. (a) XPS survey spectrum and (b) high resolution scans in Mo 3d and S 2p regions. 141

Figure 5-4. Crystallinity analyses of the GCNT/CP and MoS_x/GCNT/CP electrodes with (a) Raman spectroscopy, with an inset showing the closed up spectrum of additional Raman bands from MoS_x and (b) X-ray diffraction..... 143

Figure 5-5. HER polarization curves of the MoS_x/GCNT/CP electrodes and reference samples presented on (a) linear scale and (b) Tafel plot. 146

Figure 5-6. Electrochemical impedance spectra of the MoS_x catalysts measured at overpotential η = 150 mV, presented on (a) Nyquist plot and (b) Bode plots. EIS spectra of the 3 mg cm^{-2} MoS_x/GCNT/CP electrode measured at overpotentials η of 100, 150 and 200 mV, presented on (c) Nyquist plot and (d) Bode plots. 151

Figure 5-7. Turnover frequency estimation for the 3 mg cm^{-2} MoS_x/GCNT/CP electrode. (a) Cyclic voltammetry curves measured in a potential window of 0-0.3 V *vs.* SHE at scan rates of 10, 20, 50 and 100 mV s^{-1}, and (b) deconvolution of the MoS_x/GCNT/CP electrode capacitive behavior by a linear fitting of the (capacitive current density)*(scan rate)$^{-1/2}$ *vs.* (scan rate)$^{1/2}$. 155

Figure 5-8. Degradation test of the MoS_x/GCNT/CP electrode, with HER polarization curves of the electrode before and after degradation presented on iR-corrected and (inset) non-iR-corrected potential scales. 157

Figure 5-9. XPS high resolution scans in Mo 3d and S 2p regions of the MoS_2 microcrystals and the MoS_x/GCNT/CP electrode after MoS_x deposition, after reductive activation and after degradation test. 159

Figure 5-10. HER polarization curves of the MoS_x/CNT/CP electrodes and reference samples presented on (a) linear scale and (b) Tafel plot. 163

Figure 5-11. Turnover frequency estimation for the 3 mg cm^{-2} MoS_x/CNT/CP electrode. (a) Cyclic voltammetry curves measured in a potential window of 0-0.3 V *vs.* SHE at scan rates of 10, 20, 50 and 100 mV s^{-1}, and (b) deconvolution of the MoS_x/CNT/CP electrode capacitive behavior by a linear fitting of the (capacitive current density)*(scan rate)$^{-1/2}$ *vs.* (scan rate)$^{1/2}$. 165

Figure 5-12. Degradation test of the MoS_x/CNT/CP electrode, with HER polarization curves of the electrode before and after degradation presented on iR-corrected and (inset) non-iR-corrected potential scales. 166

Figure 6-1. Supercapacitive performance of electrodes assessed by cyclic voltammetry. (a) Cyclic voltammograms of the MoS_x/GCNT/CP electrode at different scan rates from 10 mV s^{-1} to 100 mV s^{-1}, and those of the bare GCNT/CP support and MoS_x/Carbon paper electrode at a 20 mV s^{-1} scan rate. (b) The dependence of electrode specific capacitance on scan rate. (c) The deconvolution of capacitive behavior of the MoS_x/GCNT/CP electrode using a linear fitting method..... 172

Figure 6-2. Supercapacitive performance of electrodes assessed by galvanostatic charge/discharge test. (a) Charge/discharge curves of the MoS_x/GCNT/CP electrode performed at different charge/discharge rates from 0.67 A g^{-1} to 16.7 A g^{-1}. (b) The dependence of electrode specific capacitance on charge/discharge rate. (c) A comparison of the discharge capacitance of MoS_x/GCNT/CP with crystalline MoS_2-based electrode materials reported in the literature..... 175

Figure 6-3. Electrochemical impedance spectrum of the MoS_x/GCNT/CP electrode measured at –0.1 V, and (inset) the closed up view of the spectrum at high frequency region. 179

Figure 6-4. Degradation test of the MoS_x/GCNT/CP electrode performed by 500 charge/discharge cycles at 5 A g^{-1}, showing the degradation of electrode specific capacitance during the test, with (insets) plots of the first and last 10 charge/discharge cycles (time axes are referenced to the beginning of each 10-cycle set). 180

Figure 6-5. Supercapacitive performance of electrodes assessed by cyclic voltammetry. (a) Cyclic voltammograms of the MoS_x/CNT/CP electrode at different scan rates from 10 mV s^{-1} to 100 mV s^{-1}, and those of the bare CNT/CP support and MoS_x/Carbon paper electrode at a 20 mV s^{-1} scan rate. (b) The dependence of electrode specific capacitance on scan rate. (c) The deconvolution of capacitive behavior of the MoS_x/CNT/CP electrode using a linear fitting method. 182

Figure 6-6. Supercapacitive performance of electrodes assessed by galvanostatic charge/discharge test. (a) Charge/discharge curves of the MoS_x/CNT/CP electrode performed at different charge/discharge rates from 1.67 A g^{-1} to 16.7 A g^{-1}. (b) The dependence of electrode specific capacitance on charge/discharge rate. 185

Figure 6-7. Electrochemical impedance spectrum of the MoS_x/CNT/CP electrode measured at –0.1 V, and (inset) the closed up view of the spectrum at high frequency region. 186

Figure 6-8. EIS spectra and equivalent circuit fittings of the MoS_x/GCNT/CP, MoS_x/CNT/CP, and MoS_x/CP electrodes presented in (a) Nyquist plot and (b) Bode plots. (c) Equivalent circuit used for all fittings in (a, b). 187

Figure 6-9. Degradation test of the MoS_x/CNT/CP electrode performed by 500 charge/discharge cycles at 5 A g^{-1}, showing the degradation of electrode specific capacitance during the test, with (insets) plots of the first and last 10 charge/discharge cycles (time axes are referenced to the beginning of each 10-cycle set). 189

Figure 7-1. Effect of silicone resin infiltration and EsB imaging mode on the acquired SEM image quality. Secondary electron SEM images of the Pt/VXC72 PEMFC cathode catalyst layer (a) without and (b) with silicone resin infiltration. (c) EsB SEM image of the Pt/VXC72 PEMFC cathode catalyst layer with silicone resin infiltration. 198

Figure 7-2. The SEM image segmentation of the Pt/VXC72 cathode catalyst layer. (a) Original EsB SEM image of the cathode catalyst layer and (b) the corresponding segmented image, with identified phases of carbon materials (black), silicone-filled porous channels (gray), and Pt-containing phase (white). 201

Figure 7-3. 3D reconstructed nanostructure of the Pt/VXC72 PEMFC cathode catalyst layer, presenting (a) both carbon phase (green) and Pt-containing phase (red), (b) carbon phase only, and (c) Pt-containing phase only..... 203

Figure 7-4. 3D reconstructed nanostructure of the Pt/GCNT PEMFC cathode catalyst layer, presenting (a) both carbon phase (green) and Pt-containing phase (red), (b) carbon phase only, and (c) Pt-containing phase only..... 204

List of Abbreviations

2D	Two dimensional
3D	Three dimensional
ADT	Accelerated Degradation Test
Al/Fe	A bi-layer catalyst configuration of an aluminum buffer layer and an iron catalyst layer
BE	Binding Energy
BET	Brunauer–Emmett–Teller surface area and porosity analysis
CL	Catalyst Layer
CNT	Carbon Nanotubes
CNT/CP	Carbon Nanotubes grown on carbon paper
CP	Carbon fiber paper
CV	Cyclic Voltammetry
CVD	Chemical Vapor Deposition
ECSA	Electrochemical Surface Area
EDLC	Electrochemical Double Layer Capacitance/Capacitor
EDS	Energy Dispersive X-ray Spectroscopy
EIS	Electrochemical Impedance Spectroscopy
EsB	Energy selective Backscattered electron detection mode
FE-SEM / SEM	Field Emission Scanning Electron Microscopy
FIB	Focused Ion Beam
GCNT	Graphene-Carbon Nanotube hybrids
GCNT/CP	Graphene-Carbon Nanotube hybrids grown on carbon paper

GDL	Gas Diffusion Layer
HER	Hydrogen Evolution Reaction
HR-TEM	High Resolution Transmission Electron Microscopy
iR-corrected	Corrected for Ohmic loss
MEA	Membrane Electrode Assembly
MoS_x	Amorphous Molybdenum Sulfide
MoS_x/Carbon paper	MoS_x-deposited carbon paper
MoS_x/CNT/CP	MoS_x-deposited Carbon Nanotubes grown on carbon paper
MoS_x/Flat graphite	MoS_x-deposited flat graphite paper
MoS_x/GCNT/CP	MoS_x-deposited GCNT hybrids grown on carbon paper
non-iR-corrected	Original, not corrected for Ohmic loss
ORR	Oxygen Reduction Reaction
PEM	Proton Exchange Membrane / Polymer Electrolyte Membrane
PEMFC	Proton Exchange Membrane Fuel Cell
Pt/CNT	Pt-deposited CNT, or electrode based on Pt-deposited CNT
Pt/GCNT	Pt-deposited GCNT, or electrode based on Pt-deposited GCNT
Pt/VXC72	Pt-deposited Vulcan XC72 (carbon black), or electrode based on Pt-deposited Vulcan XC72
PTFE	Polytetrafluoroethylene
RF-PECVD / PECVD	Radio Frequency Plasma-Enhanced Chemical Vapor Deposition
RHE	Reversible Hydrogen Electrode potential
SHE	Standard Hydrogen Electrode potential

SOFC	Solid Oxide Fuel Cell
TEM	Transmission Electron Microscopy
TOF	Turnover Frequency
VXC72 / VXC72R	Vulcan XC72 / Vulcan XC72R (carbon black)
XPS	X-ray Photoelectron Spectroscopy
XRD	X-ray Diffraction

Chapter 1 : Introduction

1.1. The role of renewable energy and energy storage/conversion technologies in the future global energy landscape

In recent years, energy security has strongly emerged as one of the topmost global concerns. The world population is likely to continue increasing, and estimated to reach 9 billion in 2050. [1] The global energy demand is therefore expected to constantly increase in the future, especially with the rapidly increasing contribution from populous and emerging economies. This trend is reinforced by the energy demanding lifestyle of the world population. On the other hand, the non-renewable energy supply of the world is diminishing. Currently, the global energy supply relies heavily on fossil fuels. However, these sources of energy are no longer easily extractable, further exacerbated by the political instability of fossil fuel supplying countries. [2] The energy crisis is indeed happening and will be even more severe in the near future. It is therefore critical for humankind to find alternative energy sources to bridge the gap between the increasing energy demand and the diminishing energy supply. Coupled with the shortage of energy supply, environmental concerns, such as global warming and climate change due to the emission of greenhouse gases, provide a further push for the development of clean and renewable alternative energy sources. Such renewable energy sources are essential for sustainable development.

As interest in clean and renewable energy technologies increases, numerous technologies have been proposed and developed in parallel. Although tremendous efforts have been made to develop efficient and reliable clean alternative energy sources, there is no single clean energy technology superior enough to take the pivotal role for the global energy supply. The global clean energy supply will likely be from cooperative contributions of multiple environmentally friendly energy sources. Each technology has its own characteristic advantages and limitations. For example, although being non-renewable, nuclear energy is probably among the most mature clean energy sources and contributes significantly to global energy supply. Hydroelectricity, geothermal energy, wind energy, and solar energy are examples of renewable energy sources with virtually no greenhouse gas emissions. However, these technologies are restricted to specific geographical areas and are not available in all areas or countries. The aforementioned clean energy sources, namely nuclear energy, hydroelectricity, geothermal energy, wind energy and solar energy, are largely restricted to power grid and stationary applications. On the other hand, utilization of clean energy in high power mobile applications such as transportation requires high energy and power density energy storage and conversion devices, such as supercapacitors, rechargeable lithium batteries and fuel cells.

Supercapacitors are high-capacity electrochemical capacitors that bridge the gap between electrolytic capacitors and rechargeable batteries. Supercapacitors generally have much higher capacitances than electrolytic capacitors and higher rates of charging and discharging than rechargeable batteries. Supercapacitors store energy through electrostatic charge accumulation at the electrode/electrolyte

interfaces and/or through very fast and reversible redox reactions on the electrode surface. The characteristic advantages of supercapacitors are the high rates of charging and discharging, high power density, excellent cyclability, low self-discharging, safe operation and relatively low cost. [3] However, the energy density of supercapacitors is generally much lower than the requirements for a standalone power system for transportation, such as personal cars or public buses. Therefore, instead of aiming for a standalone power source, supercapacitors are most suitable as a secondary power source. One of the most promising applications of supercapacitors is their use in fuel cell vehicles, where supercapacitors are coupled with the high-energy density primary power sources (fuel cells) to absorb energy during car braking and release energy for a quick boost during acceleration. [3]

Rechargeable lithium batteries are electrochemical energy storage devices that store and generate electricity by conversion of chemical energy via reversible redox reactions between the electrolyte and the electrodes. Currently, the most common rechargeable lithium batteries are lithium-ion batteries (LIB). Compared to supercapacitors, lithium batteries have lower power densities and cannot be charged and discharged as fast. On the other hand, lithium batteries have higher energy density than supercapacitors. Lithium batteries can be used as standalone power sources for personal transportation. Nevertheless, there are two major drawbacks in the lithium battery technology. Firstly, lithium batteries store energy through the redox reactions between electrode materials and electrolyte. The electrode materials act as both the charge-transfer media and the active masses in the redox reactions. [4] Due to this closed-system characteristic of lithium batteries, once fully discharged,

lithium batteries have to be recharged to be operational. The recharging process generally takes long time, of the order of several hours. Secondly, the energy density held by lithium batteries is currently still lower than that of internal combustion engines. The lower energy density of lithium batteries renders a short drive range per charging cycle in these vehicles.

In contrast to supercapacitors and batteries, fuel cells are energy conversion devices. Fuel cells are electrochemical devices that convert directly chemical energy stored in fuels into electricity through electrochemical reactions of fuels with oxidants such as oxygen. [5] The most commonly used fuel is hydrogen, although other fuels such as alcohol are also proposed. In contrast to supercapacitors and lithium batteries, fuel cells function as a continuous power supply as long as fuels are available. In contrast to the closed-systems in lithium batteries, fuel cells are considered open systems, where the electrodes only act as the charge-transfer media for the redox reactions whilst the active masses (fuels and oxidants) are stored outside of the fuel cells. [4] The energy density of fuel cells depends explicitly on the volume of the fuel reservoir. The energy density of fuel cells can therefore be very high and comparable to internal combustion engines. Fuel cells are therefore capable of delivering a long drive range and considered a highly promising green energy technology for automotive applications. In addition, vehicles powered by fuel cells do not require a long time for refueling as in the case of lithium battery recharging. The refuel time for fuel cell vehicles is of the order of a few minutes, comparable to the regular internal combustion engine-based vehicles.

Simplified comparisons among different electrochemical energy conversion and storage systems, in terms of power density and energy density, are shown in Figure 1-1.

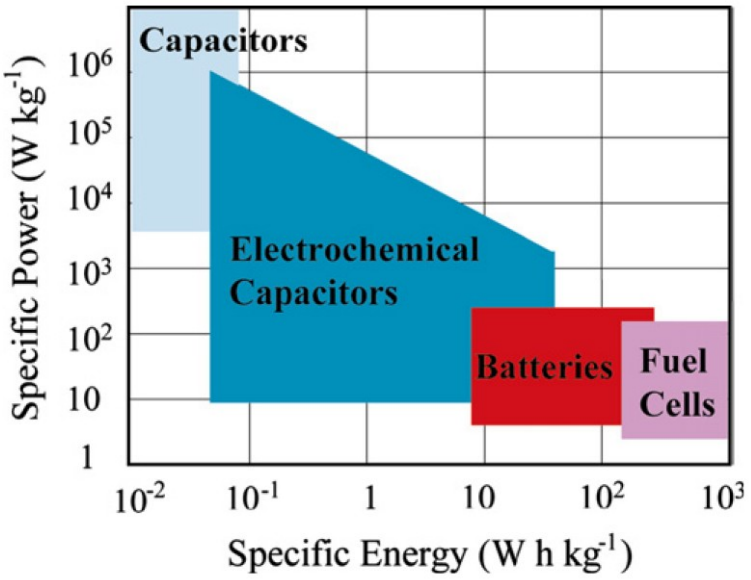


Figure 1-1. Simplified Ragone plot comparisons between different electrochemical energy conversion and storage systems. (Reprinted with permission from ref. [6] Copyright © 2012 Elsevier Ltd.)

Currently none of the electrochemical power sources has both power density and energy density comparable to the internal combustion engines. However, an appropriate combination of electrochemical power sources may be able to replace internal combustion engines. One promising combination is to use fuel cells as the primary power sources which have comparable energy density to combustion engines, coupled with supercapacitors as the secondary power sources which have high power density for instances when peak power is required. In this scenario, hydrogen — as the main fuel for fuel cell technologies — will become the primary energy carrier.

Hydrogen, possessing a high energy density, functions as an effective energy storage medium. In this ideal scenario, hydrogen is produced to store energy created by renewable energy sources, especially from intermittent sources such as solar or wind energy or from excess nuclear energy during off-peak hours of a day. [7-10] Hydrogen is available virtually infinitely in the form of water. Hydrogen gas, however, is not readily available in our earth atmosphere. Hydrogen gas has to be produced from water in various processes. Currently, the most widely used industrial process to produce hydrogen is the steam reforming reaction from coal or natural gases, [8,11] with CO and CO_2 generated as side products. For a fully sustainable and environmentally friendly scenario, hydrogen should be produced directly from water via hydrogen evolution reactions (HER) using renewable energy sources, [7] through processes such as photoelectrochemical water splitting or water electrolysis. [12] Hydrogen is then used to produce electricity on demand through energy conversion devices such as fuel cells, with the only byproducts being water and heat. [8] In this manner, hydrogen is cycled and ideally no greenhouse gases is emitted throughout the process. [8]

1.2. Introduction to Proton Exchange Membrane Fuel Cells (PEMFCs)

1.2.1. Main types of fuel cells

Fuel cells have attracted great attention recently owing to their high efficiency and low level of CO_2 emission. [5] The energy conversion efficiency of fuel cells can be as high as 60% [5] (fuel-to-electricity conversion efficiency), or up to 80-

90% (total energy conversion efficiency, when the wasted heat is recovered in a co-generation scheme). [2,13] Fuel cells are generally classified based on the electrolyte used. The five major types of fuel cells are: proton exchange membrane fuel cells (PEMFCs), solid oxide fuel cells (SOFCs), alkaline fuel cells (AFCs), phosphoric acid fuel cells (PAFCs) and molten carbonate fuel cells (MCFCs). [5] The choice of electrolyte in each type of fuel cells decides the suitable operating temperature range of the device, and in turn dictates other characteristics of the system, including material choices and fuels used. Table 1-1 provides a brief comparison of the key characteristics of the five main fuel cell types.

Table 1-1. A comparison of key characteristics of the main fuel cell types. (Adapted with permission from ref. [14] Copyright © 2003 John Wiley and Sons, and ref. [15] Copyright © 2009 Elsevier Ltd.)

	Electrolyte	**Mobile ion**	**Operating temperature**	**Fuel**	**Suitable applications**
PEMFC	Polymeric membrane	H^+	30-100 °C	Pure H_2	Vehicles and mobile applications
AFC	KOH	OH^-	50-200 °C	Pure H_2	Space vehicles
PAFC	Phosphoric acid	H^+	≈ 220 °C	Pure H_2	200 kW power stations
MCFC	Molten carbonate in $LiAlO_2$	CO_3^{2-}	≈ 650 °C	H_2, CO, CH_4, other hydrocarbons	Medium to large scale power stations
SOFC	Stabilized solid oxide (Y_2O_3/ZrO_2)	O^{2-}	500-1000 °C	H_2, CO, CH_4, other hydrocarbons	2 kW to multi-MW power stations

Among these five technologies, proton exchange membrane fuel cells (PEMFCs) are the most preferred option for vehicle and mobile applications. This is due to excellent characteristics of PEMFCs: high energy conversion efficiency, high power density, zero or low CO_2 emission, quiet operation, low operating temperature, quick start-up and fast response to changing of loads. [5,16]

1.2.2. PEMFC structure and components

Proton Exchange Membrane Fuel Cells (PEMFCs) are fuel cells that use proton conducting polymeric membranes as the electrolyte. Presently, the most successful and most common polymer electrolyte membrane is the Nafion® membrane series developed and manufactured by the E. I. DuPont Company. Typical reactant gases are purified hydrogen and oxygen/air. PEMFCs typically operate at between room temperature and 100 °C, and are the most suitable fuel cell technology for vehicles and mobile applications.

In a typical PEMFC system, multiple identical working units are serially connected together in "fuel cell stacks" to provide the required voltage and power as specified by the application. Each of the single functional units (or single cells) of the PEMFC stack includes a Membrane Electrode Assembly (MEA), where all electrochemical reactions take place, and a pair of current collectors/bipolar plates with gas flow channels providing both current collecting and reactant supplying/byproduct removing functions. An MEA consists of an anode, a proton conducting polymeric membrane and a cathode. Each electrode (i.e. anode or cathode) consists of a gas diffusion layer and a catalyst layer. An illustration of the fuel cell stack, a single cell, and the structure of an MEA is provided in Figure 1-2.

Gas diffusion layers (GDLs) and microporous layers

Gas diffusion layers (GDLs) are the two layers adjacent to the current collectors. The gas diffusion layer is commonly made of Polytetrafluoroethylene (PTFE)-coated Polyacrylonitrile (PAN) based carbon fiber paper.

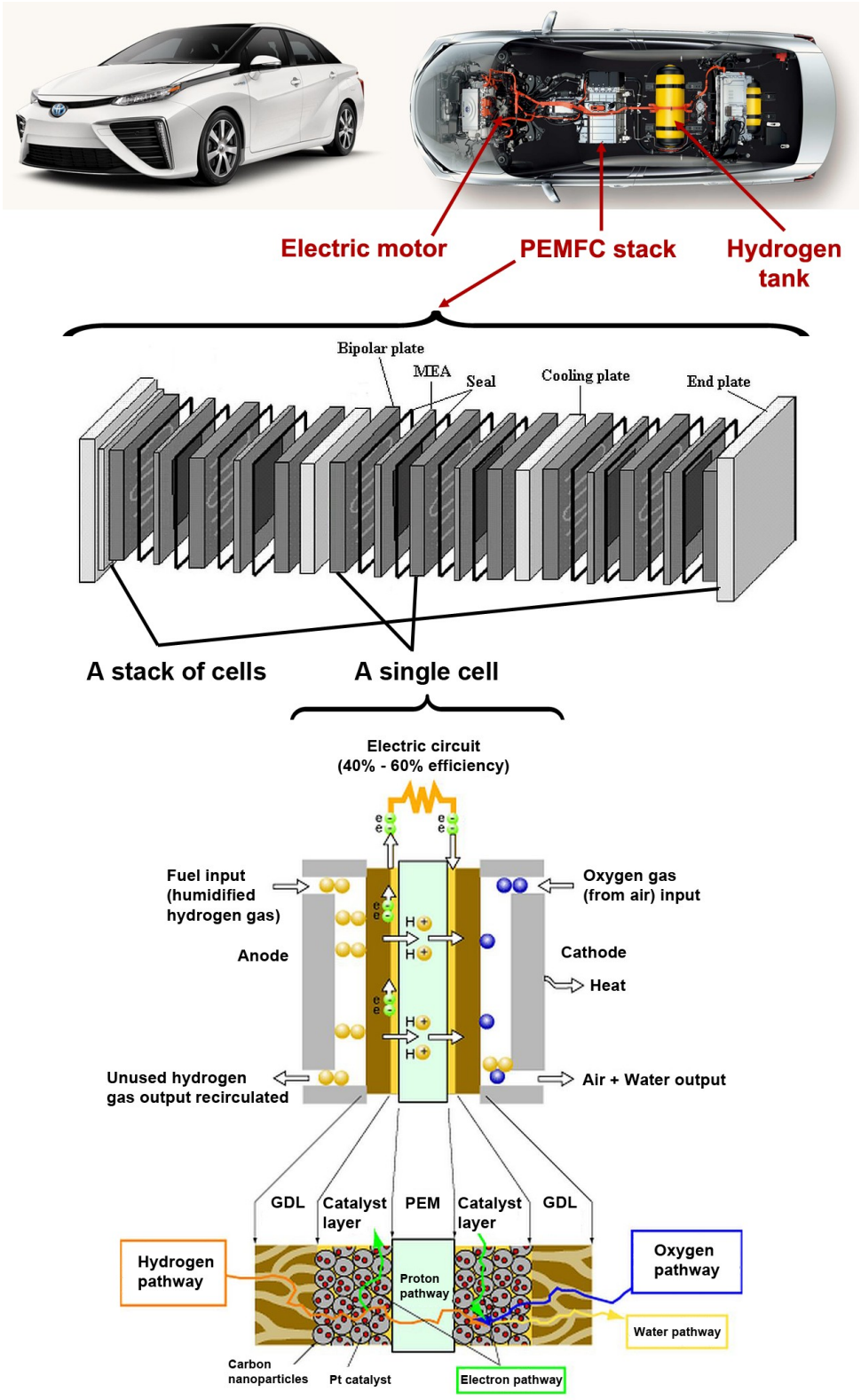


Figure 1-2. An illustration of the PEM fuel cell stack, a single cell, and the structure of a membrane electrode assembly. [5,16-19] (Adapted with permission from ref. [16] Copyright © 2002 Elsevier Science B.V., ref. [5] Copyright © 2010 Elsevier Ltd., and ref. [18] *"Electrochemistry Encyclopedia"* (http://knowledge.electrochem.org/encycl/) on 14/12/2015)

These macroporous carbon paper GDLs provide the mechanical support, electron pathways and reactant/byproduct transport pathways for the electrode. Typically, an additional microporous layer is added to each GDL. The microporous layer is constructed from high surface area carbon black, such as Vulcan XC72, and PTFE as the binder. The microporous layer is added to improve the uniformity of reactants and byproduct transport. Reactants are delivered from the current collectors through the gas flow channels, distributed by the carbon paper GDLs, and further evenly dispersed by the microporous layers before reaching the electrochemically active catalyst layers. The hydrophobicity in the microporous layers and GDLs also facilitate water removal from the fuel cell. In Figure 1-2, the carbon paper GDLs and microporous layers are simplified and together represented by the GDLs.

Catalyst layers

Catalyst layers are the two porous layers adjacent to the microporous layers, and sandwiching the polymeric membrane. These are the catalytically most important layers in the MEA, where all electrochemical reactions in PEMFCs take place. The electrochemical reactions in PEMFCs include the hydrogen oxidation reaction (HOR) in anode and the oxygen reduction reaction (ORR) in cathode. The electrochemical reactions in PEMFCs, especially the ORR, are sluggish. To achieve practical reaction rates, electrocatalysts are used for both reactions. Currently, the most common catalysts are nanosized platinum catalysts deposited on high surface area carbon black nanoparticles, such as Vulcan XC72. The catalyst layers are commonly constructed of carbon black-supported platinum catalysts and Nafion ionomer. The Nafion ionomer serves as both the binder and the proton conductor.

The impregnation of proton conducting Nafion ionomer in the catalyst layers is to maximize the availability of the triple-phase boundary (where protons, reactants and electrons concurrently meet on the platinum catalyst surfaces). The triple-phase boundaries (TPB) are the reaction sites of PEMFCs. The availability of TPB is critical for the catalytic activity and performance of PEMFCs.

1.2.3. PEMFC operation and electrochemistry

PEMFC operation principles

PEMFCs are electrochemical energy conversion devices, where the chemical energy stored in fuels and oxidants is directly converted to electrical energy through electrochemical reactions. The electrochemical reactions are essentially redox reactions, with the exception that the electron transfer processes in oxidation and reduction reactions are spatially separated. Instead of being transferred directly from reductants to oxidants, electrons are transferred through electrodes and rerouted to the external circuit to perform useful work.

In PEMFCs, all electrochemical reactions take place in the MEA. The electrochemical reactions in PEMFCs include the hydrogen oxidation reaction (HOR) in anode and the oxygen reduction reaction (ORR) in cathode. At the anode, after diffusing through the GDL and microporous layer to reach the anode catalyst layer, H_2 is catalytically split into protons and electrons on the surface of Pt catalyst nanoparticles through the HOR reaction. The newly formed protons diffuse through the polymer electrolyte membrane to the cathode. The newly formed electrons in the HOR are forced to flow to the cathode through the external circuit. At the cathode,

after diffusing through the GDL and microporous layer to reach the cathode catalyst layer, O_2 meets protons and electrons. O_2, protons and electrons are altogether catalytically combined on the surface of Pt catalyst nanoparticles through the ORR reaction. In this ORR reaction, water and heat are produced as byproducts. A schematic illustration of the MEA structure and the electrochemical processes in PEMFCs is shown in Figure 1-3.

The electrochemical reactions in PEMFCs are: [20]

- HOR at anode: $H_2 \rightarrow 2H^+ + 2e^-$ $E_a^\theta = 0.00\ V_{vs.\ SHE}$ (1-1)
- ORR at cathode: $\frac{1}{2}O_2 + 2H^+ + 2e^- \rightarrow H_2O$ $E_c^\theta = 1.229\ V_{vs.\ SHE}$ (1-2)
- Overall reaction: $H_2 + \frac{1}{2}O_2 \rightarrow H_2O$ $E^\theta = 1.229\ V$ (1-3)

(SHE denotes the Standard Hydrogen Electrode potential.)

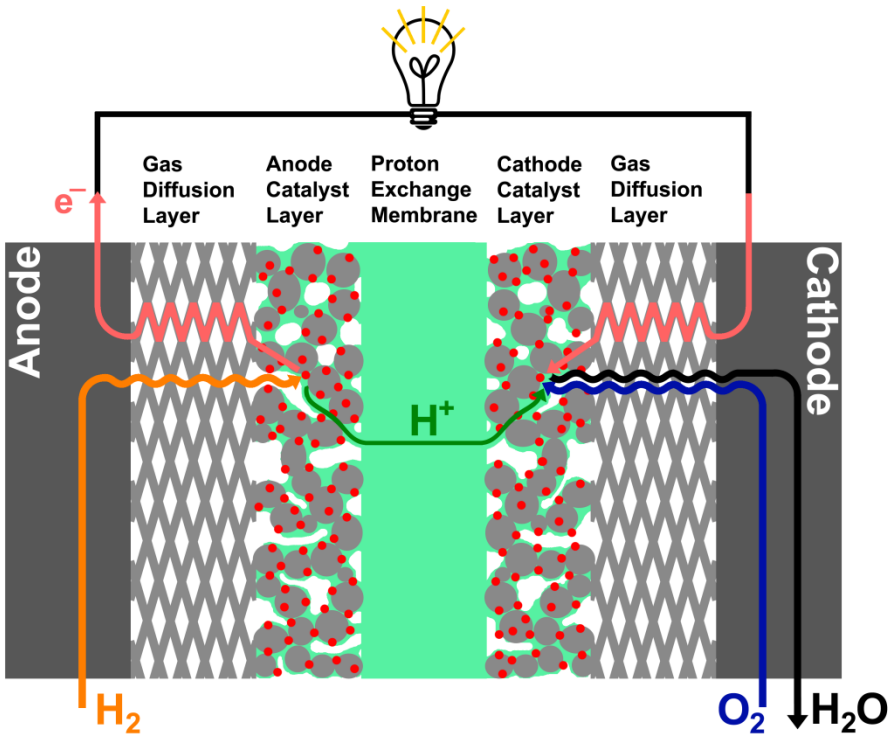


Figure 1-3. A schematic illustration of the MEA structure and the electrochemical processes in PEMFCs.

Open circuit potential

The theoretical open circuit potential of hydrogen fuel cells is dependent on both temperature and pressure according to the Nernst equation: [20]

$$E = \frac{-\Delta G}{nF} = E^{\theta} + (T - T^{0})\frac{\Delta S^{0}}{nF} + \frac{RT}{nF}\ln\left[\frac{p_{O_2}^{1/2}\, p_{H_2}}{p_{H_2O}}\right] \quad (1\text{-}4)$$

in which E is the voltage of the fuel cell, ΔG is the Gibbs free energy change of the reaction, F is Faraday constant (96485 C mol^{-1}), and n is the number of moles of electrons transferred in the reaction (n = 2 in this case). E^{θ} = 1.229 V is the theoretical open circuit potential at standard temperature and pressure (T^{0} = 298.15 K, 1 atm), T is the cell temperature, ΔS^{0} is the entropy change of the reaction which is approximately constant. R is the universal gas constant (8.314 J mol^{-1} K^{-1}). p_{H_2}, p_{O_2}, p_{H_2O} are partial pressures of hydrogen, oxygen and vapor, respectively.

PEMFC efficiency

The efficiency of fuel cells is defined as the ratio between the useful energy output (electrical energy produced) and the energy input (enthalpy of reaction). [20] The maximum (theoretical) efficiency of a PEMFC at 25 °C is: [20]

$$\eta_{max} = \frac{\Delta G^{\theta}}{\Delta H^{\theta}} = \frac{-237\ \text{kJ mol}^{-1}}{-286\ \text{kJ mol}^{-1}} = 83\% \quad (1\text{-}5)$$

in which ΔG^{θ} = –237 kJ mol^{-1} and ΔH^{θ} = –286 kJ mol^{-1} are the standard Gibbs energy and enthalpy changes of reaction at the standard states (298.15 K, 1 atm).

The actual efficiency of the fuel cell during operation is defined as the actual cell voltage divided by the thermoneutral potential ($E = -\Delta H^{\theta}/nF$ = 1.48 V): [20]

$$\text{Cell efficiency} = \frac{E_{cell}}{1.48} \times 100\% \quad (1\text{-}6)$$

Polarization / Overpotential

The previously discussed theoretical cell potential at equilibrium is purely from the thermodynamic viewpoint. In practical operating conditions, a finite current has to be drawn from the fuel cell to perform useful work. In this case, the fuel cell reaction deviates from the thermodynamic equilibrium conditions. The actual cell potential deviates from the equilibrium open circuit potential by a potential drop known as overpotential or polarization, denoted as ΔE. There are three major overpotential elements that cause the cell potential loss at a finite current, namely activation overpotential, ohmic overpotential, and concentration/mass transport overpotential. The actual cell potential can be expressed as:

$$E_{cell} = E_{OCV} - \Delta E_{act} - \Delta E_{ohm} - \Delta E_{con} \quad (1\text{-}7)$$

where E_{OCV} is the equilibrium open circuit voltage at the actual temperature, pressure and supplied reactant concentrations, ΔE_{act} is the activation overpotential, ΔE_{ohm} is the ohmic overpotential, and ΔE_{con} is the concentration/mass transport overpotential.

Activation overpotential or activation loss arises from the need to extract a practical current density or reaction rate from the two half-cell reactions (HOR and ORR). The overpotential is required to activate and speed up the charge transfer processes in the reactions, particularly due to the sluggish reaction kinetics of the ORR. The HOR is generally considered fast and reversible, especially with the present of platinum catalysts. The activation overpotential caused by HOR is negligible. In contrast, a significant activation overpotential for ORR is generally required for a practical current density.

Ohmic overpotential arises from the voltage drop caused by the internal resistance of the fuel cell, including ionic resistance of the polymer electrolyte membrane, electronic resistance of electrodes and contact resistance. The ohmic overpotential follows the simple Ohm's law, $\Delta E_{ohm} = iR_{ohm}$, where R_{ohm} is the total internal resistance of the fuel cell. In most PEMFCs, the total resistance is dominated by the ionic resistance of the membrane, whilst the electronic resistances are much smaller.

Concentration overpotential or mass transport overpotential arises from the drop in reactant concentrations at the reaction sites as they are consumed in the reaction, especially at high current densities. The available reactant concentrations at a particular current density are dependent on the diffusion rate of the reactants through the GDLs and catalyst layers, which ultimately depends on the microstructure of the GDLs and catalyst layers as well as the supplied reactant pressures and water accumulation inside the electrodes.

1.2.4. Challenges of PEMFCs

Despite their great potential, PEMFCs have not yet reached the stage of worldwide commercialization. The two main commercialization barriers for PEMFCs are the high cost and insufficient durability. [5] The performance of PEMFCs often degrades slowly during their lifetime. The performance degradation is believed to be caused by at least several phenomena, including Pt catalyst aggregation/coalescence, Pt dissolution (and re-deposition inside the membrane), and Pt detachment due to the corrosion of carbonaceous supports. [21,22] Pt catalyst aggregation/coalescence

happens when Pt catalyst is dissolved in the form of soluble ions (such as Pt^{2+}) at high potentials and then re-deposited on nearby Pt catalyst nanoparticles. [21,23] The aggregation/coalescence process results in a decrease of the active Pt electrochemical surface area, and therefore a degradation of the device performance. Pt re-deposition in Nafion membrane happens when platinum ions diffuse into the membrane and re-deposit as isolated Pt nanoparticles. [21,24-26] These isolated Pt nanoparticles are not active in electrochemical reactions and result in a loss of electrode activity. Pt loss can also happen in the form of Pt catalyst detachment caused by the corrosion of carbonaceous supports. [27,28] The carbon support is thermodynamically unstable under the operating condition of PEMFCs (high water content, high potential, and elevated temperature) and can be oxidized according to the following reaction: [29]

$$C + 2H_2O \rightarrow CO_2 + 4H^+ + 4e^- \qquad E^\theta = 0.207\ \text{V}\ vs.\ \text{SHE} \qquad (1\text{-}8)$$

Carbon corrosion is however kinetically limited, and is slowed down with an increase in the crystallinity of carbon support. Carbon corrosion may lead to a severe degradation of PEMFC performance due to the detachment of Pt catalysts from the carbon support. [27]

1.2.5. Design of carbon support for PEMFCs

Presently, the most popular electrocatalysts in PEMFC electrodes are Pt nanoparticles deposited on carbon black materials, such as Vulcan XC72. Carbon black materials possess high porosity and high surface area, which are useful for Pt catalyst dispersion. However, these characteristics in carbon black materials are largely contributed by micropores smaller than 1 nm. [30] Catalyst nanoparticles located within small pores (< 20 nm) are poorly accessible by Nafion ionomers and

do not contribute to the electrochemical reactions in fuel cells, resulting in low catalyst utilization. [30] The tortuous channels of small pores within carbon black electrodes also limit the reactant diffusion processes. In addition, carbon black materials are susceptible to corrosion under PEMFC working conditions due to their low crystallinity, exacerbated by the present of platinum catalysts. [31]

A good carbon support for electrocatalysts in PEMFC electrodes should have a large fraction of pores sized 20-40 nm to enhance catalyst utilization, good electrical conductivity and high crystallinity. [30] Graphitic nanomaterials including carbon nanotubes (CNTs) and graphene, with their extraordinary electrical and mechanical properties, can offer more advanced alternatives. CNTs have been employed as alternative catalyst supports in PEMFCs with promising performance and durability. [27,32,33] However, in order to achieve a higher dispersion of Pt nanoparticles, the inert graphitic basal plane surface of CNTs generally requires functionalization, which may significantly reduce their electrical conductivity. [34] In contrast to CNTs, graphene can offer edge plane anchor sites for Pt catalyst nanoparticles. Furthermore, it has been suggested that the heterogeneity of carbon support with edge planes can better stabilize and enhance catalytic activity of Pt catalysts. [34] However, the two-dimensional morphology of graphene could impede the transport of reactants inside the fuel cell, due to the tendency to re-stack graphene unless graphene is suitably aligned. It is, therefore, useful to arrange graphene in such a structure that maximizes the exposure of graphene edge planes and does not block the reactant transport pathways. By directly growing graphene onto the CNT structure, one could have both the exposed edge planes from the

graphene and the porous structure of the CNT in a single material, suitable for an advanced catalyst support in PEMFCs.

In order to best utilize the potential of graphene as catalyst support for PEMFCs, we propose the growth and use of a hierarchical carbon nanostructure in which CNTs are grown directly on Toray carbon paper and freestanding graphene is directly grown on the porous CNT scaffold. We refer to this material as Graphene-Carbon Nanotube hybrids (GCNT). Ideally, CNTs should be grown directly on carbon fiber paper for the best possible conductivity of the carbon support. Graphene is grown directly on CNT scaffold. The GCNTs will then be deposited with Pt catalyst and impregnated with Nafion ionomer. This electrode structure is hypothesized to provide better reactant diffusion, enhanced catalyst activity, lower internal resistance, and therefore improve the overall PEMFC's performance. The Pt/GCNT catalyst is further hypothesized to provide superior electrochemical durability over the conventional carbon black supported Pt catalysts, due to the high crystallinity of GCNT. A schematic illustration of the proposed GCNT carbon support structure is provided in Figure 1-4.

It is well known that CNTs can be grown on various substrates, most commonly silicon wafer, using chemical vapor deposition methods. [35-37] CNTs have also been successfully grown on carbon fiber paper for various applications. [32,38,39] Freestanding graphene, also known as carbon nanowalls, was successfully grown on various substrates using microwave plasma enhanced chemical vapor deposition (MWPECVD), [40-43] inductively coupled PECVD, [44] parallel plate PECVD with H-

radical injection, [45-47] hot filaments chemical vapor deposition (CVD), [48] and radio frequency PECVD. [49]

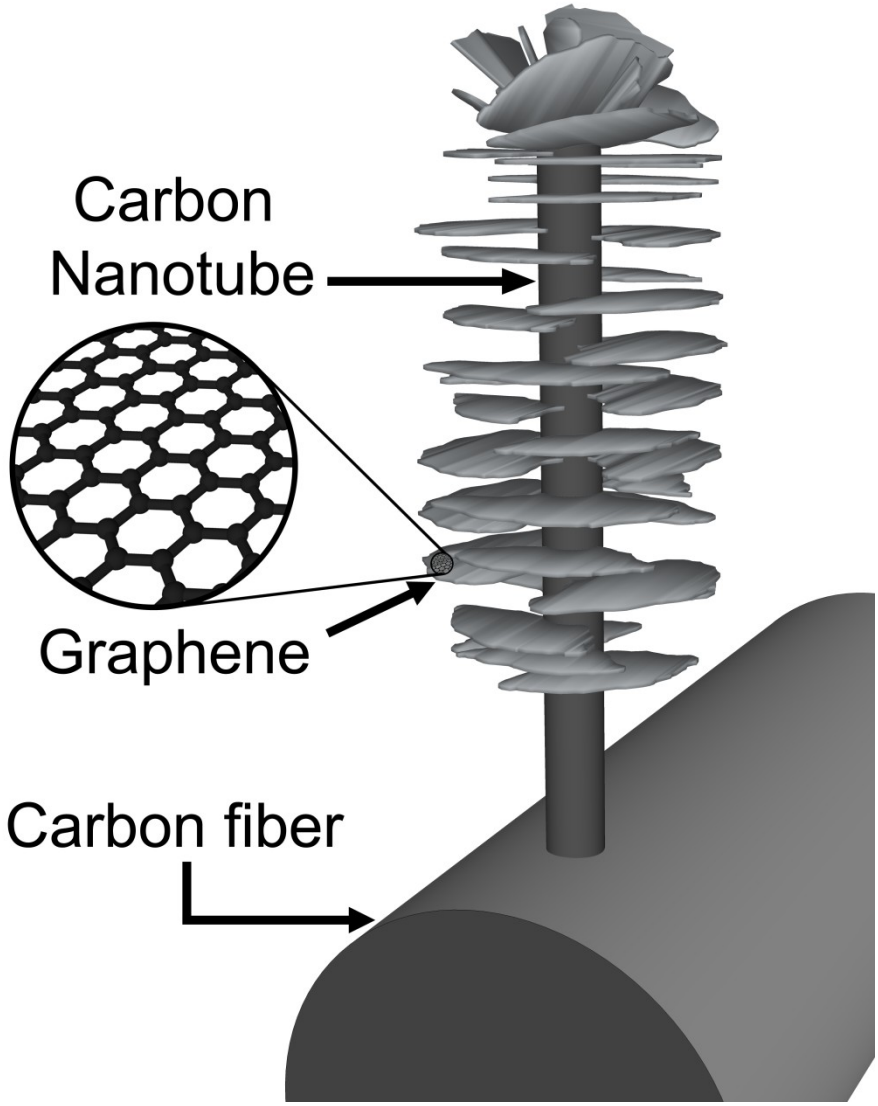


Figure 1-4. A schematic illustration of the proposed GCNT structure.

Graphenated CNT is a relatively new member of the carbon nanomaterial family. There have been a number of publications investigating this new promising material. Saito *et al.* successfully grew carbon nanowalls onto pre-grown single-walled CNT surface using hot-filament CVD method. [50] Parker *et al.* reported the

growth of three-dimensional arrays of graphenated CNTs using MWPECVD. [51] Rout *et al.* similarly grew arrays of graphene on CNTs using a three-step MWPECVD method. [52] Feng *et al.* reported the growth of graphene on CNTs using the water-assisted CVD method. [53] A number of exciting properties of this novel carbon material have been reported in the literature. [50,51,54-56] These include high surface area [50] and enhanced charge storage capacity in electrochemical capacitor applications, explained by the inherent high charge density of the graphene edges in the graphenated CNT material. [51] The graphene sheets are also believed to bond inherently to CNTs through sp^2 carbon and result in low graphene-CNT junction resistance. [54] Graphenated carbon nanotube hybrid structures were investigated for various applications, including electronic and optoelectronic applications, [54] supercapacitors, [55,56] and recently the application of a related structure (carbon nanowalls on carbon nanofibers) in electron field emission. [57] Chen *et al.* reported the growth of graphitic nanoflakes on CNT template using bias assisted MWPECVD method and suggested the application of such material in fuel cells, but without as yet any information on a working fuel cell reported. [58] Du *et al.* reported the growth of graphene nanosheets on CNTs on carbon cloth using MWPECVD and applied in PEMFCs. [59] The graphene-on-CNT electrode showed promising power output performance. However, the graphene nanosheets were grown only sparsely on the CNT surface. No investigation of the electrochemical stability of such electrode was reported in the publication. Further study of the graphene-carbon nanotube hybrids as catalyst support in PEMFCs is required, in term of both catalytic activity and electrochemical stability.

1.3. Introduction to Hydrogen Evolution Reaction (HER)

1.3.1. Hydrogen Evolution Reaction (HER)

In the previous section, we have discussed fuel cell technologies, specifically PEMFCs, which are the key energy conversion devices to produce electricity from hydrogen fuel. A reversed and equally important process is the production of hydrogen. Whilst hydrogen element is available virtually infinitely in the form of water, hydrogen gas, however, is not readily available in our earth atmosphere. For a fully sustainable and environmentally friendly scenario, hydrogen should be produced directly from water using renewable energy sources, [7] through processes such as photoelectrochemical water splitting or water electrolysis. [12] The water splitting reactions in acidic media are summarized as following: [60,61]

- Total reaction: $H_2O \rightarrow H_2 + \frac{1}{2}O_2$ $E^{\theta} = 1.23$ V (1-9)
- HER at cathode: $2H^+ + 2e^- \rightarrow H_2$ (1-10)
- OER at anode: $H_2O \rightarrow \frac{1}{2}O_2 + 2H^+ + 2e^-$ (1-11)

To split water efficiently, catalysts are required in both half-reactions, namely hydrogen evolution reaction (HER) and oxygen evolution reaction (OER). In this thesis, we focus on the hydrogen evolution reaction (HER) catalysts.

Electrochemistry of Hydrogen Evolution Reaction

The hydrogen evolution reaction in acidic media is believed to involve three possible reaction steps: [60]

- Volmer step: $H^+ + e^- \rightarrow H_{ad}$ (1-12)
- Heyrovsky step: $H^+ + H_{ad} \rightarrow H_2$ (1-13)
- Tafel step: $2H_{ad} \rightarrow H_2$ (1-14)

The first step in the HER reaction is the generation of adsorbed hydrogen atom (H_{ad}) on the electrode surface (Volmer step). After the generation of H_{ad}, the HER may proceed through the Heyrovsky step (Volmer-Heyrovsky mechanism) or through the Tafel step (Volmer-Tafel mechanism). [61] Regardless of the two mechanisms, H_{ad} is always involved in the HER. The free energy of the hydrogen adsorption process (ΔG_H) is widely considered the descriptor for the catalytic activity of HER catalytic materials. [61] If the hydrogen-catalyst surface bond is too weak, the reaction rate is limited by the slow hydrogen adsorption process. If the bond is too strong, the reaction rate is limited by the slow desorption step. Optimal HER catalysts should have a free energy of hydrogen adsorption close to $\Delta G_H = 0$. [60] Figure 1-5 illustrates the dependence of exchange current density (or catalytic activity) on the free energy of hydrogen adsorption for various HER catalyst materials, demonstrating a "volcano plot" relationship. [62]

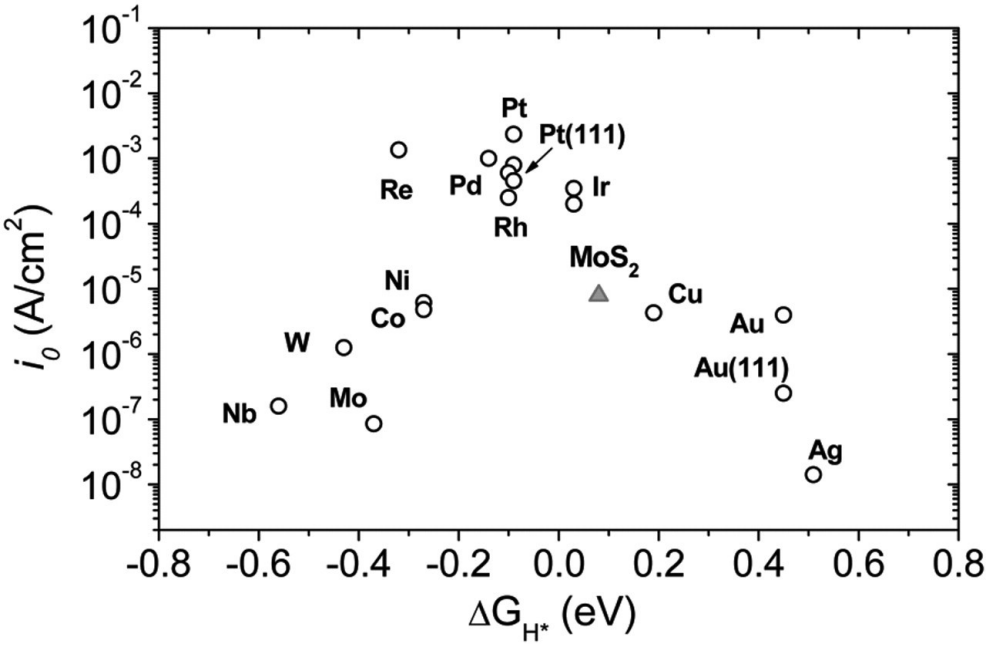


Figure 1-5. Dependence of exchange current density on hydrogen adsorption free energy for various HER catalyst materials. (Reprinted with permission from ref. [62] Copyright © 2007, American Association for the Advancement of Science)

Parameters for catalytic activity comparisons

There are two major merits for the catalytic activity comparison of HER catalyst materials. The first merit is the total electrode activity, based on the geometric electrode area-normalized total activity. The total electrode activity is important from the practical device performance point of view. The second merit is the intrinsic activity of the material, based on the per-reaction site Turnover frequency (TOF) which is the number of reactions at a reaction site per second.

Total electrode activity

Total electrode activity is an important parameter from the practical device performance point of view. It provides information on the actual catalytic current density obtained when a specific potential is applied to the electrode. For non-precious catalyst materials, the cost of materials is not a major concern. In such cases, the total electrode activity is the most relevant parameter. The total electrode activity can be measured through a cyclic voltammetry or a linear sweep voltammetry, similar to a polarization curve discussed in the PEMFC measurements. From the linear sweep voltammogram/polarization curve, generally the following parameters can be extracted to facilitate the comparison of catalytic activity among HER catalyst materials:

- Overpotential required to obtain a current density of 10 mA $cm^{-2}_{electrode}$: a lower required overpotential indicates a higher total electrode activity.
- Tafel slope and exchange current density: A Tafel plot depicts the dependence of the required overpotential on the desired catalytic current density. Generally,

the overpotential (η) is related logarithmically to the current density (j) according to the Tafel equation $\eta = a + b \log (j)$. [61] From the Tafel equation, the Tafel slope (b), and the exchange current density (j_0) (j at $\eta = 0$) can be extracted. The Tafel slope b partly reflects the reaction mechanism on the catalyst material. A small Tafel slope is desirable, as it predicts a higher obtained current density with an increase in overpotential. The exchange current density j_0 describes the catalytic activity of the electrode under equilibrium condition. A high j_0 is desirable for catalyst materials.

Intrinsic activity (Turnover frequency, TOF)

Turnover frequency depicts the intrinsic activity of the catalytic reaction sites. It is important for the fundamental understanding of the catalytic activity of the materials. Practically, it is challenging to directly determine the TOF of the material from experimental measurements. It can, however, be inferred indirectly from other measurements. The TOF is fundamentally related to the total electrode activity. With the knowledge of the total electrode activity ($j(\eta)$) and the reaction site areal density, the TOF can be estimated. The reaction site density is also challenging to measure directly. However, it can be estimated through a measurement of the electrochemically active surface area (ECSA) as well as a reference to a standard flat sample.

1.3.2. Molybdenum Sulfide catalysts for HER

To enhance the hydrogen evolution reaction efficiency, electrocatalysts are required. Currently, the most active HER catalysts are precious metal-based

catalysts, such as platinum. [12] However, both the high cost and scarcity of these precious metals have been limiting their uses. Non-precious catalysts are therefore critical for a large scale implementation of hydrogen economy. Molybdenum sulfide has recently emerged as a very promising class of non-precious HER catalyst with high catalytic activity and good stability in acid. It has been known for decades that bulk crystalline molybdenum disulfide (MoS_2) is inactive towards HER. [60] However, in a seminal bio-inspired computational study, Hinnemann *et al.* found that the hydrogen adsorption free energy on the edge of MoS_2 crystals is very close to zero, similar to Pt, [63] as shown in Figure 1-6. The result raises the possibility of a high catalytic activity of MoS_2 crystal edge sites towards HER. Jaramillo *et al.* further confirmed that the electrocatalytic activity of MoS_2 nanoparticles in hydrogen evolution reaction correlates linearly with the number of edge sites, rather than surface area, of the MoS_2 crystals. [62]

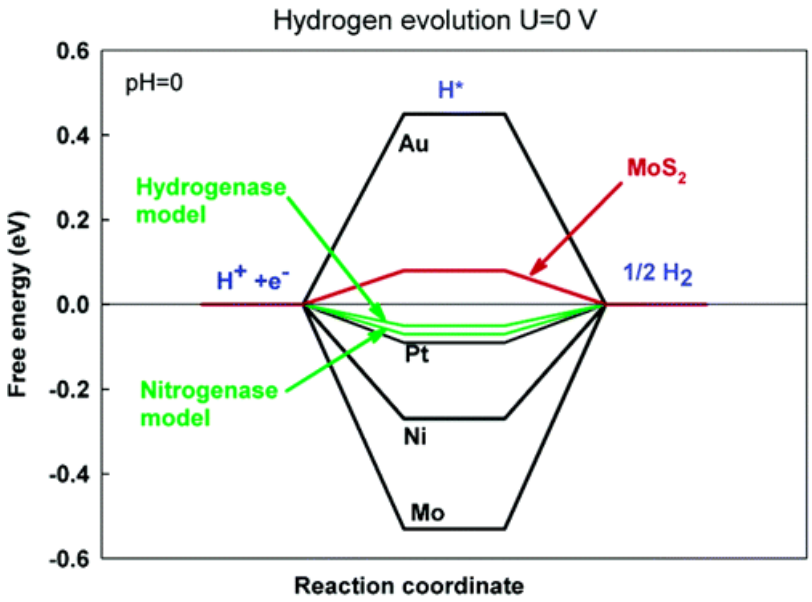


Figure 1-6. Calculated free energy diagram for hydrogen evolution reaction at standard hydrogen electrode potential and pH = 0 for various materials. (Reprinted with permission from ref. [63] Copyright © 2005, American Chemical Society)

Crystalline MoS_2

Following the theoretical prediction of the edge site high catalytic activity and the pioneering identifications of the active edge sites of MoS_2 crystals, numerous efforts have been made to engineer the nanostructure of MoS_2 crystals to maximize the exposure of the edge sites available for HER reaction. Several representative approaches to maximize the availability of MoS_2 edge sites are summarized in Figure 1-7. In the first approach, MoO_{3-x} nanowires were used as a high surface area and conductive support for MoS_2, synthesized by surface sulfidization of the MoO_3 core. [64] The structure promises a large exposed surface area for MoS_2. However, MoS_2 layers are found to preferentially curve around the circumference of the nanowire and result in a low density of exposed active edge sites. The catalytic activity of the material is rather modest. In the second approach, MoS_2 layers are vertically aligned to the substrate. [65] This geometry promises a high density of exposed active edges. Nevertheless, the measured catalytic activity is low, probably due to the low specific surface area of electrode. With further optimization of the electrode surface area, this approach may result in very exciting catalytic activity. In the third approach, MoS_2 nanosheets were purposefully synthesized with a high defect density to create extra active reaction centers. With the introduction of defect sites, the material shows an obvious enhancement in the catalytic activity compared to defect-free MoS_2. [66] Reduced graphene oxide was also used to support the growth of MoS_2 nanoparticles. Graphene provides both internal electron transport channels and strong chemical coupling to disperse the MoS_2 nanoparticles. The material shows excellent activity, with a Tafel slope of 41 mV $decade^{-1}$ and a current density of 10 mA cm^{-2} at ≈150 mV overpotential. [67]

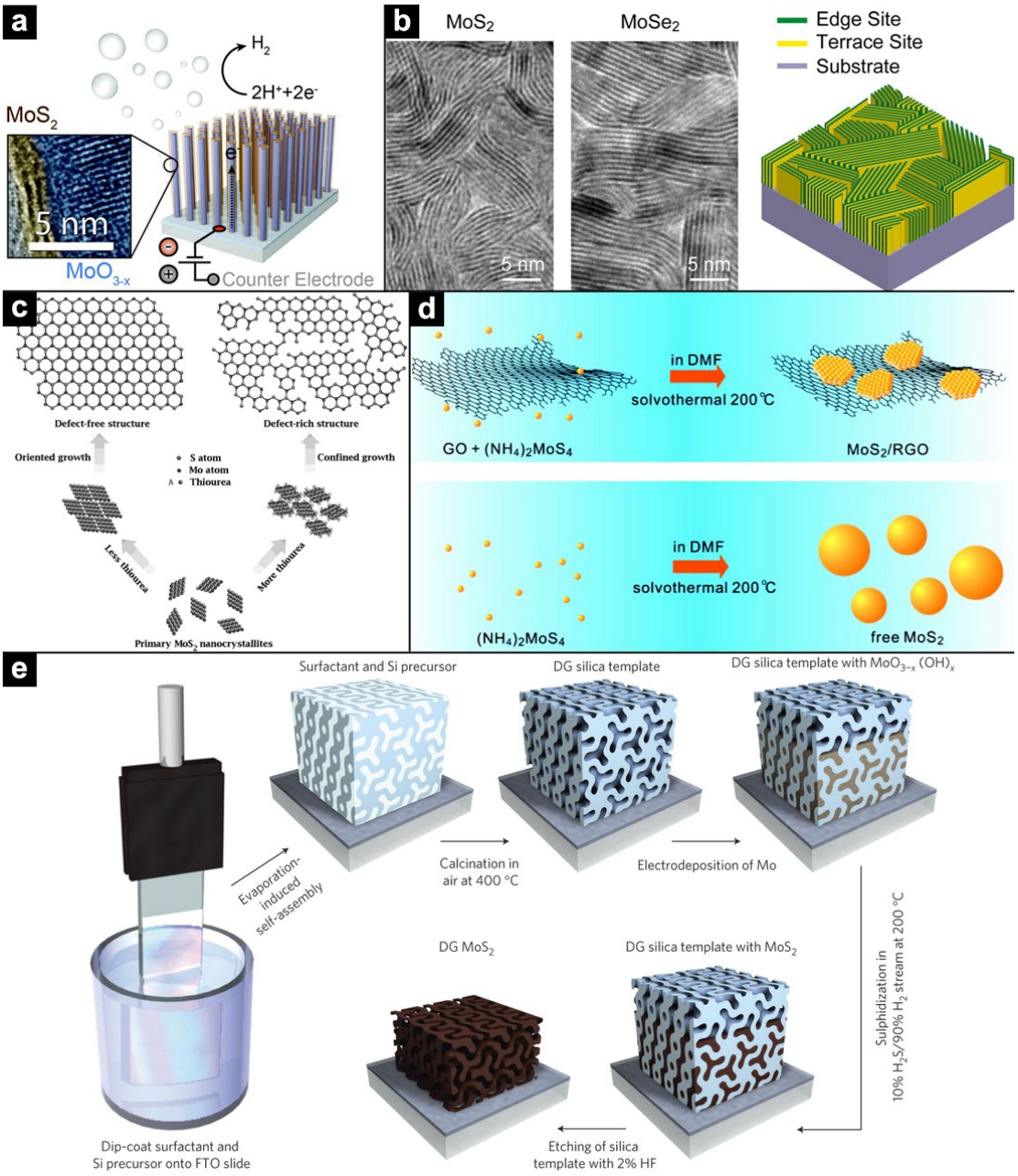


Figure 1-7. Representative optimization approaches for crystalline MoS_2 nanomaterials for HER. (a) MoS_2/MoO_{3-x} nanowires, [64] (b) vertically aligned MoS_2 and $MoSe_2$, [65] (c) defect-rich MoS_2 nanosheets, [66] (d) MoS_2 nanoparticles on graphene, [67] and (e) MoS_2 double-gyroid mesoporous structure. [68] (Adapted with permission from ref. [64] Copyright © 2011, American Chemical Society, ref. [65] Copyright © 2013, American Chemical Society, ref. [66] Copyright © 2013 WILEY-VCH Verlag GmbH & Co. KGaA, Weinheim, ref. [67] Copyright © 2011, American Chemical Society, and ref. [68] Copyright © 2012, Nature Publishing Group)

Lastly, MoS_2 was also fabricated to form a mesoporous double-gyroid structure using templating methods. The structure possesses high surface area and high density of exposed active edge. Nevertheless, the measured activity remains modest with a current density of 10 mA cm^{-2} at 220 mV overpotential. [68] The above approaches show that whilst enhanced activities are indeed obtained by maximizing the density of exposed active edges, coupling MoS_2 with high surface area conductive support is also highly important for enhanced catalytic activity of MoS_2.

Amorphous MoS_x

Amorphous materials are often ignored due to the uncertainty in the atomic structure of the materials. However, as found in the previous studies, defects and edge sites are highly valuable in the catalytic activity of MoS_2 towards HER. Amorphous molybdenum sulfide (MoS_x) intrinsically possesses abundance of defect sites and under-coordinated sulfur atoms, and is therefore a promising catalyst for HER reaction. [69] In contrast to the limited edge sites of crystalline MoS_2, the HER-active defect sites of amorphous molybdenum sulfide are present throughout the entire surface of the catalyst and are readily available for catalytic reactions. The high activity towards HER of amorphous molybdenum sulfide has been successfully demonstrated in the literature. [69-73] As an additional advantage, amorphous molybdenum sulfide can be synthesized easily at room temperature using wet chemical methods [71,74] or electrodeposition methods, [12,69] in contrast to the elevated temperature syntheses of crystalline MoS_2. With both high catalytic activity and benign synthesis conditions, amorphous molybdenum sulfide is a highly promising

catalyst material for hydrogen evolution reaction applications. In this thesis, we will use amorphous molybdenum sulfide (MoS_x) as the active HER catalyst material.

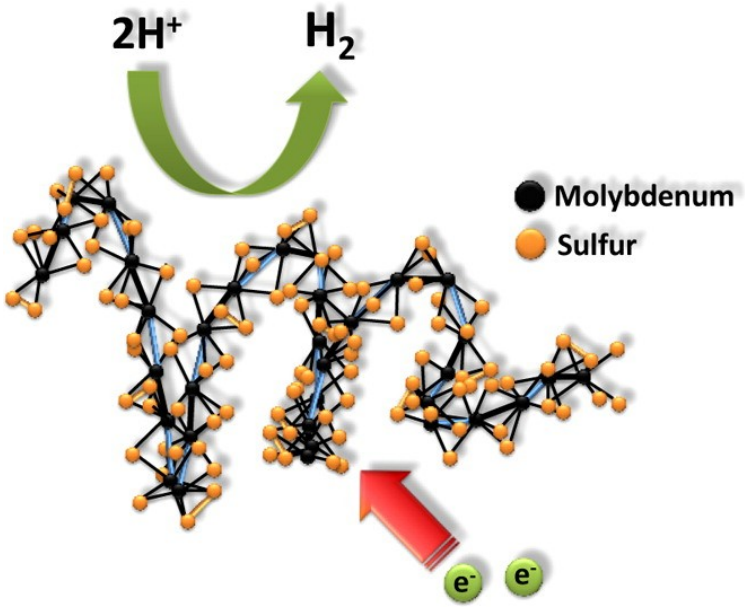


Figure 1-8. Amorphous MoS_x as HER catalyst materials. (Reprinted with permission from ref. [12] Copyright © 2014, American Chemical Society)

1.3.3. Graphene-Carbon Nanotube hybrids as catalyst support for amorphous Molybdenum Sulfide in HER applications

Molybdenum sulfide materials generally have low electronic conductivity. [75] The low electronic conductivity of molybdenum sulfide materials is detrimental to their catalytic activity towards HER. [12] The low electronic conductivity of molybdenum sulfide may also limit the maximum electrochemically active catalyst loading in practical devices. It is therefore rational to design a composite electrode structure with molybdenum sulfide catalysts deposited on a high surface area conductive support, to enhance the electron transport towards the catalytic active sites and therefore maximize the activity of the catalysts. As previously

demonstrated in the literature, [67] by electronically coupling MoS_2 to a conductive support of reduced graphene oxide, the catalytic activity of MoS_2 is substantially enhanced. The graphene-supported MoS_2 is among the most active MoS_2 catalyst materials. However, similar to other electrochemical devices such as PEMFCs, the HER reaction on the electrode requires constant reactant supply and product removal. The mass transport inside the electrode is critical for the high performance of devices, especially at high current density ranges. Graphene and reduced graphene oxide have a two-dimensional morphology and have a tendency to re-stack. The re-stacking of graphene and reduced graphene oxide could hinder the mass transport processes inside the electrode and is therefore detrimental to the electrode performance at high current density ranges.

To address a similar issue in PEMFCs, we previously proposed in section 1.2.5 a hierarchical nanostructure of Graphene-Carbon Nanotube hybrids (GCNT) on Toray carbon paper as catalyst support material. In this nanostructure, CNTs are grown directly on carbon paper, and subsequently, graphene is directly grown onto CNT surface. The growth of graphene directly on the porous CNT scaffold effectively eliminates the re-stacking issue of regular 2D graphene, and at the same time provides more secured anchor points for deposited catalyst materials than CNTs alone. Such an electrode structure could also be suitable as the catalyst support for the deposition of amorphous molybdenum sulfide in HER applications. In this proposed electrode structure, GCNT serves as a high specific surface area, porous and conductive support for the deposition of amorphous molybdenum sulfide. Carbon paper serves as both a mechanical support and a current collector. As GCNT

is grown directly onto the carbon paper current collector, the electronic conductive pathways from amorphous molybdenum sulfide to the current collector are enhanced. The integrated, conductive, high surface area and porous nanostructure of GCNT can effectively enhance both electron transport and mass transport in the HER electrode.

1.4. Introduction to supercapacitors

In section 1.1, we recognized that none of the current electrochemical power sources has both power density and energy density comparable to internal combustion engines. However, an appropriate combination of electrochemical power sources can be a viable candidate. One promising combination is to use fuel cells as the primary power sources which have comparable energy density to the combustion engines, coupled with supercapacitors as the secondary power sources which have high power density for instances when a peak power is required. In fact, the application as a secondary power source in fuel cell vehicles is one of the most promising aspects of supercapacitors. [3] Supercapacitors have attracted much research attention for their high power density, long service life and quick charge/discharge capability. [75-77]

1.4.1. Operating principle of supercapacitors

Supercapacitors (or ultracapacitors) are electrochemical energy storage devices that store electrical energy in form of electrostatic charge accumulation at the electrode/electrolyte interfaces (in electrical double layer capacitors – EDLCs) and/or

via fast and reversible redox reactions (in *pseudo*-capacitors). *Pseudo*-capacitors store energy through fast and reversible redox reactions between electrolyte and electro-active species on the electrode surface. [3] Due to the Faradaic origin, *pseudo*-capacitors generally have much higher capacitance than EDLCs. However, the downside is the lower power density, slower response and lack of stability during cycling. [3,76] One classic example of the *pseudo*-capacitor electrode materials is hydrous ruthenium oxide ($RuO_2.xH_2O$), with a very high specific capacitance of 1300 F g^{-1} reported. [78] Upon charge and discharge, the following reversible redox reaction takes place on the electrode surface: [78]

$$RuO_a(OH)_b + \delta H^+ + \delta e^- \leftrightarrow RuO_{a-\delta}(OH)_{b+\delta} \quad (1\text{-}15)$$

Schematic illustrations of charge storage process of electrochemical double-layer capacitance, and *pseudo*-capacitance are provided in Figure 1-9.

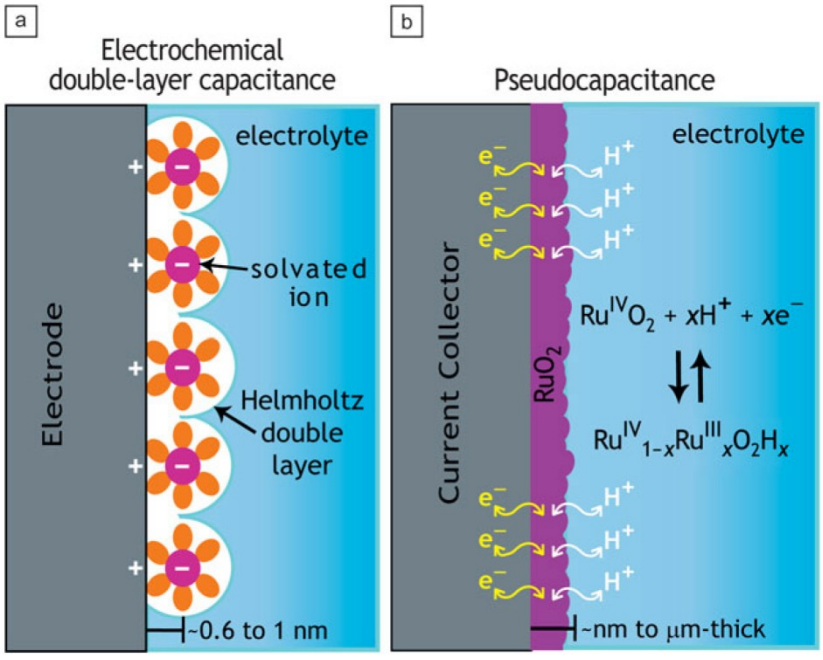


Figure 1-9. Schematic illustrations of charge storage process of (a) electrochemical double-layer capacitance, and (b) *pseudo*-capacitance. (Reprinted with permission from ref. [79] Copyright © 2011, Materials Research Society)

1.4.2. Amorphous molybdenum sulfide (MoS_x) as a supercapacitor electrode material

Whilst hydrous ruthenium oxide exhibits superior *pseudo*-capacitance, the high cost of the precious metal oxide limits its practical applications. To find cheaper and more practical alternatives, other electrode materials have been actively investigated for application in supercapacitors, for example, metal oxides, [80,81] metal hydroxides, [82,83] metal sulfides, [84,85] to name a few. Transitional metal chalcogenides such as WS_2, MoS_2, Ni_3S_4 have recently emerged as promising supercapacitor electrode materials. [75,84-92] One notable example in this family of materials is molybdenum disulfide (MoS_2). Naturally occurring crystalline MoS_2 has a layered crystal structure similar to graphite. MoS_2 has been actively studied for various applications such as hydrogen evolution reaction catalysts, [60,63,67] lithium batteries electrode materials, [93,94] and supercapacitor electrode materials. [81,88] MoS_2 is used as a supercapacitor electrode material due to its higher ionic conductivity than metal oxides and its higher specific capacitance than graphite. [75] Whilst much research attention has been paid so far on crystalline MoS_2, [75,85,88-91] little attention has been paid to its amorphous form, except for one recent study reporting the use of amorphous MoS_2 as an encapsulating material for Ni_3S_4. [92] Amorphous molybdenum sulfide possesses many advantageous merits that can warrant further attention. In supercapacitors, charge storage in MoS_2 can occur via the double layer charging on the external surface of the material or via the diffusion of ions into the inter-layer space of MoS_2. The diffusion of ions into the inter-layer space occurs only through the open edge sites of MoS_2, due to the anisotropic layered structure of

crystalline MoS_2. To enhance this diffusion process, Soon and Loh strategically oriented the open edge planes of MoS_2 to maximize the availability of these "entry" sites. [87] In contrast, the amorphous form of materials generally has more open and isotropic atomic structure. [95] The diffusion of ions in amorphous molybdenum sulfide is therefore not limited by the availability of edge sites. The diffusion of ions may happen throughout the entire surface of the material. In fact, the diffusion coefficient of lithium ions in amorphous molybdenum sulfide was found to be several orders of magnitude higher than that in crystalline MoS_2. [95,96] The electrical conductivity of amorphous molybdenum sulfide was also found to be two orders of magnitude higher than that of crystalline MoS_2. [95] The higher electronic conductivity of amorphous molybdenum sulfide is highly beneficial for a better supercapacitive performance. Furthermore, in layered materials such as graphene and MoS_2, it was suggested that edge sites and defect sites in the material structure are more electro-active than the basal plane atoms and can enhance the electrode capacitance. [97] Amorphous molybdenum sulfide potentially contains an abundance of defect sites. We believe that the contribution of defect sites in amorphous molybdenum sulfide to the total capacitance is non-trivial and deserves further attention. As an additional advantage, amorphous molybdenum sulfide can be synthesized easily at room temperature using wet chemical methods [71,74] or electrodeposition methods, [12,69] in contrast to the higher temperature syntheses of crystalline MoS_2. In this thesis, we investigate the supercapacitive properties of amorphous molybdenum sulfide (MoS_x) as the main active material.

1.4.3. Graphene-Carbon Nanotube hybrids as support materials for amorphous Molybdenum Sulfide in supercapacitor applications

Although molybdenum sulfide potentially has higher specific capacitances than graphite, it is generally less electronically conductive than graphitic materials. [75] The lower electronic conductivity of molybdenum sulfide could be detrimental to its high charge/discharge rate performance. It is therefore rational to design a composite electrode structure with amorphous molybdenum sulfide deposited on a high surface area conductive support, to enhance the electron transport towards the active material and therefore maximize the electrode capacitance and high power performance. In section 1.3.3, we proposed the GCNT hybrid nanostructure to support the deposition and to enhance the electronic conductivity for MoS_x HER catalyst materials. We find that the two applications pose nearly identical material requirements. We therefore consider that the proposed GCNT-supported MoS_x electrode structure is equally suitable for the supercapacitor electrode applications. The same material structure therefore will be used for both HER and supercapacitor electrode applications.

1.5. Research objectives

Throughout our earlier discussions, we recognize a common need for an advanced carbon support material in electrochemical device applications, including Pt catalyst support in PEMFC cathodes, as well as carbon support for MoS_x in HER

and supercapacitor applications. The ideal carbon supports for these applications share the following material requirements:

- High specific surface area conductive carbon support for an efficient dispersion of active materials and efficient electron transport towards electro-active sites of the active materials.
- High porosity for efficient mass transport of reactants and products.
- High crystallinity for a high electronic conductivity and better electrochemical stability.
- High density of graphitic edges for enhanced catalytic activity and stability.

To address these requirements of an advanced carbon support, we proposed a hierarchical carbon nanostructure of Graphene-Carbon Nanotube hybrids grown directly on Toray carbon paper, as described in detail in section 1.2.5. The core intrinsic properties of the proposed GCNT-on-carbon paper nanostructure include: high specific surface area, high crystallinity, high density of graphitic edges, integrated and conductive nanostructure for direct and efficient electron transport, highly porous nanostructure for efficient mass transport. The porous carbon paper substrate allows the mass transport to proceed from both sides of the electrode.

Possessing these desirable properties, the proposed GCNT-on-carbon paper nanostructure presents a versatile platform for deposition of active materials in electrochemical applications. As proofs of concept, the proposed GCNT hybrids will be developed and used as the carbon support material for Pt catalyst in PEMFC cathodes, for MoS_x in HER and supercapacitor electrode material applications.

The objectives of this thesis, therefore, include:

- ***Systematically develop a fabrication procedure to synthesize the proposed nanostructure of GCNT hybrids on carbon paper.*** — The growth of GCNT directly on carbon fiber paper at high density has not been well demonstrated in the literature.

- ***Study the application of GCNT hybrids as the Pt catalyst support in PEMFC cathodes.*** — Presently, the most commonly used carbon support material for Pt in PEMFCs is carbon back (e.g. Vulcan XC72). The material suffers from strong degradation during PEMFC operation. Whilst GCNT materials suggest interesting properties (i.e. high crystallinity, high density of graphitic edge, etc.) and can be suitable as an advanced support material in PEMFCs, such an application has not been studied in detail. Both catalytic activity and electrochemical durability are important properties of PEMFC catalysts. The effects of GCNT on these properties have not been well documented. In this thesis, the effect of the GCNT hybrids on the device performance, Pt catalytic activity and electrochemical durability will be investigated. The GCNT hybrids are hypothesized to provide enhanced catalytic activity due to the high density of graphitic edges and enhanced electrochemical durability due to the high crystallinity of GCNT hybrids.

- ***Study the application of GCNT hybrids as the conductive support materials for MoS_x as HER catalysts.*** — Whilst MoS_x has been identified as a highly active non-precious HER catalyst material, MoS_x has been commonly

deposited on low surface area supports such as glassy carbon electrode or simple carbon paper. The low electronic conductivity of MoS_x is highly detrimental to the total activity of the material. An efficient method to well disperse, and enhance both electron transport and mass transport to the active sites of MoS_x has not been well achieved. Depositing MoS_x on a high surface area, conductive, integrated and highly porous carbon structure could be a new avenue to maximize the catalytic activity of MoS_x. In this thesis, GCNT hybrids directly grown on carbon paper will be used as the carbon support material for the deposition of MoS_x and applied as a catalyst material for HER. This work would be the first report on such a structure of MoS_x/GCNT/CP and its application in HER. The GCNT hybrids are hypothesized to enhance the catalytic activity of MoS_x towards HER due to the enhanced material dispersion, efficient electron transport to the electro-active sites, and efficient mass transport due to the high porosity of the electrode.

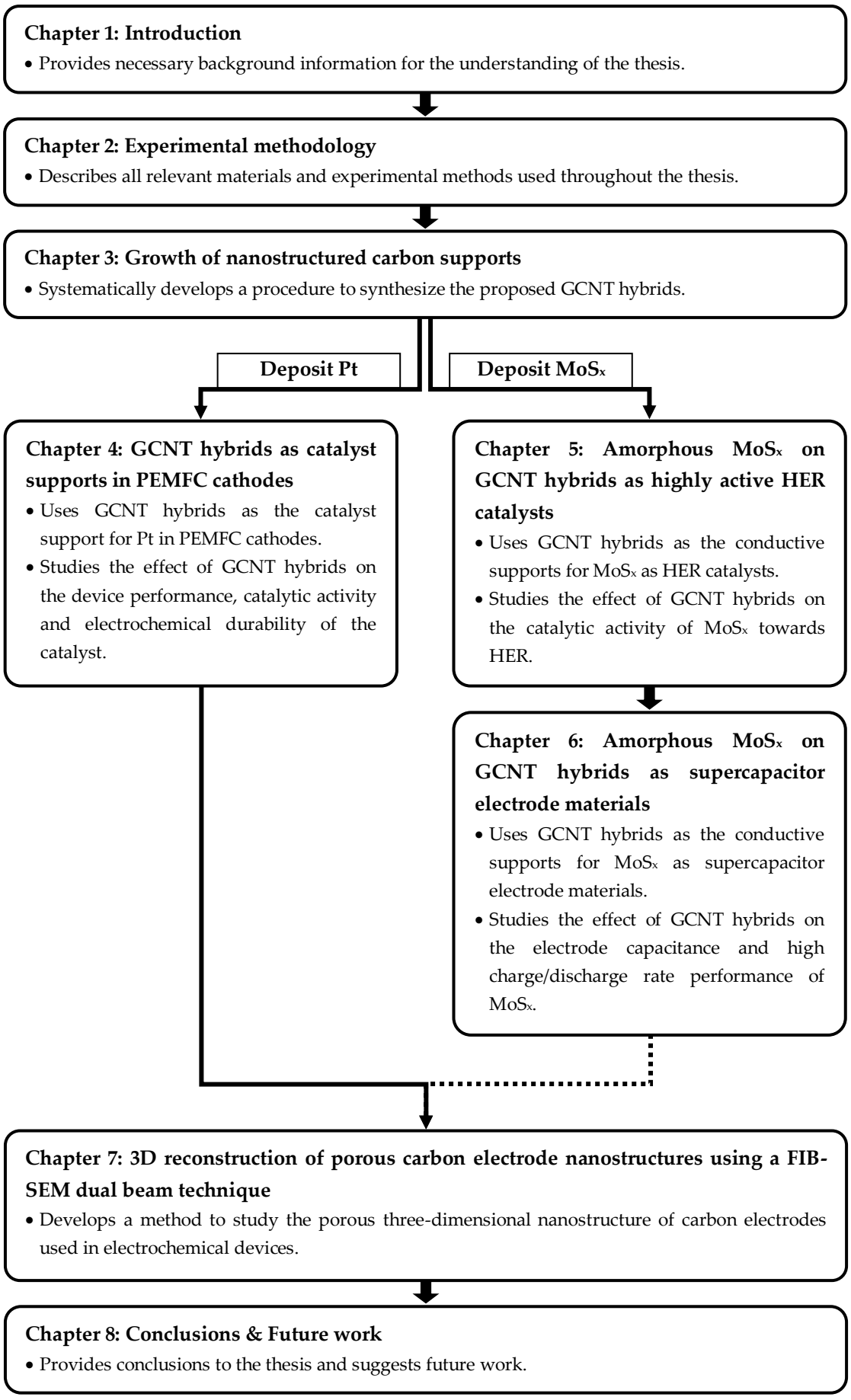
- ***Study the application of GCNT hybrids as conductive support materials for MoS_x as supercapacitor electrode materials.*** — MoS_x has been identified as a potential supercapacitor electrode material with advantageous properties compared to the crystalline MoS_2. The use of MoS_x as the main supercapacitor electrode material has not been reported in the literature. MoS_x in general and MoS_x/GCNT/CP in particular will be for the first time investigated for such application. Effects of the GCNT support on the capacitance of MoS_x will be studied. The GCNT hybrids are hypothesized to

enhance the electrode capacitance and high charge/discharge rate performance, due to the enhanced material dispersion and efficient electron transport to the electro-active sites.

- ***Develop a method to study the three-dimensional (3D) porous nanostructure of carbon electrodes commonly used in electrochemical devices.*** — Understanding the truly 3D characteristics of electrode structures is of great interest in the development and optimization of electrochemical devices. FIB-SEM tomography is an invaluable tool for 3D reconstruction of electrode structures. However, the FIB-SEM-based 3D reconstruction technique for carbon electrodes is frequently challenged by the lack of contrast between carbon electrode materials and impregnated epoxy resin. In this thesis, a combination of silicone resin impregnation and Energy selective Backscattered electron imaging mode will be used to overcome the lack of contrast issue. As a proof of concept, the method is focused on the catalyst layer of PEMFC cathodes. The method is, however, hypothesized to be easily applicable for other related carbon-based electrodes used in other electrochemical devices.

1.6. Thesis structure

Following the stated objectives, the thesis devotes one chapter for each and every one of the aforementioned five research objectives. The structure of thesis is summarized in the following flowchart:


Chapter 1: Introduction
• Provides necessary background information for the understanding of the thesis.
Chapter 2: Experimental methodology
• Describes all relevant materials and experimental methods used throughout the thesis.
Chapter 3: Growth of nanostructured carbon supports
• Systematically develops a procedure to synthesize the proposed GCNT hybrids.
Deposit Pt
Deposit MoSx
Chapter 4: GCNT hybrids as catalyst supports in PEMFC cathodes
• Uses GCNT hybrids as the catalyst support for Pt in PEMFC cathodes.
• Studies the effect of GCNT hybrids on the device performance, catalytic activity and electrochemical durability of the catalyst.
Chapter 5: Amorphous MoSx on GCNT hybrids as highly active HER catalysts
• Uses GCNT hybrids as the conductive supports for MoSx as HER catalysts.
• Studies the effect of GCNT hybrids on the catalytic activity of MoSx towards HER.
Chapter 6: Amorphous MoSx on GCNT hybrids as supercapacitor electrode materials
• Uses GCNT hybrids as the conductive supports for MoSx as supercapacitor electrode materials.
• Studies the effect of GCNT hybrids on the electrode capacitance and high charge/discharge rate performance of MoSx.
Chapter 7: 3D reconstruction of porous carbon electrode nanostructures using a FIB-SEM dual beam technique
• Develops a method to study the porous three-dimensional nanostructure of carbon electrodes used in electrochemical devices.
Chapter 8: Conclusions & Future work
• Provides conclusions to the thesis and suggests future work.

Chapter 2 : Experimental methodology

This chapter is devoted to a thorough description of materials and experimental methods used throughout the thesis. The experimental methods are broadly categorized into three sections, namely sample preparation, *ex situ* material characterization, and electrochemical evaluation methods. The sample preparation section describes the methods for carbon supports (CNT, free-standing graphene and GCNT) fabrication, PEM fuel cell electrodes and membrane electrode assembly fabrication, and the electrodeposition method for MoS_x in HER and supercapacitor electrode applications. The *ex situ* material characterization section describes various physical methods to characterize the properties of the carbon support and electrode materials. Lastly, the electrochemical evaluation section describes the electrochemical methods to characterize the electrochemical properties of the electrodes in PEMFC, HER and supercapacitor applications.

2.1. Sample preparation methods

2.1.1. Carbon support fabrication methods

Magnetron sputtering deposition of catalyst materials

Sputtering deposition is a physical vapor deposition method used for thin film deposition with precise controls of the thin film thickness. The process involves the ejection of target materials due to the bombardment of plasma ions on the target

surface. Sputtering sources commonly use strong magnetic fields to confine charged particles (i.e. ions and electrons) close to the target surface, and hence are given the name "Magnetron sputtering". The confinement of electrons near the target surface intensifies the ionization of the sputtering gas (i.e. Ar) and sustains the plasma at low pressure. A schematic illustration of the magnetron sputtering deposition process is shown in Figure 2-1. In the sputtering chamber, an inert gas such as argon is filled at a low pressure. Under a high radio frequency electric field, Ar atoms are ionized, accelerated toward the cathode, and bombard on a target of desired materials for deposition. Due to the high energy bombardment, atoms and ions of the target material are ejected, then travel toward the substrate and deposit as a thin film of the target material on the substrate surface.

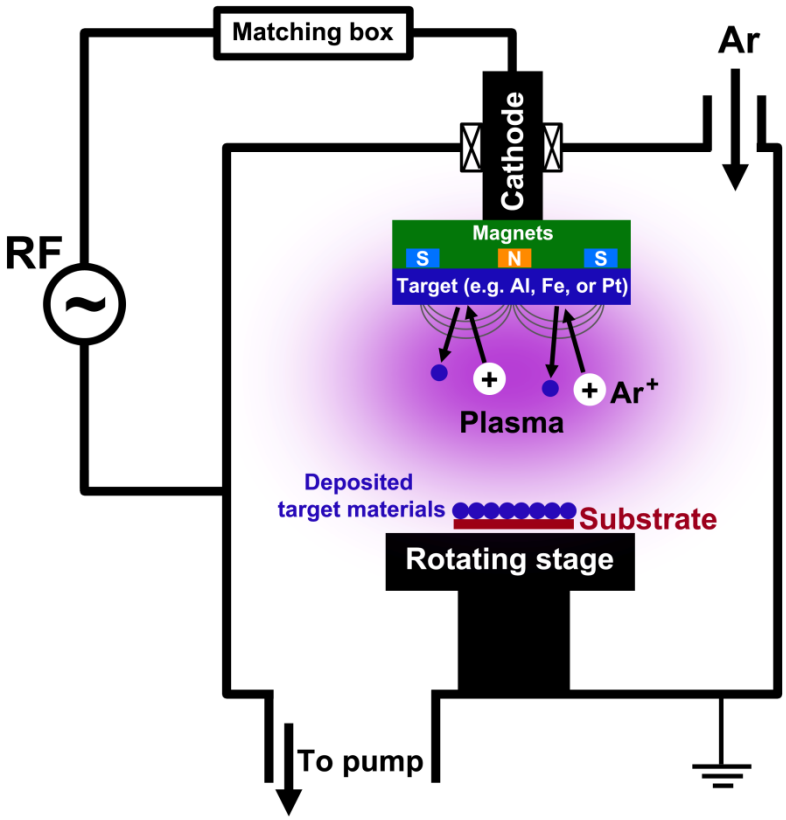


Figure 2-1. A schematic illustration of the magnetron sputtering deposition process.

In this study, a radio frequency magnetron sputtering system (Denton Vacuum Discovery 18) was used to subsequently deposit thin films of aluminum and then iron onto carbon paper as the catalysts for the growth of CNTs on carbon paper. The carbon paper used throughout the thesis was TGP-H-090 carbon fiber paper from Toray Industries (carbon paper thickness of 280 μm, bulk density 0.44 g cm^{-3}, porosity 78%, electrical resistivity 80 mΩ cm (through plane) / 5.6 mΩ cm (in plane)). Both RF and DC magnetron sputtering can provide excellent deposition conditions for metallic materials. Nevertheless, the RF magnetron sputtering was used in this study, firstly due to the immediate availability of the system to our lab. Secondly, for the same parameters, RF magnetron sputtering provides lower deposition rates, and therefore provides a finer control of the thin film thickness (10–25 nm thick). Thirdly, RF sputtering can operate at lower pressures than DC sputtering, and therefore possibly reduces contamination to the deposited films. The thin film thicknesses were controlled by plasma power and deposition time. For a typical experiment, carbon paper substrate size was 2.25 × 2.25 cm^2 (5 cm^2). Radio frequency was 13.56 MHz. Process pressure was 12 mTorr. Base pressure (before starting sputtering process) was < 5 × 10^{-6} Torr. Substrate stage rotation speed was 12 rpm. For the catalyst deposition of 25 nm Al / 10 nm Fe, the plasma power and deposition time were 100 W, 5 min (25 nm Al) and 50 W, 160 s (10 nm Fe).

Thermal chemical vapor deposition (CVD) for CNT growth

Thermal chemical vapor deposition (CVD) is a method to deposit solid materials from their gaseous precursors onto substrates. Among different applications, CVD is well known as an efficient method to grow CNTs. A schematic

illustration of the thermal CVD setup used for the CNT growth is shown in Figure 2-2. The CVD is simply constructed of a quartz tube placed inside an electric furnace. The gaseous precursor are passed through the quartz tube, where a substrate is placed inside. At high temperature inside the furnace, the gaseous precursors decompose, especially when assisted with a suitable catalyst on the substrate, and deposit as a solid material on the substrate. Thermal CVD is a widely used deposition technique, due to its simple construction and operation.

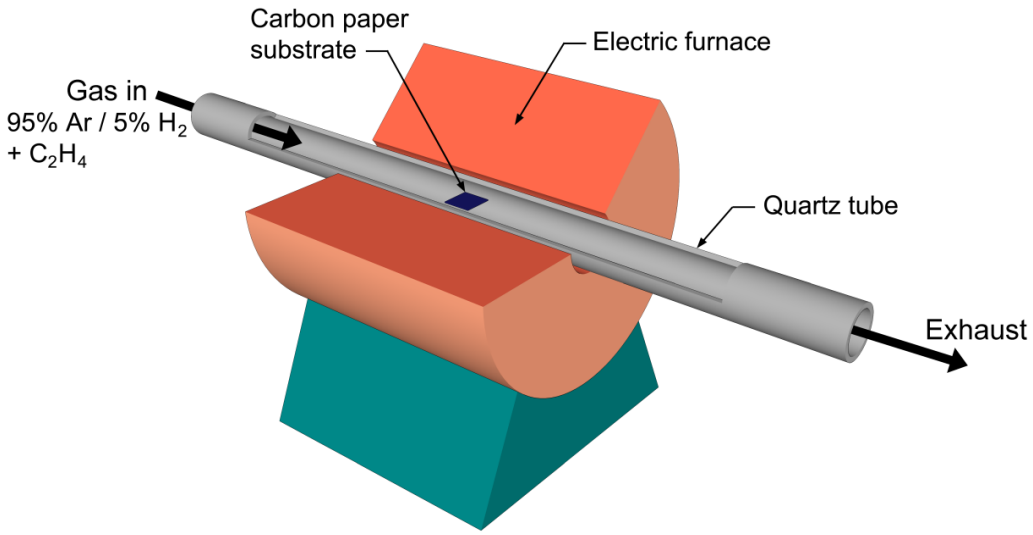


Figure 2-2. A schematic illustration of the thermal CVD setup used for the CNT growth.

In our CNT growth process, carbon papers with magnetron-sputtering deposited Al and Fe catalysts were used as the substrates. C_2H_4 (99.9% purity) and Ar/H_2 mixture (95%/5% by volume) were used as the gaseous carbon precursors and carrier gases, respectively. Firstly, the CVD tube furnace (Carbolite, ⌀ 25 mm quartz tube) was ramped up to the deposition temperature under a continuous flow of Ar/H_2 carrier gases. Once it reached the deposition temperature, carbon feedstock C_2H_4 was introduced into the furnace for a specified deposition time. After the

deposition was completed, C_2H_4 flow was cut-off. The furnace was cooled down to room temperature under the flow of Ar/H_2 carrier gases. The growth process of CNTs was controlled by deposition temperature, deposition time, gas flow rates, and catalyst conditions. The CNT growth was carried out at ambient pressure.

Radio frequency plasma enhanced chemical vapor deposition (PECVD) for free-standing graphene and GCNT hybrid growth

Similar to the thermal CVD method, PECVD is also a method to deposit materials from their gaseous precursors. However, in PECVD, the decomposition of gaseous precursors is assisted by a plasma created by a high electric field, instead of relying on the high deposition temperature. The deposition of materials is therefore more efficient and can be carried out without any catalyst materials, although a combination of plasma and catalysts is possible. A schematic illustration of the PECVD setup used for free-standing graphene and GCNT hybrid growth is provided in Figure 2-3. In our material growth process, a radio frequency PECVD (Plasma Quest, Model 157) was used to grow free-standing graphene and GCNT hybrids. C_2H_2 (99.8%) and H_2 (99.9995%) were used as carbon precursor and carrier gas, respectively. Firstly, the substrates were heated up to the deposition temperature under vacuum and then under a flow of H_2. Once it reached the deposition temperature, the plasma was turned on and stabilized for a few minutes. Subsequently, C_2H_2 was introduced into the chamber for a specific deposition time. Once the deposition was completed, C_2H_2 and H_2 flows were cut-off. The samples cooled down naturally to room temperature under vacuum before being taken out.

The deposition was controlled by deposition temperature, deposition pressure, gas flow rates, plasma power, and deposition time.

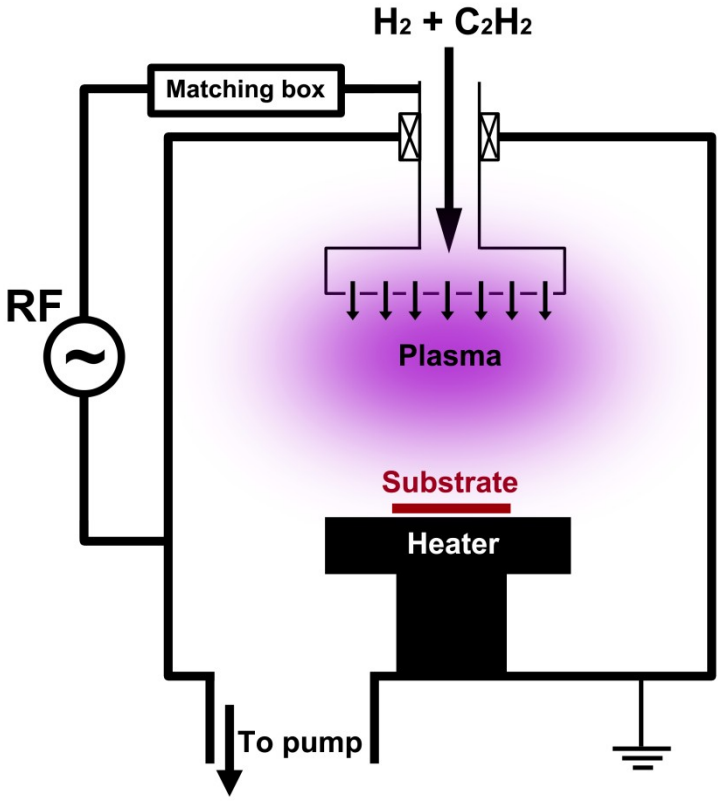


Figure 2-3. A schematic illustration of the PECVD setup used for free-standing graphene and GCNT hybrid growth.

2.1.2. PEMFC electrode fabrication methods

In this thesis, we used two methods for the preparation of PEMFC electrodes. The first method based on magnetron sputtering catalyst deposition was used to prepare cathodes based on CNTs and GCNT hybrids. The second method known as catalyst ink method is a conventional method commonly used in the literature for the preparation of PEMFC electrodes based on carbon black-supported Pt catalysts. In this thesis, the second method was used to fabricate standard anodes

based on carbon black-supported Pt catalysts. It was also used to fabricate reference cathodes based on carbon black-supported Pt catalysts for comparison purposes.

Catalyst deposition with magnetron sputtering method

The magnetron sputtering deposition method was used to deposit Pt catalyst on the CVD/PECVD-grown CNT and GCNT hybrid supports. In this method, CNTs and GCNT hybrids were first grown on carbon paper, and then used as the substrates in the magnetron sputtering deposition technique as described above. A platinum (Pt) target (99.99%) was used to deposit a thin film of Pt of 19 nm nominal thickness, equivalent to an ultra-low loading of 0.04 mg_{Pt} cm^{-2} on the CNT or GCNT hybrid substrates. For depositing 19 nm nominal thickness of Pt, the plasma power and deposition time were 50 W, 4 min. Other sputtering parameters were identical to those specified in section 2.1.1.

Electrode preparation with catalyst ink method

In the catalyst ink method to fabricate carbon black-supported Pt electrodes, the following experimental steps were used. Firstly, carbon papers (TGP-H-090, Toray) were coated with polytetrafluoroethylene (PTFE, 60 wt% dispersion in water, Sigma-Aldrich) to provide the hydrophobicity to the carbon paper gas diffusion layer. The PTFE-coated carbon paper (35 wt% PTFE : 65 wt% carbon paper by dry weight) was obtained by brushing the PTFE dispersion onto carbon paper, dried and annealed at 350 °C for 30 min. A microporous layer was then spread onto the PTFE-coated carbon paper from a mixture of Vulcan XC72R carbon black (VXC72R, Cabot) and PTFE (60 wt% dispersion) in water/ethanol (1:1 by volume) to get a total loading

of 2 mg cm^{-2} (70 wt% VXC72R : 30 wt% PTFE by dry weight). A typical formulation of the mixture used was 40 mg VXC72R + 28.6 mg PTFE dispersion + 2 ml water + 2ml ethanol. The microporous layer was dried and annealed at 350 °C for 30 min. Subsequently, a catalyst layer was spread onto the microporous layer from a mixture of Pt/VXC72 (20 wt% Pt on Vulcan-XC72 carbon black, Premetek) and Nafion ionomer (5 wt%, Sigma Aldrich) in ethanol to get a final composition of 67 wt% Pt/VXC72 : 33 wt% Nafion by dry weight. A typical formulation of the mixture was 30 mg Pt/VXC72 + 345 μL Nafion solution + 2 mL ethanol. The total catalyst layer loading (Pt/VXC72 + Nafion) was 0.3 mg cm^{-2} (corresponding to a Pt loading of 0.04 mg_{Pt} cm^{-2}) or 1.5 mg cm^{-2} (corresponding to a Pt loading of 0.2 mg_{Pt} cm^{-2}). The 0.04 mg_{Pt} cm^{-2} electrode was used as the reference carbon black-supported Pt cathode for comparison purposes. The 0.2 mg_{Pt} cm^{-2} electrode was used as the standard anode for all membrane electrode assemblies. The catalyst layer was dried and annealed at 140 °C for 30 min.

Membrane Electrode Assembly (MEA) fabrication

To prepare the membrane electrode assemblies (MEAs), the standard anodes were fabricated with the commercial catalyst Pt/VXC72 (Premetek) at a high Pt loading of 0.2 mg_{Pt} cm^{-2} using the conventional catalyst-ink method as described above. Nafion 212 (DuPont) membrane was used as the polymer electrolyte membrane. All cathodes (Pt/GCNT, Pt/CNT, and Pt/VXC72) were prepared with a Pt loading of 0.04 mg_{Pt} cm^{-2}. A Nafion 212 membrane was sandwiched between a standard anode and a cathode of interest. The structure was bonded together using a Riken hydraulic hot press, at 40 atm, 140 °C, 90 s.

2.1.3. Amorphous molybdenum sulfide electrodeposition methods

Amorphous molybdenum sulfide (MoS_x) was deposited on carbon supports by an electrochemical deposition method based on the reported literature [70] with additional customizations. The deposition process was performed in two steps.

In the first step, the deposition was performed in a three-electrode electrochemical cell with the carbon supports as the working electrode, a platinum foil as counter electrode, a Ag/AgCl (saturated KCl) reference electrode ($E_{Ag/AgCl\ (sat.\ KCl)}$ = 0.2 V *vs.* standard hydrogen electrode (SHE) potential) and a 20 mM solution of ammonium tetrathiomolybdate ($(NH_4)_2MoS_4$ 99.97%, Sigma-Aldrich) in deionized water as electrolyte and MoS_x precursor. The deposition was performed by a potentiostatic anodic deposition at 0.7 V *vs.* SHE. MoS_x loading was controlled by controlling the total charge transfer (real-time integration of deposition current) during the deposition process. The deposition proceeded according to the following reaction, with the residual elemental sulfur can be readily removed by immersing in H_2SO_4: [12]

$$[MoS_4]^{2-} \rightarrow MoS_3 + \tfrac{1}{8}\, S_8 + 2e^- \qquad (2\text{-}1)$$

In the second step, the MoS_x/carbon support working electrode underwent 10 reductive activation potential sweeps performed from 0.2 V to –0.5 V *vs.* SHE in a second three-electrode electrochemical cell, with a platinum rod counter electrode, a Ag/AgCl (3 M KCl) reference electrode ($E_{Ag/AgCl\ (3\ M\ KCl)}$ = 0.21 V *vs.* SHE), and a 0.5 M H_2SO_4 electrolyte solution. The potential sweeps were performed at a scan rate of 5 mV s^{-1}. In all subsequent discussions, MoS_x/carbon support in general refers to this activated condition of MoS_x, except otherwise specified. For a typical experiment, a

deposition total charge transfer of 4.822 C $cm^{-2}_{geometric}$ produced an experimentally determined activated MoS_x loading of 3 mg cm^{-2}. The charge transfer was proportionally applied for other required MoS_x loadings. For comparison purposes, amorphous molybdenum sulfide MoS_x was deposited on a GCNT hybrid-on-carbon paper (GCNT/CP) carbon support, a CNT-on-carbon paper (CNT/CP) carbon support, a simple porous Toray carbon fiber paper and a flat graphite paper electrode using the same procedure described above.

All electrochemical depositions and measurements were performed with an Autolab potentiostat/galvanostat (PGSTAT302N, Metrohm) equipped with a frequency response analyzer (FRA2.V10) and an analog scan generator (SCANGEN). All potentials are reported against standard hydrogen electrode potential. A schematic illustration of the three-electrode electrochemical cell setups used for the electrochemical deposition of MoS_x on carbon substrates is provided in Figure 2-4.

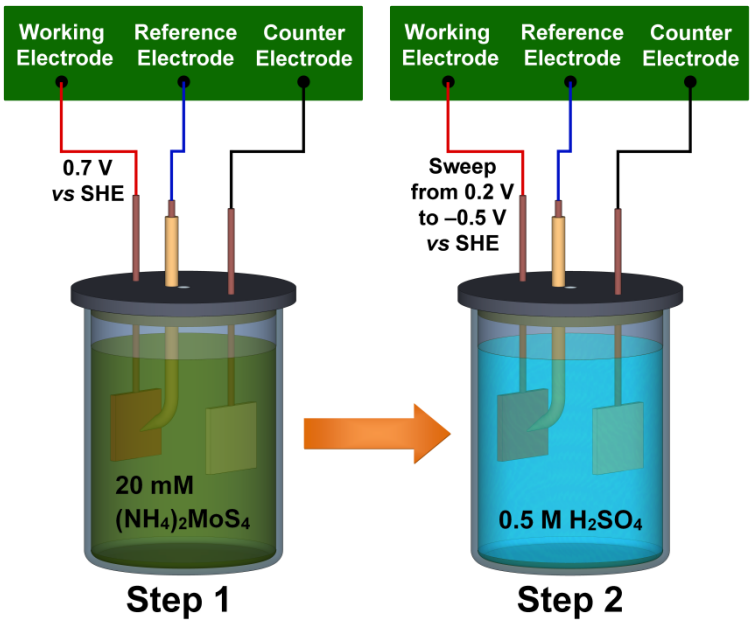


Figure 2-4. A schematic illustration of the three-electrode electrochemical cell setups used for the electrochemical deposition of MoS_x on carbon substrates.

2.2. *Ex situ* material characterization methods

2.2.1. Secondary Electron Microscopy (SEM)

Secondary Electron Microscopy (SEM) is a widely used technique to characterize physical properties of materials by scanning a focused high energy primary electron beam on the surface of sample in a raster scan pattern. Secondary signals are collected to provide morphological information (in the secondary electron mode) and compositional information of material (in the back-scattered electron and Energy Dispersive X-ray Spectroscopy (EDS) modes). In most modern SEMs, the primary electron beam is generated by a Field Emission electron source. Such instruments are known as Field Emission Scanning Electron Microscopes (FE-SEM).

FE-SEM was used extensively in this thesis, mainly to provide the morphological information of the material structures. The instruments used include JSM-6700F (JEOL), SUPRA 40 (Carl Zeiss AG), and LEO Gemini 1525 FEGSEM (Carl Zeiss AG). For morphological studies, the primary electron beam energy was 5 keV, unless otherwise specified. For EDS, the primary electron beam energy was 10 keV.

2.2.2. Transmission Electron Microscopy (TEM)

Transmission Electron Microscopy (TEM) is an electron microscopy technique used to provide ultra-high resolution information of the material nanostructure, up to atomic resolutions. Unlike SEM, TEM operates by transmitting a high energy primary electron beam through a thin sample specimen. After interacting with the sample materials, the transmitted electrons are recorded as a

micrograph. Bright field TEM is the most common operating mode and provides direct information on the nanostructure of materials. Another commonly used TEM operating mode is Selected area electron diffraction (SAED), which provides the crystallographic information of the material. Secondary X-ray photons may also be collected and provide the elemental information of the material in the EDS mode.

TEM was extensively used in this thesis, commonly in the bright field mode, to provide ultrahigh resolution nanostructure information of the materials. The instruments used were JEM-2010F, JEM-3010, and JEM-2100F (JEOL), operated at 200 keV, 300 keV, and 200 keV primary electron beam energy, respectively.

To be examined with TEM, the sample has to be in the form of a thin film. Depending on the nature of samples and the purpose of experiments, the materials were prepared using one of the following two sample preparation techniques.

TEM sample preparation using copper grids

For powder samples, the materials were dispersed in ethanol using the ultrasonicating method. The colloidal dispersion was then pipetted on a Formvar/carbon 300 mesh Cu grid (Electron Microscopy Sciences) and allowed to fully dry prior to TEM imaging.

TEM sample preparation using FIB-SEM dual beam

For thin film samples (such as free-standing graphene on silicon wafer), and for experiments in which precise controls of the sampling location and minimal damage to sample nanostructure are preferable (for example, to specifically select the sample at the cathode-membrane interface of PEMFCs), a thin film of the sample was

prepared with a Focus Ion Beam-Secondary Electron Microscopy (FIB-SEM) dual beam technique. In this technique, the FIB-SEM instrument has two separate high energy charged particle beams, namely a Ga^+ ion beam and an electron beam, focusing on the same area of the sample. SEM was mainly used to monitor the maneuver process on the sample. FIB was used for ion-milling, cutting and thinning on the sample lamellae, as well as for the deposition of materials such as Pt with the addition of a Pt organometallic precursor gas supplied via a Gas Injection System nozzle. The advantages of dual beam preparation method include precise controls of the sampling location and minimal damages to the sample nanostructure. Experimental steps involved in the preparation technique are summarized in Figure 2-5. In this thesis, a Helios NanoLab 600 (FEI) FIB-SEM dual beam microscope was used to prepare TEM lamellae.

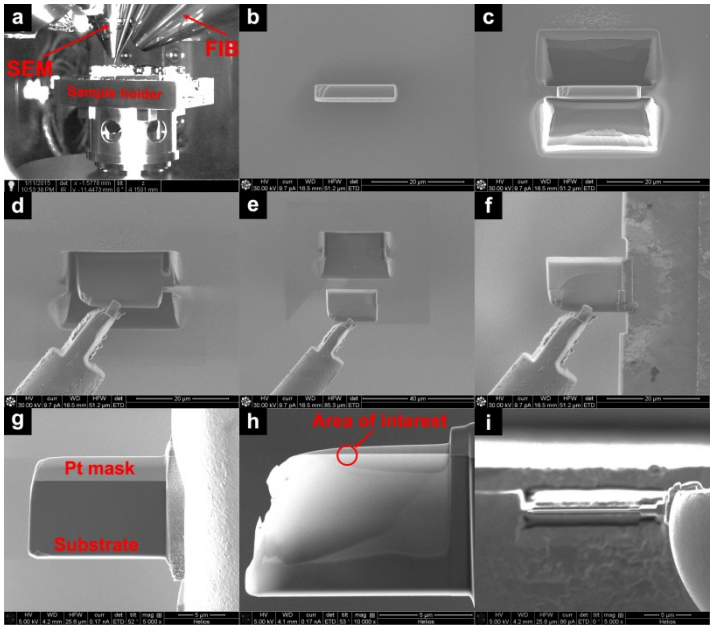


Figure 2-5. TEM sample preparation method using the FIB-SEM technique. (a) chamber configuration, (b) deposition of Pt protection mask on the sample surface, (c) ion-milling trenches around the sample, (d) attachment of the sample lamella to the lift-out probe, (e) sample lamella lift-out, (f) attachment of the lamella to the Omniprobe lift-out TEM grid, (g) initial thinning of the lamella, and final thinning of the TEM-ready lamella from (h) side view and (i) top view.

2.2.3. Raman spectroscopy

Raman spectroscopy is a non-destructive spectroscopic technique operating based on inelastic scattering of a monochromatic light with sample materials. The technique is used to observe vibrational, rotational, and other low-frequency modes of a material, [98] as a fingerprint of the material molecules. In the thesis context, Raman spectroscopy was used to probe the sp^2 and sp^3 hybridized carbon configurations present in the graphitic carbon materials such as CNTs and GCNTs, and to identify the presence/absence of the crystalline MoS_2 in the deposited MoS_x materials. In this thesis, Raman systems used were Renishaw inVia Raman microscopes with 514.5 nm argon laser and 532 nm laser.

2.2.4. X-ray Photoelectron Spectroscopy (XPS)

X-ray Photoelectron Spectroscopy (XPS) is a quantitative spectroscopic technique used for the determination of elemental compositions and chemical states of materials on the sample surface. XPS operates by irradiating the sample surface with a beam of X-ray of a specific photon energy E_{photon}, and detecting the emitted secondary photoelectrons as a function of electron kinetic energy $E_{kinetic}$. The binding energy (BE) is used as the fingerprint of present elements and their chemical states:

$$E_{binding} = E_{photon} - (E_{kinetic} + \phi) \quad (2\text{-}2)$$

in which ϕ is the analyzer work function. In this thesis, the XPS instrument used was Omicron 7-channeltron analyzer with Mg K_α (1253.6 eV photon energy) and Al K_α (1486.7 eV photon energy) X-ray sources (Omicron X-ray twin anode source). Constant analyzer energy (CAE) modes of 50 eV and 20 eV were used for survey scan and high resolution scans, respectively.

2.2.5. X-ray diffraction (XRD)

X-ray diffraction (XRD) is a technique used to study the crystallographic structures of materials. A monochromatic, collimated X-ray beam is irradiated on a sample at an incident angle θ. The X-ray beam is scattered and diffracted by the periodic arrangements of the scattering centers (e.g. atoms and molecules) in the crystal structure of materials. The diffraction is constructive only when the Bragg's law is satisfied, according to the equation:

$$2\,d \sin\theta = n\,\lambda \qquad (2\text{-}3)$$

in which d is the interplanar spacing of the scattering centers, n is an integer number, λ is the X-ray wavelength. The set of diffraction angles θ when constructive diffraction occurs is used as a fingerprint of the crystal structure of materials. In this thesis, an X-ray powder diffractometer (Philips X'Pert, Cu K_α (λ = 1.54 Å) source) was used. A symmetrical scanning mode was used, with a 2θ scanning range of 5°-90°.

2.2.6. Brunauer–Emmett–Teller (BET) surface area and porosity analysis

In the study of high specific surface area and porous carbon supports for various electrochemical applications, the determination of surface area and porosity of materials is essential. Brunauer–Emmett–Teller (BET) surface area and porosity analysis is an important analysis technique for such purpose. The BET technique determines the surface area and porosity of materials by analyzing the physical adsorption of inert gases (such as N_2 and Ar) on the surface of materials, and by assuming the BET theory of multi-molecular layer adsorption of gases on material surface. [99] In this thesis, BET measurements were performed with ASAP 2020 Surface Area and Porosity Analyzer (Micromeritics) using N_2 as the adsorbate gas.

2.2.7. 3D reconstruction of porous nanostructures using a FIB-SEM dual beam technique

The electrodes of electrochemical devices, such as PEMFCs, are frequently constructed of three-dimensionally porous nanostructures in order to have an extended interfacial area to maximize the device performance. The electrochemical performance of these devices crucially depends on the 3D characteristics of electrode nanostructures. 3D reconstruction of the porous nanostructures is an important technique to understand the full 3D information of electrode structures. FIB-SEM dual beam tomography is a versatile method to reconstruct 3D nanostructures, and has been used to characterize electrode nanostructures of solid oxide fuel cell (SOFC) electrodes [100-103] and PEMFC electrodes. [104-109] In this thesis, FIB-SEM dual beam tomography was used to study the porous carbon nanostructures. As a proof of concept, the method was developed for the imaging of PEMFC cathodes, although we believe that the method can be easily applicable for other similar carbon electrodes in supercapacitors and HER applications.

FIB-SEM instrumentations and the "Slice and view" method

In this thesis, a dual beam FIB-SEM instrument (Auriga Cross beam, Carl Zeiss) was used for the 3D reconstruction of porous carbon electrode structures. The instrument consists of an FIB column of high energy Ga^+ ions and an SEM column, placed at a 54° angle apart. Both FIB and SEM columns are focused on the same area of the sample. A schematic illustration of the experimental method is shown in Figure 2-6.

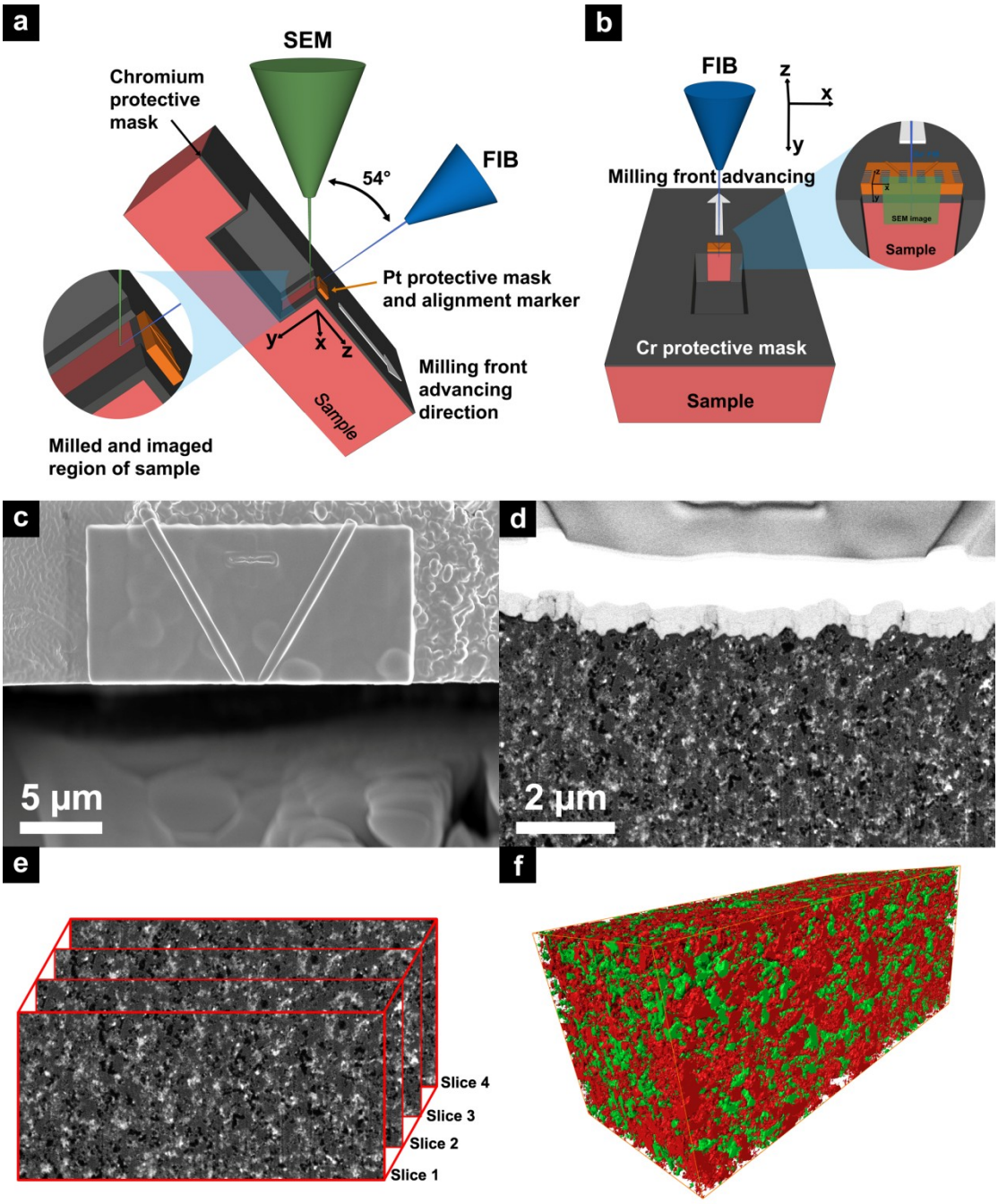


Figure 2-6. An illustration of the FIB-SEM dual beam 3D reconstruction method. Experimental setup from (a) a side view and (b) a top-down view from SEM column. (c) A micrograph of the trench, Pt protective mask and alignment markers. (d) An SEM micrograph of the freshly milled sample cross-section, taken with Energy Selective Backscattered (EsB) electrons imaging mode. (e) An illustrative alignments of consecutive "slices". (f) Processed and reconstructed 3D structure of the electrode.

Prior to the experiment, the sample was coated with a thin mask of chromium to protect the sample from unintentional bombardment of the Ga^+ ions from the FIB column and to serve as a grounding surface for the sample. The sample was placed under SEM and FIB columns, and tilted in a way that the Ga^+ beam from FIB column arrives perpendicularly to the sample surface. Prior to the imaging process, a trench was milled from the sample using the FIB column in order to reveal a cross-section of the sample. A Pt protective mask and alignment markers were deposited on the top surface of the sample at the imaging site to reduce milling artifacts and to assist image alignments during data processing, respectively. Illustrations of the trench, Pt protective mask and alignment markers are shown in Figure 2-6a-c.

The imaging process was performed in an iterative sequence referred to as "Slice and view" as described below:

- The Ga^+ beam first rastered along the x-direction and milled away the front surface of the sample cross-section, to produce a freshly prepared smooth cross-section on the x-y plane.
- The SEM was then used to capture an electron image of the sample cross-section.
- The SEM image is referred to as a "slice" of the sample.
- Once the SEM image was obtained, the Ga^+ beam moved forwards in the z-direction by a user-defined step.
- The Ga^+ beam once again freshly prepared a new cross-section of the sample at the new position on the z-direction.
- The SEM captured a second slice of the sample.

- The process continued until a desired number of slices were obtained.
- The series of SEM slices was then used to reconstruct the 3D structure of sample.
- In our experiments, a spatial resolution of 9.83 nm was used for all x, y, and z directions.

Data processing

During the "Slice and view" process, generally minor shifts among the SEM images are unavoidable. The first step in data processing involved image alignments, with the assistance of the alignment markers. The aligned images were then "segmented", which is the process of assigning different areas on the SEM images to appropriate phases present in the structure. The phase assignment was performed automatically based on the brightness of the phases in SEM images. Finally, the segmented images were used to reconstruct the 3D structure of the electrodes. The reconstructed structure can be further used in quantitative analyses to extract additional structural parameters of the electrodes. In this thesis, data processing was performed with Avizo 8.0 (FEI Visualization Sciences Group).

To prepare the sample for FIB-SEM imaging, porous carbon electrodes were infiltrated with silicone resin (Elastosil® RT 604, Wacker) by using a vacuum infiltration technique (CitoVac, Struers). Silicone resin-infiltrated samples were fully cured at room temperature in 24 hrs before imaging. To improve the SEM contrast while retaining high resolution, Energy Selective Backscattered (EsB) electrons detection mode and a low electron acceleration voltage of 2 kV were employed. An acceleration voltage of 30 kV was used for the Ga^+ ion beam in FIB column.

2.3. Electrochemical evaluation methods

2.3.1. PEMFC characterization methods

Overview

In order to have a close approximation of the real operational fuel cell systems, the PEMFC electrochemical evaluations were performed *in situ* in a full single cell configuration. The electrochemical evaluations of PEMFCs aimed to provide a comprehensive understanding of the PEMFC cathodes performance from a range of perspectives, including: (1) total device performance (measured by polarization curve), (2) overpotential loss contributing factors (measured by electrochemical impedance spectroscopy), (3) active electrochemical surface area (ECSA) of Pt catalysts (measured by cyclic voltammetry), and (4) degradation behavior (measured by accelerated degradation test).

Fuel cell testing station

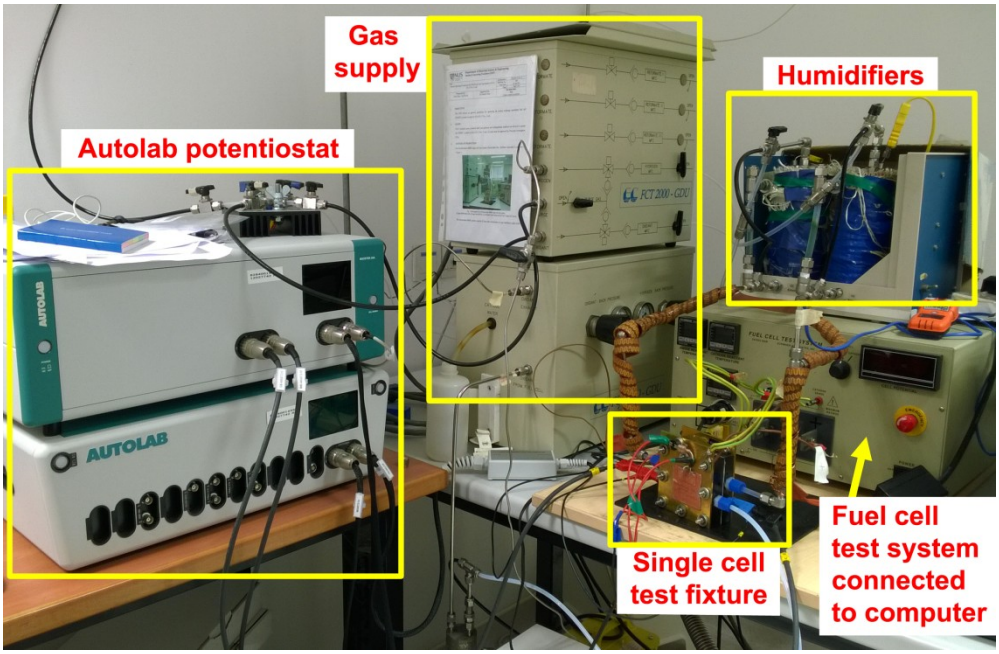


Figure 2-7. Experimental setup used for PEMFC electrochemical characterization.

All *in situ* electrochemical evaluations of PEMFCs in this study were carried out in a single cell test station (5 cm^2 electrode geometrical area, Electrochem. Inc. 890B). The testing station was consisted of five main components: (1) a gas supply unit (or gas distribution units), (2) humidifiers, (3) a single cell fixture, (4) a computer-controlled electronic load system, and (5) an Autolab potentiostat/ galvanostat. The fuel cell testing station is shown in Figure 2-7.

Starting from the gas distribution unit, O_2 and H_2 flow rates were regulated by the controlling computer, and delivered to the humidifier units. At the humidifiers, both O_2 and H_2 were fully humidified before being delivered to the fuel cell. The single cell test fixture was the facility to accommodate and to provide suitable operating conditions for the tested membrane electrode assembly, including reactant gases delivery through gas flow channels and suitable cell temperature. The single cell fixture was electrically connected to the electronic load system and the Autolab potentiostat/galvanostat. During the polarization curve measurements, the computer-controlled electronic load system varied the internal resistance value to draw a desired current from the fuel cell. The cell potential was recorded for each drawn current value and provided the basis for the polarization curve. The electronic load system and gas flow rates were controlled by the Fuelcell test software (Scribner Associates). The Autolab potentiostat/galvanostat was also used to control and measure the fuel cell potential and current during the electrochemical impedance spectroscopy, cyclic voltammetry and accelerated degradation test. The Autolab potentiostat/galvanostat was controlled by Nova 1.9 software (Metrohm).

Polarization curve

The polarization curve is a direct measurement of the total device performance, recording the dependence of cell potential on the drawn current density. A dependence of power density on the drawn current density can also be derived from the basic polarization curve.

In this study, the polarization curve measurements were carried out in the single cell test station at a cell temperature of 80 °C and under fully humidified H_2 (99.999%) and O_2 (99.7%). H_2 and O_2 were pressurized at 30 psi with base flow rates of 300 sccm and stoichiometric flow rates of 14 sccm A^{-1} and 7 sccm A^{-1}, respectively.

Electrochemical Impedance Spectroscopy (EIS)

Whilst the polarization curve is a simple and direct measurement of the total device performance, the contributing potential loss factors present in the device are unknown from the polarization curve. An understanding of the individual contributions of each potential loss factor is important for the optimization of the electrode structure for a maximum performance. In order to separate the contributing factors, Electrochemical Impedance Spectroscopy (EIS) is used. EIS operates by measuring the dynamic impedance of the fuel cell as a dependence on the frequency of applied potential. The principle of EIS relies on the fact that electrochemical processes present in the measured system respond to external perturbations (e.g. potential) at different time scales, depending on the nature of the processes. By understanding the dependence of the system impedance on perturbation frequency, the individual contribution of potential loss factors can be

separated. An EIS measurement is performed by applying a small AC potential signal on the tested operating potential and recording the corresponding AC current signal. From the AC signals of potential and current, a complex impedance (i.e. including a real and an imaginary impedance components) and phase angle are derived. By applying the AC potential in a wide range of frequency, the dependence of the complex impedance and phase angle on the frequency can be obtained. The EIS data are normally presented in a Nyquist plot (a plot of imaginary impedance component *vs.* real impedance component in the tested frequency range) and Bode plots (plots of impedance modulus and phase angle as a dependence of frequency).

In this study, the EIS was performed with an Autolab potentiostat (PGSTAT302N, Metrohm) equipped with a frequency response analyzer (FRA2.V10). EIS was performed at cell potentials of 0.7 V, 0.6 V and 0.5 V, with an AC perturbation amplitude of 40 mV and in a frequency range between 10 kHz and 0.01 Hz. During the EIS measurements, the gas flow rates, pressures, and temperatures were maintained at the same conditions as the polarization curve measurement at the corresponding current density.

Cyclic voltammetry and Accelerated Degradation Test (ADT)

Cyclic voltammetry is a potentiodynamic electrochemical measurement generally used to study redox reactions present in an electrochemical system. Cyclic voltammetry is performed by scanning the working electrode potential linearly with time, in a triangular waveform, and recording the current response. A plot of current response against applied potential is known as a cyclic voltammogram. In PEMFC

study, cyclic voltammetry is commonly used as an *in situ* characterization tool to measure the active electrochemical surface area (ECSA) of the Pt catalysts. By combining cyclic voltammetry with an accelerated degradation test, a degradation of ECSA during the degradation test can be studied. An accelerated degradation test (ADT) is an experiment designed to study the degradation behavior of the device in a fast and efficient way. The ADT mimics the harsh working conditions when the degradation is most severe and is believed to cause the major degradation during the lifetime of the device.

In this PEMFC study, to assess the electrochemical stability of the cathodes, *in situ* accelerated degradation tests (ADTs) were performed using the aforementioned Autolab potentiostat. While conducting ADT, O_2 in the cathode compartment was replaced by N_2. N_2 and H_2 flow rates were 30 sccm and 50 sccm, respectively, under ambient pressure. ADT was performed by a rectangular-waveform oxidative potential cycling of the cathode (working electrode) between 0.6 V (for 40 s) and 1.4 V (for 20 s) *vs.* hydrogen anode per cycle, for 100 cycles. The anode served as both a counter electrode and a reversible hydrogen electrode (RHE). Cyclic Voltammetry (CV) measurements were performed before ADT and after every 10 oxidative cycles. The CV measurements were carried out between 0.05 V and 1.2 V *vs.* RHE, at a scan rate of 50 mV s^{-1} using the aforementioned Autolab potentiostat fitted with a SCANGEN analogue scan generator.

Finally, after ADT, polarization and EIS measurements were performed again to assess the post-ADT performance of the MEAs.

2.3.2. HER characterization methods

Overview

In this section, the electrochemical evaluations for MoS_x as an HER catalyst were performed in a three-electrode electrochemical cell setup. The electrochemical evaluations aimed to study the properties of MoS_x from several perspectives, including: (1) total electrode activity (measured by polarization curve and EIS), (2) intrinsic activity (or Turnover frequency (TOF), measured by cyclic voltammetry), and (3) electrochemical stability (measured by a degradation test).

Three-electrode electrochemical cell setup

All HER electrochemical evaluations were performed in a three-electrode electrochemical cell setup, with a platinum rod counter electrode, a Ag/AgCl (3 M KCl) reference electrode ($E_{Ag/AgCl\ (3\ M\ KCl)}$ = 0.21 V *vs.* SHE), and a 0.5 M H_2SO_4 electrolyte solution. The electrochemical cell was in fact the same electrochemical cell used in the second step of MoS_x deposition, as described in section 2.1.3. All electrochemical measurements were performed with an Autolab potentiostat/galvanostat (PGSTAT302N, Metrohm) equipped with a frequency response analyzer (FRA2.V10) and an analog scan generator (SCANGEN). All potentials were reported against standard hydrogen electrode potential. A schematic illustration of the experimental setup used is shown in Figure 2-8.

Total electrode activity measurements

The total electrode activity was directly measured by the polarization curve. The polarization curve measurements were performed by linear potential sweeps

from 0.2 V to –0.5 V *vs.* SHE at a scan rate of 5 mV s^{-1}. The polarization curves were presented in both linear plots and Tafel plots to extract relevant parameters (i.e. Tafel slope and exchange current density). Electrochemical impedance spectroscopy was also used to compare the catalytic activity of the catalysts and to extract the ohmic resistances for ohmic-loss correction of the polarization curves. EIS experiments were measured at –0.15 V *vs.* SHE in a frequency range of 10 kHz to 0.05 Hz with an AC perturbation voltage of 5 mV.

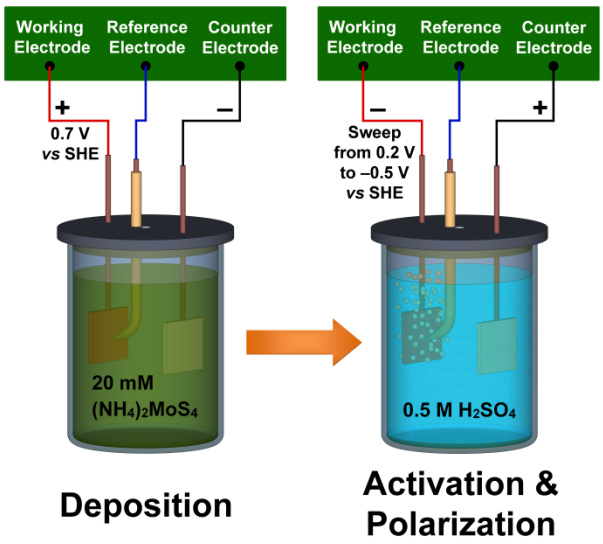


Figure 2-8. A schematic illustration of the three-electrode electrochemical cells setup used for HER electrochemical evaluations.

Intrinsic activity (or Turnover frequency) estimation by Cyclic voltammetry

Cyclic voltammetry was used to estimate the electrode capacitance. After a comparison with a flat standard sample reported in literature, the electrode capacitance was used in conjunction with the total electrode activity to estimate the Turnover frequency (or intrinsic activity) of the catalyst. Cyclic voltammetry experiments were performed in a potential window of 0 V to 0.3 V *vs.* SHE at scan rates of 10, 20, 50 and 100 mV s^{-1}.

Degradation

To assess the electrochemical stability of the catalyst, a stability testing was performed using 500 potential sweeps from 0.2 V to –0.5 V *vs.* SHE at a scan rate of 100 mV s^{-1}.

2.3.3. Supercapacitor electrode characterization methods

Overview

Supercapacitive properties of amorphous molybdenum sulfide were studied using a three-electrode electrochemical cell setup. The specific capacitance of materials was measured through two methods, namely cyclic voltammetry and galvanostatic charge/discharge. EIS was used to study the idealistic capacitive behavior of the materials. Lastly, a degradation test using galvanostatic charge/discharge was used to examine the electrochemical stability of the materials.

Three-electrode electrochemical cell setup

After the deposition process, the MoS_x/carbon support electrode was transferred to a new three-electrode electrochemical cell, and was used as working electrode. A platinum rod, a Ag/AgCl (3 M KCl) electrode ($E_{Ag/AgCl\ (3\ M\ KCl)}$ = 0.21 V *vs.* SHE) and a 1 M Na_2SO_4 solution were used as counter electrode, reference electrode and electrolyte, respectively. All electrochemical measurements were performed with an Autolab potentiostat/galvanostat (PGSTAT302N, Metrohm) equipped with a frequency response analyzer (FRA2.V10) and an analog scan generator (SCANGEN). All potentials were reported against standard hydrogen electrode potential. A schematic illustration of the experimental setups used is shown in Figure 2-9.

Cyclic voltammetry was used as the first method to measure the specific capacitance of the material. The cyclic voltammetry was performed in a series of scan rates. The dependence of electrode capacitance on the scan rate was studied in this method. Galvanostatic charge/discharge was used as the second method to measure the specific capacitance of material. The galvanostatic charge/discharge was performed by galvanostatically charging and discharging the electrode within a pre-defined potential window at different charge/discharge current densities. The dependence of electrode capacitance on the charge/discharge rate was studied in this method. Cyclic voltammetry and galvanostatic charge/discharge experiments were both performed in a potential window of –0.5 V to 0.3 V *vs.* SHE.

Electrochemical impedance spectroscopy (EIS) was measured at –0.1 V *vs.* SHE in the frequency range of 10 kHz to 0.01 Hz with an AC perturbation voltage of 5 mV. Stability testing was performed using 500 galvanostatic charge/discharge cycles at a constant charge/discharge rate of 5 A g^{-1}.

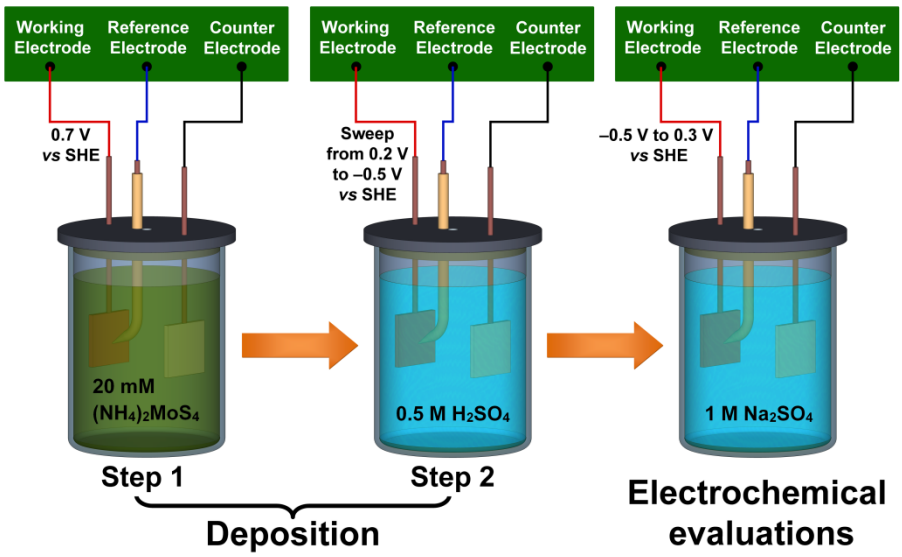


Figure 2-9. A schematic illustration of the three-electrode electrochemical cells setup used for supercapacitor electrochemical evaluations.

Chapter 3 : Growth of nanostructured carbon supports

This chapter describes the growth and characterization of carbon nanotubes, free-standing graphene, and graphene-carbon nanotube hybrids, as well as the respective optimization of the growth conditions. The optimization of growth conditions for carbon nanotubes and free-standing graphene were performed separately and independently from each other. The graphene-carbon nanotube hybrids were then fabricated by growing free-standing graphene on carbon nanotube scaffolds using a two-step growth procedure with the optimized CNTs and graphene growth conditions.

3.1. Growth of Carbon Nanotubes on carbon paper

3.1.1. Growth of CNTs by the thermal CVD method

It is well known that CNTs can be grown on various substrates, most commonly silicon wafer, using various chemical vapor deposition methods. [35-37] CNTs have also been successfully grown on carbon fiber paper for a number of applications. [32,38,39,110,111] Among different chemical vapor deposition methods, thermal CVD is well known as an efficient method to grow CNTs, with simple setup, simple operation and is easy to scale-up. Thermal CVD was, therefore, used to grow

CNTs in this study. In this study, carbon papers with magnetron-sputtering deposited catalysts were used as the substrates. The catalysts for CNT growth were either a thin layer of Fe, or a bi-layer of an Al buffer layer beneath an Fe catalyst layer. C_2H_4 (99.9% purity) and Ar/H_2 mixture (95%/5% by volume) were used as the gaseous carbon precursors and carrier gases, respectively. The growth process of CNTs was controlled by deposition temperature, gas flow rates, catalyst conditions, and deposition time.

3.1.2. Effect of growth conditions on the deposition of CNTs on carbon paper

CNT growth conditions by thermal CVD were firstly optimized for basic growth parameters, including deposition temperature and gas flow rates. In a previous study, Tang *et al.* reported a successful growth process of CNTs on carbon papers using the thermal CVD method for the application in PEMFCs. [111] The reported CNT growth process was carried out on carbon papers deposited with a thin Fe catalyst layer, at a deposition temperature of 750 °C, using C_2H_4 and Ar/H_2 as the precursor gases. The reported growth conditions were used as a starting point in this study. Experiments in this optimization process were first carried out on carbon papers with a thin magnetron-sputtering deposited Fe catalyst layer. The deposition temperature was studied at 650 °C, 750 °C, and 850 °C. Gaseous precursor flow rates were studied with C_2H_4 flow rate of 20 sccm, 30 sccm, and 40 sccm, whilst the carrier gas mixture (Ar/H_2) flow rate was kept constant at 100 sccm. Subsequently, Al/Fe bi-layer catalyst configurations were studied for an enhanced CNT growth on carbon papers. A summary of experimental conditions in CNT growth process optimization is shown in Table 3-1.

Table 3-1. Summary of experimental conditions for CNT growth optimization.

		C_2H_4 flow rate		
		20 sccm	30 sccm	40 sccm
Deposition temperature	650 °C		• Fe, 1 hr	
	750 °C	• Fe, 1 hr (*)	• Fe, 1 hr • Al/Fe, 1 hr • Al/Fe, 30 min	• Fe, 1 hr
	850 °C		• Fe, 1 hr	

(*) Denotes the catalyst condition and deposition duration.

Deposition temperature

Deposition temperature is one of the most important determining factors for the growth of nanostructures. As the deposition temperature of 750 °C was taken as the first starting point, the deposition temperature was studied at three conditions of 650 °C, 750 °C, and 850 °C. While optimizing the deposition temperature, all other parameters were fixed as following: precursor gas composition of 30 sccm C_2H_4 + 100 sccm Ar/H_2, Fe catalyst, and 1 hr deposition time. Morphological characterization with SEM of CNTs grown on carbon paper at the three different temperatures is shown in Figure 3-1. Figure 3-1a shows that the deposition temperature of 650 °C is too low for an efficient growth of CNTs. The grown features are large in diameter (mostly 100-200 nm) and more likely to be nanofibers, although the exact nature of the features is uncertain from SEM images. At the deposition temperature of 750 °C (Figure 3-1b), although formed together with other non-CNT features, the deposited CNTs have smaller diameters (< 100 nm) and are grown at a higher density than at the 650 °C deposition temperature. At the deposition temperature of 850 °C (Figure 3-1c), large and flake-like features are deposited instead of CNTs, probably due to the excessive coarsening of Fe catalyst or the excessive pyrolysis of C_2H_4 and

amorphous carbon formation at high deposition temperature. The optimal deposition temperature of 750 °C is in good agreement with the reported literature, in which the CNT deposition temperature of 750 °C – 800 °C was commonly reported. [37,38,110-112] The optimal deposition temperature of 750 °C was, therefore, used for subsequent experiments.

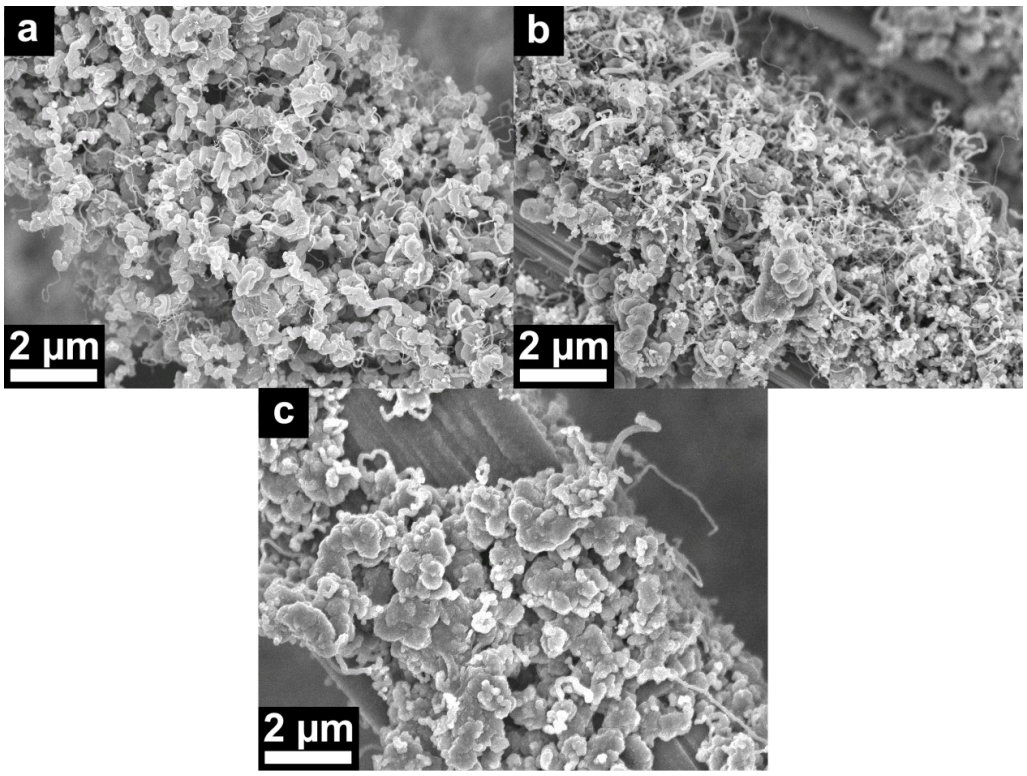


Figure 3-1. SEM micrographs of CNTs grown on carbon paper at (a) 650 °C, (b) 750 °C and (c) 850 °C.

Gaseous precursor flow rate

To investigate the effect of carbon precursor flow rate on the CNT growth, three different flow rates of C_2H_4 were used (20 sccm, 30 sccm and 40 sccm). Other experimental conditions were kept unchanged as following: 100 sccm Ar/H_2 flow rate, 1 hr growth time, deposition temperature of 750 °C, and Fe catalyst. SEM micrographs of the CNTs grown at different precursor gas compositions is shown in Figure 3-2. Figure 3-2a-b show that the lower C_2H_4 flow rates of 20 sccm and 30 sccm

produce similar CNT growth with a mixture of thin CNTs and non-CNT features. In contrast, the high C_2H_4 flow rate of 40sccm results in a preferential growth of non-CNT features, probably due to the excessive deposition of amorphous carbon materials that cover and deactivate Fe catalyst during the CNT growth process. For subsequent experiments, a C_2H_4 flow rate of 30 sccm was used.

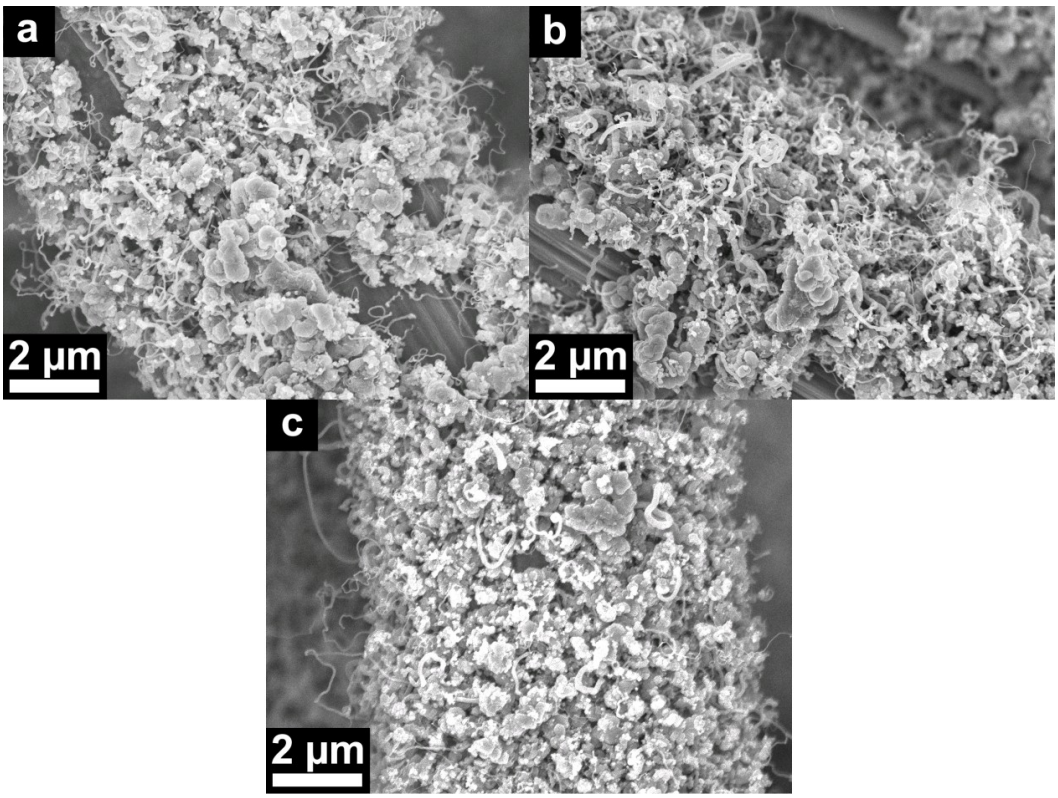


Figure 3-2. SEM micrographs of CNTs grown on carbon paper at C_2H_4 flow rates of (a) 20 sccm, (b) 30 sccm, and (c) 40 sccm.

Catalyst configuration

The optimization of growth temperature and precursor gas flow rates for CNT growth process reaches the optimal growth conditions of 750 °C and 30 sccm C_2H_4 + 100 sccm Ar/H_2. However, even with the optimized growth conditions, CNTs are grown poorly on carbon paper, with low CNT density and short CNT length as well as the concurrent deposition of non-CNT features. In order to improve the CNT growth efficiency, an aluminum buffer layer was deposited on the carbon paper

before the deposition of the Fe catalyst layer. Al/Fe bi-layer catalyst configuration was reported to be an effective catalyst for the growth of CNT on carbon paper in a study reported by Kim *et al.* [110] A comparison of the grown CNT morphology on carbon papers with a simple Fe catalyst layer and on carbon papers with an Al/Fe bi-layer catalyst configuration is shown in Figure 3-3a-a' and b-b'. In these two samples, other growth conditions were kept constant as following: deposition temperature of 750 °C, 30 sccm C_2H_4 + 100 sccm Ar/H_2, and 1 hr growth time. It is evident from Figure 3-3a-a' that CNTs are grown poorly on the Fe-deposited carbon paper, with deposited materials (including both CNTs and non-CNT features) barely cover the carbon fiber surface. In contrast, it is evident from Figure 3-3b-b' that the CNT growth is tremendously enhanced on the carbon paper deposited with an Al/Fe bi-layer catalyst configuration. The grown CNTs completely cover the carbon paper surface and fill the void spaces between carbon fibers. The grown carbon materials are exclusively CNTs with uniform morphology and high porosity. Other non-CNT features are not found to grow on the Al/Fe-deposited carbon paper. The Al/Fe bi-layer catalyst configuration on carbon paper indeed significantly enhances the growth of CNTs on carbon paper. The CNTs were also grown on the Al/Fe-deposited carbon paper in a shorter deposition time of 30 min, as shown in Figure 3-3c-c', whilst all other growth conditions were kept unchanged (750 °C, 30 sccm C_2H_4 + 100 sccm Ar/H_2). The CNTs grown at 30 min deposition time demonstrate no significantly different morphology to the longer deposition time of 1 hr. Provided the similar morphology of CNTs grown in 1 hr and 30 min, a deposition duration of 30 min is selected for subsequent experiments for a faster and more efficient growth process.

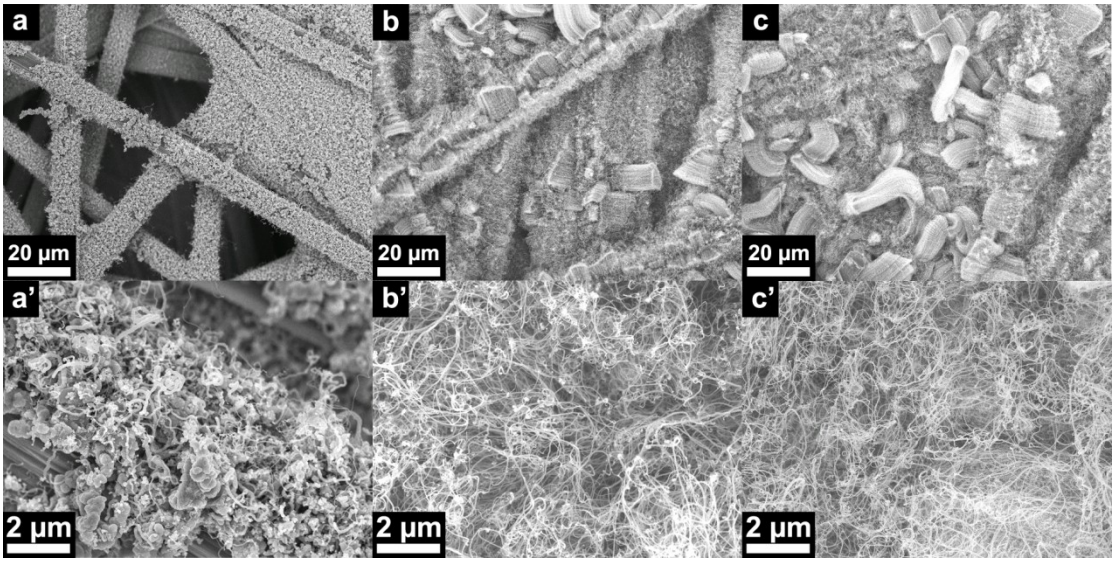


Figure 3-3. SEM micrographs of CNTs grown on (a, a') Fe-deposited carbon papers after 1 hr CNT deposition time; and Al/Fe-deposited carbon papers after (b, b') 1 hr and (c, c') 30 min CNT deposition time.

Effect of Al buffer layer thickness on the enhancement of CNT growth

To study the effect of the Al buffer layer on the growth of CNTs on carbon paper, a series of experiments was carried out, with the variable parameter the nominal thickness of the Al buffer layer. In this series of experiments, CNTs were grown on carbon paper using the thermal CVD technique. All parameters for CVD condition were kept unchanged. The CNT growth was carried out at the previously optimized conditions (deposition temperature of 750 °C, Ar/H_2 flow rate of 100 sccm, and when C_2H_4 was used, the flow rate of C_2H_4 was 30 sccm). The deposition time was 30 min. The nominal thickness of Fe catalyst layer was kept unchanged at 10 nm. The Al buffer layer nominal thickness was studied at three experimental points of 5, 15 and 25 nm. In addition, three other catalyst conditions were used as the controls:

- Plain carbon paper, without any metal catalysts deposited.
- Carbon paper with 25 nm of Al deposited.
- Carbon paper with 10 nm of Fe deposited.

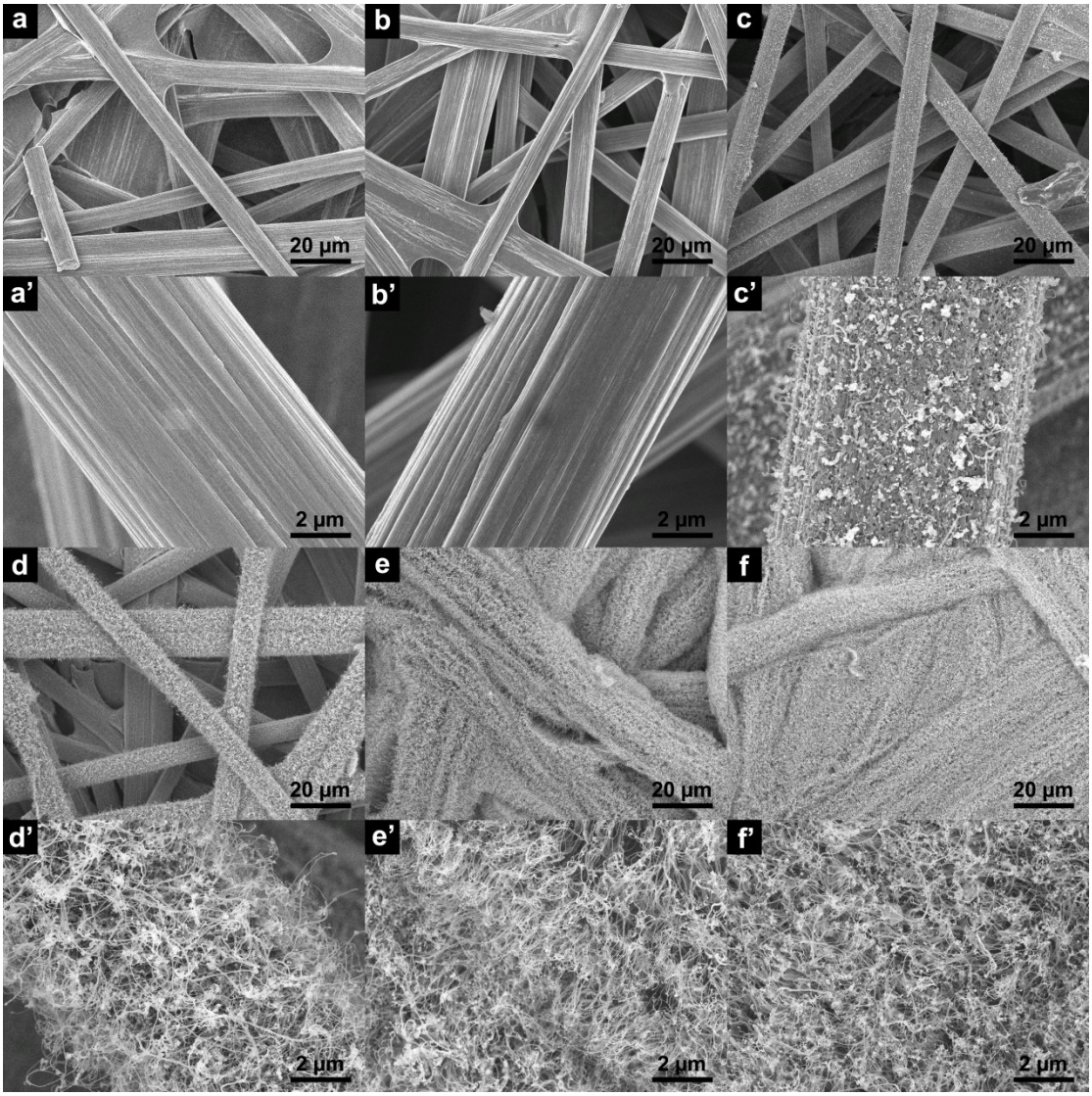


Figure 3-4. SEM micrographs of the as-grown CNTs on carbon paper with different Al buffer layer thicknesses using thermal CVD growth method. Post-CVD growth micrographs of (a, a') plain carbon paper, (b, b') carbon paper with 25 nm Al deposited, (c, c') carbon paper with 10 nm Fe deposited, (d, d') carbon paper with 5 nm Al/10 nm Fe deposited, (e, e') carbon paper with 15 nm Al/10 nm Fe deposited, and (f, f') carbon paper with 25 nm Al/10 nm Fe deposited.

SEM micrographs of the as-grown CNTs on carbon paper with various catalyst conditions are provided in Figure 3-4. From the presented SEM micrographs, the following findings are made. As it can be expected, the carbon paper without any metal catalysts deposited (Figure 3-4a-a') does not support the growth of CNTs. The addition of an Al buffer layer alone does not support the growth of CNTs either

(Figure 3-4b-b'). Therefore, the direct additional CNT growth due to addition of Al can be eliminated from the future analysis. Carbon paper with Fe catalyst deposited (10 nm) but without an Al buffer layer (Figure 3-4c-c') supports the growth of CNTs very poorly. With the addition of an Al buffer layer, the growth of CNTs is effectively enhanced. Starting with a 5 nm Al buffer layer (Figure 3-4d-d'), the CNT growth is visibly enhanced compared to the sample without an Al buffer layer. The CNTs are grown longer and more densely. As the thickness of Al buffer layer reaches 15 nm (Figure 3-4e-e'), the CNT growth is strongly enhanced. CNTs are grown as a dense mat covering the majority of spaces in between the carbon fibers of carbon paper. With an Al buffer layer thickness of 25 nm (Figure 3-4f-f'), CNTs are grown densely and fully cover the surface of carbon paper substrate.

The strong enhancement effect of the Al buffer layer on the growth of CNTs can be clearly seen from cross-sectional SEM micrographs of the post-CVD growth substrates, as presented in Figure 3-5. As shown in Figure 3-5, there is no CNTs grown on the plain carbon paper and the carbon paper with only a 25 nm Al buffer layer, consistent with the top-view SEM micrographs. CNTs are grown poorly on carbon paper with 10 nm Fe catalyst layer and extend only about 1 μm from the carbon fiber surface. With the addition of a 5 nm Al buffer layer, CNTs are grown more densely on the carbon paper and form a CNT mat of about 5 μm thick on the surface of carbon fibers. When the Al buffer layer thickness reaches 25 nm, a tremendous enhancement of CNT growth is observed, as shown in Figure 3-5e-e'''. CNTs are grown densely and form an aligned CNT forest on the carbon paper. The as-grown CNTs appear uniform in morphology. It is clearly seen from Figure 3-5e''' that CNTs are grown directly on the carbon fiber, with a CNT length of ≈ 45 μm.

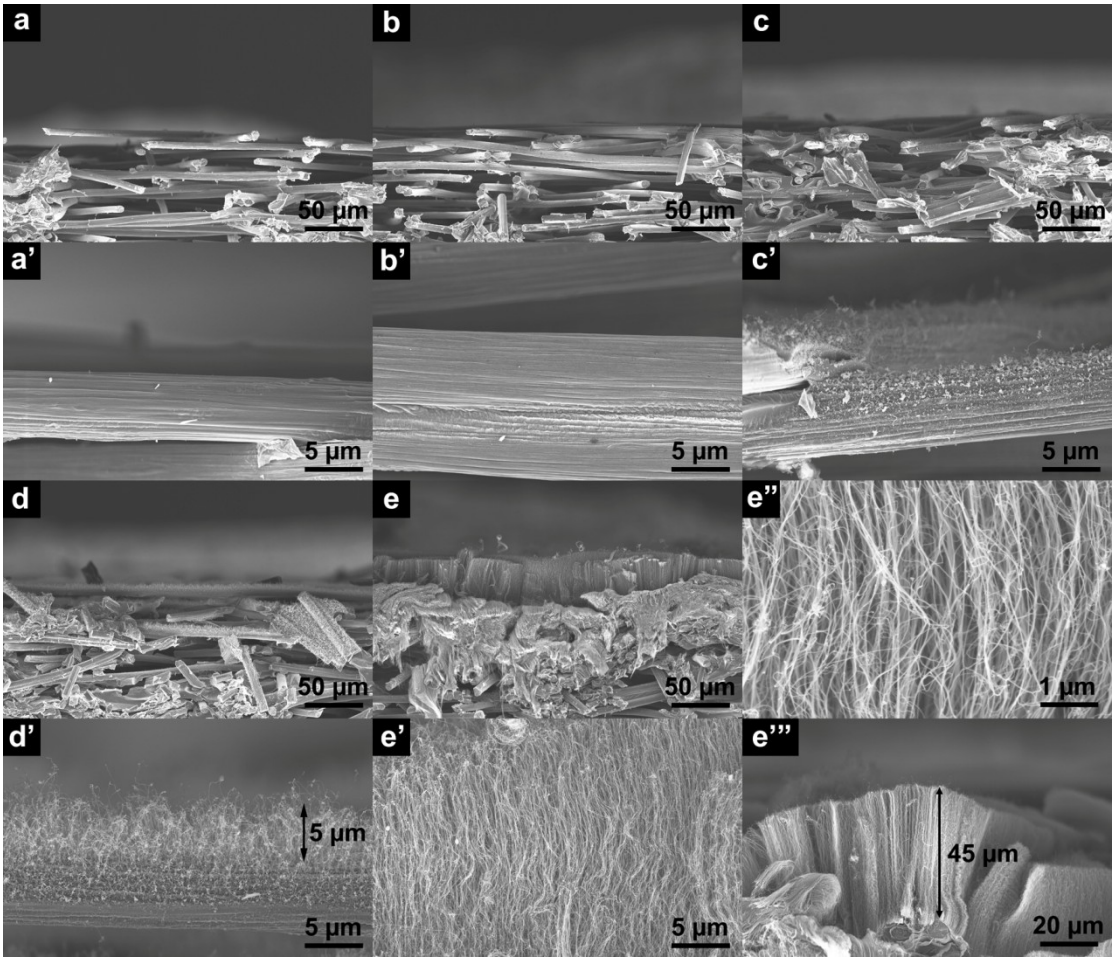


Figure 3-5. Cross-sectional SEM micrographs of the as-grown CNTs on carbon paper with different Al buffer layer thicknesses using thermal CVD growth method. Post-CVD growth micrographs of (a, a') plain carbon paper, (b, b') carbon paper with 25 nm Al deposited, (c, c') carbon paper with 10 nm Fe deposited, (d, d') carbon paper with 5 nm Al/10 nm Fe deposited, and (e, e', e'', e''') carbon paper with 25 nm Al/10 nm Fe deposited.

To understand the demonstrated enhancement effect of the Al buffer layer on the growth of CNT, the formation of catalyst nanoparticles during the CVD process right before CNT growth were investigated. In order to characterize the morphology of catalyst nanoparticles right before the CNT growth, carbon paper substrates with different catalyst conditions underwent a typical CVD growth process, however with the experiments stopped as soon as the deposition temperature of 750 °C was reached. C_2H_4 precursor gas was not introduced in this

series of experiments. SEM micrographs of the annealed catalysts on carbon paper at different catalyst conditions are shown in Figure 3-6.

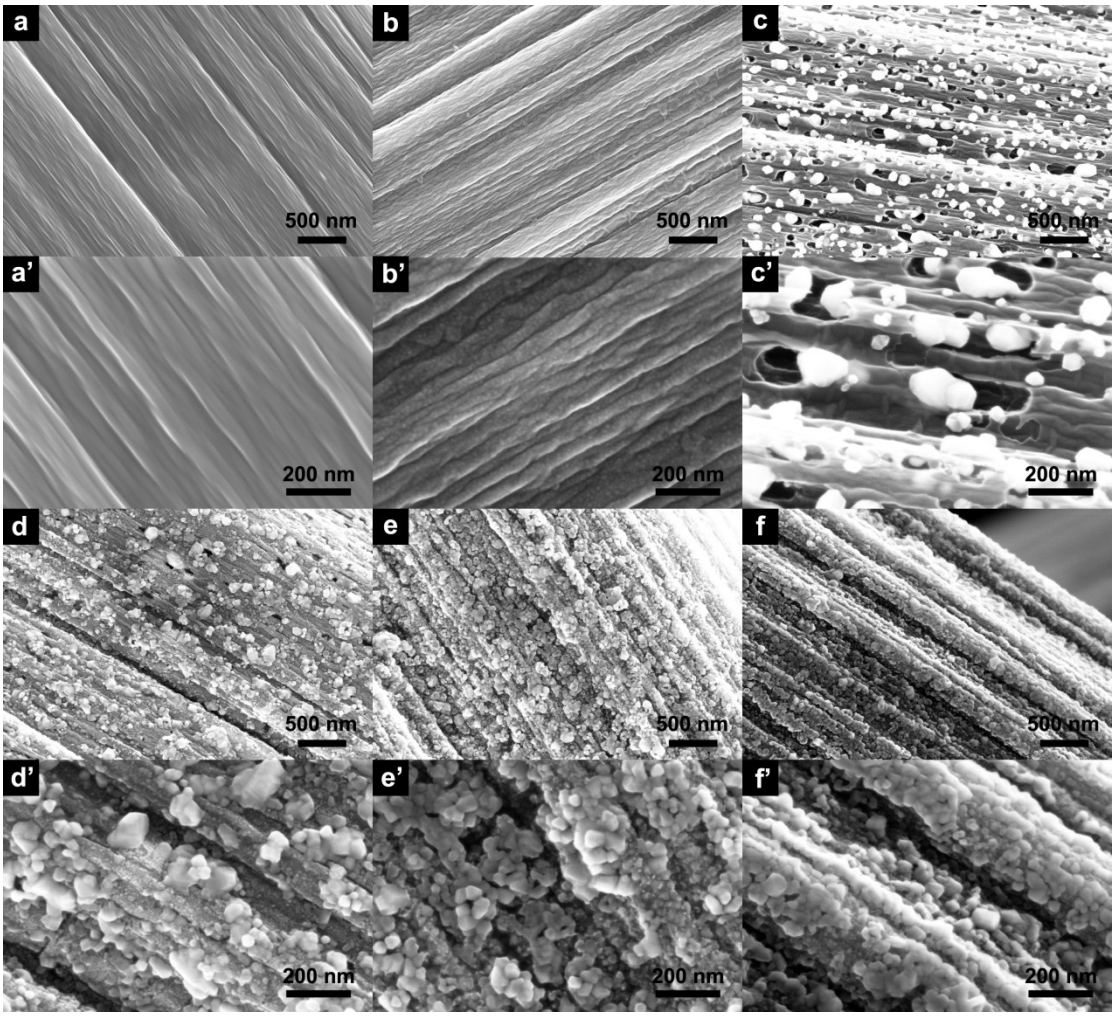


Figure 3-6. SEM micrographs of the annealed catalysts on carbon paper with different Al buffer layer thicknesses. Morphology of the annealed (a, a') plain carbon paper, (b, b') carbon paper with 25 nm Al deposited, (c, c') carbon paper with 10 nm Fe deposited, (d, d') carbon paper with 5 nm Al/10 nm Fe deposited, (e, e') carbon paper with 15 nm Al/10 nm Fe deposited, and (f, f') carbon paper with 25 nm Al/10 nm Fe deposited.

As shown in Figure 3-6, the surface of plain carbon paper does not contain possibly active catalyst nanoparticles to promote the growth of CNTs. The absence of CNTs grown on the plain carbon paper is therefore expected. The surface of annealed carbon paper with a 25 nm Al buffer layer does not contain active nanoparticles. The surface remains mostly smooth, other than wrinkles and trenches

of a typical carbon paper surface. With close inspection, there is nanoscale roughness on the surface of carbon fibers, resembling the formation of ultrafine nanoparticles. The surface of annealed carbon paper with a 10 nm Fe catalyst layer deposited shows two notable characteristics. Firstly, the Fe catalyst layer coalesces into large nanoparticles of up to ≈ 200 nm in diameter. The large size of Fe particles is commonly not considered active for the growth of CNTs. Secondly, there are apparent losses of carbon fiber materials in the vicinity to the Fe nanoparticles, evident in the form of voids on the surface of carbon fibers. The presence of voids are not typically found in either pristine or annealed carbon paper. The loss of carbon materials suggests possible reactions between the Fe catalyst layer and the carbon materials in its vicinity. It is possible that, at the deposition temperature, Fe reacts with carbon to form carbide and becomes largely inactive for the promoting of CNT growth. With the addition of an Al buffer layer, especially with an Al layer thickness of more than 15 nm, annealed Fe catalysts are finely divided into smaller nanoparticles and therefore possibly more active for promoting CNT growth. One possible explanation is that, at high temperature, Al acts as a sacrificial material to react with carbon to form aluminum carbide, and effectively forms a protection barrier for Fe nanoparticle formation. It was suggested that, at growth temperatures of CNTs, Al reacts with carbon fiber materials to form a thin film of Al_4C_3. [110,113]

As demonstrated, the bi-layer catalyst configuration of 25 nm Al / 10 nm Fe deposited on carbon paper provides an effective condition to promote the growth of CNTs on carbon paper. This catalyst condition is therefore used as the optimized condition for CNT growth, together with the aforementioned CVD conditions (750 °C, 30 sccm C_2H_4 + 100 sccm Ar/H_2, 30 min growth time).

3.1.3. Physical characterization of the as-grown CNTs

The as-grown CNTs on carbon paper using the optimized catalyst and CVD growth conditions were further characterized with TEM, spectroscopic physical characterization techniques (i.e. Raman spectroscopy and XPS), and BET surface area analysis.

Figure 3-7 shows a TEM micrograph of the as-grown CNTs. CNTs are shown to have hollow tubular structures of well crystalline multi-walled nanotubes. The CNT external diameter is commonly measured at ≈ 10 nm, although larger CNTs (e.g. ≈ 30 nm in diameter) are occasionally found.

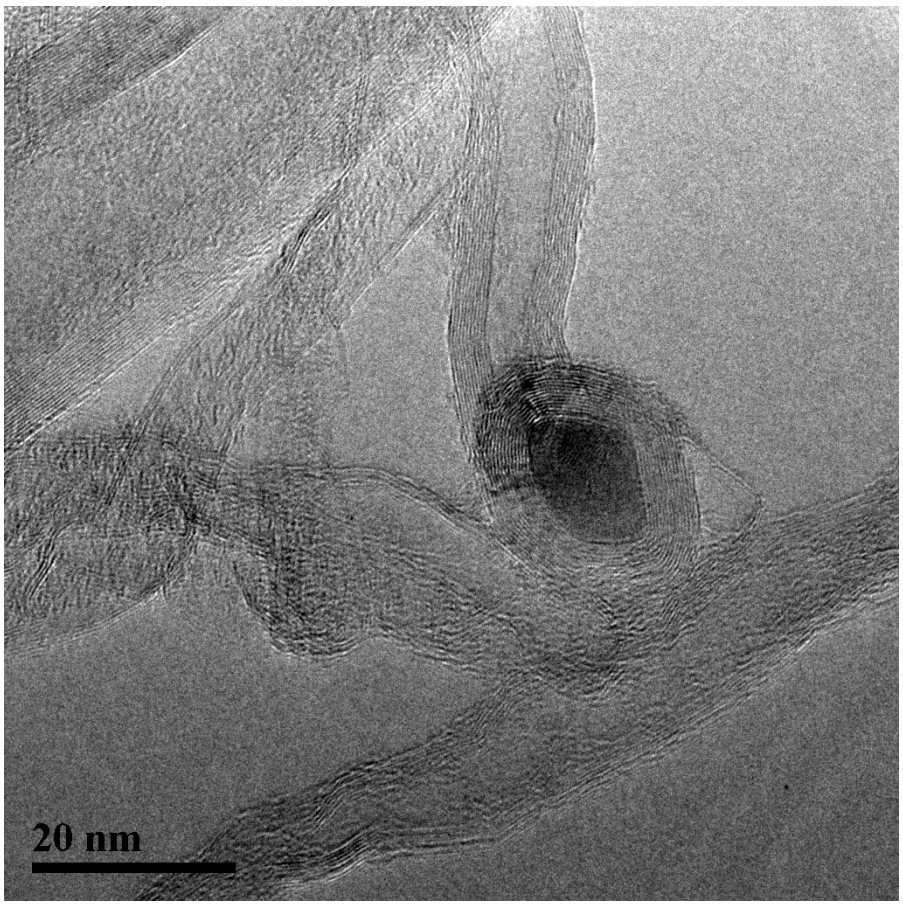


Figure 3-7. TEM micrograph of the as-grown CNTs on carbon paper.

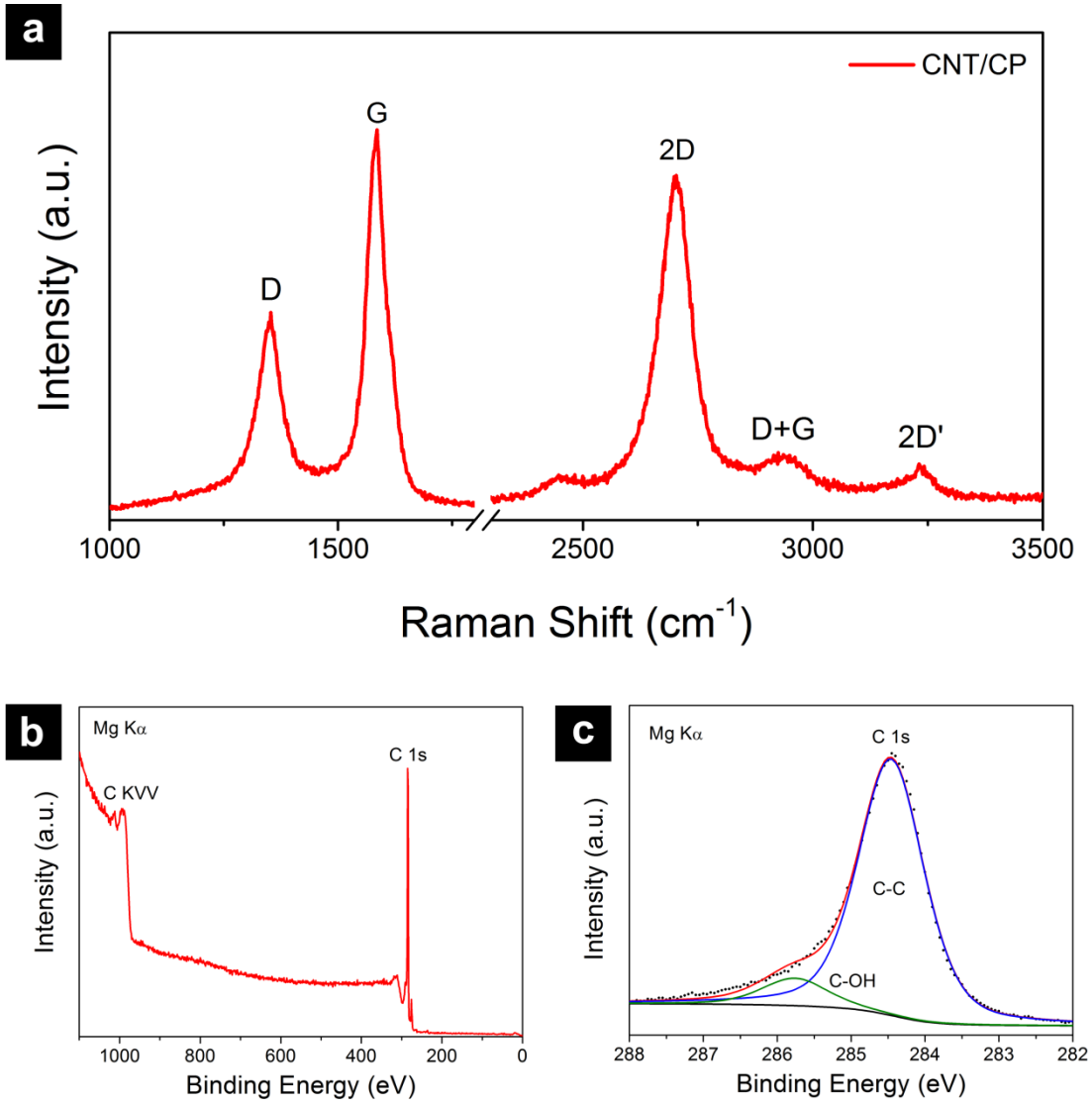


Figure 3-8. Spectroscopic characterization of the as-grown CNTs on carbon paper. (a) Raman spectroscopy, (b) XPS survey scan and (c) C 1s high resolution scan of the as-grown CNTs on carbon paper.

Figure 3-8 provides the spectroscopic characterization of the as-grown CNTs. CNTs were characterized with Raman spectroscopy to further confirm their crystalline graphitic nature. The Raman spectrum shows strong characteristic peaks of graphitic materials, including the disorder-induced D band and graphitic in-plane vibration mode E_{2g} [114-116] G band, as well as second order peaks 2D, D+G and 2D'. The presence of strong graphitic characteristic peaks suggests a high sp^2 content in

the as-grown CNTs. The purity and chemical state of the constituent elements in the as-grown CNTs were examined with XPS. As shown in Figure 3-8b, the survey scan spectrum is exclusively dominated by the signature C 1s peaks in the 280-290 eV binding energy region. The result confirms the high purity of the as-grown CNTs, with carbon is the only detected constituent element. The high resolution scan of the C 1s peaks region is shown in Figure 3-8c. The spectrum is fitted with two mixed Gaussian-Lorentzian peaks, after subtracting a Shirley background. The two peaks located at binding energies of 284.5 eV and 285.8 eV are attributed to the elemental carbon and the oxidized carbon (C-OH) states, respectively. The elemental state of carbon accounts for 90.3% of the signal, based on the peak areas of the two chemical states. The surface oxidation of the as-grown CNTs is expected due to the exposure to the air. The surface area of CNTs was estimated using the BET surface area and porosity analysis. The BET specific surface area of CNTs is measured at 270 m^2 g^{-1}, comparable to the range 250-300 m^2 g^{-1} reported for commercial Nanocyl™ NC 7000 MWCNTs with average diameter of 9.5 nm according to the manufacturer. [117]

3.2. Growth of free-standing graphene

3.2.1. Growth of free-standing graphene by the RF-PECVD method

Free-standing graphene, also known as carbon nanowalls, was first successfully grown on sapphire substrates by Wu *et al.* using the microwave plasma enhanced chemical vapor deposition method. [40] Since then, free-standing graphene was successfully grown on various substrates using microwave plasma enhanced

chemical vapor deposition (MWPECVD), [40-43] inductively coupled PECVD, [44] parallel plate PECVD with H-radical injection, [45-47] hot filaments chemical vapor deposition (CVD), [48] and radio frequency PECVD. [49]

In this study, free-standing graphene was grown by using the radio frequency PECVD method. C_2H_2 (99.8%) and H_2 (99.9995%) were used as carbon precursor and carrier gas, respectively. The growth process was controlled by deposition temperature, deposition time, and gaseous precursor flow rates.

3.2.2. Effect of growth conditions on the deposition of free-standing graphene

In this section, individual effect of growth conditions on the structure of as-grown free-standing graphene is studied. From an understanding of the process-material properties relationship, a suitable combination of growth conditions is then selected for specific material requirements (e.g. a desirable pore size range of 20-40 nm in PEMFC carbon support). The growth process of graphene was investigated for three parameters, including gas composition, deposition temperature and growth time. Other growth conditions were fixed at a pressure of 500 mTorr, radio frequency plasma power of 100 W and Al/Fe-deposited carbon papers as substrates. A summary of experimental conditions used is provided in Table 3-2.

Table 3-2. Summary of experimental conditions for free-standing graphene growth optimization.

		C_2H_2 flow rate (*)				
		60 sccm	40 sccm	30 sccm	20 sccm	10 sccm
Deposition temperature	700 °C	1 hr (**)	1 hr, 2 hrs	1 hr	1 hr	1 hr
	600 °C		1 hr			

(*) H_2 flow rate was fixed at 60 sccm.
(**) Denotes deposition duration.

Precursor gas composition

To study the effect of precursor gas composition on the growth of free-standing graphene, the flow rate of C_2H_2 was studied at five experimental points of 60 sccm, 40 sccm, 30 sccm, 20 sccm and 10 sccm, whilst the flow rate of carrier gas H_2 was fixed at 60 sccm. All other parameters were fixed at a deposition temperature of 700 °C and a deposition time of 1 hr.

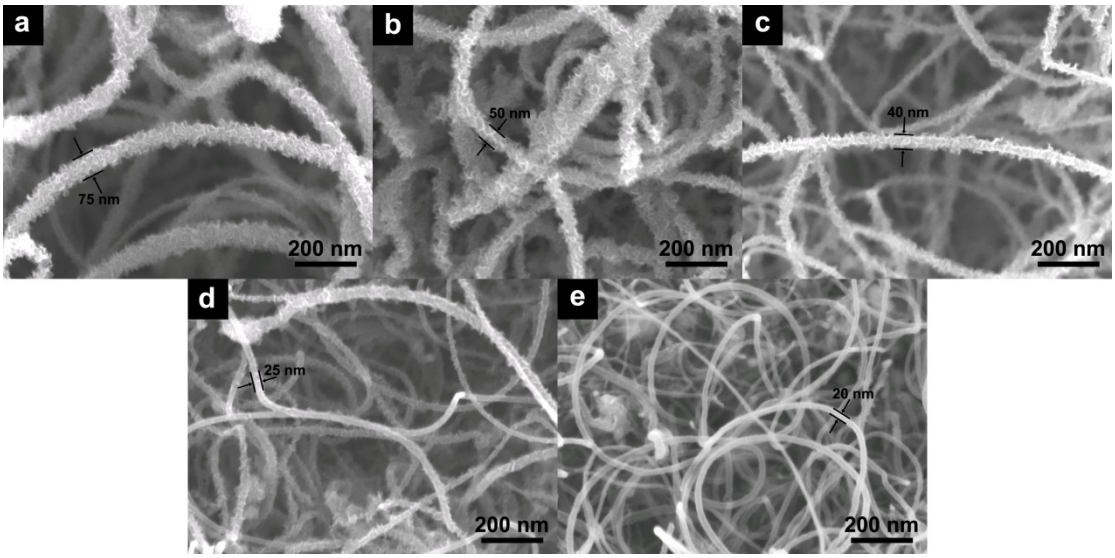


Figure 3-9. Effect of precursor gas composition on the PECVD growth of free-standing graphene. SEM images of the as-grown free-standing graphene with 60 sccm H_2 and a C_2H_2 flow rate of (a) 60 sccm, (b) 40 sccm, (c) 30 sccm, (d) 20 sccm, and (e) 10 sccm.

Figure 3-9 shows SEM micrographs of the as-grown free-standing graphene at different C_2H_2 flow rates. As RF-PECVD is also an effective growth method for CNTs when suitable catalysts are available, the nanostructured materials grown on carbon paper with deposited Al/Fe catalysts show unique morphology of free-standing graphene grown on carbon nanotube scaffolds. The density of deposited graphene is, however, dependent on the gas composition. As shown in Figure 3-9, the density of deposited graphene decreases with a decrease of C_2H_2 flow rate. At a

high flow rate of 60 sccm C_2H_2, graphene is deposited densely on the surface of CNTs. With decreasing C_2H_2 flow rates, graphene is deposited sparsely. At a flow rate of 10 sccm C_2H_2, virtually no deposited graphene is observed beside the smooth fibrous CNT morphology. The overall diameter of the graphene-on-CNT grown at C_2H_2 flow rate of 60 sccm, 40 sccm, 30 sccm, 20 sccm and 10 sccm is approximately 75 nm, 50 nm, 40 nm, 25 nm and 20 nm, respectively. The precursor gas composition proves to be an effective mean to control the density of deposited free-standing graphene. During the PECVD growth of free-standing graphene, C_2H_2 acts as the carbon precursor source favoring the carbon deposition while H_2 acts as the etching agent favoring the carbon removal process. At a higher ratio of C_2H_2/H_2, the carbon deposition is more dominant and results in higher nucleation and growth rates of graphene. At a lower ratio of C_2H_2/H_2, the etching process is dominant, and results in lower nucleation density and growth rate of graphene. The interplay of carbon precursor gas and etching gas, and its effects on the deposited graphene density were also similarly reported by other studies. [118,119]

Deposition temperature

The effect of deposition temperature on the growth of free-standing graphene was investigated at 700 °C and 600 °C. All other parameters were fixed at gas flow rates of 60 sccm H_2 + 40 sccm C_2H_2 and a deposition time of 1 hr. Free-standing graphene was deposited on both Al/Fe-deposited carbon papers and plain carbon papers for comparison purposes.

Figure 3-10 shows SEM micrographs of the as-grown free-standing graphene on carbon papers at the two different deposition temperatures. As shown

in Figure 3-10a-b, it is clear that the lower deposition temperature of 600 °C does not support the growth of CNTs well, compared to the higher deposition temperature of 700 °C. The poor CNT growth at 600 °C results in a less distinctive graphene-on-CNT morphology, as opposed to the nanostructure grown at 700 °C. In addition, the density of deposited graphene obtained at 600 °C is lower than that at 700 °C. A lower deposited graphene density at 600 °C compared to 700 °C is also evident on plain carbon paper substrates, as shown in Figure 3-10c-d. The lower density of deposited graphene is explained by the lower deposition and nucleation rate at the lower temperature. The deposition temperature proves to be an effective parameter, in addition to the gas composition, to control the deposited density of graphene.

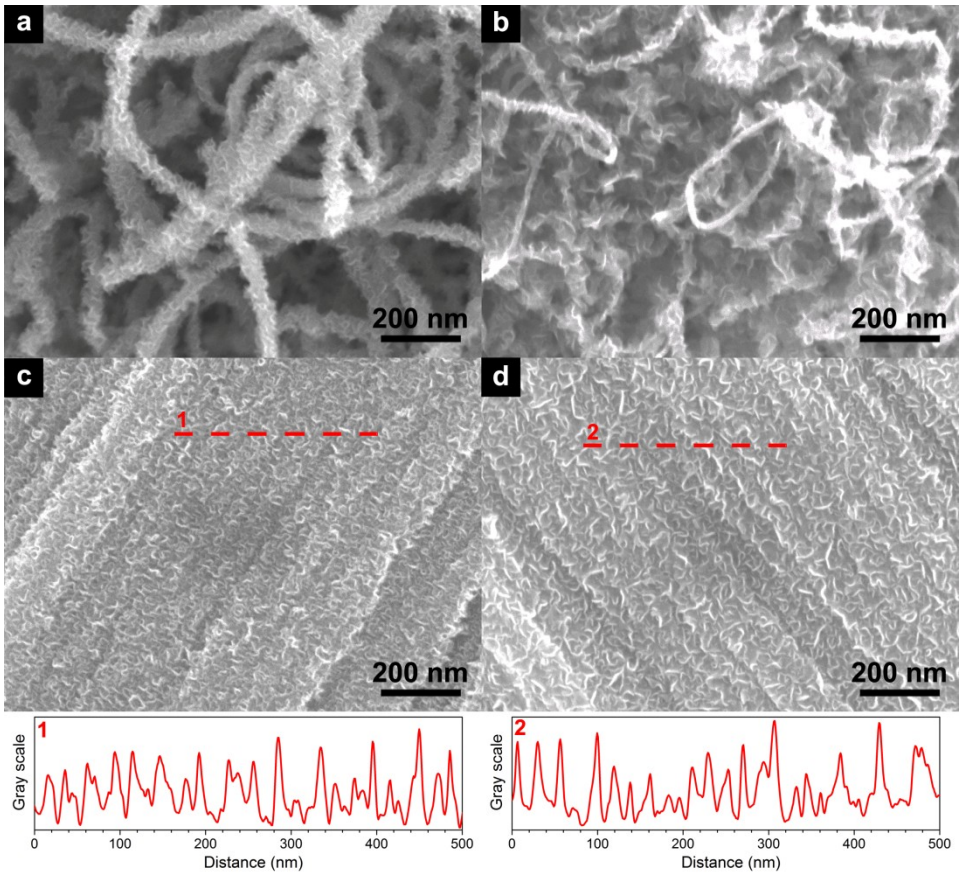


Figure 3-10. Effect of deposition temperature on the PECVD growth of free-standing graphene. SEM images of free-standing graphene grown on Al/Fe-deposited carbon papers at (a) 700 °C and (b) 600 °C, and on plain carbon papers at (c) 700 °C and (d) 600 °C.

To estimate the average inter-graphene sheet distance (not inter-atomic layer distance) of free-standing graphene grown at different temperatures, a 500-nm-long line profile of SEM image was taken for each growth temperature. The profiled location of the as-grown graphene on plain carbon paper is marked by the red dashed lines in Figure 3-10c-d. The corresponding gray scale profiles of the SEM images are attached in Figure 3-10. From the profiles, the average inter-graphene sheet distance of free-standing graphene grown at 700 °C and 600 °C is estimated 20 nm and 24 nm, respectively.

Growth time

Beside the deposition temperature and gas composition, the effect of growth time on the deposition of free-standing graphene was also investigated. Two deposition durations of 1 hr and 2 hrs were studied, whilst other parameters were fixed at 700 °C and 60 sccm H_2 + 40 sccm C_2H_2. As shown in Figure 3-11, the lateral size of graphene can be increased by increasing the growth duration. The overall diameter of the graphene-on-CNT obtained after 2 hrs of deposition is ≈ 2.4 times larger than that obtained after 1 hr of deposition.

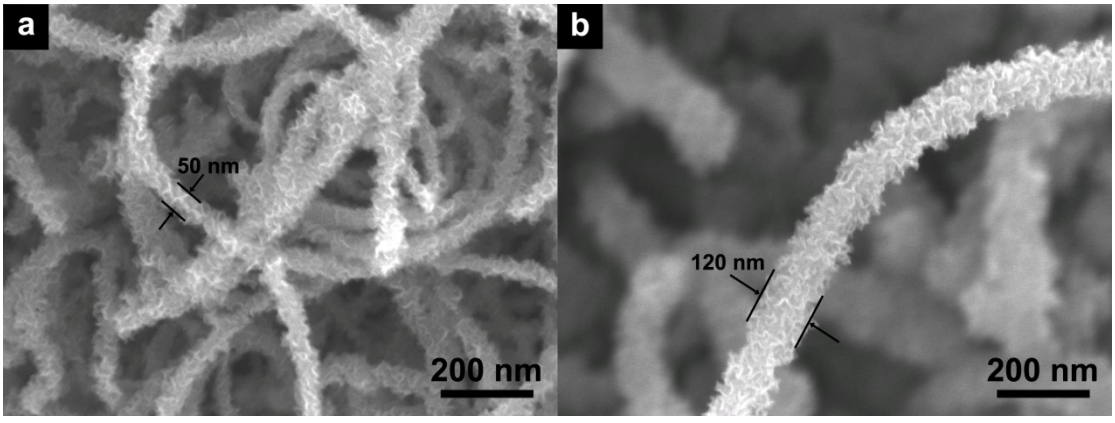


Figure 3-11. Effect of growth time on the deposition of graphene. SEM micrographs of the as-grown graphene on carbon paper after (a) 1 hr and (b) 2 hrs of deposition.

In the above discussions, the density and size of free-standing graphene can be controlled by precursor gas composition, deposition temperature and deposition time. A suitable combination of these parameters can be selected for specific requirements. As discussed in section 1.2.5, a desirable carbon support for Pt catalysts in PEMFCs should have pore sizes close to the 20-40 nm range. Among the demonstrated growth conditions, the deposition conditions of 60 sccm H_2 + 40 sccm C_2H_2 and 600 °C (Figure 3-10b&d) produce free-standing graphene with spacing between graphene sheets close to this 20-40 nm range. These conditions are therefore chosen for further studies. To compensate for the slower growth rate at lower deposition temperature, a growth duration of 2 hrs is used.

3.2.3. Physical characterization of the as-grown free-standing graphene

As demonstrated in the above section, PECVD is a versatile method to grow free-standing graphene. With a suitable catalyst available, an unique structure of graphene deposited on carbon nanotube scaffolds is achieved. Without any catalysts, free-standing graphene can be grown directly on carbon papers, instead of on carbon nanotube scaffolds. In fact, free-standing graphene can be grown with catalyst-free PECVD methods on various substrates, as demonstrated in the literature. [37,43] To exclusively characterize the free-standing graphene and to avoid the ambiguous contributions of other carbon substrate materials, free-standing graphene was deposited directly on a silicon wafer using the catalyst-free RF-PECVD method. The growth conditions were 600 °C, 60 sccm H_2 + 40 sccm C_2H_2, and 2 hrs growth time. The as-grown free-standing graphene was characterized with electron microscopy

techniques (SEM and TEM) and spectroscopy techniques (i.e. Raman spectroscopy and XPS).

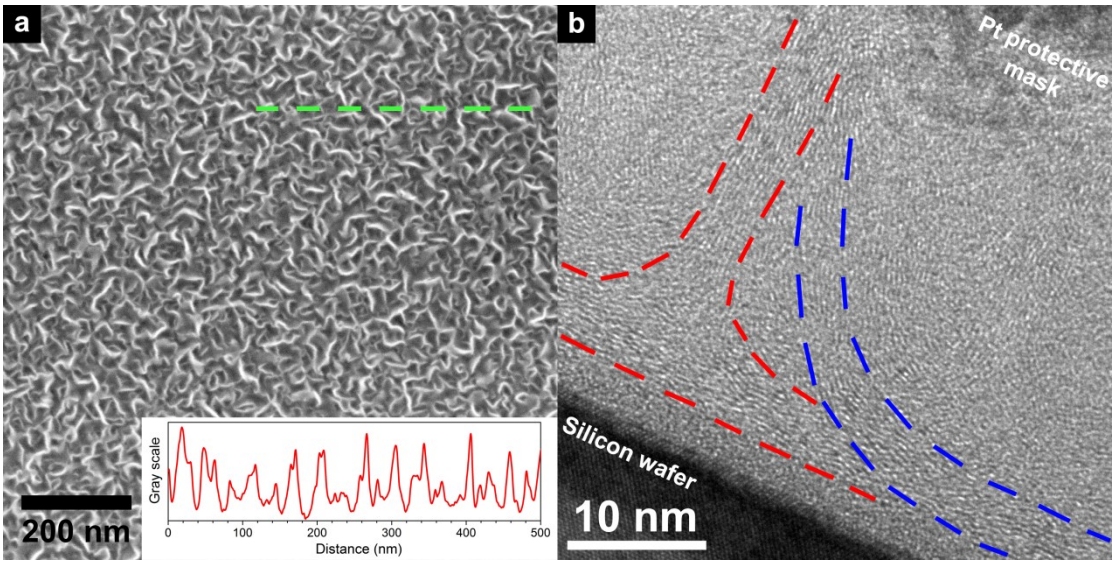


Figure 3-12. Electron microscopy characterization of the free-standing graphene grown on Silicon wafer. (a) SEM micrograph of the top surface with (inset) a line profile of the as-grown graphene in the location marked by the green dashed line, and (b) TEM cross-sectional micrograph of the free-standing graphene grown on Silicon wafer, with outlines of graphene sheets marked in red and blue.

Figure 3-12 shows the electron micrographs of the as-grown free-standing graphene on silicon wafer. Figure 3-12a shows an SEM micrograph of the top surface of free-standing graphene. As shown, graphene is grown directly on silicon wafer in the form of vertically aligned thin sheets. The graphene is grown uniformly across the field of view. The inter-sheet spacing between free-standing graphene sheets is estimated 25 nm, which is in the desirable pore size range 20-40 nm for a PEMFC catalyst support. Whilst free-standing graphene was successfully grown on various substrates by many research groups, the exact growth mechanism of the free-standing graphene by PECVD methods is still under debate. Malesevic *et al.* studied

the early stage growth of the free-standing graphene and proposed a three-step growth mechanism of free-standing graphene. According to the proposed mechanism, graphitic base layers are firstly formed parallel to the substrate surface, with the presence of irregular cracks over the entire surface. The upward curling cracks then serve as the nucleation sites for the growth of free-standing graphene. Finally, free-standing graphene is grown vertically from these nucleation sites. [43] To verify this mechanism, a TEM cross-sectional lamella of the free-standing graphene on silicon wafer was prepared using the FIB-SEM lamellae preparation method. Figure 3-12b shows the cross-sectional TEM micrograph of the free-standing graphene. As identified and outlined with colored markers, the free-standing graphene consists of a few graphitic layers that are firstly aligned in parallel to the silicon substrate before continuously curling upwards and forming vertically aligned graphene sheets. Our cross-sectional TEM analysis supports the growth mechanism proposed by Malesevic *et al.* [43]

The crystallinity and chemical purity of the graphene were further characterized with Raman spectroscopy and XPS, as shown in Figure 3-13. Similar to the results obtained for CNTs, the Raman spectrum of free-standing graphene shows strong characteristic peaks of graphitic materials, including D, G, 2D, D+G, and 2D' bands, suggesting a high concentration of sp^2 carbons. The disorder-induced D band is present strongly, explained by the preferential exposure of graphitic edges in the vertically aligned configuration of graphene. The XPS survey spectrum in Figure 3-13b is dominated by the characteristic C 1s peaks in the 280–290 eV binding energy range. Two adventitious impurity elements found are oxygen and fluorine, present

with very low contributions to the total spectrum. Overall, the free-standing graphene mainly consists of carbon element. The C 1s high resolution scan is fitted with two peaks attributed to elemental carbon and C-OH carbon. The elemental carbon state accounts for 89.0% of signal based on fitted peak areas.

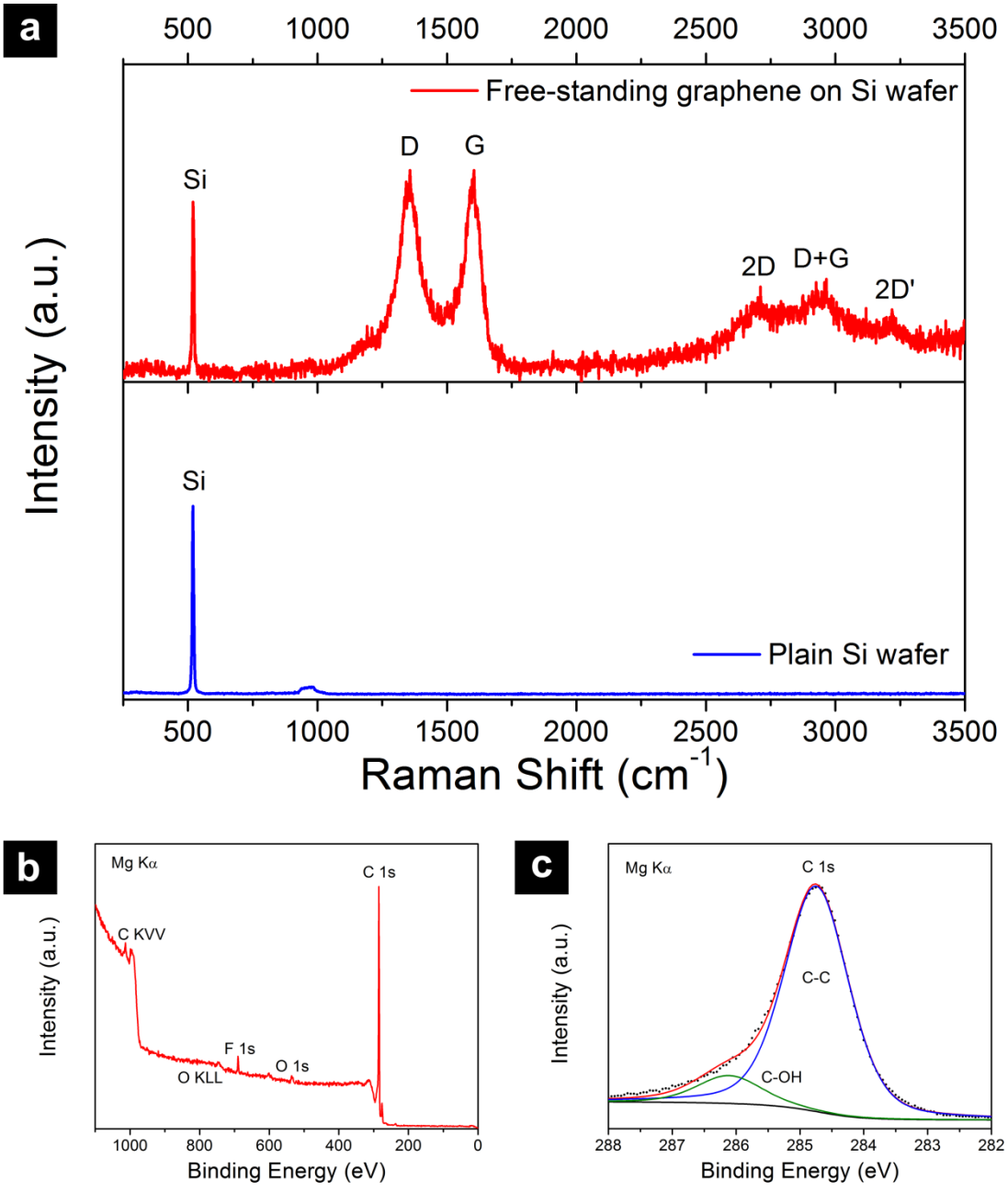


Figure 3-13. Spectroscopic characterization of the free-standing graphene grown on Silicon wafer. (a) Raman spectra of the free-standing graphene grown on Silicon wafer and of a reference Silicon wafer. (b) XPS survey spectrum and (c) C 1s high resolution scan of the free-standing graphene grown on Silicon wafer.

3.3. Growth of Graphene-Carbon Nanotube hybrids on carbon paper

3.3.1. Growth of Graphene-Carbon Nanotube hybrids using a two-step growth method

As demonstrated in section 3.2, graphene can be deposited directly on carbon nanotube scaffolds to form graphene-on-carbon nanotube nanostructures (referred to as Graphene-Carbon Nanotube hybrids) in a single step using the RF-PECVD method if suitable catalysts are available. However, in order to individually control the morphology of carbon nanotube scaffolds and free-standing graphene, we adopt a two-step growth method. CNTs are firstly grown on carbon paper using the thermal CVD method, with the optimized CVD and catalyst conditions. Graphene is subsequently deposited on CNT scaffolds using the catalyst-free RF-PECVD method. At the lower PECVD deposition temperature of 600 °C, the growth of CNTs is not well facilitated. The CNT morphology is therefore expected to be mainly determined by the first thermal CVD growth step.

The two-step growth process of Graphene-Carbon Nanotube hybrids on carbon papers is summarized as following:

- Carbon paper is deposited with 25 nm Al / 10 nm Fe bi-layer catalysts.
- CNTs are grown on carbon paper using the thermal CVD method at 750 °C, 30 sccm C_2H_4 + 100 sccm Ar/H_2, and 30 min growth time.
- Graphene is then deposited on CNT scaffolds using the catalyst-free RF-PECVD method at 600 °C, 40 sccm C_2H_2 + 60 sccm H_2, and 2 hrs growth time.

3.3.2. Physical characterization of the GCNT hybrids

The morphological characterization with FE-SEM of the as-grown GCNT hybrids on carbon paper is shown in Figure 3-14. Figure 3-14a, b, and c show the SEM micrographs of the hybrid at medium, low and high magnifications, respectively. As depicted by Figure 3-14a, the hybrids show a unique nanostructure featuring a long, fiber-like main structure, associated with the characteristics of CNT, and thin leaf-like features grafted directly on and along the CNTs with an ultra-high density. The hybrids are uniform in size and morphology, with an average overall diameter of approximately 100 nm.

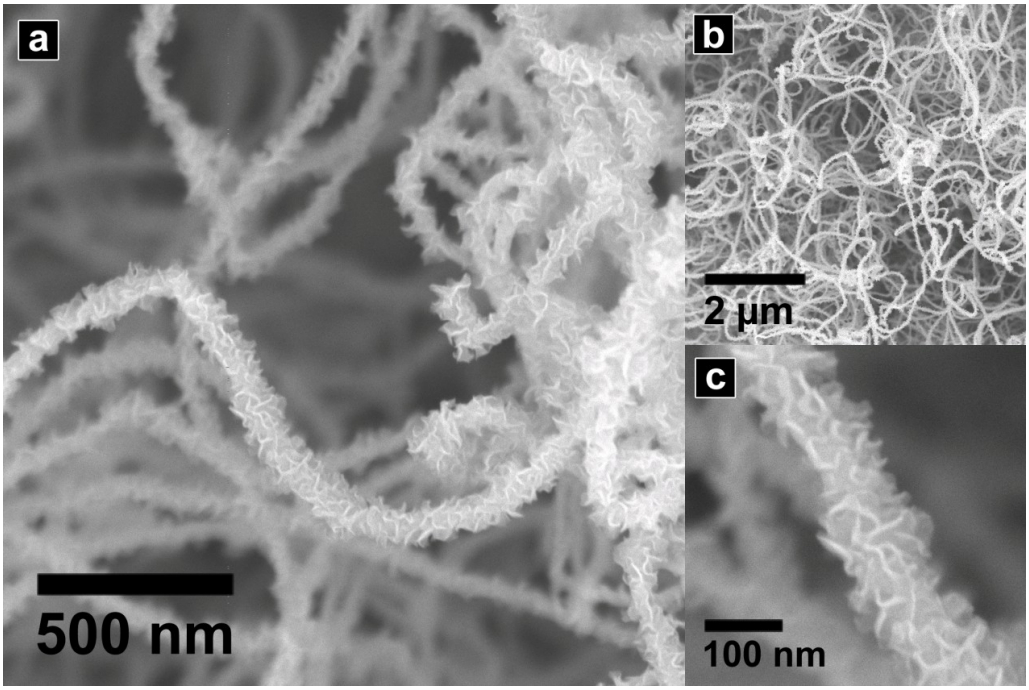


Figure 3-14. Morphological characterization of the GCNT hybrids on carbon paper. SEM micrographs of the hybrids at (a) medium magnification, (b) lower magnification and (c) higher magnification.

Figure 3-14b shows the lower magnification SEM micrograph of the hybrids. The hybrids are grown densely and uniformly while retaining good porosity. These

characteristics are highly valuable for the electrochemical electrode applications, offering a high surface area carbon support while ensuring efficient mass transport and good active material accessibility. The overall structure of the hybrids resembles that of ordinary CNTs grown on carbon paper. A close-up view of the hybrids is shown in Figure 3-14c. At high magnification, it is clear that the hybrids offer a high density of exposed edges, which is not possible for ordinary CNTs where inert basal graphitic planes are exposed instead. When such hybrids are used as carbon supports for active materials in an electrochemical electrode, the high density of graphene edges could offer numerous anchor points for the active materials.

The microstructure of hybrids was further examined with TEM as shown in Figure 3-15a-b. These micrographs agree well with the SEM micrographs shown in Figure 3-14. Figure 3-15a similarly reveals a long fiber central structure and leaf-like features grafted on. The white dashed lines in the TEM micrograph outline the boundary region between the CNT and the leaf-like features. The leaf-like features have a semi-transparent appearance, suggesting an ultra-thin sheet morphology. Figure 3-15b shows a high resolution TEM micrograph of the GCNT hybrids in the region outlined by the black-colored square in Figure 3-15a, featuring the edge of a leaf-like structure outlined by the white dashed curves. The HR-TEM micrograph reveals the layered structure of this leaf-like feature. The feature has a few layers, comprising 5-6 layers in this particular example. The interlayer distance is approximately 0.386 nm, close to that of graphitic materials. We associate these ultra-thin sheets with the two dimensional graphene. The as-grown hybrids are referred to as Graphene-Carbon Nanotube hybrids (GCNT).

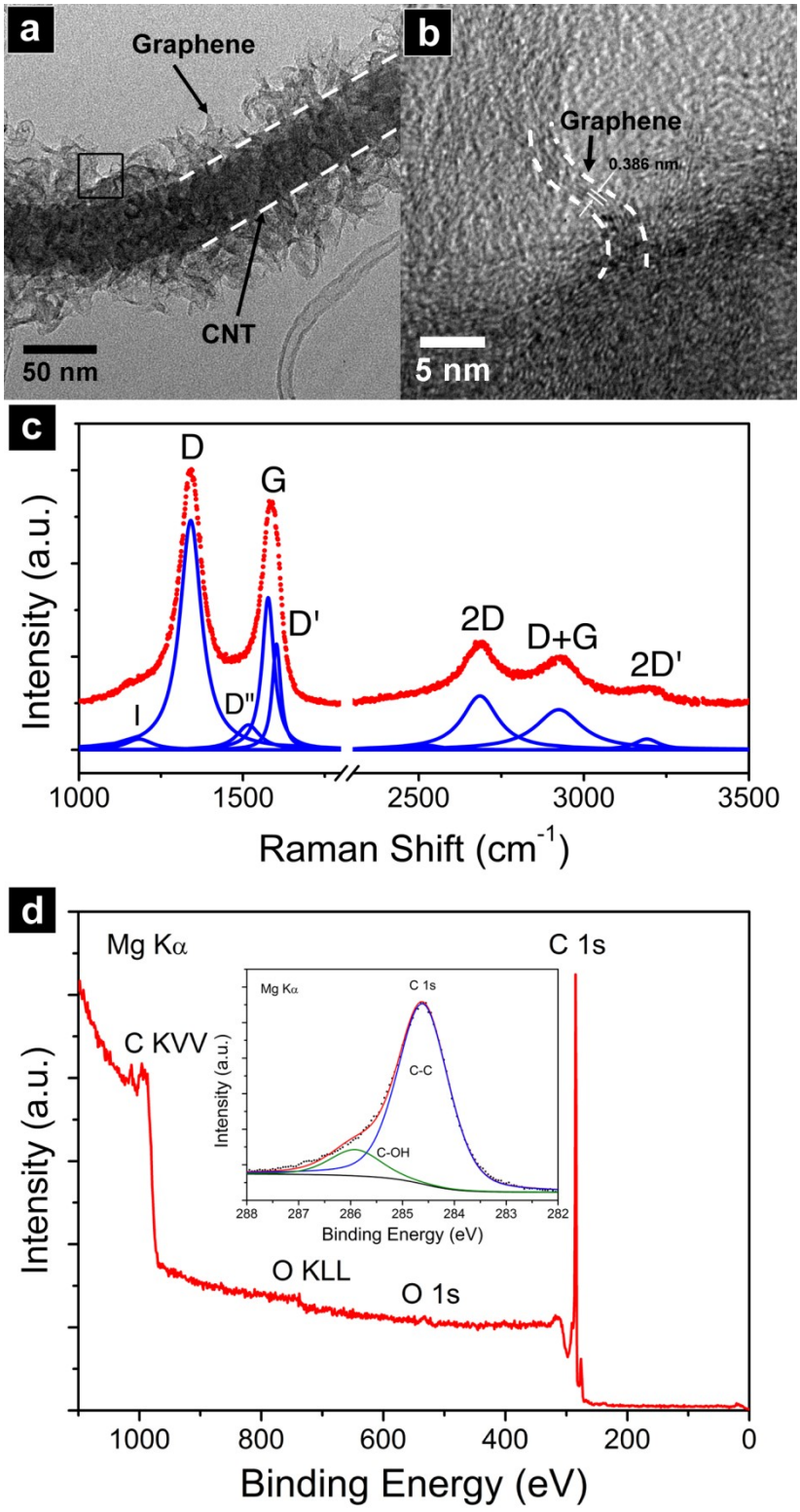


Figure 3-15. Microscopic and spectroscopic characterization of the GCNT hybrids. (a) Bright field TEM micrograph of the hybrids; (b) HR-TEM micrograph of the GCNT in the region outlined by the black-colored square in figure (a); (c) Background-corrected Raman spectrum (red curve) with Lorentzian peak fittings (blue curves) of the hybrids; (d) Survey scan XPS spectrum and (inset) high resolution scan of C 1s peaks of the hybrids.

The hybrids were further characterized with Raman spectroscopy to confirm their crystalline graphitic nature. The background-corrected Raman spectrum of the GCNT hybrids is shown in Figure 3-15c. The spectrum was fitted with Lorentzian peaks. The fitting reveals characteristic peaks for graphitic materials, including the D peak at Raman shift ~1341 cm^{-1}, the G peak at ~1577 cm^{-1}, the D' peak at ~1603 cm^{-1}, and second order peaks 2D (~2685 cm^{-1}), D+G (~2924 cm^{-1}) and 2D' (~3191 cm^{-1}). Three other minor shoulder peaks (~1184 cm^{-1}, ~1517 cm^{-1} and ~2528 cm^{-1}) are identified, with minor contributions to the overall spectrum. The two dominant and signature peaks (D and G) show strong intensities and sharp profiles, suggesting a high sp^2 content in the GCNT hybrids. The intensity ratio I_D/I_G between these two peaks is generally used to estimate the crystallinity of the graphitic materials. The disorder-induced D band is thought to originate from crystal defects such as grain boundaries, while the G band originates from in-plane vibration mode E_{2g}. [114-116] The I_D/I_G intensity ratio gives high values of 1.51 by fitted peak heights and 2.68 by fitted peak areas. These high values are attributed to the ultra-high density of exposed graphene edges along the GCNT surfaces and the small size of the graphene sheets. High intensities of the D peak in graphitic materials with edge exposure were reported in existing literature. [115,116] No D peak or a weak D peak was observed for the basal plane of well crystallized graphite. [114,116] This result further supports the observation of graphene edges in SEM and TEM micrographs.

The purity and chemical state of the constituent elements in the GCNT hybrids were examined with XPS. Figure 3-15d shows the XPS spectra of the hybrid, including the XPS wide spectrum survey scan and (inset) high resolution scan of C 1s

peaks region. The survey scan spectrum is exclusively dominated by the signature C 1s peaks in the 280–290 eV binding energy region. The contaminant identified is oxygen, with a minor contribution from the O 1s peak in the 525–535 eV binding energy region due to exposure to ambient air. The XPS wide spectrum confirms carbon as the main constituent element. The high resolution scan of the C 1s peaks region is shown in the inset. The spectrum is fitted with two mixed Gaussian-Lorentzian peaks, after subtracting a Shirley background. The two peaks located at binding energies of 284.6 eV and 285.9 eV are attributed to the elemental carbon and the oxidized carbon (C-OH) states, respectively. The elemental state of carbon accounts for 87.3% of the signal, based on the peak areas of the two chemical states. The surface oxidation of the GCNT hybrids is expected due to the exposure to the air. The GCNT hybrids were further characterized with BET surface area analysis. The BET specific surface area of GCNT hybrids was measured at 214 $m^2 g^{-1}$.

3.3.3. Growth mechanism of the GCNT hybrids

Free-standing graphene has been successfully grown on various substrates without the aid of any catalyst using chemical vapor deposition methods, as widely reported in the literature. [40-49] In fact, it was suggested that free-standing graphene can be grown on any substrates that can withstand the high deposition temperature of up to 700 °C. [43] In this thesis, free-standing graphene was indeed successfully grown on various substrates without any catalysts deposited, including plain carbon paper and silicon wafer. It is therefore reasonable to expect free-standing graphene to grow on pre-formed CNT scaffolds to form the graphene-carbon nanotube hybrids using the same deposition method.

Currently the growth mechanism of free-standing graphene is not well understood and remains inconclusive. There were several studies proposing the growth mechanism of free-standing graphene. Nevertheless, a consensus has not been reached. In a previous study, Malesevic *et al.* proposed that the growth mechanism of free-standing graphene involved three steps. Firstly, a basal graphitic layer is formed parallel to the substrate surface. Subsequently, due to the internal stress caused by temperature gradients or a lattice mismatch between graphitic materials and substrate materials, cracks are formed from the base layer, and serve as the nucleating sites for the free-standing graphene. Free-standing graphene continues to grow from these crack sites. [43] Parker *et al.* studied the growth of graphenated-CNTs and proposed a stress-buckling growth mechanism of graphene on CNT. The authors suggested that the outer sidewalls of the CNTs grew faster than the inner walls, causing internal stress to the sidewalls. Once the stress exceeded the strength of CNT sidewalls, buckling of the sidewalls occurred and formed fractures on the CNT surface, serving as the nuclei for graphene growth. Free-standing graphene continued to grow from these nucleation sites. [51] Other studies suggested a mechanism where plasma-induced defects on the CNT surface served as the preferential nucleating points for free-standing graphene. [54,120] Yu *et al.* suggested that whilst CNTs can serve as scaffolds for growing additional walls at a slower growth rate under PECVD growth condition, the preferential growth of graphene at the defect site ultimately led to the formation of free-standing graphene. [54] Zeng *et al.* further suggested that the density of graphene was related to the plasma-induced defect density on CNT surface. [120] The possible growth of additional CNT walls and

the thickening of the CNT walls during the growth process of graphene were found by several studies. [50,54,120]

In this study, the TEM micrographs of free-standing graphene grown on silicon wafer and CNTs (Figure 3-12b and Figure 3-15b) show that the as-grown free-standing graphene indeed starts as basal graphitic layers formed parallel to the substrate surface and continuously curves upwards to form free-standing graphene sheets. The observations agree well with the previous studies by Malesevic *et al.* [43] and Parker *et al.*, [51] and other researchers. [52,54] However, in this study, it is also found that the density of the as-grown graphene increases with C_2H_2 flow rate and deposition temperature. Free-standing graphene is also successfully grown on a silicon wafer, without any pre-deposition of carbon materials. Although the stress-buckling mechanism and defect-induced nucleation mechanism are not fully excluded, we alternatively propose that the growth of free-standing graphene may start with a nucleation process of individual graphitic nuclei. The formation of planar nanographene in the early nucleation stage of free-standing graphene grown on Ti-coated Si substrate was also reported by Hiramatsu *et al.* [121] The proposed growth mechanism is as following:

i. The nucleation starts with the formation of individual graphitic nuclei on the surface of substrate. The graphitic nuclei are aligned parallel to the substrate surface. The nucleation rate of graphitic nuclei is positively dependent on the carbon precursor concentration (e.g. C_2H_2 flow rate) and deposition temperature. The higher carbon precursor concentration and higher deposition temperature

result in a higher nucleation rate of graphitic nuclei and ultimately a smaller inter-graphene sheet spacing.

ii. With the additional deposition of carbon species, the graphitic nuclei preferentially grow laterally from the active graphitic edges, although the additional nucleation of graphitic nuclei is possible.

iii. The growing graphitic islands would ultimately collide with the neighboring graphitic islands. The colliding edges buckle and curl upwards. The upwards curling of graphitic edges may also be caused by the local electric field near the surface of substrate, as proposed by Zhu *et al.* [122] It is commonly believed that the growth of free-standing graphene by PECVD methods is strongly supported by the local electric field present near the sample surface, as demonstrated in previous studies. [118,123]

iv. With the additional deposition of carbon species, graphene continues growing from the curled edges and forms the free-standing graphene sheets on CNTs.

An illustration of the proposed growth mechanism is shown in Figure 3-16.

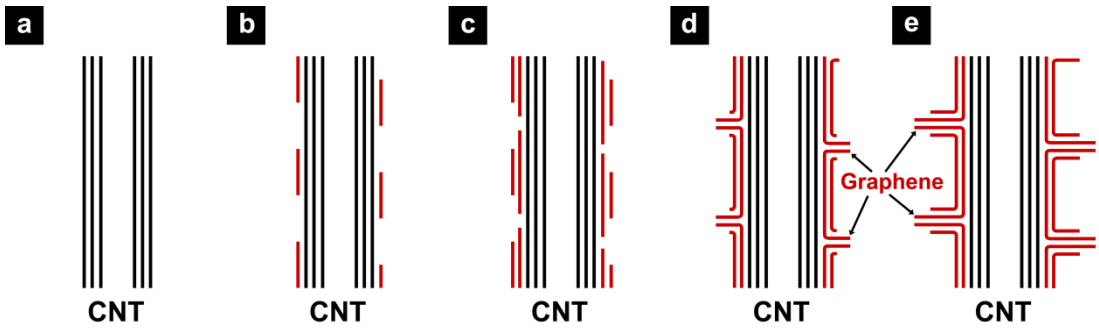


Figure 3-16. Proposed growth mechanism of the GCNT hybrids. (a) Original CNT scaffold, (b) nucleation of graphene, (c) lateral growth of graphene islands and additional nucleation, (d) buckling of graphene edges upon the collision of a growing graphene island with its neighboring graphene islands, and (e) free-standing graphene continues to grow from the curled graphene edges.

3.4. Summary

As illustrated, the GCNT hybrids on carbon paper possess a unique all-carbon hierarchical structure where CNTs are grown directly on carbon fibers and graphene is densely grown on the CNTs. Such a hierarchical structure could offer direct electrical conducting pathways from graphene to the carbon paper. Compared to the more commonly reported graphenated CNTs grown on silicon wafer, this study demonstrates the direct growth of GCNT on porous carbon paper substrate, which provides a flow-through electrode structure and is readily suitable for electrochemical applications. The impervious, brittle and poorly conductive silicon wafer substrate is not well suitable for such applications. GCNT hybrids on carbon paper are grown with high density of graphene and CNTs, providing high surface area for deposited active materials. The GCNT hybrid hierarchical structure combines the advantages of both graphene and CNTs, including the ultra-high density of the active graphene edges and the porous CNT structure. The hybrids possess high graphitic contents and high specific surface area. The characteristics that the hybrids offer match well with the criteria for a good carbon support in electrochemical devices, such as PEMFCs, HER catalysts and supercapacitor electrodes. The GCNT hybrids are, therefore, investigated in the subsequent chapters as the carbon support materials for Pt catalysts in PEMFC cathodes and as the carbon support for amorphous molybdenum sulfide as HER catalyst materials and supercapacitor electrode materials.

Regarding the growth mechanism of GCNT, most of our experimental observations agree well with other studies, such as the presence of graphitic base

layers parallel to substrate surface before the emergence of free-standing graphene. However, in this study, it is also found that the density of free-standing graphene positively correlates with the carbon precursor flow rate and deposition temperature. In light of these observations, instead of the stress-buckling mechanism and the defect-induced nucleation mechanism of free-standing graphene, we propose an alternative mechanism first starting with the nucleation of individual graphitic nuclei parallel to the substrate surface. The preferential growth at the edge of nuclei ultimately leads to the collision of growing edges. The buckled and curved up edges serve as the nucleation sites of free-standing graphene.

Chapter 4 : Graphene-Carbon Nanotube hybrids as catalyst supports in Proton Exchange Membrane Fuel Cells

4.1. Introduction

In Chapter 3, we discussed the fabrication and characterization of the graphene-carbon nanotube hybrids (GCNT) grown directly on carbon paper. We demonstrated that the GCNT hybrids on carbon paper possess a unique all-carbon hierarchical structure where CNTs are grown directly onto carbon fibers and graphene is densely grafted onto the CNTs. The GCNT hybrid hierarchical structure combines the advantages of both graphene and CNTs, including the ultra-high density of the active graphene edges and the porous CNT structure. The hybrids possess high crystallinity and high specific surface area. The characteristics that the hybrids offer match well with the criteria for a good carbon support in PEMFC cathodes. In this chapter, the GCNT hybrids are, therefore, investigated as the carbon support materials for Pt catalysts in PEMFC cathodes.

The magnetron sputtering electrocatalyst preparation method was used to deposit an ultra-low loading of Pt onto the GCNT hybrids to fabricate an integrated, polytetrafluoroethylene (PTFE) binder-free cathode for PEMFCs. Such a hierarchical structure can offer direct electrical conducting pathways from Pt catalysts through

graphene and carbon nanotubes to carbon paper. In this electrode structure, the GCNT hybrids serve as both the catalyst supports and an integrated microporous layer, negating the need for a separate carbon black-PTFE microporous layer. An illustration of the Pt/GCNT cathode fabrication process is provided in Figure 4-1.

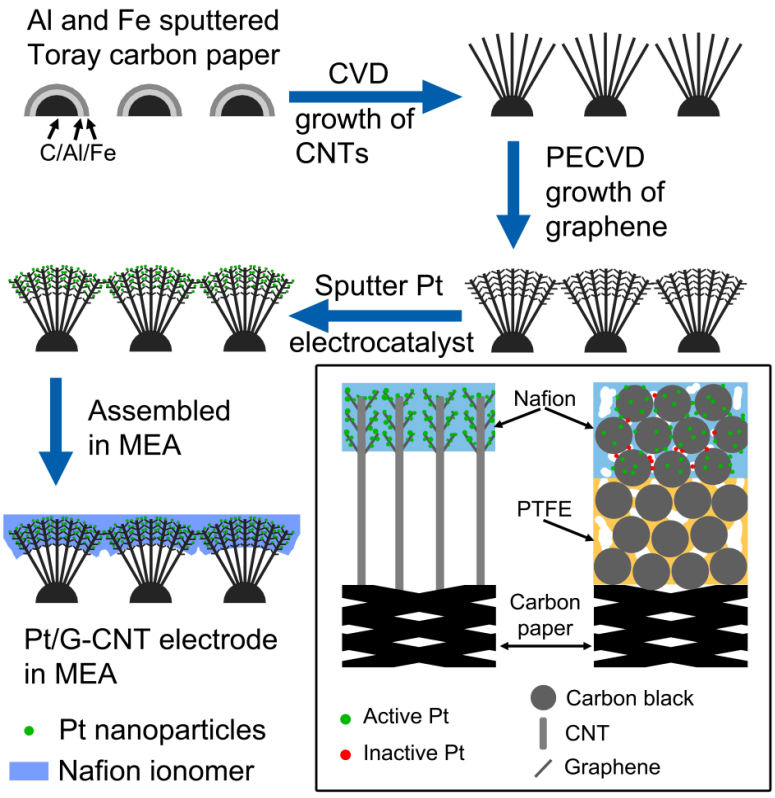


Figure 4-1. Schematic illustration of the Pt/GCNT cathode fabrication process and (inset) the structural comparison of the Pt/GCNT cathode and the conventional carbon black-based cathode.

The Pt/GCNT electrode structure is hypothesized to provide better reactant diffusion (due to the high porosity of aligned CNT structure), enhanced catalytic activity (due to the high density of exposed active graphitic edges of graphene), lower internal resistance (due to the integrated electrode structure), and therefore improve the overall PEMFC's performance. The Pt/GCNT catalyst is further hypothesized to provide superior electrochemical durability over the conventional carbon black supported Pt catalysts, due to the high crystallinity of GCNT hybrids.

4.2. Physical characterization of the Pt/GCNT catalysts

To fabricate a GCNT-based cathode for PEMFCs, Pt catalysts with a nominal thickness of 19 nm (corresponding to a Pt loading of 0.04 mg_{Pt} cm^{-2}) were deposited on the GCNT hybrids grown on carbon paper using the magnetron sputtering electrocatalyst deposition method. The resulting Pt-deposited GCNT hybrids (Pt/GCNT) were characterized for catalyst nanostructures and chemical purity using electron microscopy techniques and XPS, respectively.

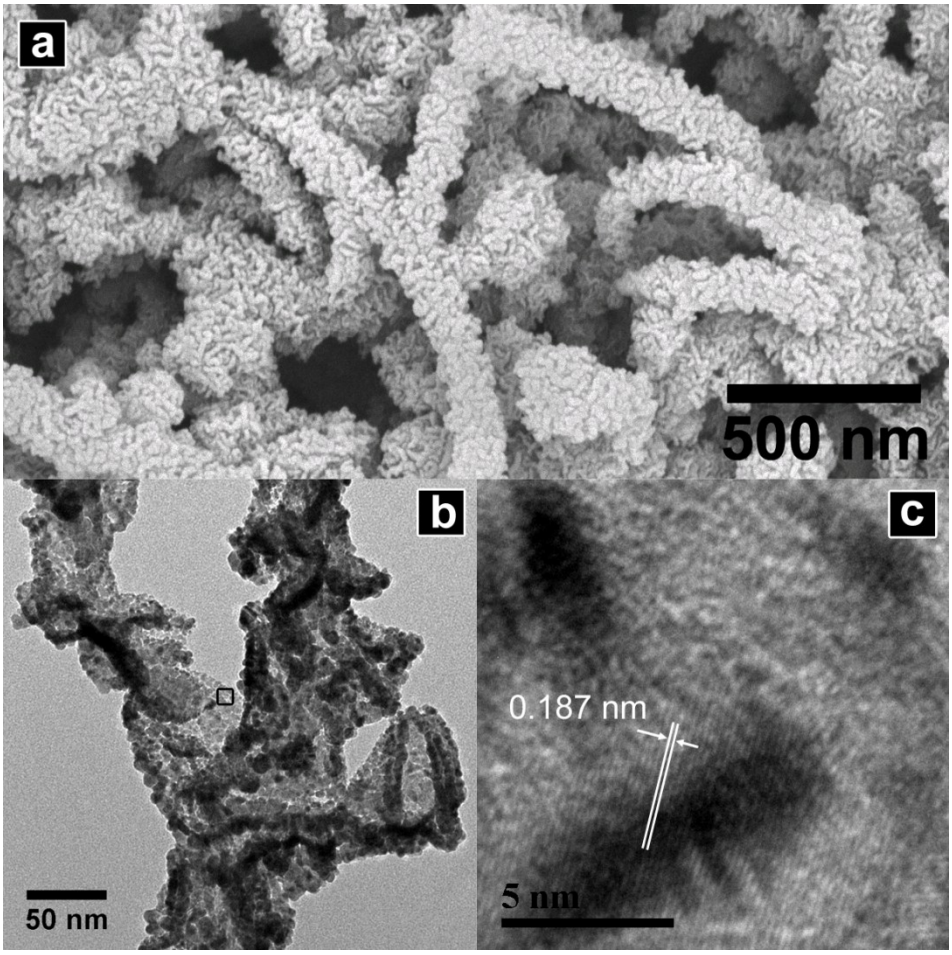


Figure 4-2. Electron microscopic characterization of the Pt/GCNT hybrids. (a) FE-SEM micrograph of the Pt/GCNT hybrids; (b) Bright field TEM micrograph of the Pt/GCNT hybrids and (c) HR-TEM micrograph of the Pt/GCNT hybrids in the region outlined by the black-colored square in figure (b).

Figure 4-2 shows the electron microscopic characterization of the Pt/GCNT hybrids. The SEM micrograph in Figure 4-2a suggests that the resulting material retains the overall structure of GCNT hybrids, with a thickening of the leaf-like features due to the deposition of Pt. Figure 4-2b shows a bright field TEM micrograph revealing the detailed structure of the Pt/GCNT hybrids. On the surface of the GCNT hybrids the Pt nanoparticles attach densely. Whilst attaching throughout the surface of GCNT hybrids, the Pt nanoparticles distribute more densely along the edges of graphene sheets, as evident from the variation in the contrast of TEM micrograph. Figure 4-2c shows a high resolution TEM micrograph of the Pt-nanoparticle-containing region outlined by the black-colored square in Figure 4-2b. The HR-TEM micrograph suggests a crystalline nature of the nanoparticles.

The purity and chemical state of the Pt/GCNT catalysts were characterized with XPS. Figure 4-3 shows the XPS spectra of the Pt/GCNT catalysts. Figure 4-3a shows the survey scan XPS wide spectrum of the material. The spectrum is dominated by a set of characteristic peaks of Pt, most dominantly Pt 4f peaks. The two additional elements identified are oxygen and carbon, as evident by O 1s peak in the 525–535 eV binding energy region and C 1s peaks in the 280–290 eV binding energy region. The presence of both elements are expectable, due to the air exposure and the signal contribution from the carbon-based GCNT support. The Pt 4f high resolution scan is presented in Figure 4-3b. After subtracting a Shirley background, the Pt 4f XPS spectrum is fitted using three Gaussian-Lorentzian "f" doublets with a spin-orbit splitting of 3.3 eV. The three doublets are identified by the position of the Pt $4f_{7/2}$ peak at binding energies of 71.1 eV, 72.4 eV and 74.0 eV, attributed to the

elemental state Pt^0, oxidized states Pt^{2+} and Pt^{4+}, respectively. [124] The binding energies are referenced to the C 1s binding energy of 284.44 eV. The respective concentrations of the three chemical states are 72.5%, 22.4% and 5.1%. The surface oxidation of Pt upon exposure to air is expectable, as oxygen is readily chemisorbed onto the surface of Pt nanoparticles, especially at the kink and step sites of the nanocrystals. [124] The elemental state Pt^0 $4f_{7/2}$ binding energy is found to be in good agreement with the reported literature, with no significant energy shifts identified. Tang *et al.* reported a Pt^0 $4f_{7/2}$ binding energy of 71.1 eV as referenced to the C 1s binding energy of 284.4 eV, for the magnetron sputtered Pt-on-CNT catalyst. [27] Lewera *et al.* reported a Pt^0 $4f_{7/2}$ binding energy of 71.19 eV as referenced to the C 1s binding energy of 284.44 eV, for a commercial Pt/carbon black catalyst. [125] The elemental state Pt^0 $4f_{7/2}$ binding energy of bulk Pt is 71.2 eV. [126]

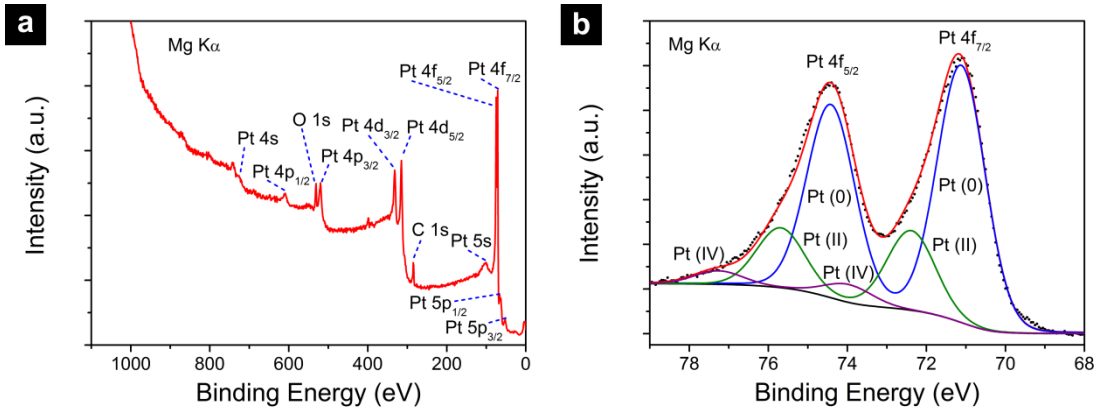


Figure 4-3. XPS characterization of the Pt/GCNT hybrids. (a) XPS survey spectrum and (b) Pt 4f high resolution scan of the Pt/GCNT hybrids.

For comparison purposes, a Pt-deposited carbon nanotube cathode (Pt/CNT) was also prepared using the magnetron sputtering electrocatalyst deposition method, with a same Pt loading of 0.04 mg_{Pt} cm^{-2}. The electron microscopic characterization of Pt/CNT catalysts is shown in Figure 4-4.

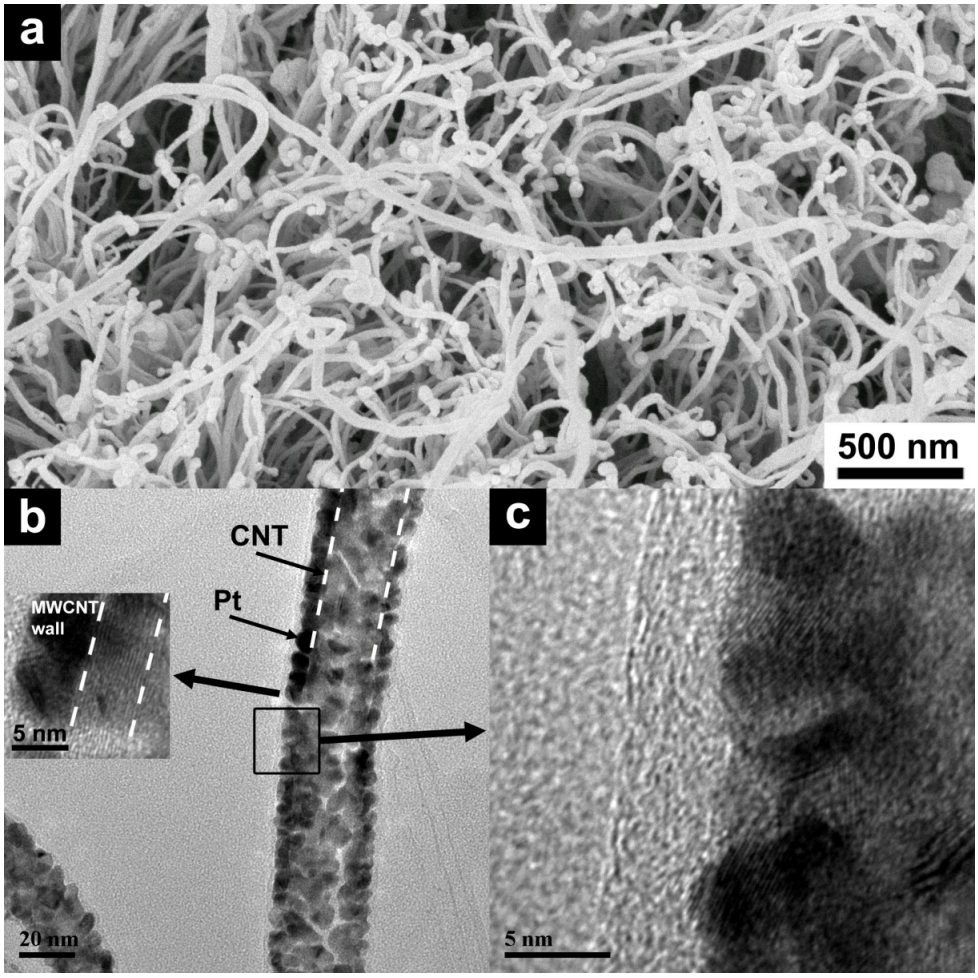


Figure 4-4. Electron microscopic characterization of the Pt/CNT electrode. (a) FE-SEM micrograph of the Pt/CNT electrode; (b) Bright field TEM micrograph of the Pt/CNT electrode with (inset) HR-TEM micrograph of the CNT multi-wall, and (c) HR-TEM micrograph of the Pt/CNT electrode in the region outlined by the black-colored square in figure (b).

Figure 4-4a shows an SEM micrograph of the Pt/CNT catalysts. After being deposited with Pt, the Pt/CNT catalysts retain the smooth fibrous morphology of CNTs, without any distinctive additional features. The result suggests that Pt catalysts were deposited uniformly on the CNT surface. The Pt/CNT catalysts retain the overall porous nanostructure of CNT scaffolds. Figure 4-4b presents a bright field TEM micrograph showing the nanostructure of Pt/CNT catalysts. As shown, Pt nanoparticles are deposited densely and uniformly on the surface of CNTs, consistent with the overall smooth surface of Pt/CNT catalysts in the SEM

micrograph. The inset shows a high resolution TEM micrograph of the Pt-CNT interface. The crystalline multi-walled structure of CNT core is clearly demonstrated. Figure 4-4c shows an HR-TEM micrograph of the Pt-containing region outlined by the black-colored square in Figure 4-4b. The crystalline nature of Pt catalyst nanoparticles is evident from the HR-TEM micrograph.

From the SEM and TEM micrographs, the Pt/GCNT and Pt/CNT catalysts show a distinctive difference. In the case of Pt/CNT, Pt nanoparticles are deposited on the graphitic basal plane of CNT. In the case of Pt/GCNT, Pt nanoparticles are deposited on both basal and edge planes of graphene, with higher density near the graphitic edges. The deposition of Pt catalyst on the graphitic edge of GCNT may enhance the catalytic activity of Pt. It has been suggested that the heterogeneity of carbon support with edge planes can enhance catalytic activity of Pt catalysts. [34]

4.3. Electrochemical evaluations for the catalytic activity and electrochemical stability of the Pt/GCNT catalysts

In Chapter 1, we recognized that the two main commercialization barriers for PEMFCs are the high cost and insufficient durability. [5] Enhancements of both catalytic activity and electrochemical stability of Pt catalysts are critical for PEMFC's competitiveness. The performance of PEMFCs often degrades slowly during their lifetime. The performance degradation is believed to be caused by at least several phenomena, [21,22] including Pt catalyst aggregation/coalescence, [21,23] Pt dissolution (and re-deposition as isolated Pt nanoparticles inside the membrane), [21,24-26] and Pt detachment due to the corrosion of carbonaceous supports. [27,28]

In this section, the Pt/GCNT catalysts are evaluated for both catalytic activity and electrochemical stability. The Pt/GCNT catalysts are hypothesized to provide both enhanced catalytic activity (due to the high density of exposed active graphitic edges) and superior electrochemical stability (due to the high crystallinity of the GCNT hybrids). It was suggested that the heterogeneity of carbon support with graphitic edges can enhance the catalytic activity of Pt catalysts, [34] whilst it is widely accepted that the carbon corrosion process is slowed down with a higher crystallinity of the carbon supports.

In this study, the catalytic activity and electrochemical durability of the Pt/GCNT cathode are compared to a commercial carbon black-supported Pt cathode (Pt/VXC72) and a Pt/CNT cathode. All three cathodes were prepared with the same Pt loading of 0.04 mg_{Pt} cm^{-2}. The catalytic activity is characterized by polarization curve and electrochemical impedance spectroscopy techniques. The electrochemical durability is characterized through an accelerated degradation test. Due to the experimentally intertwining nature of the catalytic activity study and electrochemical stability study, this work is presented using the electrochemical stability study as the framework, whilst the catalytic activity characterization and analyses are discussed as part of the process. The electrochemical stability study is, in fact, a study of the degradation of catalytic activity and other governing parameters throughout the accelerated degradation test. The electrochemical stability study was performed by measuring polarization curve, EIS, and cyclic voltammetry both before and after an accelerated degradation test. The detailed procedure is described in section 2.3.1. The degradation of materials is investigated from several perspectives, including: (1) total

device polarization performance losses, with deconvolution of the electrochemical processes using electrochemical impedance spectroscopy; (2) evidences of Pt catalyst electrochemical surface area loss and carbon corrosion from cyclic voltammetry measurements; and (3) electrode structural study using the transmission electron microscopy technique.

4.3.1. The degradation of device performance from a polarization perspective

The performance of the Pt/GCNT cathode was first assessed for the total device polarization. The Pt/GCNT, Pt/VXC72 and Pt/CNT cathodes were tested for polarization performance. The three cathodes have the same Pt loading of 0.04 mg_{Pt} cm^{-2}. Figure 4-5a shows the polarization curves for the fresh Pt/GCNT, Pt/VXC72 and Pt/CNT cathodes. The Pt/GCNT cathode demonstrates a remarkably improved polarization performance over both commercial Pt/VXC72 and Pt/CNT cathodes throughout the current density range. The maximum power densities per cathode Pt loading of Pt/GCNT, Pt/VXC72 and Pt/CNT cathodes are 12.9, 10.6 and 3.79 W mg^{-1}_{Pt}, respectively. The maximum power density of the Pt/GCNT cathode is 21% and 240% higher than those of the Pt/VXC72 and Pt/CNT cathodes, respectively. Another benchmark for the comparison of polarization curves is the power density obtained at 0.6 V. [127] Similarly, the Pt-mass specific power densities at 0.6 V of the Pt/GCNT, Pt/VXC72 and Pt/CNT cathodes are 9.58, 8.05 and 2.94 W mg^{-1}_{Pt}, respectively. The power density at 0.6 V of the Pt/GCNT cathode is 19% and 226% higher than those of the Pt/VXC72 and Pt/CNT cathodes. By both measures, the Pt/GCNT cathode shows approximately a 20% improvement in power densities over the Pt/VXC72 cathode and a great improvement over the Pt/CNT cathode.

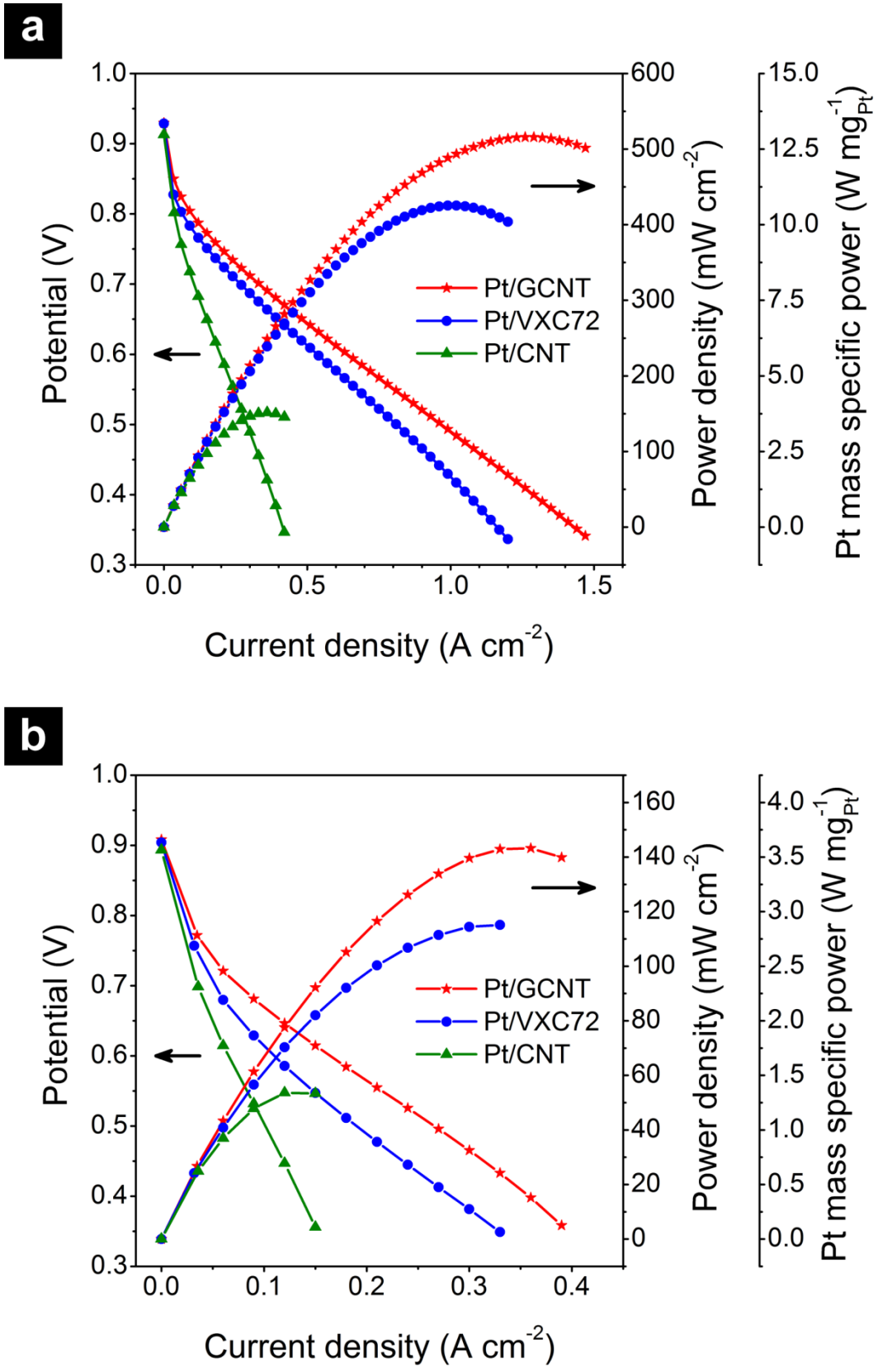


Figure 4-5. Polarization curves of the Pt/GCNT, Pt/VXC72 and Pt/CNT cathodes (a) before and (b) after the accelerated degradation test.

In order to examine the electrochemical stability of the Pt/GCNT cathode in comparison with the Pt/VXC72 and Pt/CNT cathodes, all cathodes underwent the accelerated degradation test (ADT), as elaborated in section 2.3.1. The dynamic oxidative potential cycling in ADT was used to mimic the real working conditions of PEMFCs. [27] The lower potential of 0.6 V *vs.* RHE simulates the normal working state of PEMFCs. The upper potential of 1.4 V *vs.* RHE simulates the fuel cell start-up/shut-down events. High cathode potentials during such events accelerate the Pt loss and carbon corrosion in the cathode and result in severe degradation of PEMFC performance. [128] After the ADT, the polarization performance were compared again, as shown in Figure 4-5b. The Pt/GCNT cathode once again demonstrates a superior power output to the Pt/VXC72 and Pt/CNT cathodes in the entire range of the polarization curve. The maximum power density and the power density at 0.6 V of the Pt/GCNT cathode are 24% and 49% higher than those of the Pt/VXC72 cathode, up from the 21% and 19% enhancements demonstrated in the fresh electrodes. The results suggest a much better electrochemical stability in the Pt/GCNT cathode compared to the Pt/VXC72 cathode from the polarization curve perspective.

4.3.2. Deconvolution of polarization losses using Electrochemical Impedance Spectroscopy

Whilst the Pt/GCNT cathode shows remarkable enhancements in polarization performance and durability from the polarization perspective compared to the Pt/VXC72 cathode, the polarization performance of an electrode depends on several processes, including electrode reaction kinetics, ohmic loss and mass transfer. In order to compare the electrode reaction kinetics and its changes after the

degradation test, a deconvolution of the polarization losses using electrochemical impedance spectroscopy is required.

For a deconvolution of polarization losses present in studied cathodes, electrochemical impedance spectroscopy measurements were performed at a series of cell potentials of 0.7 V, 0.6 V and 0.5 V for the Pt/GCNT, Pt/VXC72 and Pt/CNT cathodes, both before and after the degradation test. Figure 4-6 shows the EIS plots of the studied electrodes at various cell potentials, as well as the equivalent circuit fittings of the data. Figure 4-6a-b show the Nyquist plot and Bode plots of the EIS measurement for the Pt/GCNT electrode before ADT, performed at a cell potential of 0.6 V which is considered a regular working potential of PEMFCs. The EIS plots in Figure 4-6a-b are representative for other electrodes and at other cell potentials. The equivalent circuit fitting is performed using the circuit presented in Figure 4-6c.

In Figure 4-6a, the Nyquist plot shows following features. Firstly, it is noted that at high frequency range, the plot shows an inductive response. This is commonly seen in electrochemical systems with very low impedances such as fuel cells. The high frequency inductive response is explained by the parasitic inductance present in the instrument and cables (represented by a L_{cab} element in Figure 4-6c). The presence of this high frequency inductance necessitates a proper equivalent circuit fitting to determine the ohmic resistance present in the system. With the presence of the high frequency inductance element, the first intersection point at high frequency between the Nyquist plot and the real impedance axis Z' may slightly deviate from the ohmic resistance value. [129] The ohmic resistance present in the

system, including membrane, electrodes and contact resistances, is represented by a R_{ohm} element in Figure 4-6c.

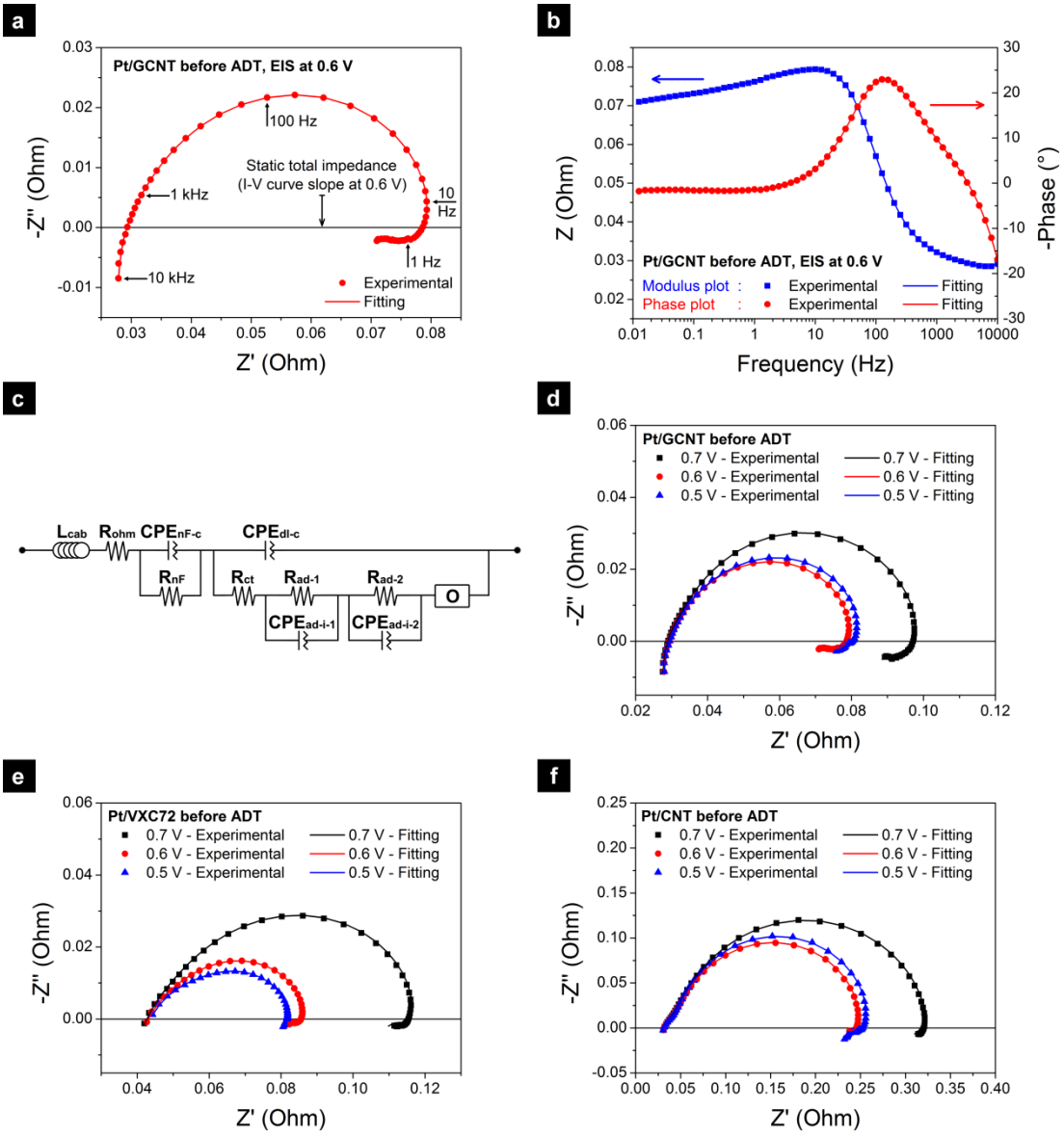


Figure 4-6. Electrochemical impedance spectroscopy and equivalent circuit fitting of the Pt/GCNT, Pt/VXC72 and Pt/CNT cathodes. The EIS spectrum presented in (a) Nyquist plot and (b) Bode plots of the Pt/GCNT cathode obtained at 0.6 V before the degradation test. (c) equivalent circuit model used for the EIS data fitting. EIS spectra of (d) Pt/GCNT, (e) Pt/VXC72 and (f) Pt/CNT measured at 0.7 V, 0.6 V and 0.5 V, before the degradation test.

Secondly, the main capacitive arc of the EIS plot is considered a compound arc formed from at least two constituent arcs. As it will become clear later, the first constituent arc present at high frequency range is independent of the cell potentials, and is therefore attributed to non-Faradaic origins, such as distributed ionic resistance/double layer charging within the porous catalyst layer or electrical contact resistance/contact capacitance. [130] This arc is represented by a non-Faradaic resistance R_{nF} in parallel with a capacitive constant phase element $CPE_{nF\text{-}c}$. The second constituent arc present at medium and low frequency range is potential-dependent, and is therefore attributed to electrochemical reaction kinetics and mass transfer process. The impedance is represented by a charge transfer resistance (R_{ct}, representing the electrochemical reaction kinetics), a bounded Warburg impedance (O, representing the finite mass transfer process), and a capacitive constant phase element ($CPE_{dl\text{-}c}$, representing the double layer capacitance of electrode). Thirdly, it is noted that the Nyquist plot exhibits two inductive loops present at low frequency range. This low frequency inductive response was also reported in some other studies. [130-134] In contrast to the high frequency inductance, the low frequency inductance is considered part of the real electrochemical processes happening in the system. [131] The low frequency inductance is suggested to originate from Pt oxidation [131] or additional relaxation processes involving the adsorption of reaction intermediates in the oxygen reduction reaction. [130,131] The inductive response is observed in our experiments at various cell potentials, including a lower cell potential of 0.5 V. The Pt oxidation is not likely at this low cell potential. The adsorption of reaction intermediates are, therefore, more likely to be the cause of this inductive response. The two inductive loops are represented by two resistance

elements $R_{ad\text{-}1}$ and $R_{ad\text{-}2}$ as well as two corresponding inductive constant phase elements $CPE_{ad\text{-}i\text{-}1}$ and $CPE_{ad\text{-}i\text{-}2}$. These two inductive loops may be attributed to two relaxation processes of adsorbed reaction intermediates during the oxygen reduction reaction on Pt nanoparticles. [130] We note that, with the presence of the inductive loops at low frequency, the intersection of the Nyquist plot with the real impedance axis Z′ at low frequency can significantly deviate from the steady state total impedance of the electrochemical system. A similar observation was also reported by Roy *et al*. [131] As a simplified model of PEMFCs, a simple Randle circuit is commonly used to fit the EIS data. However, we strongly suggest that the low frequency inductive response, if present, cannot be ignored. In such case, a simple Randle circuit fitting is unrealistic and can result in significant errors in the determination of electrode parameters. A more appropriate model such as in Figure 4-6c is required. Mathematical expressions of the circuit elements used in our circuit fitting are presented in Table 4-1. Figure 4-6d-f show the Nyquist plots and the equivalent circuit fitting curves of the Pt/GCNT, Pt/VXC72 and Pt/CNT electrodes before ADT at various cell potentials. All equivalent circuit fittings use the circuit presented in Figure 4-6c.

Table 4-1. Mathematical expressions of the circuit elements used in the EIS fittings.

Element	Impedance expression	Impedance at limit frequency
L_{cab}	$Z_L = j\omega L$	$Z = 0$ at $\omega = 0$ $Z \to \infty$ at $\omega \to \infty$
R_{ohm}, R_{nF}, R_{ct}, $R_{ad\text{-}1}$ and $R_{ad\text{-}2}$	$Z_R = R$	$Z = R$
$CPE_{nF\text{-}c}$ and $CPE_{dl\text{-}c}$	$Z_{CPE} = \frac{1}{Y_0(j\omega)^n}$ with $0 < n \leq 1$ (capacitive)	$Z = 0$ at $\omega \to \infty$ $Z \to \infty$ at $\omega = 0$
$CPE_{ad\text{-}i\text{-}1}$ and $CPE_{ad\text{-}i\text{-}2}$	$Z_{CPE} = \frac{1}{Y_0(j\omega)^n}$ with $0 > n \geq -1$ (inductive)	$Z = 0$ at $\omega = 0$ $Z \to \infty$ at $\omega \to \infty$
O	$Z_O = \frac{1}{Y_0\sqrt{j\omega}}\tanh(B\sqrt{j\omega})$	$Z = B/Y_0$ at $\omega = 0$ $Z = 0$ at $\omega \to \infty$

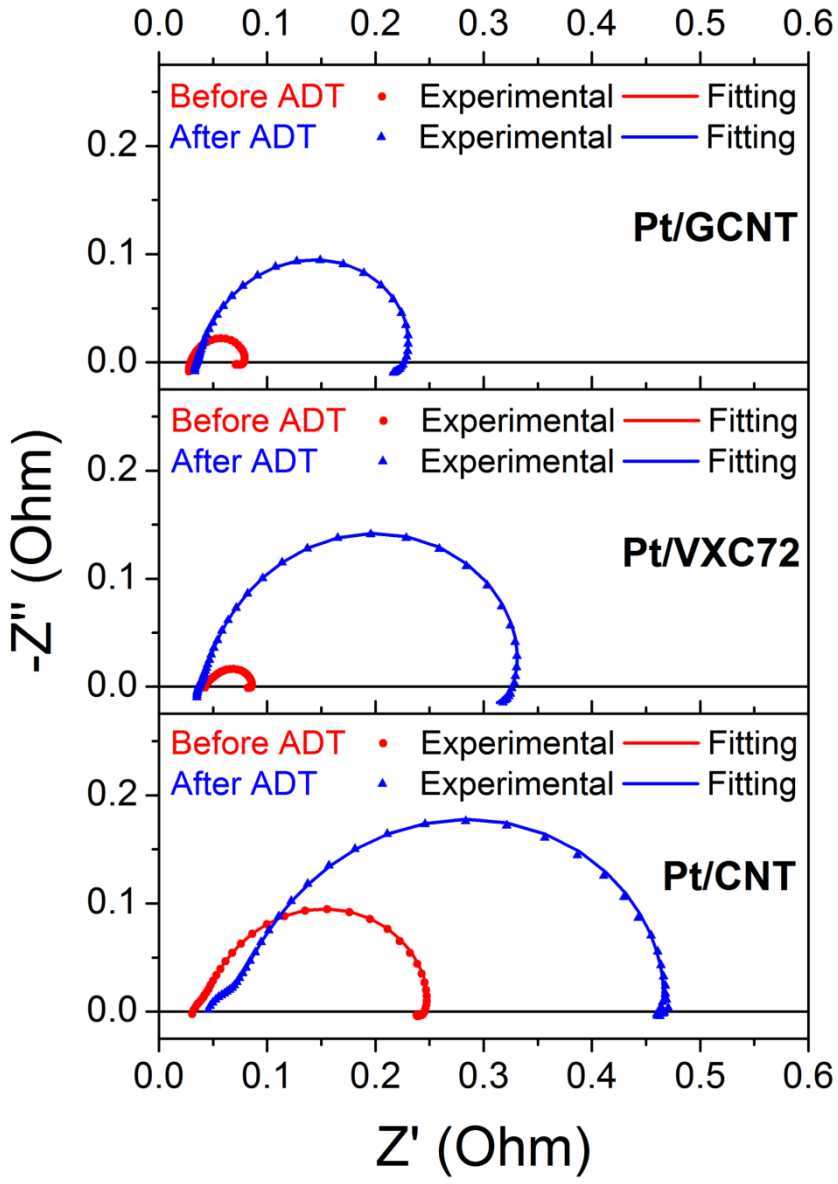


Figure 4-7. EIS spectra of the Pt/GCNT, Pt/VXC72 and Pt/CNT cathodes measured at 0.6 V, before and after the accelerated degradation test.

To compare the durability of electrodes, EIS measurements of the Pt/GCNT, Pt/VXC72 and Pt/CNT electrodes are contrasted between their respective before-ADT and after-ADT states. Figure 4-7 shows the EIS measurements at 0.6 V of the studied electrodes both before ADT and after ADT. Qualitatively, the Pt/GCNT electrode

clearly shows a smaller relative broadening of the EIS curve than that of the Pt/VXC72 electrode, which suggests a better stability demonstrated by the Pt/GCNT electrode. Whilst the Pt/CNT electrode shows the smallest relative broadening of the EIS curve, its EIS curves are always broader than those of the Pt/GCNT and Pt/VXC72 electrodes, which suggests a low catalytic activity of the Pt/CNT electrode compared to the Pt/GCNT and Pt/VXC72 electrodes. For a quantitative comparison of the electrode activity and durability, fitting parameters of the key circuit elements are summarized in Table 4-2.

Table 4-2. Equivalent circuit element fitting parameters.

			R_{ohm}	R_{nF}	R_{ct}	$R_{ad\text{-}1}$	$R_{ad\text{-}2}$	$Z_{O,\omega=0}$ (B/Y_0)
			mΩ	**mΩ**	**mΩ**	**mΩ**	**mΩ**	**mΩ**
Pt/GCNT	**Before ADT**	**0.7 V**	26.0	11.2	**29.7**	13.9	17.7	3.52
		0.6 V	26.0	11.2	**16.4**	14.6	8.85	8.27
		0.5 V	26.0	11.2	**8.68**	5.58	17.8	15.4
	After ADT	**0.7 V**	26.0	11.2	**200**	212	125	29.1
		0.6 V	26.0	11.2	**109**	79.0	18.9	53.6
		0.5 V	26.0	11.2	**54.9**	94.0	33.3	109
Pt/VXC72	**Before ADT**	**0.7 V**	34.5	10.4	**32.0**	146	29.5	5.14
		0.6 V	34.5	10.4	**17.5**	22.4	10.5	9.52
		0.5 V	34.5	10.4	**10.9**	13.1	7.60	17.9
	After ADT	**0.7 V**	34.5	10.3	**365**	347	458	30.0
		0.6 V	34.5	10.3	**190**	132	28.2	48.0
		0.5 V	34.5	10.3	**92.0**	81.2	37.1	92.2
Pt/CNT	**Before ADT**	**0.7 V**	26.0	17.3	**173**	43.8	68.0	21.1
		0.6 V	26.0	17.3	**110**	128	26.0	57.0
		0.5 V	26.0	17.3	**54.6**	31.2	27.2	120
	After ADT	**0.7 V**	37.0	31.4	**645**	47.9	15.4	31.2
		0.6 V	37.0	31.4	**301**	271	15.1	77.8
		0.5 V	37.0	31.4	**185**	1210	28.7	147

From Table 4-2, it is clear that the enhanced overall polarization performance of the Pt/GCNT cathode compared to the Pt/VXC72 cathode, as

discussed in section 4.3.1, arises from lower impedances in all three major polarization loss processes, namely ohmic loss (R_{ohm} + R_{nF}), charge transfer resistance R_{ct} and mass transfer related impedance Z_O. From the electrode reaction kinetics perspective, the charge transfer resistance present in the Pt/GCNT cathode is smaller than that in the Pt/VXC72 cathode and much smaller than that in the Pt/CNT cathode. In other word, the Pt/GCNT cathode is more catalytically active than the Pt/VXC72 and much more active than the Pt/CNT cathode. In term of electrode durability, an increase in charge transfer resistance of each electrode reflects a decrease in the electrode catalytic activity. The Pt/GCNT cathode shows much smaller relative increases in the charge transfer resistance, and therefore better stability, than the Pt/VXC72 cathode. For example, at 0.6 V, the Pt/GCNT electrode shows a 6.6-fold increase (from 16.4 mΩ to 109 mΩ), whilst the Pt/VXC72 electrode shows a 10.9-fold increase (from 17.5 mΩ to 190 mΩ) in charge transfer resistance. The Pt/GCNT electrode is both more catalytically active and more electrochemically durable than the Pt/VXC72 electrode.

4.3.3. Pt electrochemical surface area loss and carbon corrosion caused by the accelerated degradation test (ADT)

In the above discussions, the Pt/GCNT cathode shows better electrochemical durability than the Pt/VXC72 cathode. However, the reasons behind the durability enhancement are unclear from the polarization and EIS results. In this section, cyclic voltammetry is used to measure the change in the Pt electrochemical surface area of the cathodes during the accelerated degradation test. Figure 4-8a-c show the cyclic voltammograms of the Pt/GCNT, Pt/VXC72 and Pt/CNT cathodes before ADT and

after 10, 20, 50 and 100 cycles of oxidative potential cycling during ADT. The cyclic voltammograms show typical pairs of oxidation-reduction peaks for Pt catalysts, including the hydrogen adsorption-desorption peaks between 0.075 V and 0.35 V *vs.* RHE and the Pt oxidation-reduction peaks at ≈0.8 V *vs.* RHE. The active Pt electrochemical surface area present in each electrode is estimated by integrating the adsorption peaks between 0.075 V and 0.35 V *vs.* RHE in the cathodic scan direction with corrections from the double layer charging background current, as exemplified by the shaded area in Figure 4-8a. The adsorption of protons on Pt catalyst surface in the cathodic scan direction proceeds according to:

$$Pt + H^+ + e^- \rightarrow Pt\text{-}H_{ads} \quad (4\text{-}1)$$

By integrating the cyclic voltammograms in the shaded area, the total charge transfer Q_{ads} involving the adsorption of protons is estimated. The active Pt electrochemical surface area is estimated by assuming the charge required to reduce a monolayer of protons on Pt equals 210 μC cm^{-2}_{Pt}. [135] The gravimetric specific Pt electrochemical surface areas of the Pt/GCNT, Pt/VXC72 and Pt/CNT electrodes throughout the degradation test expressed in absolute surface area and in relative surface area (with respect to the fresh respective electrodes) are shown in Figure 4-8d and e, respectively. From Figure 4-8d, it is clear that all fresh cathodes have similar Pt electrochemical surface areas of between ~40 $m^2\ g^{-1}_{Pt}$ (Pt/GCNT and Pt/CNT) and ~45 $m^2\ g^{-1}_{Pt}$ (Pt/VXC72). Whilst the Pt/GCNT cathode has slightly lower Pt electrochemical surface area than the Pt/VXC72 cathode, the Pt/GCNT electrode, as discussed earlier however, has higher catalytic activity than the Pt/VXC72 electrode. This suggests that Pt catalysts deposited on GCNT are intrinsically more active than Pt catalysts deposited on carbon black VXC72. Similarly, whilst the Pt/GCNT and

Pt/CNT electrodes have nearly identical Pt electrochemical surface areas, the Pt/GCNT cathode is much more active than the Pt/CNT cathode. The Pt catalysts deposited on GCNT are therefore intrinsically much more active than the Pt catalysts deposited on CNT support. This could be supported by the explanation that the high density of graphitic edges present in the GCNT support effectively promotes the reaction kinetics on Pt catalysts, as also suggested by other researchers. [34] The graphitic edges of graphene provide high charge density and reactivity as opposed to the side walls of CNTs. [51] With high density of states present at the graphitic edges, a similar material with high graphitic edge density referred to as graphenated CNTs, as reported by Henry *et al.*, showed strongly enhanced electron transfer kinetics compared to regular CNTs. A two orders of magnitude enhancement in the heterogeneous electron-transfer rate constant was reported in their work. [136] The high charge density and fast electron transfer kinetics provided by graphitic edges may facilitate the charge transfer processes on the GCNT-supported Pt catalyst. Similarly, VXC72 carbon black support has low crystallinity and more homogeneous surface sites compared to GCNT. It is therefore less effective in enhancing the activity of Pt catalyst compared to GCNT.

In term of catalyst stability, both Pt/GCNT and Pt/CNT cathodes show minimal changes in the Pt electrochemical surface area throughout the degradation test. In contrast, the Pt/VXC72 cathode shows continuous and significant decreases in the Pt electrochemical surface area throughout the degradation test. After 100 cycles of oxidative cycling, the Pt/VXC72 electrode retains a Pt surface area of only 17.6 $m^2 g^{-1}_{Pt}$ (a half of the retained Pt surface area on the Pt/GCNT and Pt/CNT electrodes), as

shown in Figure 4-8d. The Pt surface area retention of the Pt/VXC72 electrode is only 39% as opposed to ≈90% in the Pt/GCNT and Pt/CNT electrodes, as shown in Figure 4-8e. The result suggests the superior stability of the Pt catalysts deposited on crystalline graphitic nanomaterials.

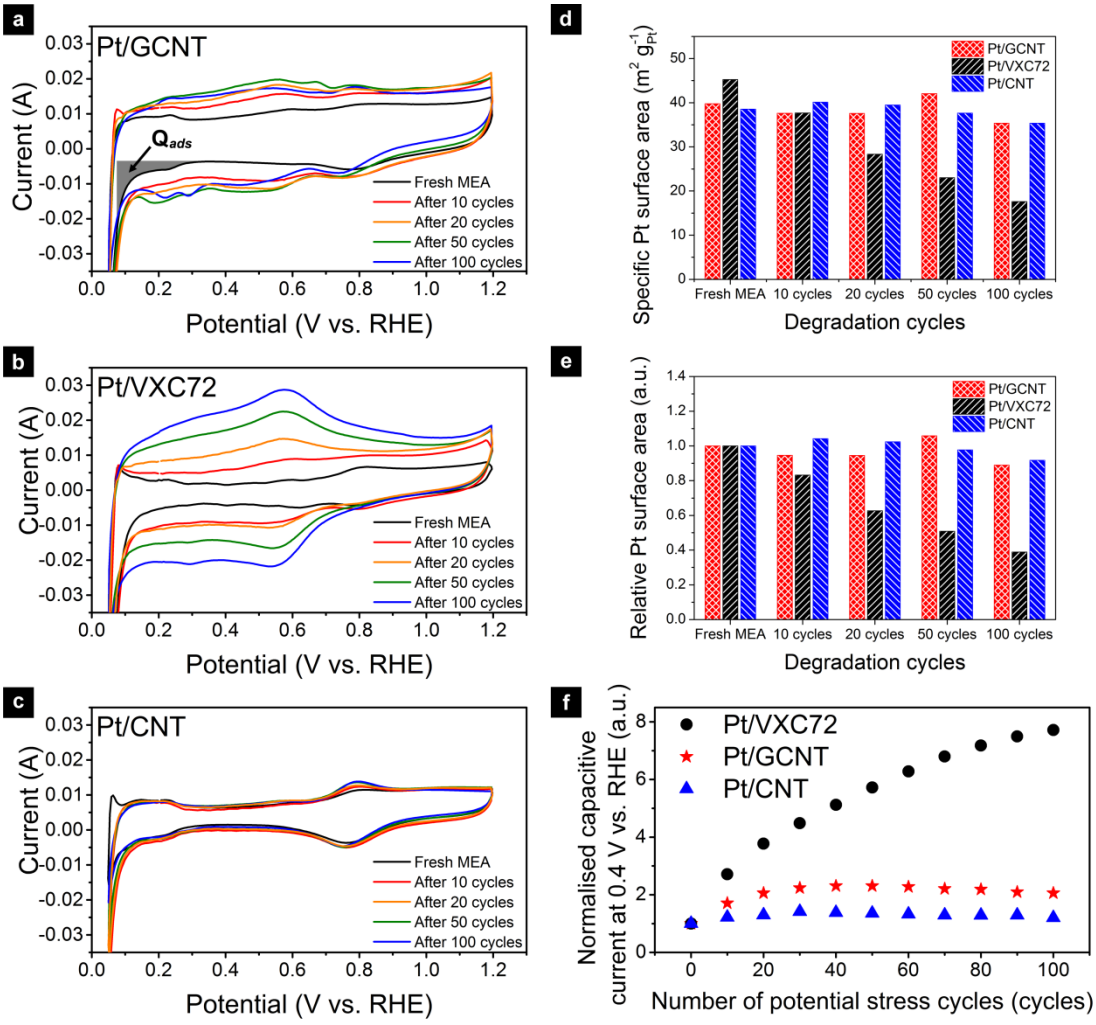


Figure 4-8. Cyclic voltammetry study of the Pt/GCNT, Pt/VXC72 and Pt/CNT cathodes during the accelerated degradation test. Cyclic voltammograms of the (a) Pt/GCNT, (b) Pt/VXC72 and (c) Pt/CNT cathodes measured before ADT and after 10, 20, 50, 100 cycles of oxidative potential cycling. The degradation of Pt electrochemical surface area of the Pt/GCNT, Pt/VXC72 and Pt/CNT cathodes during ADT, plotted in (d) absolute specific surface area and (e) relative surface area with respect to the fresh electrodes. (f) carbon corrosion of the Pt/GCNT, Pt/VXC72 and Pt/CNT cathodes during ADT, expressed in term of relative changes in double layer capacitance.

We note that, whilst the Pt surface area remains stable in the Pt/GCNT and Pt/CNT electrodes, the electrode catalytic activities do decrease after the degradation test, although at much less degradations compared to the Pt/VXC72 electrode. The activity decrease is probably caused by a restructuring of the Pt nanoparticle surfaces to less active crystal surfaces, as suggested by a shift in the hydrogen adsorption-desorption peaks to slightly higher potentials of between ≈ 0.2–0.3 V *vs.* RHE, as seen in Figure 4-8a-c. It was demonstrated that the catalytic activity of Pt crystal surfaces decreases in the order Pt (110) > Pt (111) > Pt (100). The corresponding hydrogen adsorption peak potentials of these crystal surfaces shift to higher potentials in the order Pt (110) < Pt (111) < Pt (100). [137]

With the harsh working environment in PEMFCs, such as elevated temperature, high humidity, low pH and high potentials, the carbon support corrosion can be a major cause of the device degradation. The carbon corrosion is evident from the broadening of the CV curves in the double layer charging potentials of 0.4 V – 0.6 V *vs.* RHE. At a high potential of 1.4 V used in the degradation test, the carbon oxidation takes place. This results in an increase of the double layer capacitance of the electrode due to the formation of functional groups on the carbon surface and the roughening of the carbon surface. [138,139] The carbon corrosion is therefore evident from the relative changes in the double layer capacitance of the electrode. The cyclic voltammogram of the Pt/GCNT cathode in Figure 4-8a shows relatively moderate increases of the double layer capacitance. In contrast, the cyclic voltammogram of the Pt/VXC72 cathode in Figure 4-8b shows dramatic increases in the double layer capacitance. This dramatic increase in the double layer capacitance

suggests a severe carbon corrosion in the Pt/VXC72 cathode, which may result in the Pt catalyst detachment. [27,28]

To quantitatively compare the increase in the double layer capacitance, and therefore the carbon corrosion, the capacitive current of the cathodes (a half of anodic-cathodic current difference) at the potential of 0.4 V *vs.* RHE is extracted from the cyclic voltammograms for the fresh cathodes and after every 10 cycles of potential cycling up to 100 cycles. The capacitive current readings are normalized to the respective fresh cathodes and plotted in Figure 4-8f. The normalized capacitive currents evolve during ADT differently for the three cathodes. The capacitive current of the Pt/GCNT cathode increases slightly in the first 20 cycles of potential cycling then stabilizes afterwards to 2.1 times the capacitive current of the fresh cathode. This is probably due to the corrosion of any amorphous carbon content present within the first 20 cycles, and the remaining graphitic content is stable afterwards. In contrast, the capacitive current of the Pt/VXC72 cathode continuously increases throughout the 100 cycles of potential cycling and reaches 7.7-fold increase after 100 cycles. The capacitive current of the Pt/VXC72 cathode does not show stabilizing trend within 100 cycles of potential cycling. The results confirm that, compared to the Pt/GCNT catalyst, the Pt/VXC72 catalyst is much more prone to carbon corrosion. This may explain the severe degradation of Pt catalyst activity and the significant loss of Pt electrochemical surface area in the Pt/VXC72 cathode, as discussed earlier. Lastly, the Pt/CNT cathode experiences the least from the carbon corrosion, with the double layer capacitance stabilizes at 1.2 times that of the fresh cathode. Both the GCNT and CNT supports, being highly crystalline graphitic nanomaterials, exhibit

superior electrochemical stability to the carbon black support with lower crystallinity.

4.3.4. Electrode structural study with transmission electron microscopy (TEM)

To elucidate the present Pt electrochemical surface area loss mechanisms, such as Pt aggregation and/or Pt re-deposition inside Nafion membrane, the electrode structural study was performed with transmission electron microscopy. Cross-sectional TEM lamellae of the assembled MEAs with Pt/GCNT and Pt/VXC72 cathodes, both before and after the degradation test, were prepared for TEM examinations. A FIB-SEM sample preparation technique (FEI Helios NanoLab 600) was used to prepare the TEM lamellae specifically selected from the interface region between the studied cathodes and the Nafion membrane. The FIB sample preparation technique is much less destructive to the MEA structure than other TEM sample preparation techniques such as ultramicrotomy technique where damages to the sample structure and Pt nanoparticles smearing/cross-contamination are hard to avoid. TEM lamellae prepared by FIB method, therefore, reflect more faithfully the microstructure of MEAs and their changes caused by ADT.

As discussed in the cyclic voltammetry study, the Pt/VXC72 cathode shows a severe degradation after the degradation test, with a ≈ 60% decrease in the active Pt electrochemical surface area, whilst the Pt/GCNT shows a minimal loss in the Pt surface area. The Pt surface area loss may happen via several processes such as Pt aggregation/coalescence and Pt re-deposition in the Nafion membrane. To investigate these processes, TEM micrographs of the cathode-membrane interfaces

are taken for the fresh MEAs and degraded MEAs. Figure 4-9 shows the TEM micrographs of the Pt/VXC72 and Pt/GCNT cathodes, before and after the degradation test, at the cathode-Nafion membrane interface.

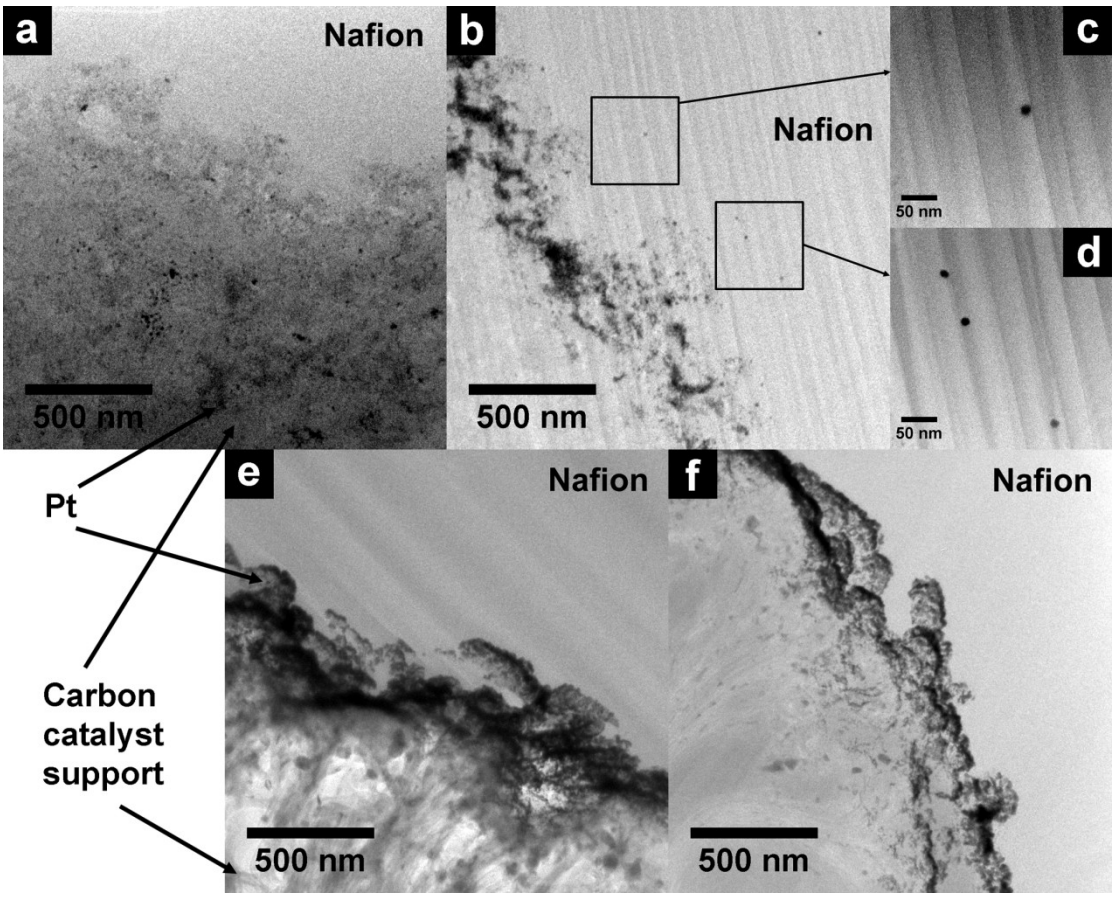


Figure 4-9. Electrode structural study using transmission electron microscopy. TEM micrographs of the Pt/VXC72 cathode (a) before and (b) after ADT, with (c) and (d) magnified views of the re-deposited Pt nanoparticles inside Nafion membrane. TEM micrographs of the Pt/GCNT cathode (e) before and (f) after ADT.

Figure 4-9a shows the cathode-membrane interface region of the Pt/VXC72 cathode before the degradation test. It is observed that the Pt catalyst nanoparticles are well dispersed inside the catalyst layer (bottom-left corner). The Nafion membrane is identified as the homogeneous featureless region at the top-right corner of the micrograph. No Pt catalysts is found in the Nafion membrane. The absence of

Pt nanoparticles smearing into the membrane confirms the high quality of the sample preparation method using FIB-SEM dual beam technique. Figure 4-9b shows the cathode-membrane interface region of the Pt/VXC72 cathode after the degradation test. The structure of the degraded cathode is highly different from that of the fresh cathode. Firstly, it is clear that the Pt catalyst nanoparticles aggregate densely at the interface between the catalyst layer (bottom-left corner) and the Nafion membrane (top-right corner), in contrast to the well dispersed Pt catalysts in the fresh sample. The dense aggregation of the Pt catalyst after the degradation test may cause a severe decrease of the Pt surface area, consistent with the results from the cyclic voltammetry study. Secondly, Pt nanoparticles are now found inside the Nafion membrane as isolated nanoparticles. Magnified views of selected Pt nanoparticles re-deposited inside the Nafion membrane are shown in Figure 4-9c-d. The re-deposition of Pt nanoparticles inside Nafion membrane near the cathode was also reported by other studies. [24-26] Both the aggregation of the Pt catalyst at the cathode-membrane interface and the re-deposition of Pt catalyst inside the membrane explain the great loss of Pt catalyst electrochemical surface area in the Pt/VXC72 cathode after the degradation test. The lack of electrochemical stability in the Pt/VXC72 cathode is well demonstrated by the electrode structural study. In contrast, Figure 4-9e-f show the TEM micrographs of the Pt/GCNT cathode before and after the degradation test, respectively. The degradation behavior of the Pt/GCNT cathode is distinctively different from that of the Pt/VXC72 presented above. Firstly, the location and overall structure of Pt catalyst in the catalyst layer of the Pt/GCNT cathode are very similar in both before and after the degradation test. No significant changes in the electrode structure is observed after the degradation test. The Pt catalyst nanoparticles are

located near the cathode-membrane interface, as a characteristic result of the magnetron sputtering catalyst preparation technique used. Secondly, there is no Pt nanoparticles found inside the Nafion membrane after the degradation test. The results suggest the high stability of the Pt/GCNT cathode, consistent with the cyclic voltammetry study where only a minimal change of the Pt electrochemical surface area is detected in the Pt/GCNT electrode after the degradation test.

4.4. Summary

Through a series of electrochemical evaluation methods and transmission electron microscopy technique, it is found that the highly crystalline graphitic nanomaterials, including the GCNT and CNT supports, exhibit much more superior electrochemical stability than the commercial carbon black-supported Pt catalyst. Pt/GCNT and Pt/CNT cathodes retain ≈ 90% active Pt surface area after the degradation test, as opposed to only 39% Pt surface area retention demonstrated by the Pt/VXC72 catalyst. The CNT-supported Pt catalyst, however, possesses a lower catalytic activity than the carbon black-supported Pt catalyst. The lower activity of the Pt/CNT catalyst renders it less competitive to the commercial Pt/VXC72 catalyst. In contrast, the Pt/GCNT catalyst possesses an enhanced catalytic activity compared to the Pt/VXC72 catalyst. The Pt/GCNT cathode shows approximately a 20% improvement in power density compared to the Pt/VXC72 cathode and a great improvement over the Pt/CNT cathode. A combination of both higher catalytic

activity and superior electrochemical stability makes the Pt/GCNT much more promising as an advanced catalyst to replace the Pt/VXC72 catalyst.

In summary, we investigate the use of graphene-carbon nanotube hybrids as the Pt catalyst support in PEMFCs. The Pt/GCNT catalyst exhibits high intrinsic catalytic activity and superior electrochemical stability compared to a commercial carbon black supported Pt catalyst. The enhanced intrinsic catalytic activity of the Pt/GCNT catalyst is attributed to the high density of graphitic edges present in the hybrids. The superior electrochemical stability of the Pt/GCNT catalyst is attributed to the high crystallinity of the GCNT support. The superior stability is expressed by a lower loss in polarization performance, a smaller increase in charge transfer resistance, a lower loss in the active platinum electrochemical surface area, a lower rate of carbon corrosion, and a more stable catalyst microstructure. With both high catalytic activity and superior electrochemical stability, the GCNT hybrid is demonstrated to be an excellent candidate for an advanced catalyst support in Proton Exchange Membrane Fuel Cells.

Chapter 5 : Amorphous Molybdenum Sulfide on Graphene-Carbon Nanotube hybrids as highly active Hydrogen Evolution Reaction catalysts

5.1. Introduction

As discussed in section 1.3.2, amorphous molybdenum sulfide (MoS_x) has emerged as a very promising class of non-precious hydrogen evolution reaction (HER) catalyst with high catalytic activity, [69-73] and benign room temperature syntheses. [12,69,71,74] Molybdenum sulfide materials in general, however, have low electronic conductivity, [75] which is highly detrimental to the catalytic activity towards HER. [12] Deposition of molybdenum sulfide catalysts on high surface area conductive supports is an effective strategy to enhance the electron transport towards the catalytic active sites and therefore maximize the activity of the catalysts. In addition, similar to many electrochemical devices, the HER reaction inside the electrode requires constant reactant supply and product removal. The mass transport inside the electrode is critical for the high performance of devices, especially at high current density ranges. In addition to the high surface area, a high porosity is also an essential property of the conductive support for efficient mass transport.

In Chapter 3, we demonstrated the growth of Graphene-Carbon Nanotube (GCNT) hybrids directly on carbon paper. In this hierarchical nanostructure, CNTs

are grown directly on carbon paper, and subsequently, graphene is directly grown onto CNT surface. The GCNT hybrids possess high surface area, high crystallinity and high porosity. Such an electrode structure is suitable as the catalyst support for the deposition of MoS_x in HER applications. In this electrode structure, GCNT serves as a high specific surface area, porous and conductive support for the deposition of MoS_x. Carbon paper serves as both a mechanical support and a current collector. As the GCNT hybrids are grown directly onto the carbon paper current collector, the electronic conductive pathways from MoS_x to the current collector are enhanced. The porous structure of both GCNT and carbon paper current collector can facilitate the mass transport inside the electrode.

In this chapter, MoS_x is deposited on the GCNT hybrids and is evaluated for HER catalytic properties. The GCNT is hypothesized to enhance the catalytic activity of MoS_x by effectively enhancing electron transport and mass transport with its high surface area, conductive and porous nanostructure.

5.2. Deposition and activation of MoS_x on carbon supports

MoS_x was deposited on conductive substrates using an anodic electrodeposition process performed at 0.7 V *vs.* SHE in a 20 mM $(NH_4)_2MoS_4$ solution. Subsequently, the MoS_x-deposited electrodes underwent a reductive activation process in a 0.5 M H_2SO_4 solution. The detailed experimental procedure was provided in section 2.1.3.

5.2.1. Deposition of MoS_x catalyst

For comparison purposes, MoS_x was deposited on low specific surface area electrodes, including a flat graphite paper and a simple porous Toray carbon paper, and on a high specific surface area electrode made of GCNT hybrids grown on carbon paper (GCNT/CP). Figure 5-1a shows the deposition current density profiles of these electrodes during the deposition of MoS_x. In these deposition current profiles, it is evident that in all three samples the deposition current density quickly decays in the first few minutes and then slowly approaches their limiting current densities. The deposition of MoS_x becomes slower with additional MoS_x deposited. This could be due to the low electronic conductivity of MoS_x that limits the current density as the deposited MoS_x film thickens. It is clear from Figure 5-1a that the supported deposition current density increases with higher specific surface area electrodes. In the case of the flat graphite electrode, the deposition current density quickly approaches zero within five minutes. This quick current decay limits the practically maximum catalyst loading on a flat electrode. While a similar trend happens to higher specific surface area electrodes, the limiting current densities are approached at longer deposition times. In the case of a porous carbon fiber paper electrode, the deposition current density approaches zero after approximately 40 minutes. With an even higher specific surface area, the GCNT/CP electrode supports a much higher deposition current density, and therefore much higher possible catalyst loadings. With similar deposition times of approximately 40 minutes, catalyst loadings of 0.15, 0.75 and 3 mg cm^{-2} can be obtained on a flat graphite paper, a porous carbon fiber paper and a GCNT/CP electrode, respectively. The GCNT

hybrids demonstrate that a high specific surface area electrode is essential for the deposition of a high catalyst loading.

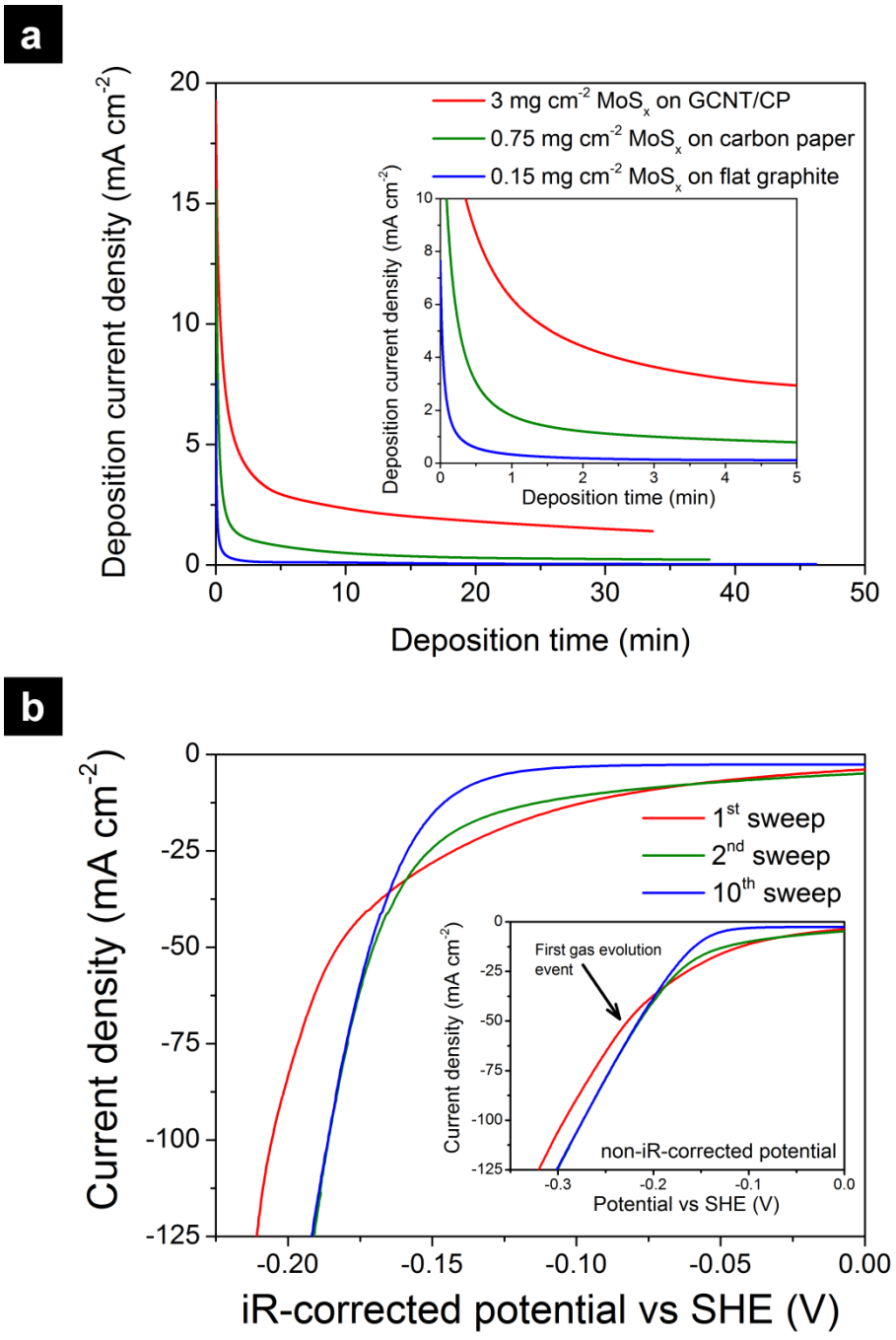


Figure 5-1. MoS_x-based catalysts preparation process. (a) Deposition current profile during the electrodeposition of MoS_x on conductive supports, with (inset) a magnified representation of the first five minutes of deposition, and (b) polarization curves during the reductive activation process of the 3 mg cm^{-2} MoS_x/GCNT/CP electrode reported on iR-corrected potential and (inset) non-iR-corrected potential scales.

The high specific surface area of GCNT/CP can be demonstrated by the BET specific surface area and surface area enhancement factor (or "roughness factor", defined as the ratio between the microscopic surface area and the projected geometric surface area of the electrode). The BET surface area and roughness factor of the porous carbon paper and the GCNT/CP electrode are provided in Table 5-1.

Table 5-1. The BET specific surface area and roughness factor of carbon paper and GCNT/CP electrodes.

	BET specific surface area	**Roughness factor** (*)
	$m^2\ g^{-1}$	
Carbon paper	0.26	31.5
GCNT/CP	12.3 (**)	1577
GCNT	214 (***)	—

(*) Defined as the ratio between the microscopic surface area and the projected geometric surface area of the electrode. Areal density of carbon paper is measured at 12.1 mg cm^{-2}.

(**) Average BET specific surface area, based on the total weight of GCNT and Carbon paper.

(***) Calculated BET specific surface area, based on the measured weight content (5.62 wt%) of GCNT hybrids in the GCNT/CP electrode.

As shown in Table 5-1, a simple carbon paper may sometimes be considered a high surface area electrode compared to a flat electrode geometry, with a roughness factor of 31.5. However, with the growth of GCNT hybrids on the carbon paper, the GCNT/CP electrode shows a tremendous enhancement in specific surface area, with a roughness factor of 1577, which is ≈ 50 times higher than that of a simple porous carbon paper. The enhancement in microscopic surface area is beneficial for a good dispersion of MoS_x and efficient electron transports towards MoS_x active sites. High specific surface area conductive supports such as carbon nanotubes and graphene have been effectively used to support electro-active materials for electrochemical energy applications. [140,141]

5.2.2. Reductive activation of MoS_x catalyst

After MoS_x had been deposited on the conductive substrates, the MoS_x-deposited electrodes underwent a reductive activation process. The activation was performed by 10 potential sweeps from 0.2 V to –0.5V *vs.* SHE. Figure 5-1b shows the current responses of the 3 mg cm^{-2} MoSx/GCNT/CP electrode during the potential sweeps. The results are representative for all MoS_x-based electrodes. During the first potential scan, whilst there is a strong shoulder reductive peak present between 0 V and approximately –0.2 V, no visible hydrogen evolution is observed in this potential range. We attribute this shoulder reductive peak to the chemical reduction of the catalyst itself. The exact activation mechanism and chemical reduction processes are currently not fully understood. A similar reductive peak in the first potential scan was also reported in previous studies by Hu and co-workers. [12,69,70] The authors attributed the reductive peak in the first potential scan to a conversion of S_2^{2-} to S^{2-}. [69] The first hydrogen gas evolution event was visibly observed in the first potential sweep when the potential scanned pass a potential of approximately –0.23 V (without Ohmic loss correction or "non-iR-corrected"), corresponding to approximately –0.18 V in Ohmic loss-corrected ("iR-corrected") potential. In the subsequent potential scans, the shoulder peak becomes progressively less pronounced. Hydrogen evolution was observed earlier than in the first potential scan. Generally, within 10 reductive potential sweeps, the HER polarization curve stabilizes and signifies a completed activation of the MoS_x catalyst. In fact, the reductive activation is nothing but the first 10 HER polarization curves before a stable and reproducible HER polarization curve can be obtained.

5.3. Physical characterization of the MoS_x/GCNT hybrids

5.3.1. Morphological characterization

The morphological characterization of the GCNT/CP support and the activated MoS_x/GCNT/CP electrode was obtained with FE-SEM and is shown in Figure 5-2. Figure 5-2a shows the FE-SEM micrograph of the GCNT/CP support prior to the deposition of MoS_x. The highly porous structure of the GCNT/CP support is clearly observed. The GCNT hybrids possess an overall fibrous morphology of the CNT scaffold, with an ultra-high density of exposed graphitic edges of graphene as seen in the higher magnification SEM micrograph (Figure 5-2b). The highly porous and high surface area structure of the GCNT hybrids is suitable for the deposition of MoS_x with a good material dispersion. Figure 5-2c shows the FE-SEM micrograph of the MoS_x/GCNT/CP electrode. MoS_x is deposited on the GCNT scaffold and thickens the fibrous morphology of the GCNT hybrids. MoS_x is found to fully coat and is in intimate contact with the conductive GCNT support. The close contact between MoS_x and the conductive GCNT support is crucial for a good overall conductivity inside the electrode to support all electrochemical processes. The total thickness of the MoS_x/GCNT forest (excluding the thickness of porous carbon paper support) is measured 50-100 μm. The results suggest that the GCNT/CP electrode successfully serves as a high surface area conductive scaffold to support the deposition of MoS_x. A schematic illustration of the GCNT support and the MoS_x/GCNT electrode is shown in Figure 5-2d.

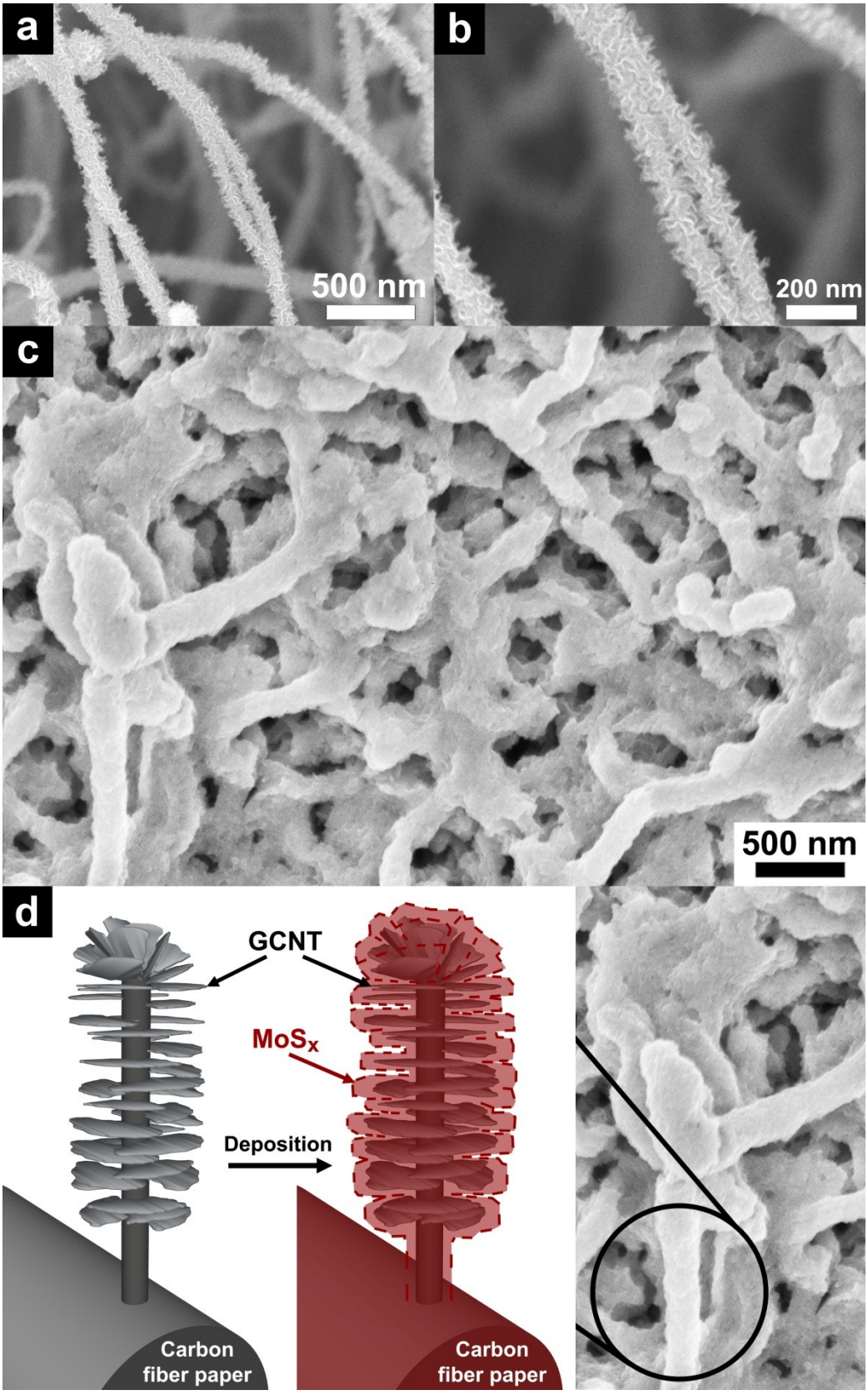


Figure 5-2. Morphological characterization with FE-SEM of (a, b) the GCNT/CP support, and (c) the MoS_x/GCNT/CP electrode. (d) A schematic illustration of the GCNT/CP support and the MoS_x/GCNT/CP electrode.

5.3.2. Chemical state analysis

The chemical state of the MoS_x/GCNT/CP electrode was assessed with XPS. Figure 5-3a shows the survey XPS spectrum of the electrode. The spectrum is dominated by peak sets of Mo, S, and C as expected from the composition of the electrode, as well as the appearance of an adventitious O 1s impurity peak. Figure 5-3b shows the high resolution XPS scans in the Mo 3d and the S 2p regions of spectrum. The Mo 3d spectrum can be deconvoluted into three peak sets, including a S 2s peak at binding energy (BE) of 226.9 eV, a Mo 3d doublet at BE of 229.3 eV – 232.5 eV, and a Mo 3d doublet at BE of 231.7 eV – 234.9 eV. Molybdenum is present in two chemical states, here denoted as $Mo^{(A)}$ at higher binding energy and $Mo^{(B)}$ at lower binding energy. The lower binding energy of $Mo^{(B)}$ can be assigned to the oxidation state of Mo^{4+} as in MoS_2 or MoS_3. [70] The higher binding energy of $Mo^{(A)}$ can be attributed to the oxidation state of Mo^{5+} [74] or of Mo^{4+} in molybdenum oxysulfide $Mo^{(A)}S_xO_y$. [12,70] The S 2p spectrum can be deconvoluted into two doublets at BE of 162.9 eV – 164.1 eV and 161.4 eV – 162.6 eV, denoted as $S^{(A)}$ and $S^{(B)}$, respectively. The $S^{(A)}$ 2p doublet can be attributed to apical S^{2-} or bridging S_2^{2-}. The $S^{(B)}$ 2p doublet can be attributed to basal plane S^{2-} or terminal S_2^{2-}. [142] The chemical states of both Mo and S suggest that the deposited material can be described as mixed valence states of molybdenum sulfide. Using XPS spectra of MoS_2 micro-crystals as references, the relative stoichiometry of Mo and S in MoS_x/GCNT/CP was determined as Mo : S = 1 : 3.02. The fact that both Mo and S appear in multiple chemical states with broad XPS peaks suggests the deposited MoS_x closely resembles amorphous MoS_3. [142]

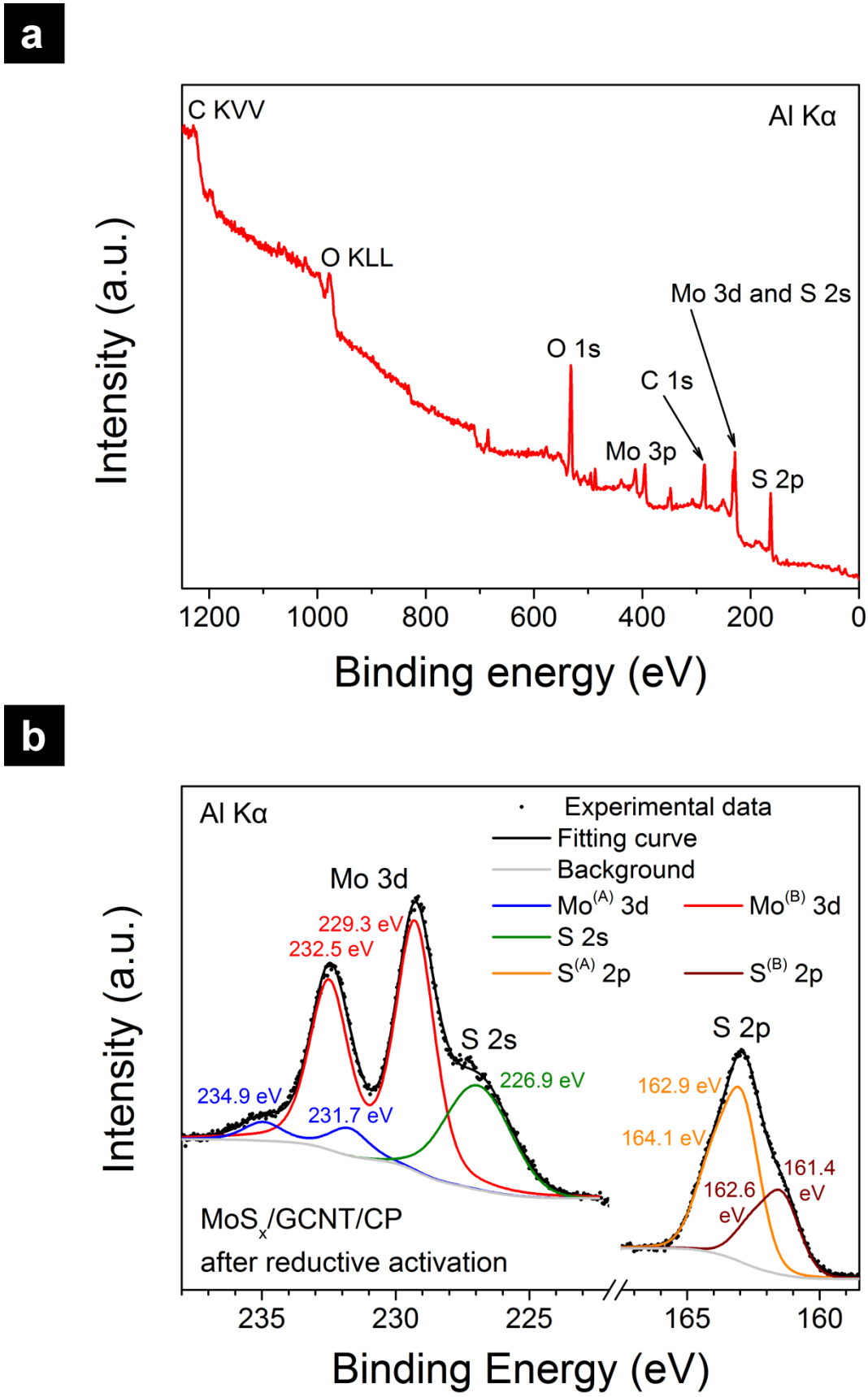


Figure 5-3. Chemical analysis with XPS of the activated MoS_x/GCNT/CP electrode. (a) XPS survey spectrum and (b) high resolution scans in Mo 3d and S 2p regions.

5.3.3. Crystallinity analysis

In order to assess the crystallinity of deposited MoS_x, the MoS_x/GCNT/CP electrode and the GCNT/CP support were examined with Raman spectroscopy and XRD, as shown in Figure 5-4.

Figure 5-4a shows the Raman spectra of GCNT/CP support and MoS_x/GCNT/CP electrode. The Raman spectrum of GCNT/CP shows typical characteristic peaks D, G, as well as second order peaks 2D, D + G, and 2D′. As the MoS_x coats well the top surface of the GCNT/CP support, the graphitic characteristic peaks of GCNT are greatly suppressed in the Raman spectrum of MoS_x/GCNT/CP electrode. The Raman spectrum of MoS_x/GCNT/CP is dominated by additional bands from MoS_x with Raman shift between 150 cm^{-1} to 1000 cm^{-1}. However, the Raman spectrum of MoS_x does not show characteristic peaks E^1_{2g} and A_{1g} corresponding to crystalline MoS_2, but instead shows broad band between 150 cm^{-1} to 1000 cm^{-1}. The Raman spectrum resembles that of amorphous MoS_3. [142,143]

To further confirm the amorphous nature of the deposited MoS_x, XRD measurements were performed on the GCNT/CP support and MoS_x/GCNT/CP electrode. The resulting XRD spectra are shown in Figure 5-4b. Both spectra show sharp and strong characteristic peaks of graphitic carbon (002) plane, and therefore confirm the high crystallinity of the GCNT/CP support. The XRD spectrum of MoS_x/GCNT/CP does not show any strong additional characteristic peak that could otherwise suggest the presence of crystalline MoS_2, except very weak and broad diffraction bands of 2θ from 10° to 20° and from 30° to 40°. The XRD result further

confirms the amorphous nature (or a very low crystallinity at most) of the deposited MoS_x.

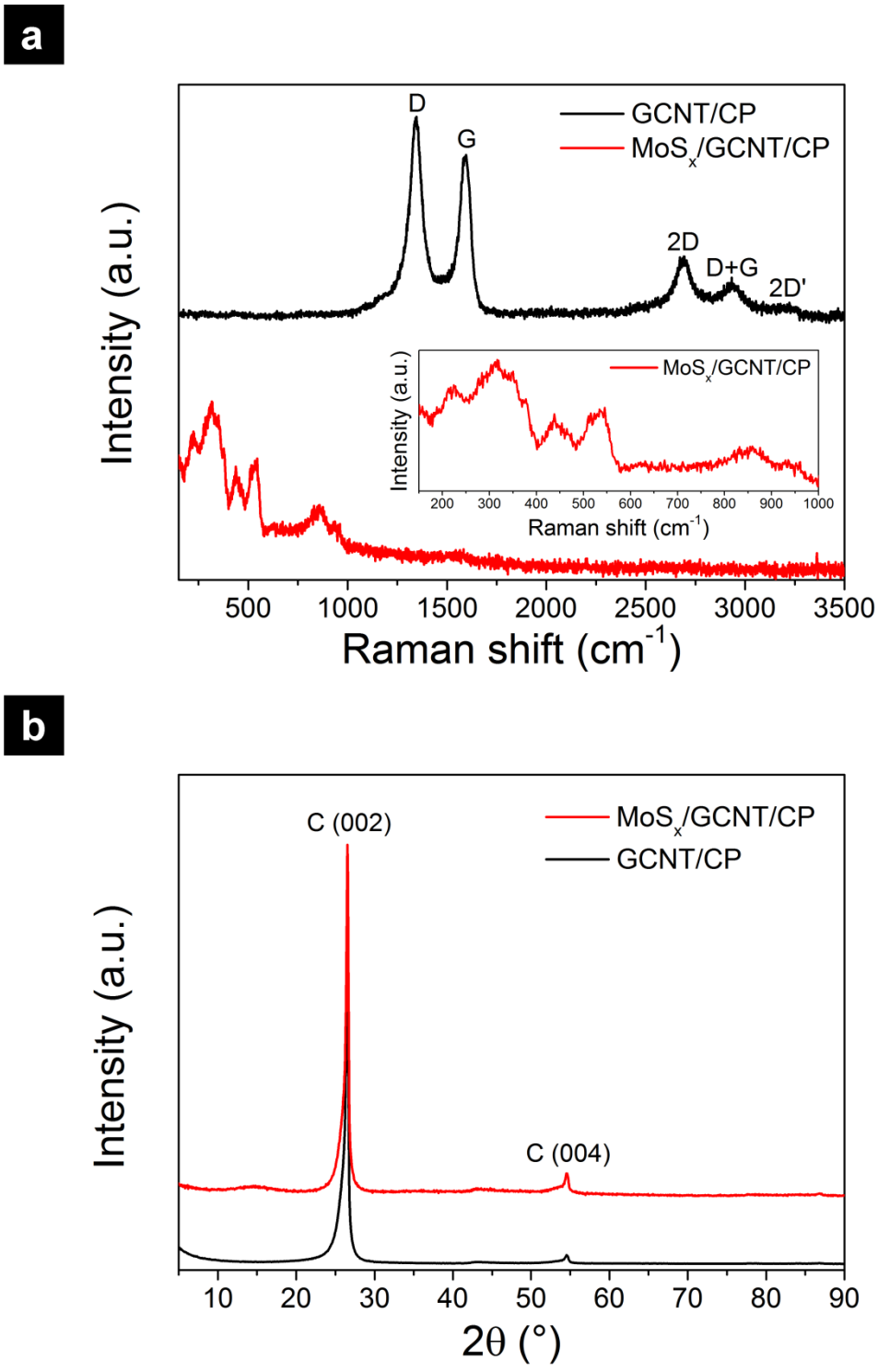


Figure 5-4. Crystallinity analyses of the GCNT/CP and MoS_x/GCNT/CP electrodes with (a) Raman spectroscopy, with an inset showing the closed up spectrum of additional Raman bands from MoS_x and (b) X-ray diffraction.

5.4. Electrochemical evaluations of the MoS_x/GCNT hybrids as HER catalyst materials

The electrochemical evaluations aim to study the HER catalytic activity of MoS_x from several perspectives, including: (1) total electrode activity (measured by polarization curve and EIS), (2) intrinsic activity (or Turnover frequency (TOF), measured by cyclic voltammetry), and (3) electrochemical stability (measured by a degradation test). All electrochemical evaluations for HER catalytic activity were performed in a 0.5 M H_2SO_4 solution, as described in detail in section 2.3.2.

5.4.1. Total electrode catalytic activity

The total electrode activity of catalysts was characterized with the HER polarization curves. For comparison purposes, 0.15 mg cm^{-2} MoS_x on flat graphite, 0.75 mg cm^{-2} MoS_x on porous carbon paper and 3 mg cm^{-2} MoS_x on GCNT/CP were prepared as described in section 5.2. For additional comparisons and references, 1.5 mg cm^{-2} MoS_x on GCNT/CP, 4.5 mg cm^{-2} MoS_x on GCNT/CP, a plain carbon paper (without any catalysts deposited) and a Pt foil electrode were also prepared and tested for HER polarization. Figure 5-5a shows the polarization curves of these electrodes reported on iR-corrected potential scale. The Ohmic losses were calculated based on the ohmic resistances extracted from electrochemical impedance spectra of these electrodes. Detailed calculations will not be presented here. As expected, the plain carbon paper electrode is inert to HER reaction, with nearly zero current density. On the other hand, the platinum foil electrode, being a precious metal catalyst, is highly active towards HER with an early onset of hydrogen evolution

reaction. Among MoS_x-based catalysts, it is obvious that MoS_x/GCNT/CP electrodes showed much earlier onsets of hydrogen evolution reaction than MoS_x catalysts deposited on lower surface area electrodes, including porous carbon paper and flat graphite. Regardless of catalyst loadings between 1.5 and 4.5 mg cm^{-2} MoS_x, MoS_x/GCNT/CP electrodes show relatively similar performances and are all much better than MoS_x/flat graphite and MoS_x/carbon paper electrodes. It is noteworthy that at overpotentials of above 200 mV, the MoS_x/GCNT/CP electrodes produce higher current densities than the platinum foil electrode does. This is mainly due to the mass transport effect. It was visually observed that gas bubbles produced during hydrogen evolution on MoS_x/GCNT/CP electrodes generally had sub-millimeter sizes and easily detached from the electrode surface. This is probably due to the good hydrophilicity of the MoS_x, especially after being deposited on a highly porous nanostructure of GCNT hybrids. On the other hand, the platinum foil produced large hydrogen bubbles that adhered relatively strongly on the surface of the platinum electrode and blocked parts of the active electrode surface. For a better extraction of total electrode activity parameters, the HER polarization curves are presented in Tafel plot, as shown in Figure 5-5b. The red-colored segments denote the ranges where the Tafel plot linear fittings are performed and Tafel parameters are extracted. From Figure 5-5, the following parameters are extracted for comparison: overpotential required for the electrodes to produce an HER current density of 10 mA cm^{-2} (which is generally used as a benchmark for comparison of HER catalysts), Tafel slope (which partly reflects the reaction mechanism of the HER on the catalyst) and exchange current density (which is the dynamic current at zero overpotential). These parameters are extracted and summarized in Table 5-2.

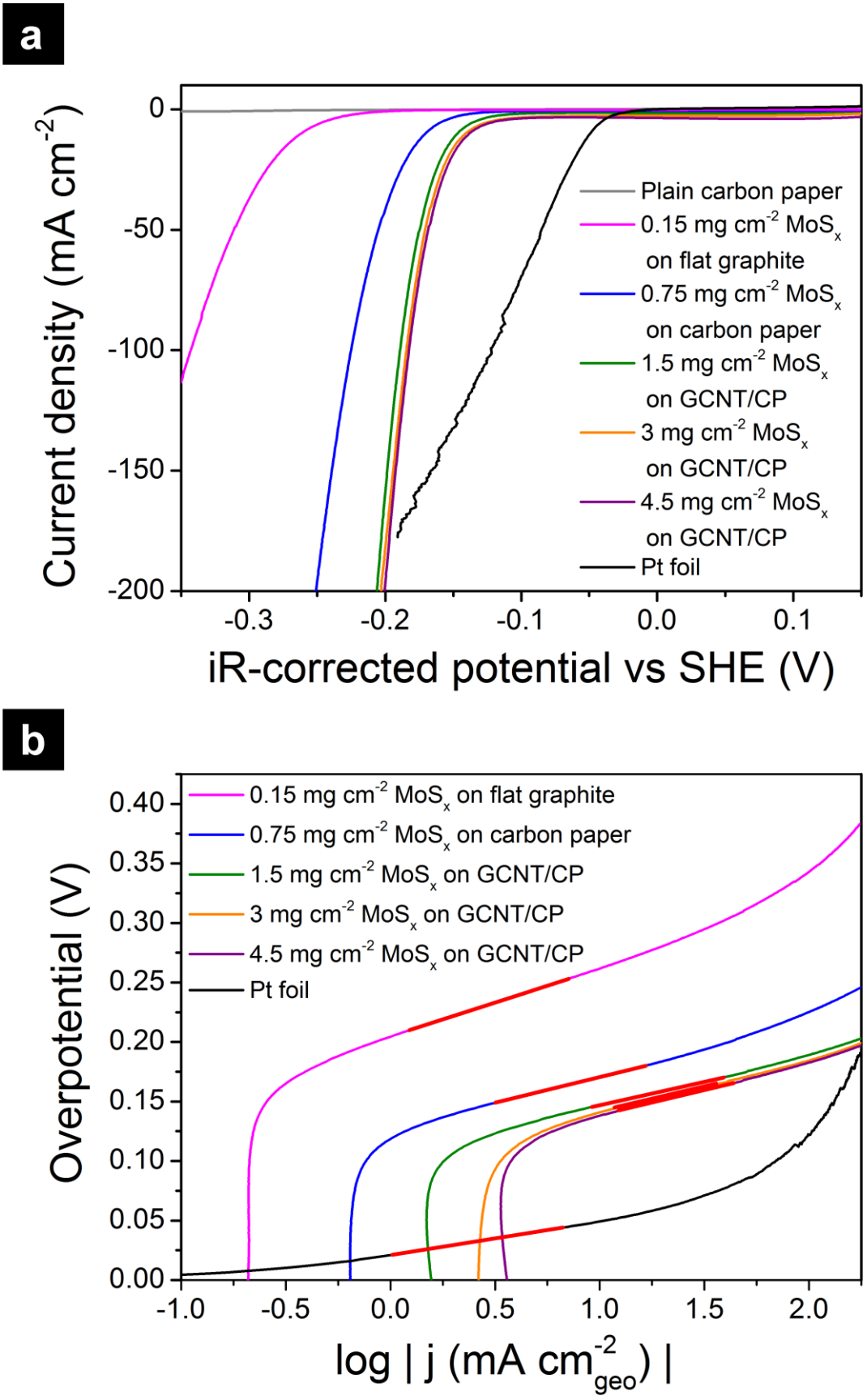


Figure 5-5. HER polarization curves of the MoS_x/GCNT/CP electrodes and reference samples presented on (a) linear scale and (b) Tafel plot.

Table 5-2. Extracted parameters from the HER polarization curves and Tafel plots.

	Tafel slope	**Exchange current density**	**Overpotential at $\|j\|$ = 10 mA cm^{-2}**
	mV decade^{-1}	mA cm^{-2}	mV
0.15 mg cm^{-2} MoS_x on flat graphite	56.4	2.34×10^{-4}	262
0.75 mg cm^{-2} MoS_x on carbon paper	42.9	1.06×10^{-3}	170
1.5 mg cm^{-2} MoS_x on GCNT/CP	39.3	1.82×10^{-3}	146
3 mg cm^{-2} MoS_x on GCNT/CP	41.0	3.52×10^{-3}	141
4.5 mg cm^{-2} MoS_x on GCNT/CP	41.8	4.77×10^{-3}	138
Platinum foil electrode	28.0	1.78×10^{-1}	49
(Degraded) 3 mg cm^{-2} MoS_x /GCNT/CP	45.7	2.31×10^{-3}	166

Table 5-3. A comparison of the overpotential at $|j|$ = 10 mA cm^{-2} with the state of the art molybdenum sulfide catalysts. (Adapted with permission from ref. [60] Copyright © 2014, American Chemical Society)

	Reference	**Overpotential at $\|j\|$ = 10 mA cm^{-2}**
		mV
MoO_3-MoS_2 nanowires	[64]	254
Electrodeposited amorphous MoS_3	[69]	242
1T – MoS_2	[144]	207
Double gyroid MoS_2	[68]	206
Wet-chemical amorphous MoS_x	[74]	200
MoS_x / Carbon paper	[73]	194
100 μg cm^{-2} $[Mo_3S_{13}]^{2-}$ / Graphite Paper	[145]	174
Li_xMoS_2 / Carbon paper	[146]	168
MoS_2 / Reduced graphene oxide	[67]	154
MoS_x / Piranha Carbon paper	[73]	152
$[Mo_3S_{13}]^{2-}$ / anodized Graphite Paper	[60]	149
4.5 mg cm^{-2} MoS_x/GCNT/Carbon Paper	This work	138
Li-MoS_2 / Carbon Paper	[147]	110
MoS_x / N-CNT	[71]	110
Pt foil	This work	49

As shown in Table 5-2, the 0.15 mg cm^{-2} MoS_x on flat graphite electrode shows a moderate performance with 262 mV overpotential required to obtain a current density of 10 mA cm^{-2}. The required overpotential decreases significantly when MoS_x was deposited on higher specific surface area electrodes, with only 170 mV required for MoS_x deposited on carbon paper. The required overpotential decreases even further when MoS_x was deposited on GCNT hybrids, with an overpotential of as low as 138 mV for the case of 4.5 mg cm^{-2} MoS_x on GCNT/CP. This is among the lowest required overpotentials reported to date for molybdenum sulfide-based HER catalysts. [60,64,67-69,71,73,74,144,146,148] A comparison of the required overpotential with the state of the art molybdenum sulfide catalysts is provided in Table 5-3. The required overpotential for MoS_x/GCNT/CP decreases with the increase of catalyst loading. However, the overpotential decreases are relatively small compared to the significant overpotential reduction over the MoS_x catalysts deposited on low surface area electrodes. This difference implies that the enhanced catalytic activity in MoS_x/GCNT/CP is beyond the catalyst loading difference reasons. This can be demonstrated further with the Tafel parameters. The exchange current density for all MoS_x-based electrodes scales almost linearly with the catalyst loading. However, there are large differences in Tafel slope for MoS_x deposited on different substrates. With a low specific surface area electrode of a flat graphite paper, the Tafel slope is relatively high at 56.4 mV per decade even for a low catalyst loading of 0.15 mg cm^{-2}. The Tafel slope reduces to 42.9 mV per decade for MoS_x deposited on carbon paper. The Tafel slope reduces even further to between 39.3 and 41.8 mV per decade even with much higher catalyst loadings between 1.5 and 4.5 mg cm^{-2}. In general, for a same substrate, the Tafel slope increases with an increase in MoS_x

loading due to the slow electron transport in MoS_x. [12] The higher Tafel slopes even for low catalyst loadings on low specific surface area electrodes, such as carbon paper and flat graphite paper, are probably linked to the low electronic conductivity of MoS_x. By depositing MoS_x on a high specific surface area conductive electrode such as GCNT hybrids, the overall electronic conductivity in the catalyst can be improved. The conductive paths inside the MoS_x catalyst are effectively shortened. The electrode kinetics are therefore enhanced. Whilst the MoS_x/GCNT/CP also experiences some increase in the Tafel slope with the increases in MoS_x loading, the increases are relatively minimal. The Tafel slopes of between 39.3 to 41.8 mV per decade suggests that the HER reaction on MoS_x/GCNT/CP follows the Volmer-Heyrovsky mechanism [149] (Volmer step ($H^+ + e^- \rightarrow H_{ad}$) followed by Heyrovsky step ($H^+ + H_{ad} \rightarrow H_2$)).

EIS is an important electrochemical technique that provides a wealth of information, including kinetic and surface information, of electrochemical reactions in general and HER in particular. [150] The enhanced catalytic activity of the MoS_x/GCNT/CP electrodes over that of the MoS_x on low surface area electrodes can be demonstrated by significant reductions in the charge transfer resistance, as characterized by EIS and shown in Figure 5-6.

Figure 5-6a–b show the EIS spectra of MoS_x catalysts obtained at an overpotential of η = 150 mV, presented in Nyquist plot (Figure 5-6a) and Bode plots (Figure 5-6b). As evidenced from Figure 5-6a, the EIS spectra of all five MoS_x catalyst samples are dominated by a single capacitive semicircle at medium frequency range, suggesting the catalytic reaction is characterized by a single time constant. The single

time constant characteristic of the reaction is also evidenced by a single peak at frequency of $f \approx 1$ Hz in the Bode phase plot (Figure 5-6b). Beside the dominant semicircle at medium frequency, the EIS spectra in Figure 5-6a also contain a minor capacitive semicircle at high frequency region. This minor semicircle is overpotential-independent, as will be evidenced in Figure 5-6c–d. This high frequency semicircle is thus attributed to non-Faradaic origins. Qualitatively, the EIS spectra of MoS_x/GCNT/CP show much smaller semicircles (and therefore higher catalytic activity) than the EIS spectra of MoS_x/carbon paper and MoS_x/flat graphite electrodes.

Figure 5-6c–d show the EIS spectra of the 3 mg cm^{-2} MoS_x/GCNT/CP electrode measured at three different overpotentials η of 100 mV, 150 mV and 200 mV. The high frequency semicircle is overpotential-independent, as evidenced by the overlap of the three EIS spectra at high frequency range in both Nyquist and Bode plots. As the overpotential increases from 100 mV to 200 mV, the medium frequency semicircle shrinks dramatically, indicating an increase in reaction rate. Similarly, the peak in Bode phase plot shifts to higher frequency, indicating a shorter reaction time constant as the overpotential increases.

For quantitative comparisons of the charge transfer resistance, all EIS spectra in Figure 5-6 are fitted using the equivalent circuit presented in Figure 5-6a (inset). In this circuit, L_{cab} represents the parasitic inductance caused by connecting cables or measuring instrument, as evidenced by minor inductive responses at high frequency of $\approx 10^4$ Hz. R_{ohm} represents the ohmic resistance, which is mainly attributed to the uncompensated electrolyte resistance. R_{nF} and CPE_1 are the

resistance and constant phase element corresponding to the minor overpotential-independent high frequency semicircle. These elements are of non-Faradaic origins, and are attributed to the distributed resistance/capacitance inside the electrode or the contact resistance/capacitance. R_{ct} and CPE_{dl} are the charge transfer resistance and the constant phase element representing the double layer capacitance of the electrode. The major fitting parameters for MoS_x catalysts are summarized in Table 5-4.

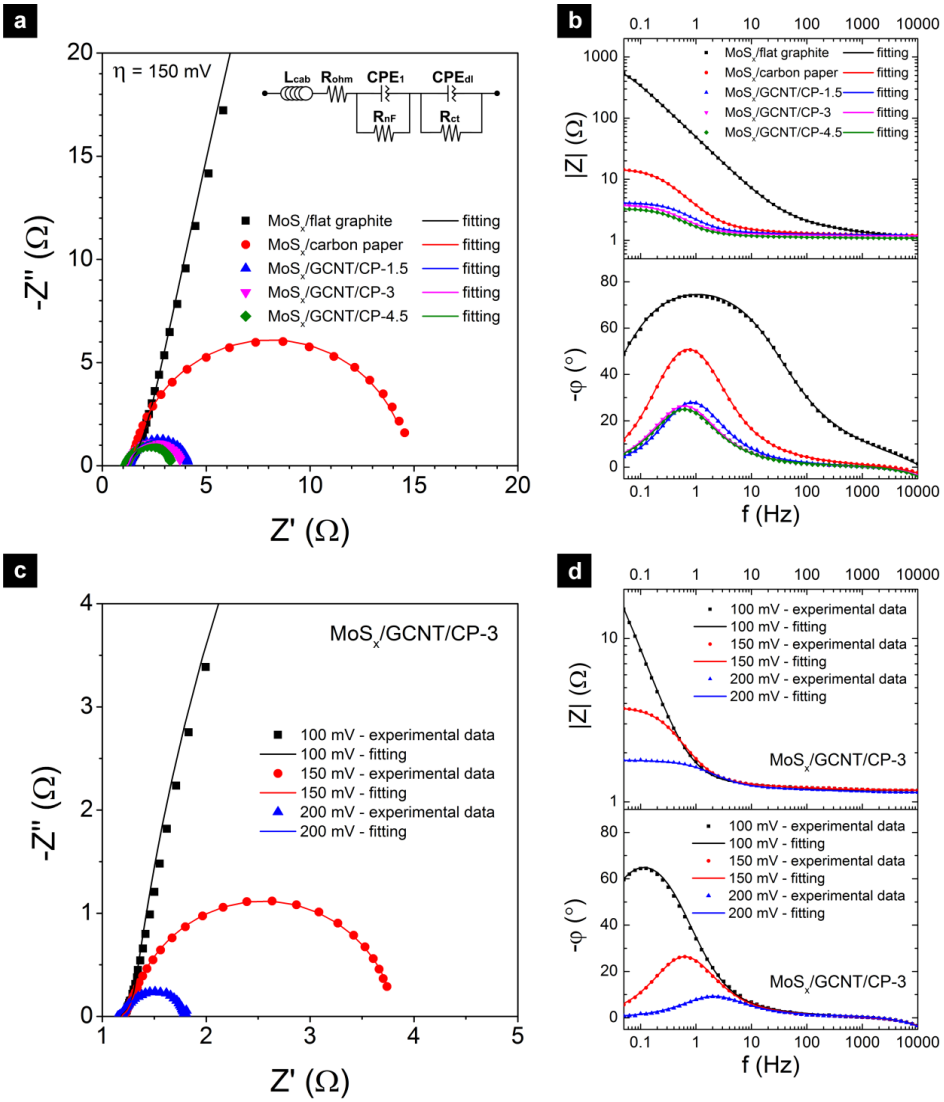


Figure 5-6. Electrochemical impedance spectra of the MoS_x catalysts measured at overpotential η = 150 mV, presented on (a) Nyquist plot and (b) Bode plots. EIS spectra of the 3 mg cm^{-2} MoS_x/GCNT/CP electrode measured at overpotentials η of 100, 150 and 200 mV, presented on (c) Nyquist plot and (d) Bode plots.

Table 5-4. Equivalent circuit fitting parameters for MoS_x catalysts.

	η	R_{ohm}	R_{ct}	CPE_{dl}	τ
	mV	Ω	Ω	mF	s
0.15 mg cm^{-2} MoS_x/flat graphite	150	1.06	1028	4.83	4.97
0.75 mg cm^{-2} MoS_x/carbon paper	150	1.20	13.1	55.4	0.73
1.5 mg cm^{-2} MoS_x/GCNT/CP	150	1.21	2.67	129	0.34
3 mg cm^{-2} MoS_x/GCNT/CP	100	1.17	43.6	213	9.29
3 mg cm^{-2} MoS_x/GCNT/CP	150	1.17	2.52	185	0.47
3 mg cm^{-2} MoS_x/GCNT/CP	200	1.12	0.553	174	0.10
4.5 mg cm^{-2} MoS_x/GCNT/CP	150	1.07	2.20	204	0.45

As presented in Table 5-4, the enhanced catalytic activity of MoS_x/GCNT/CP electrodes is clearly demonstrated by the small R_{ct} of between 2.20 Ω and 2.67 Ω (at η = 150 mV) compared to 13.1 Ω and 1028 Ω demonstrated by MoS_x/carbon paper and MoS_x/flat graphite, respectively. Similarly, the reaction time constant ($\tau = R_{ct}CPE_{dl}$) of MoS_x/GCNT/CP electrodes at η = 150 mV is of between 0.34 s and 0.47 s, much smaller than 0.73 s and 4.97 s demonstrated by MoS_x/carbon paper and MoS_x/flat graphite, respectively. The R_{ct} of the 3 mg cm^{-2} MoS_x/GCNT/CP electrode decreases significantly from 43.6 Ω to 0.553 Ω as η increases from 100 mV to 200 mV. The reaction time constant τ of the 3 mg cm^{-2} MoS_x/GCNT/CP electrode decreases significantly from 9.29 s to 0.10 s as η increases from 100 mV to 200 mV.

5.4.2. Intrinsic catalytic activity

The per-site intrinsic catalytic activity of the MoS_x/GCNT/CP catalyst is assessed by a Turnover frequency (TOF) estimation. Specifically, the 3 mg cm^{-2} MoS_x/GCNT/CP sample is used for the estimation. We follow the TOF estimation

process proposed by Jaramillo and co-workers. [74] To summarize, the estimation steps are:

(a) Estimate the non-Faradaic capacitance of the MoS_x/GCNT/CP electrode.

(b) Estimate a Roughness factor of the MoS_x/GCNT/CP electrode, which is the ratio between the non-Faradaic capacitance of the MoS_x/GCNT/CP electrode and that of a flat MoS_2 standard electrode.

(c) Estimate the electrode-area-specific surface site density of the MoS_x/GCNT/CP electrode by multiplying the roughness factor with the surface site density of the flat MoS_2 standard electrode.

(d) Estimate the per-site TOF of the MoS_x/GCNT/CP electrode as the electrode-area-specific total TOF at a current density of interest divided by the electrode-area-specific surface site density of the MoS_x/GCNT/CP electrode.

The capacitance of the MoS_x/GCNT/CP electrode is estimated by performing cyclic voltammetry scans at various scan rates in a potential windows of 0 V to 0.3 V *vs.* SHE. The cyclic voltammograms are shown in Figure 5-7a. The cyclic voltammograms have *pseudo*-rectangular shapes without any obvious Faradaic peaks. However, we notice that the demonstrated capacitive behavior of the MoS_x/GCNT/CP electrode is not a pure non-Faradaic response, as the current density does not scale linearly with the scan rate. It was suggested that the current density scales linearly with scan rate in a pure non-Faradaic response, and scales linearly with the square root of the scan rate in a pure Faradaic response. [74,151] We find that our MoS_x/GCNT/CP electrode demonstrates a mixed behavior. In order to deconvolute the contributions from non-Faradaic and Faradaic processes to the total

capacitive behavior, we follow the method proposed by Díaz and co-workers. [152] In their method, the current density j measured on the cyclic voltammograms can be described as a current density summation of two processes:

$$j = k_1 v + k_2 v^{1/2} \quad (5\text{-}1)$$

where v is the scan rate, k_1 and k_2 are scan rate independent constants representing the contributions from non-Faradaic and Faradaic processes. By rearranging the equation to

$$j v^{-1/2} = k_1 v^{1/2} + k_2 \quad (5\text{-}2)$$

and performing a linear fitting for $jv^{-1/2}$ versus $v^{1/2}$, the individual capacitive contributions can be estimated. The current density readings (a half of the anodic-cathodic current density differences) at 0.15 V *vs.* SHE are extracted from the cyclic voltammograms of the MoS_x/GCNT/CP electrode. The linear fitting is shown in Figure 5-7b.

Using this estimation method, a non-Faradaic capacitance of 0.204 F cm^{-2} is estimated for our electrode. By using the reported value of 60 μF cm^{-2} for a flat MoS_2 standard electrode, [74] a roughness factor of 3393 was obtained. A surface site density of 3.95×10^{18} sites cm^{-2} is estimated for our electrode. At a current density of 10 mA cm^{-2} (obtained at 141 mV overpotential), a per-site TOF of 7.9×10^{-3} s^{-1} is estimated. At an overpotential of 200 mV (corresponding to a current density of 182 mA cm^{-2}), a per-site TOF of 0.14 s^{-1} is estimated. The per-site TOF at 200 mV overpotential is in the same order of magnitude with the reported value by Jaramillo. [74] Our MoS_x/GCNT/CP has similar intrinsic per-site activity to the reported literature.

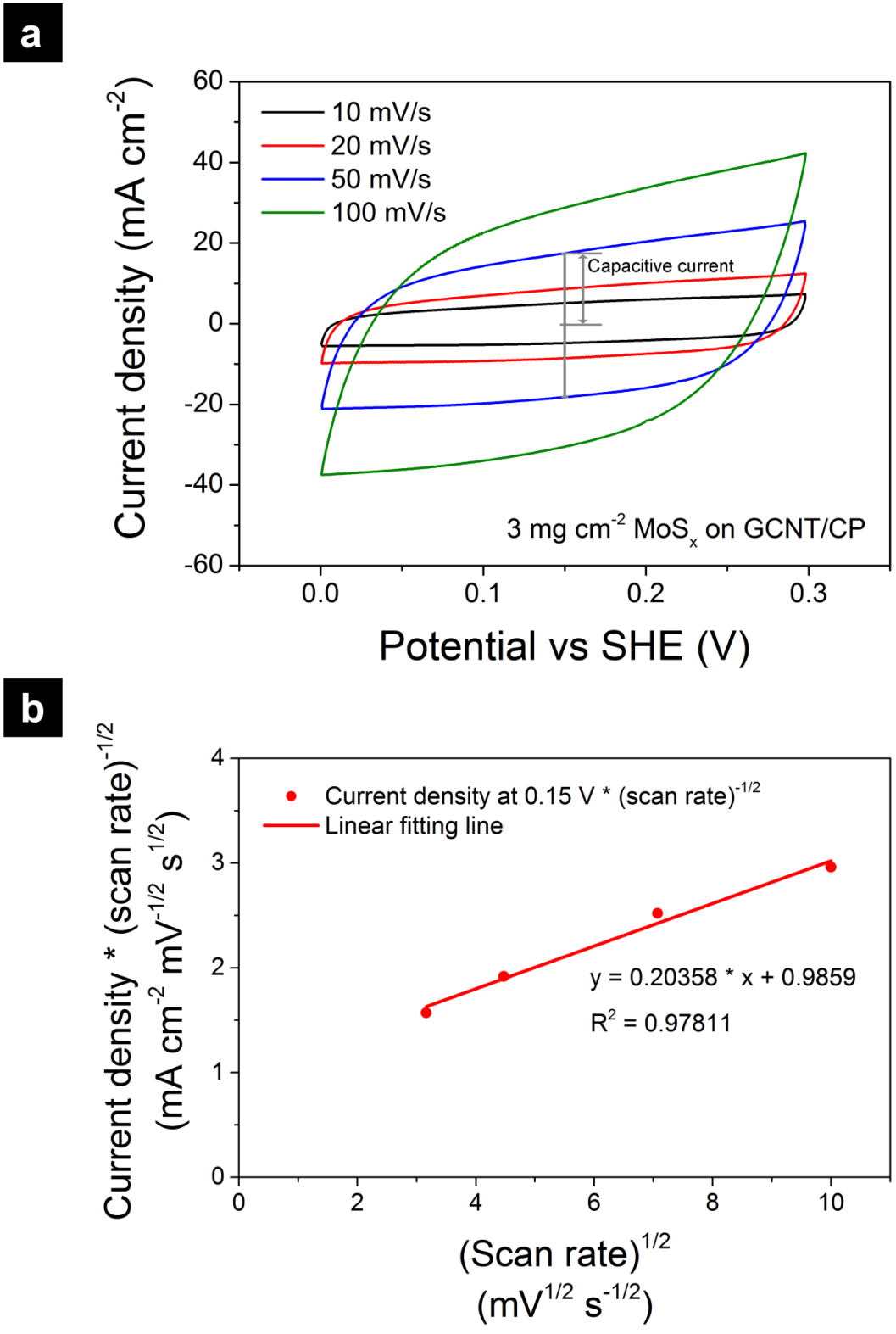


Figure 5-7. Turnover frequency estimation for the 3 mg cm^{-2} MoS_x/GCNT/CP electrode. (a) Cyclic voltammetry curves measured in a potential window of 0-0.3 V *vs.* SHE at scan rates of 10, 20, 50 and 100 mV s^{-1}, and (b) deconvolution of the MoS_x/GCNT/CP electrode capacitive behavior by a linear fitting of the (capacitive current density)*(scan rate)$^{-1/2}$ *vs.* (scan rate)$^{1/2}$.

5.4.3. Electrochemical stability of the MoS_x/GCNT/CP electrode

The electrochemical stability evaluation for the MoS_x/GCNT/CP electrode was performed with 500 potential scans from 0.2 V to –0.5 V *vs.* SHE. A polarization curve was recorded for the degraded electrode. A comparison of the polarization curves for the 3 mg cm^{-2} MoS_x/GCNT/CP electrode before and after the degradation is shown in Figure 5-8. A modest increase of only 25 mV in overpotential is required for the degraded electrode to achieve a current density of 10 mA cm^{-2}. Even with a required overpotential of 166 mV to achieve a current density of 10 mA cm^{-2}, the degraded electrode is still considered a very active non-precious HER catalyst. Tafel plot analyses of the degraded electrode estimate a Tafel slope of 45.7 mV $decade^{-1}$ and an exchange current density of 2.31×10^{-3} mA cm^{-2}, as reported in Table 5-2. The changes in Tafel slope and exchange current density with respect to the original electrode's parameters are relatively moderate. One of the possible contributing reasons for the increase in Tafel slope and the decrease in exchange current density is the mechanical detachment of MoS_x from the GCNT support, due to the vigorous bubbling present during the stability test. The maximum current density obtained during the potential scans is approximately 300 mA cm^{-2}, which is closer to the operation conditions of water electrolyzers than to that of photoelectrochemical cells. In addition, for practical experiments, ohmic loss is present. The relative degradation in a practical setting is much less significant. As shown in the inset of Figure 5-8, the current density obtained at a non-iR-corrected potential of –0.5 V *vs.* SHE only decreases from 320 mA cm^{-2} to 290 mA cm^{-2} after the stability test. The decrease is

less than 10%. We consider this an indication of a good stability demonstrated by the MoS_x/GCNT/CP electrode.

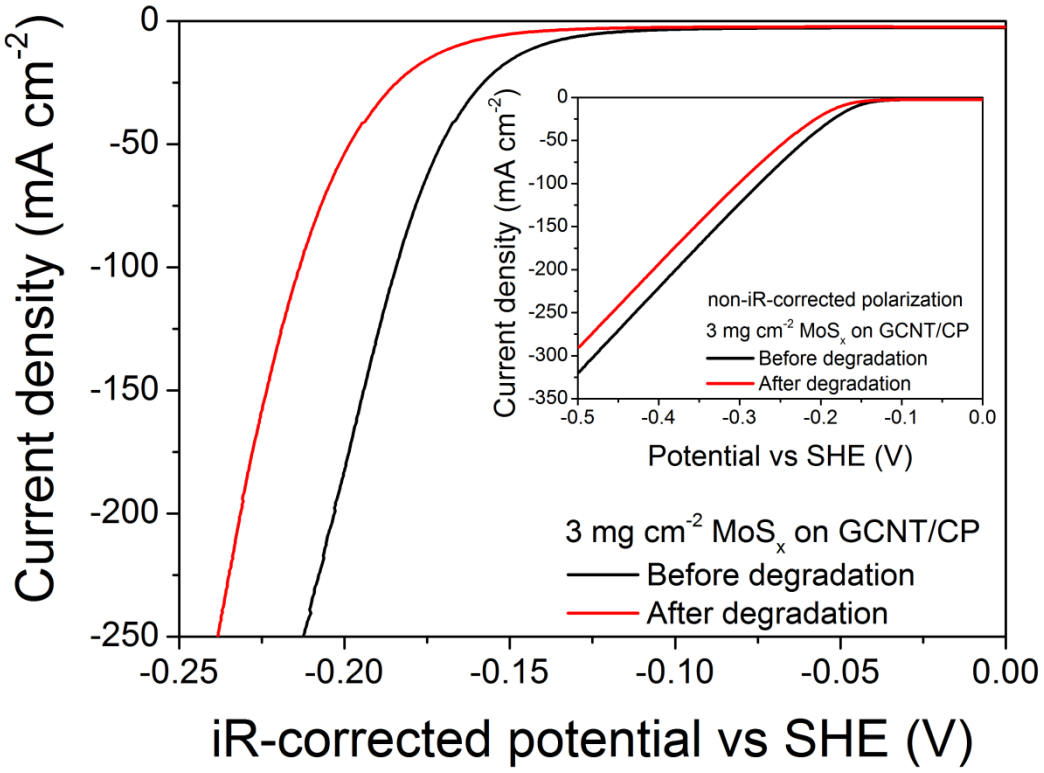


Figure 5-8. Degradation test of the MoS_x/GCNT/CP electrode, with HER polarization curves of the electrode before and after degradation presented on iR-corrected and (inset) non-iR-corrected potential scales.

5.4.4. Understanding of MoS_x active sites through XPS characterization

In order to have a better understanding of the chemical states present in MoS_x in various steps during the electrochemical characterization procedure, XPS was performed on the MoS_x/GCNT/CP electrode at three different states, namely after electrodeposition, after reductive activation and after stability test. To facilitate semi-quantitative elemental analyses, XPS spectra of MoS_2 micro-crystals were

recorded to determine our instrument-specific relative sensitivity factors for Mo and S. The XPS spectra in Mo 3d and S 2p regions for four samples are shown in Figure 5-9. In all samples, the XPS spectra in the Mo 3d region can be fitted with one or two sets of Mo 3d doublets, in addition to one S 2s peak. The Mo 3d doublet at the higher binding energy is referred to as $Mo^{(A)}$ oxidation state. The Mo 3d doublet at the lower binding energy is referred to as $Mo^{(B)}$ oxidation state. The $Mo^{(B)}$ state with Mo $3d_{5/2}$ peak at 229.3 ± 0.2 eV is assigned to Mo^{4+} oxidation state as in MoS_2 or MoS_3. [70] The $Mo^{(A)}$ state with Mo $3d_{5/2}$ peak at 231.6 ± 0.4 eV is assigned to Mo^{5+} oxidation state [74] or of Mo^{4+} in molybdenum oxysulfide MoS_xO_y. [12,70] Similarly, in all samples, the S 2p spectra can be fitted with two or three sets of S 2p doublets. The minor peak $S^{(C)}$ at the highest binding energy is assigned to the S^{6+} oxidation state from the surface oxidation of sample or residual H_2SO_4. [74] The main S 2p peak can be fitted with one or two doublets. The S 2p doublet at the higher binding energy with S $2p_{3/2}$ peak at 162.9 ± 0.2 eV is referred to as $S^{(A)}$ state. The S 2p doublet at the lower binding energy with S $2p_{3/2}$ peak at 161.5 ± 0.3 eV is referred to as $S^{(B)}$ state. The $S^{(A)}$ 2p doublet can be attributed to apical S^{2-} or bridging S_2^{2-}. The $S^{(B)}$ 2p doublet can be attributed to basal plane S^{2-} or terminal S_2^{2-}. [142]

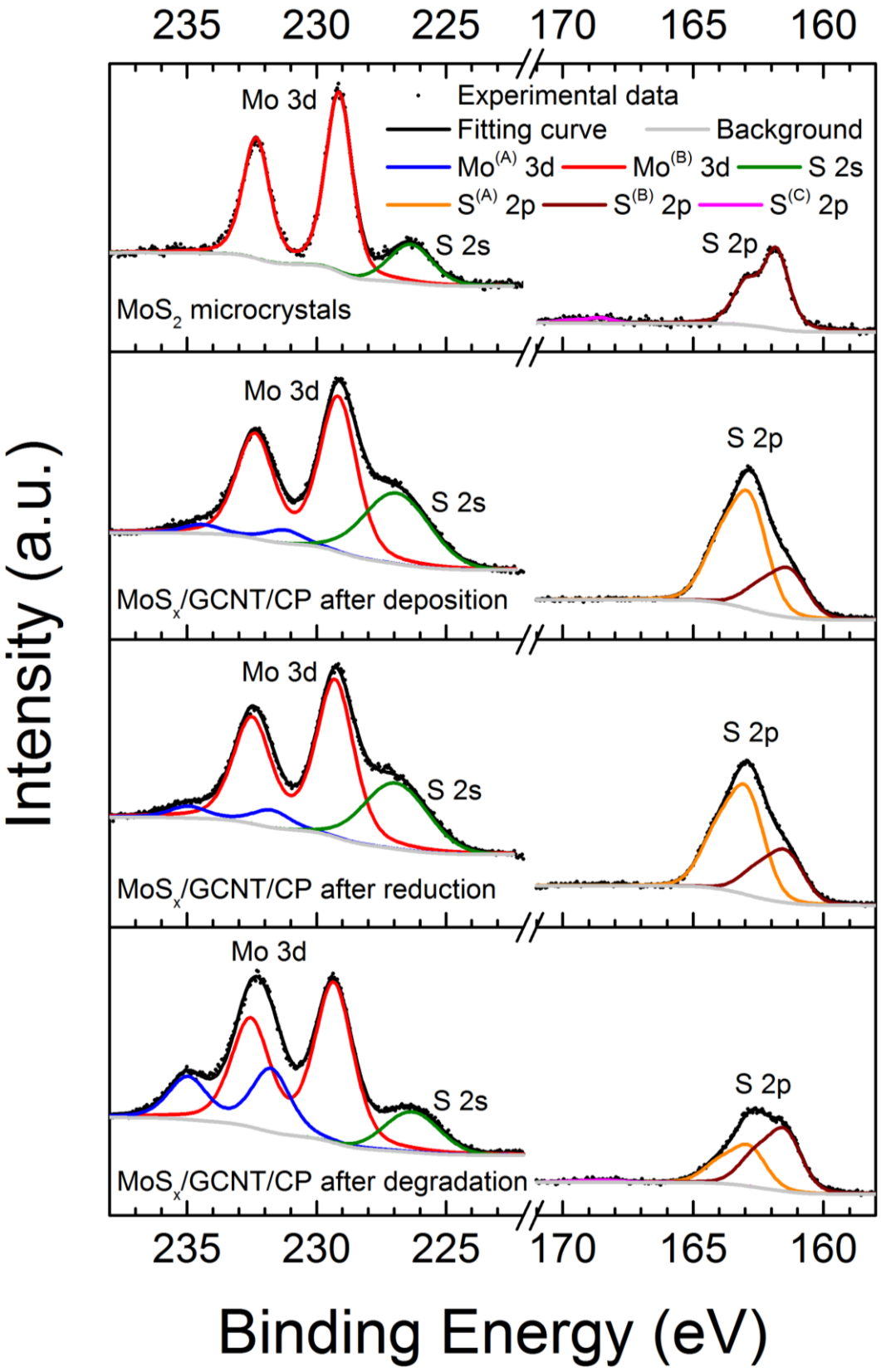


Figure 5-9. XPS high resolution scans in Mo 3d and S 2p regions of the MoS_2 microcrystals and the MoS_x/GCNT/CP electrode after MoS_x deposition, after reductive activation and after degradation test.

As expected from crystalline MoS_2 spectra, the Mo 3d and S 2p main peaks of MoS_2 micro-crystals contain only Mo^{4+} and $S^{(B)}$ states. The present chemical states of MoS_x/GCNT/CP remain nearly the same throughout the electrochemical tests, with the exception of a minor $S^{(C)}$ peak appears after the degradation test. The XPS spectra are dominated by $Mo^{(A)}$, $Mo^{(B)}$, $S^{(A)}$ and $S^{(B)}$ mixed states. The relative composition of the present chemical states, however, varies among different sample conditions. A detailed report of relative stoichiometry of all four samples can be found in Table 5-5.

Table 5-5. Detailed stoichiometry analysis of the present chemical states in the MoS_x/GCNT/CP electrode after various stages of electrochemical evaluation.

	Relative stoichiometry with respect to total Mo						**Experimentally determined formula (including unknown oxygen composition O_y)**
	S_{total}	$S^{(A)}$	$S^{(B)}$	$S^{(C)}$	$Mo^{(A)}$	$Mo^{(B)}$	
MoS_2 microcrystals	2 (*)	0 (**)	1.87	0.13	0 (**)	1	$Mo^{(B)}\,S^{(B)}_{1.87}\,S^{(C)}_{0.13}\,O_y$ (MoS_2O_y)
MoS_x/GCNT/CP after deposition	3.35	2.36	0.99	0 (**)	0.08	0.92	$Mo^{(A)}_{0.08}\,Mo^{(B)}_{0.92}\,S^{(A)}_{2.36}\,S^{(B)}_{0.99}\,O_y$ ($MoS_{3.35}O_y$)
MoS_x/GCNT/CP after reductive activation	3.02	2.04	0.99	0 (**)	0.10	0.90	$Mo^{(A)}_{0.10}\,Mo^{(B)}_{0.90}\,S^{(A)}_{2.04}\,S^{(B)}_{0.99}\,O_y$ ($MoS_{3.02}O_y$)
MoS_x/GCNT/CP after degradation	1.50	0.58	0.89	0.03	0.28	0.72	$Mo^{(A)}_{0.28}\,Mo^{(B)}_{0.72}\,S^{(A)}_{0.58}\,S^{(B)}_{0.89}\,S^{(C)}_{0.03}\,O_y$ ($MoS_{1.50}O_y$)

(*) S/Mo = 2 by default, assuming a perfect stoichiometry of the reference sample.
(**) Peaks are insignificant to warrant a fitting.

Comparing the stoichiometry of the MoS_x/GCNT/CP sample before and after reductive activation step, we find that the relative stoichiometry of Mo states remains nearly unchanged. Total S/Mo ratio, however, decreases from a sulfur-rich ratio of 3.35 to 3.02, which is close to the nominal formula of MoS_3. This decrease in sulfur content comes from the higher binding energy $S^{(A)}$ state. A small fraction of sulfur is lost in the activation process, probably in the form of soluble S^{2-}.

Comparing the stoichiometry of the MoS_x/GCNT/CP sample before and after the degradation test, we find that Mo is partially oxidized to $Mo^{(A)}$ state, which now constitutes 28% of total Mo content. Total S/Mo ratio decreases significantly from 3.02 to 1.50. The decrease once again mainly comes from the $S^{(A)}$ state. The $S^{(A)}$ state appears to be much less stable than $S^{(B)}$ state during the continuous HER polarization sweeps. The low S/Mo stoichiometry and the enhanced $Mo^{(A)}$ state suggest that MoS_x probably partially converts to molybdenum oxysulfide MoS_xO_y during the stability test.

Researchers sometimes use the S 2p XPS spectrum, especially the $S^{(A)}$ peak, to explain the HER catalytic activity of MoS_x. [72,153] However, we find that S 2p XPS spectrum may not truly reflect the possible catalytic activity of MoS_x materials. Firstly, our MoS_x/GCNT/CP electrode is not active towards HER until the first activation event. The XPS spectra of the electrodes before and after activation, however, are highly similar. The activation process may involve some chemical reduction (such as the conversion of S_2^{2-} to S^{2-} suggested by Hu and co-workers [69]) or bonding rearrangement. However, both S^{2-} and S_2^{2-} can contribute to the $S^{(A)}$ and $S^{(B)}$ peak intensities, depending on their actual local bonding configurations. The conversion of sulfur chemical states, if present, may not necessarily be reflected on the changes of S 2p XPS spectrum. The possible conversion of S_2^{2-} to S^{2-} during the activation process therefore could not be unambiguously verified in our study. Secondly, we find that the $S^{(A)}$ peak intensity may not truly linked to the catalytic activity of MoS_x. The decrease in sulfur content, especially from $S^{(A)}$, is much higher than the loss in the HER catalytic activity, such as from the exchange current density

perspective. We suggest that the active sites may arise from both sulfur states $S^{(A)}$ and $S^{(B)}$, or more likely from the $S^{(B)}$ sites such as terminal S_2^{2-} sites. Nevertheless, as previously mentioned, the S 2p peaks are not exclusively assigned for any specific structural sites. The S 2p spectrum alone, therefore, may not be a reliable prediction of the HER catalytic activity of MoS_x.

5.4.5. Electrochemical evaluations of the MoS_x/CNT/CP electrodes

To have an additional comparison of another high surface area conductive substrate, MoS_x was deposited on ordinary carbon nanotubes grown on carbon paper (without a PECVD growth of graphene). The deposited MoS_x loadings were 1.5, 3, and 4.5 mg cm^{-2}, similar to the MoS_x/GCNT/CP electrodes. The MoS_x/CNT/CP electrodes underwent electrochemical evaluations similar to the MoS_x/GCNT/CP electrodes, including total electrode activity evaluation with polarization curves, intrinsic activity evaluation with the TOF estimation, and stability evaluation.

Figure 5-10 shows the polarization curves and Tafel plots of the MoS_x/CNT/CP electrodes and reference samples. The HER polarization curves of the MoS_x/CNT/CP appear highly similar to those of the MoS_x/GCNT/CP electrodes. The HER catalytic activity of MoS_x deposited on the high surface area conductive substrate of CNT/CP is once again much higher than the MoS_x deposited on low surface area substrates, with early onsets of HER reaction. Parameters for catalytic activity comparison (i.e. Tafel slope, exchange current density, and overpotential at 10 mA cm^{-2}_{geo}) are extracted from the polarization curves and Tafel plots, and summarized in Table 5-6.

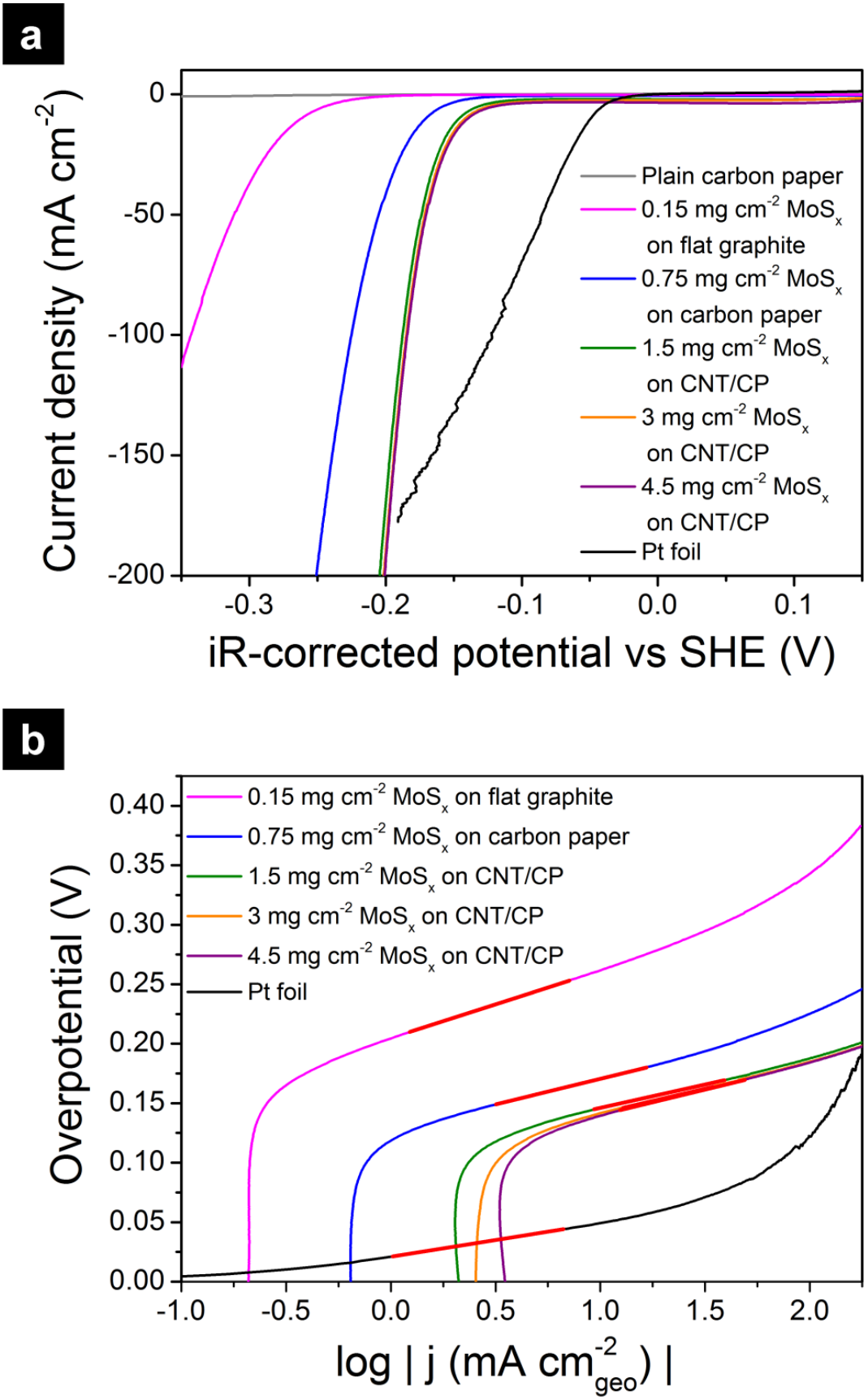


Figure 5-10. HER polarization curves of the MoS_x/CNT/CP electrodes and reference samples presented on (a) linear scale and (b) Tafel plot.

Table 5-6. Extracted parameters from the HER polarization curves and Tafel plots for MoS_x/CNT/CP electrodes.

	Tafel slope	**Exchange current density**	**Overpotential at $\|j\|$ = 10 mA cm^{-2}**
	mV decade^{-1}	mA cm^{-2}	mV
1.5 mg cm^{-2} MoS_x on CNT/CP	39.3	1.91×10^{-3}	146
3 mg cm^{-2} MoS_x on CNT/CP	41.3	3.66×10^{-3}	142
4.5 mg cm^{-2} MoS_x on CNT/CP	42.6	5.14×10^{-3}	141
(Degraded) 3 mg cm^{-2} MoS_x /CNT/CP	45.2	1.73×10^{-3}	169

Similar to the MoS_x/GCNT/CP electrodes, the MoS_x/CNT/CP electrodes exhibit high catalytic activity with low overpotentials of between 141 and 146 mV to obtain a current density of 10 mA cm^{-2}. The required overpotentials are slightly higher (and therefore lower catalytic activity) than those of the MoS_x/GCNT/CP electrodes (e.g. 138 mV in the case of 4.5 mg cm^{-2} MoS_x/GCNT/CP). With the increase of catalyst loading, the Tafel slope slightly increase from 39.3 mV decade^{-1} to 42.6 mV decade^{-1}, similar to the behavior of the MoS_x/GCNT/CP electrodes. The catalytic activity of the MoS_x/CNT/CP electrodes is therefore comparable to that of the MoS_x/GCNT/CP electrodes, and is much higher than the MoS_x deposited on low surface area electrodes of flat graphite and porous carbon paper.

The turnover frequency estimation by cyclic voltametry measurements was performed using the same procedure as for the MoS_x/GCNT/CP electrode. The cyclic voltammetry measurements and capacitance deconvolution through linear fitting for the 3 mg cm^{-2} MoS_x/CNT/CP electrode are shown in Figure 5-11.

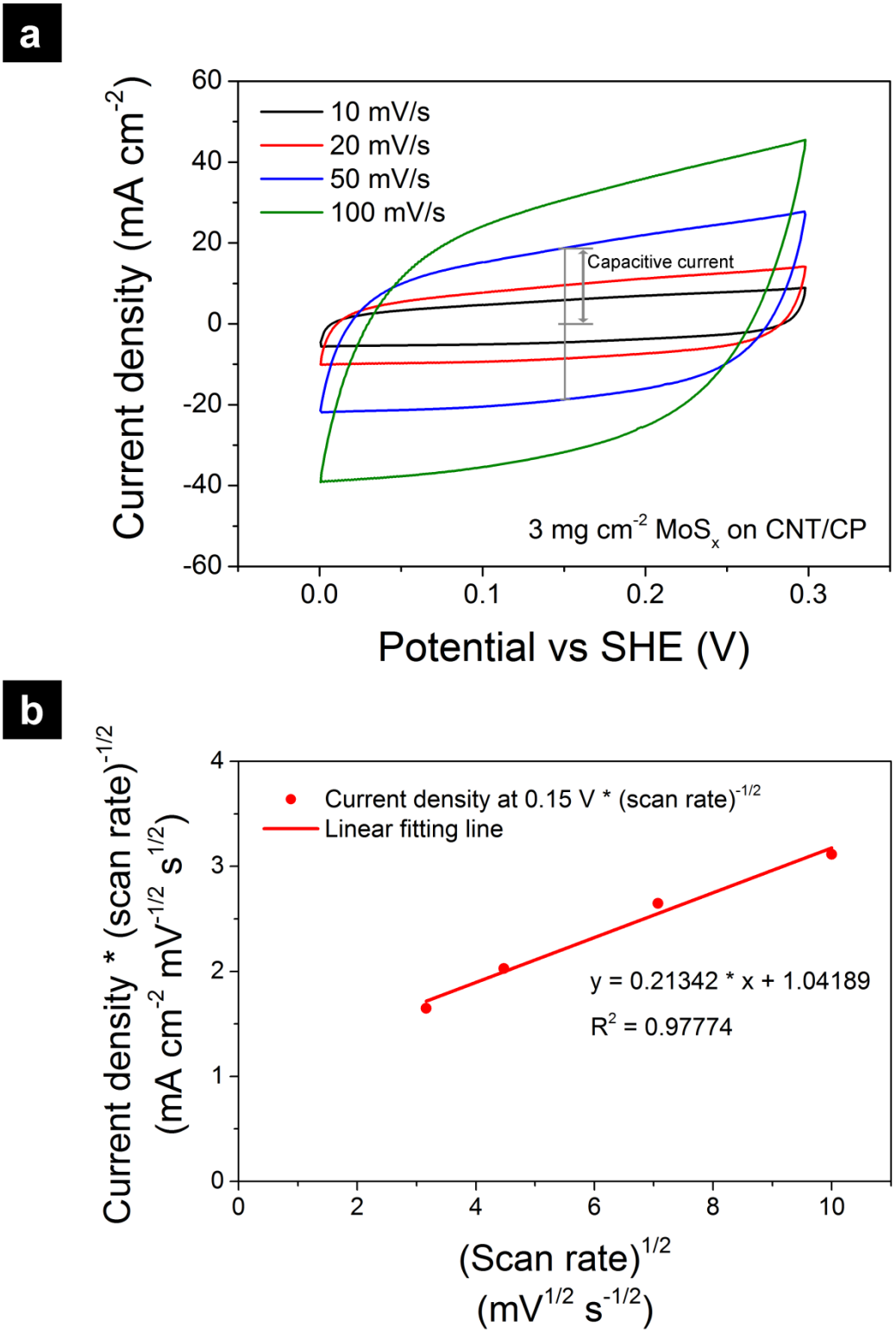


Figure 5-11. Turnover frequency estimation for the 3 mg cm^{-2} MoS_x/CNT/CP electrode. (a) Cyclic voltammetry curves measured in a potential window of 0-0.3 V *vs.* SHE at scan rates of 10, 20, 50 and 100 mV s^{-1}, and (b) deconvolution of the MoS_x/CNT/CP electrode capacitive behavior by a linear fitting of the (capacitive current density)*(scan rate)$^{-1/2}$ *vs.* (scan rate)$^{1/2}$.

Following the TOF estimation procedure, a non-Faradaic capacitance of 0.213 F cm^{-2}, a roughness factor of 3557, and a surface site density of 4.14×10^{18} sites cm^{-2} are estimated for the 3 mg cm^{-2} MoS_x/CNT/CP. At 142 mV overpotential (to obtain a current density of 10 mA cm^{-2}), a per-site TOF of 7.5×10^{-3} s^{-1} is estimated. At 200 mV overpotential (corresponding to a current density of 190 mA cm^{-2}), a per-site TOF of 0.14 s^{-1} is estimated. The estimated TOF values (or intrinsic activity) are comparable to those of the MoS_x/GCNT/CP electrode.

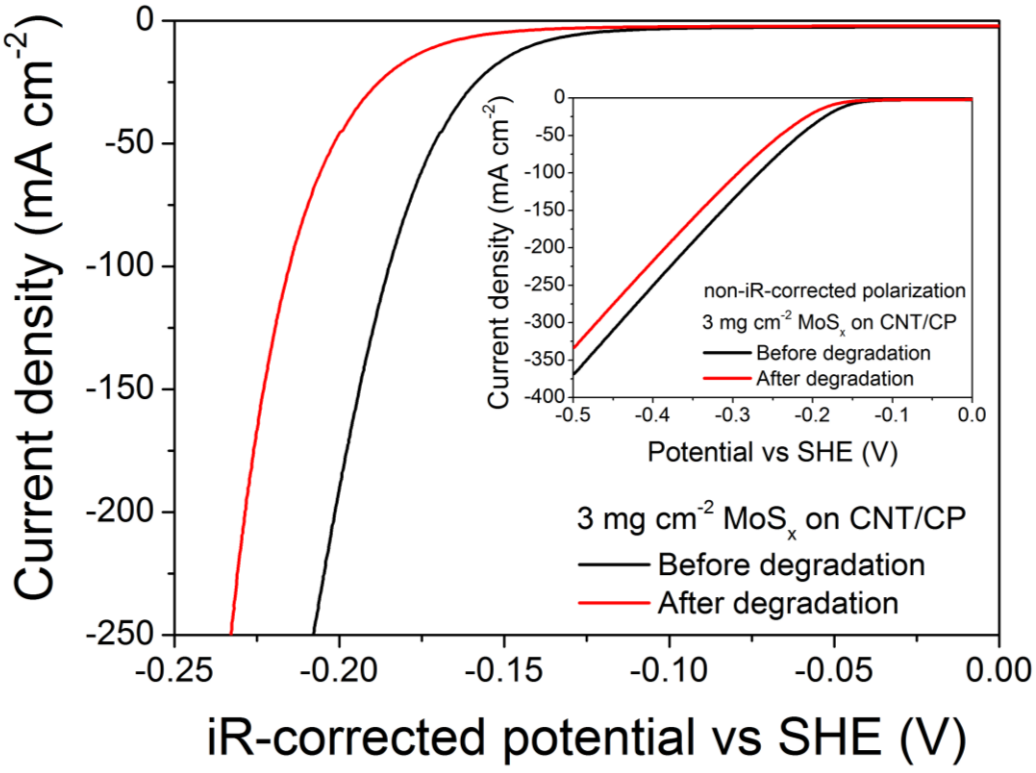


Figure 5-12. Degradation test of the MoS_x/CNT/CP electrode, with HER polarization curves of the electrode before and after degradation presented on iR-corrected and (inset) non-iR-corrected potential scales.

Figure 5-12 shows the polarization curves before and after degradation test of the 3 mg cm^{-2} MoS_x/CNT/CP electrode. After degradation, the overpotential required for 10 mA cm^{-2} increases by 27 mV from 142 mV to 169 mV. The exchange current density decreases from 3.66×10^{-3} to 1.73×10^{-3} (a 47% retention, in contrast to

a 66% retention in the case of MoS_x/GCNT/CP electrode). The better stability demonstrated by MoS_x/GCNT/CP is probably due to the more stable anchoring of MoS_x on the GCNT hybrids with numerous graphene attached on the CNT surface.

5.5. Summary

In this study, we report the deposition of amorphous molybdenum sulfide (MoS_x) on a high specific surface area, porous and conductive electrode made of graphene-carbon nanotube hybrids as the hydrogen evolution reaction catalysts. The deposition of MoS_x on a high specific surface area electrode demonstrates this to be an efficient method to increase the active loading of MoS_x while keeping the Tafel slope close to 40 mV dec^{-1}. The good electronic conductivity inside the electrode plays a crucial role in the enhancement of the MoS_x catalytic activity. With this strategy, we report one of the most active molybdenum sulfide-based HER catalysts to date. The high catalytic activity of MoS_x/GCNT is demonstrated by a required overpotential of as low as 138 mV to obtain a current density of 10 mA cm^{-2}. Tafel slopes of between 39.3 and 41.8 mV dec^{-1} are demonstrated. The catalyst also demonstrates good stability with less than 10% decrease in current density obtained at –0.5 V *vs.* SHE after the degradation test. We also investigate the changes of MoS_x chemical states after the three main steps of the electrochemical evaluation process. We find that the S 2p XPS spectrum may not be a reliable prediction of the catalytic activity of MoS_x. We suggest that cautions should be made when one correlates the XPS spectrum to the HER catalytic activity of MoS_x.

Chapter 6 : Amorphous Molybdenum Sulfide on Graphene-Carbon Nanotube hybrids as supercapacitor electrode materials

6.1. Introduction

As discussed in section 1.4.2, crystalline molybdenum disulfide MoS_2 has gained significant research attention recently as a supercapacitor electrode material, [75,85,88-91] due to its higher ionic conductivity than metal oxides and its higher specific capacitance than graphite. [75] On the other hand, little attention has been paid to its amorphous form, despite many advantageous merits of amorphous molybdenum sulfide. The advantageous properties of amorphous molybdenum sulfide include high ion diffusion coefficient, high density of electro-active defect sites, and benign synthesis conditions. We, therefore, propose amorphous molybdenum sulfide as a new supercapacitor electrode material. Molybdenum sulfide materials in general, however, have low electronic conductivity, [75] which could be detrimental to the specific capacitance and high charge/discharge rate performance. Deposition of molybdenum sulfide on high surface area conductive supports is an effective strategy to enhance the electron transport towards the electro-active sites and therefore maximize the electrode capacitance and high power performance.

In Chapter 5, we demonstrate the deposition of amorphous molybdenum sulfide (MoS_x) on a high surface area, porous and conductive support of graphene-carbon nanotube hybrids (GCNT) grown directly on carbon paper. The composite nanostructure demonstrates that the deposition of MoS_x on the GCNT hybrids effectively enhances the catalytic activity of MoS_x, thanks to the enhanced electron transport inside the electrode. The porous structure of both GCNT and carbon paper current collector can also facilitate the mass transport inside the electrode. The same approach is, therefore, believed to enhance the supercapacitive properties of MoS_x.

In this chapter, MoS_x is deposited on the GCNT hybrids, as described in sections 2.1.3 and 5.2, and is further investigated for supercapacitive properties. The GCNT is hypothesized to enhance the capacitance and high charge/discharge rate performance of MoS_x by effectively enhancing electron transport and mass transport with its high surface area, conductive and porous nanostructure. As a comprehensive physical characterization of the MoS_x/GCNT/CP electrode has already been provided in section 5.3, physical characterization is not further discussed in this chapter. The remaining of this chapter is devoted to the electrochemical evaluations of the MoS_x/GCNT hybrids as supercapacitor electrode materials.

6.2. Electrochemical evaluations of the MoS_x/GCNT hybrids as supercapacitor electrode materials

After MoS_x had been electrodeposited on conductive substrates and underwent the reductive activation as described in detail in section 2.1.3, the MoS_x-deposited electrodes were transferred to a three-electrode electrochemical cell

containing an 1 M Na_2SO_4 electrolyte solution for supercapacitor electrochemical evaluations. The detailed experimental procedure for electrochemical evaluations was provided in section 2.3.3.

Supercapacitive properties of amorphous molybdenum sulfide were studied using the three-electrode electrochemical cell setup. The specific capacitance of materials was measured through two methods, namely cyclic voltammetry and galvanostatic charge/discharge. Both cyclic voltammetry and galvanostatic charge/discharge experiments were performed in a potential window of –0.5 V to 0.3 V *vs.* SHE. Electrochemical impedance spectroscopy (EIS) was used to study the idealistic capacitive behavior of the materials. EIS was measured at –0.1 V *vs.* SHE in the frequency range of 10 kHz to 0.01 Hz with an AC perturbation voltage of 5 mV. Lastly, a degradation test using galvanostatic charge/discharge was used to examine the electrochemical stability of the materials. The degradation test was performed with 500 galvanostatic charge/discharge cycles at a charge/discharge rate of 5 A g^{-1}.

For comparison purposes, MoS_x was deposited on a high specific surface area conductive support of GCNT hybrids on carbon paper (MoS_x/GCNT/CP) and on a simple porous carbon paper substrate (MoS_x/Carbon paper). For both samples, the loading of MoS_x was 3 mg cm^{-2}. A bare GCNT/CP support (without any MoS_x deposited) was also prepared for reference purposes.

6.2.1. Specific capacitance evaluation with cyclic voltammetry

Figure 6-1a shows the cyclic voltammograms of MoS_x/GCNT/CP performed at scan rates of 10, 20, 50 and 100 mV s^{-1}. For reference purposes, the cyclic

voltammograms of bare GCNT/CP support and of MoS_x/Carbon paper were also recorded. However, for a clearer presentation, only the cyclic voltammograms performed at a scan rate of 20 mV s^{-1} are plotted for these two reference samples. It should be noted that, whilst the bare GCNT/CP sample does not contain any MoS_x, in order to present the overall capacitive contribution of the GCNT/CP support, the cyclic voltammograms of the bare GCNT/CP support are normalized for the MoS_x weight assuming a same loading as of the MoS_x/GCNT/CP electrode. The cyclic voltammograms of MoS_x/GCNT/CP appear *pseudo*-rectangular. The *pseudo*-rectangular shape is retained even at a high scan rate of 100 mV s^{-1}, which suggests good high-rate capacitive responses. The MoS_x/GCNT/CP electrode shows much higher current densities than those of the GCNT/CP support and MoS_x/Carbon paper electrode. The specific capacitance of MoS_x/GCNT/CP is calculated as: [154,155]

$$C_s = \frac{\int i(E)dE}{2mv\Delta E} \quad (6\text{-}1)$$

where C_s is the gravimetric specific capacitance of MoS_x/GCNT/CP (in F g^{-1}), $i(E)$ is the instantaneous current response (in A), m is the MoS_x loading (in gram), v is the scan rate (in V s^{-1}), ΔE is the scanned potential window of 0.8 V. $\int i(E)dE$ is the integral area enclosed by the cyclic voltammograms.

The calculated gravimetric specific capacitances of electrodes based on cyclic voltammetry response are summarized in Figure 6-1b. MoS_x/GCNT/CP shows a gravimetric specific capacitance of 194 F g^{-1} at the scan rate of 10 mV s^{-1} and retains a gravimetric specific capacitance of 111 F g^{-1} even at a high scan rate of 100 mV s^{-1}. The capacitive contribution from the GCNT/CP support to the total capacitance of the MoS_x/GCNT/CP is minimal (e.g. 8.2 F g^{-1} at the scan rate of 10 mV s^{-1}).

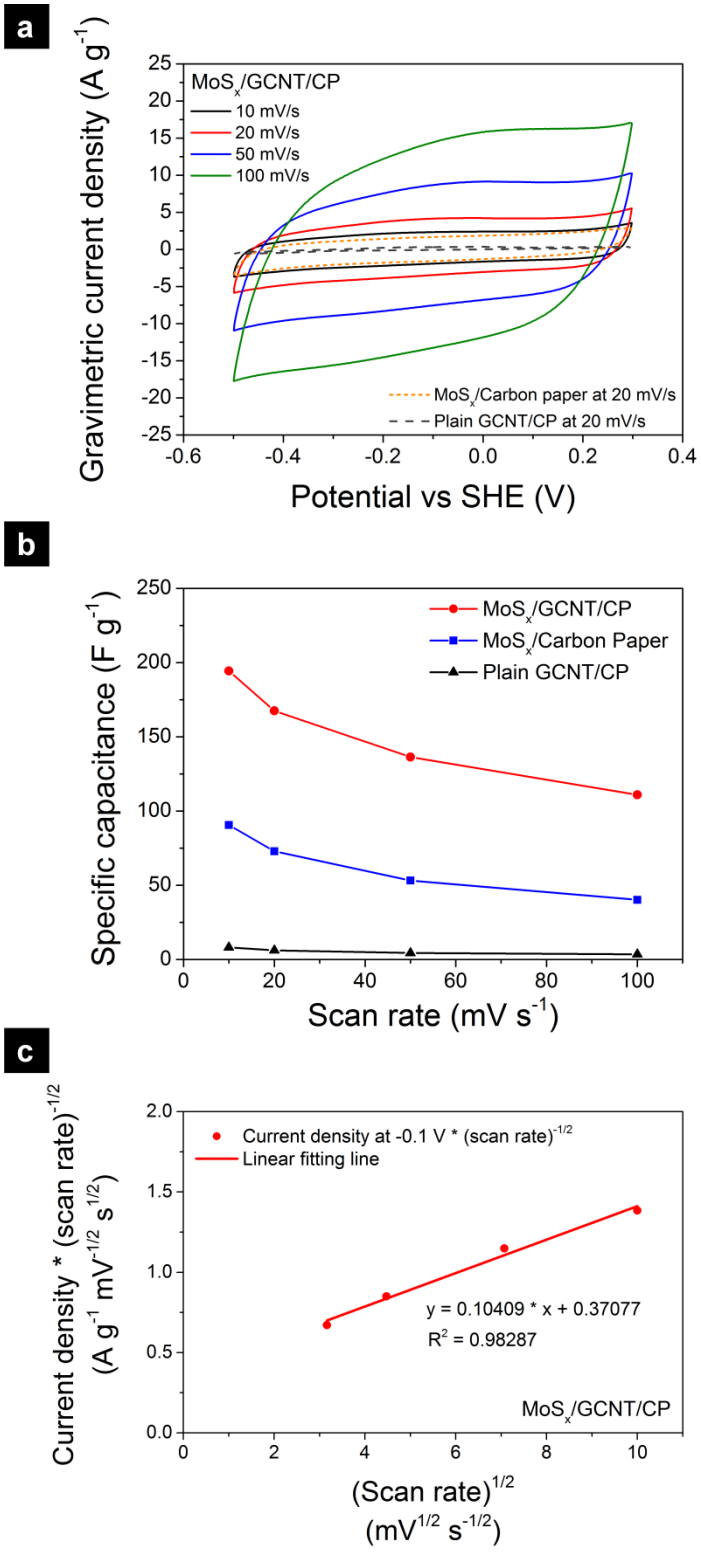


Figure 6-1. Supercapacitive performance of electrodes assessed by cyclic voltammetry. (a) Cyclic voltammograms of the MoS_x/GCNT/CP electrode at different scan rates from 10 mV s^{-1} to 100 mV s^{-1}, and those of the bare GCNT/CP support and MoS_x/Carbon paper electrode at a 20 mV s^{-1} scan rate. (b) The dependence of electrode specific capacitance on scan rate. (c) The deconvolution of capacitive behavior of the MoS_x/GCNT/CP electrode using a linear fitting method.

The MoS_x/Carbon paper electrode shows much lower gravimetric specific capacitances than those of the MoS_x/GCNT/CP electrode. The MoS_x/Carbon paper electrode shows a capacitance of 91 F g^{-1} at the scan rate of 10 mV s^{-1} and a capacitance of 40 F g^{-1} at the scan rate of 100 mV s^{-1}. The reported capacitances are 2-3 times lower than those of the MoS_x deposited on high surface area GCNT/CP support. The capacitive enhancement in MoS_x/GCNT/CP over MoS_x/Carbon paper is probably caused by a better dispersion of MoS_x and a higher electrode conductivity in MoS_x/GCNT/CP, resulted from a much higher specific surface area of GCNT/CP compared to a simple porous carbon paper. The deposition of MoS_x on a high specific surface area conductive support enhances the electrode conductivity and therefore promotes electrochemical processes on MoS_x.

Although the cyclic voltammograms of MoS_x/GCNT/CP appear *pseudo*-rectangular, the gravimetric specific capacitance of MoS_x/GCNT/CP is scan-rate dependent, as shown in Figure 6-1b. The result suggests that the supercapacitive behavior of the MoS_x/GCNT/CP electrode is not purely non-Faradaic, but instead a mixed behavior of Faradaic and non-Faradaic processes. The capacitive current density measured at –0.1 V of the cyclic voltammograms of the MoS_x/GCNT/CP electrode does not scale linearly with the scan rate. It was suggested that the current density scales linearly with scan rate in a pure non-Faradaic process, and scales linearly with the square root of the scan rate in a pure Faradaic process. [74,151] In order to deconvolute the contributions from non-Faradaic and Faradaic processes to the total capacitive behavior, we follow the method proposed by Díaz *et al.* [152] In their

method, the current density j measured on the cyclic voltammograms can be described as a summation of two processes:

$$j = k_1 v + k_2 v^{1/2} \quad (6\text{-}2)$$

where v is the scan rate, k_1 and k_2 are scan-rate independent constants representing the contributions from non-Faradaic and Faradaic processes. By rearranging the equation to

$$j v^{-1/2} = k_1 v^{1/2} + k_2 \quad (6\text{-}3)$$

and performing a linear fitting for $jv^{-1/2}$ versus $v^{1/2}$, the individual capacitive contributions can be estimated. At the particular measured potential, a scan-rate independent non-Faradaic capacitance of k_1 and a scan-rate dependent Faradaic capacitance of $k_2 v^{-1/2}$ are determined. The capacitive current density readings (a half of the anodic-cathodic current density differences) at –0.1 $V_{vs.\ SHE}$ are extracted from the cyclic voltammograms of the MoS_x/GCNT/CP electrode. The linear fitting is shown in Figure 6-1c. From the linear fitting, at the potential of –0.1 V, the MoS_x/GCNT/CP electrode has a non-Faradaic capacitance of 104 F g^{-1} and a scan-rate dependent Faradaic capacitance of 371 × $v^{-1/2}$ F g^{-1} (e.g. 117 F g^{-1} at a scan rate of 10 mV s^{-1} and 37 F g^{-1} at a scan rate of 100 mV s^{-1}). The Faradaic capacitance contribution is significant at slow scan rates. It should be noted that the calculated total capacitance is an instantaneous capacitance at –0.1 V, and can be slightly different from the average capacitance measured for the full potential window.

6.2.2. Specific capacitance evaluation with galvanostatic charge/discharge

The supercapacitive performance of MoS_x/GCNT/CP can also be characterized by the galvanostatic charge/discharge test, as shown in Figure 6-2.

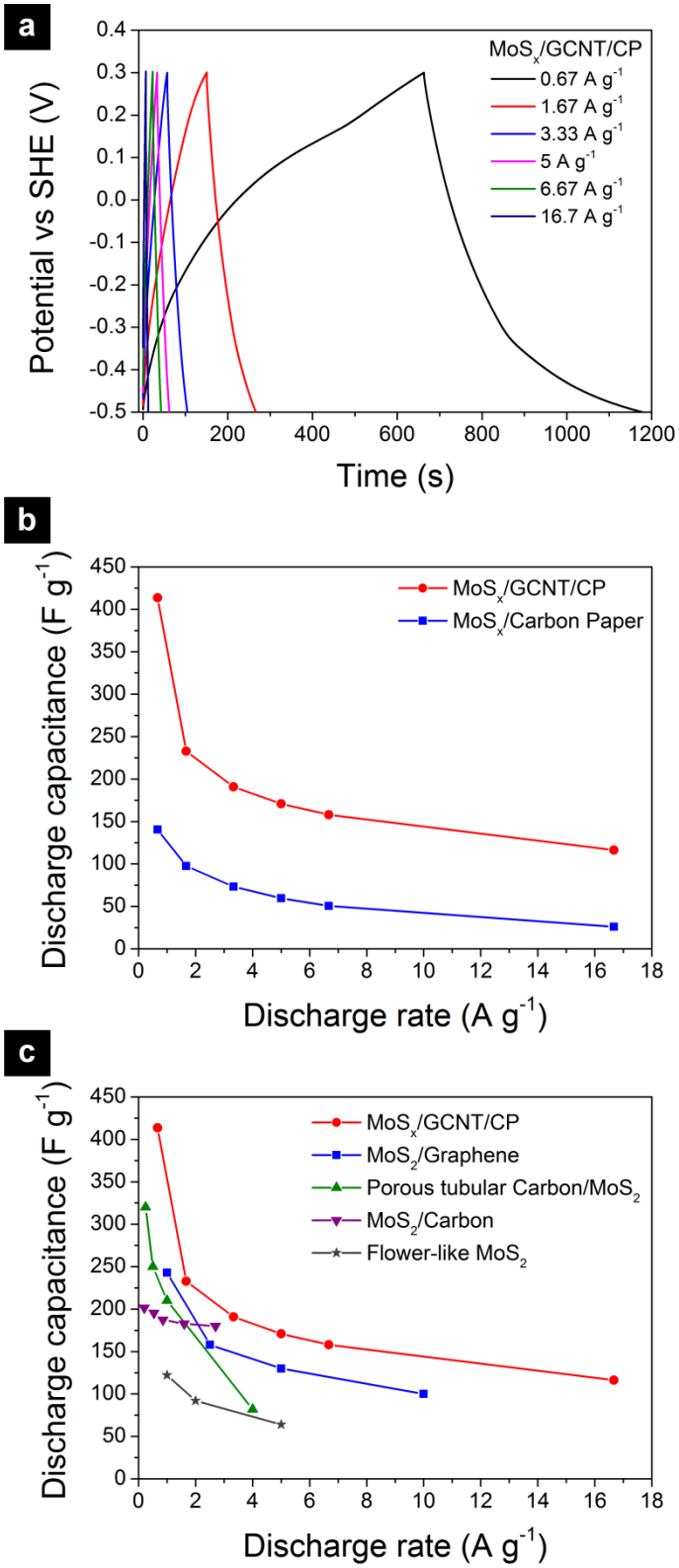


Figure 6-2. Supercapacitive performance of electrodes assessed by galvanostatic charge/discharge test. (a) Charge/discharge curves of the MoS_x/GCNT/CP electrode performed at different charge/discharge rates from 0.67 A g^{-1} to 16.7 A g^{-1}. (b) The dependence of electrode specific capacitance on charge/discharge rate. (c) A comparison of the discharge capacitance of MoS_x/GCNT/CP with crystalline MoS_2-based electrode materials reported in the literature.

Figure 6-2a shows the galvanostatic charge/discharge curves at different charge/discharge rates, from 0.67 A g^{-1} to 16.7 A g^{-1}. The charge/discharge curves are *pseudo*-triangular at a low charge/discharge rate of 0.67 A g^{-1} and become more symmetric and triangular at higher charge/discharge rates. The gravimetric specific discharge capacitance of MoS_x/GCNT/CP based on charge/discharge curves can be calculated as following: [155]

$$C_s = \frac{i\Delta t}{m\Delta E} \tag{6-4}$$

in which C_s is the gravimetric specific discharge capacitance of MoS_x/GCNT/CP (in F g^{-1}), i is the galvanostatic discharge rate (in A), Δt is the discharge time (in s), m is the MoS_x loading (in gram), ΔE is the charge/discharge potential window of 0.8 V.

The calculated gravimetric specific discharge capacitance of electrodes based on galvanostatic charge/discharge responses is summarized in Figure 6-2b. The MoS_x/GCNT/CP electrode demonstrates a discharge capacitance of 414 F g^{-1} at a constant discharge rate of 0.67 A g^{-1}. The MoS_x/GCNT/CP electrode retains a high discharge capacitance of 116 F g^{-1} even at a high discharge rate of 16.7 A g^{-1}. Similar to the cyclic voltammetry experiments, the discharge capacitance is lower at higher discharge rates. This is due to the slower diffusion-controlled response in Faradaic processes. Similar to the cyclic voltammetry experiments, the MoS_x/Carbon paper electrode once again shows much lower specific capacitances than those of the MoS_x/GCNT/CP electrode, with capacitances of 140 F g^{-1} and 26 F g^{-1} at discharge rates of 0.67 A g^{-1} and 16.7 A g^{-1}, respectively. The specific capacitance can also be presented in term of volumetric specific capacitance. The MoS_x/GCNT forest thickness (excluding the carbon paper substrate) is approximately 50 μm. With the

MoS_x loading of 3 mg cm^{-2}, the average density of the material is estimated at 0.6 g_{MoSx} cm^{-3}. The low density of the material is due to the high porosity, which has not been optimized for the volumetric specific capacitance. The volumetric specific capacitance can be converted directly from the gravimetric specific capacitance using the density as the conversion factor. For example, the gravimetric specific capacitance of 414 F g^{-1} at the discharge rate of 0.67 A g^{-1} can be converted to 248 F cm^{-3}. Nevertheless, as the porosity of material has not been optimized for high volumetric specific capacitance, the converted value may be sub-optimal.

With a specific capacitance of 414 F g^{-1} obtained at a discharge rate of 0.67 A g^{-1}, the MoS_x/GCNT/CP electrode demonstrates a significant improvement in specific capacitance over that of carbon-based supercapacitor electrode materials. [3,156] Although the demonstrated capacitance is lower than the best-in-class capacitance demonstrated by other materials such as hydrous ruthenium oxide ($RuO_2 \cdot xH_2O$), [78,157] amorphous MoS_x has the advantages of low material cost and simple room-temperature synthesis. The high cost of precious metal in RuO_2 has been preventing the material from practical applications despite the ultra-high supercapacitive performance. Figure 6-2c shows a comparison of discharge capacitance of the MoS_x/GCNT/CP electrode with examples of crystalline MoS_2-based electrode materials reported in the literature, including MoS_2/graphene, [90] porous tubular carbon/MoS_2, [86] MoS_2/carbon composite, [158] and flower-like MoS_2 nanospheres. [159] The MoS_x/GCNT/CP electrode consistently shows better high discharge rate capacitance than the crystalline MoS_2 materials, in which their capacitances decrease rapidly at higher discharge current densities. The higher capacitance at high

discharge rates of MoS_x/GCNT/CP electrode could be due to the faster ion diffusion in MoS_x as compared to crystalline MoS_2 and/or the good electron and electrolytic ion transport in the MoS_x/GCNT/CP electrode.

Table 6-1 provides a comparison for the specific capacitance of the MoS_x/GCNT/CP against other representative supercapacitor materials reported in the literature. Due to the large variety of specific material approaches, the specific capacitance of materials other than MoS_x and MoS_2-based materials are presented by the typical range of specific capacitance reported in the literature. Information on activated carbon, CNT, graphene, RuO_2, MnO_2, and conductive polymers was collected from references [76,160].

Table 6-1. Comparison for the specific capacitance of the MoS_x/GCNT/CP against the reported literature.

Electrode material	**Typical range of specific capacitance** ($F\ g^{-1}$)	**References**
Activated carbon	115–340	[161-163]
Purified CNTs	20–80	[164,165]
Graphene, reduced Graphene Oxide	135–205	[77,166]
Hydrous RuO_2	720–1300	[78,167-169]
MnO_2	195–350	[170-172]
Conductive polymers	230–1030	[173-178]
MoS_x/GCNT/CP	414 (at 0.67 A g^{-1})	This study
MoS_2/Graphene	243 (at 1 A g^{-1})	[90]
Porous tubular carbon/MoS_2	250 (at 0.5 A g^{-1})	[86]
MoS_2/Carbon	195 (at 0.54 A g^{-1})	[158]
Flower-like MoS_2	122 (at 1 A g^{-1})	[159]
1T-MoS_2	~ 100	[179]

Coulombic efficiency during charge/discharge cycles of the MoS_x/GCNT/CP electrode starts at relatively modest values between 77% and 87% – depending on the charge/discharge rate – during the first charge/discharge cycle. However, the Coulombic efficiency of the electrode quickly reaches above 97% after 10 charge/discharge cycles, and above 99% after 25 charge/discharge cycles at 5 A g^{-1}.

6.2.3. Electrochemical Impedance Spectroscopy measurement

To further test the idealistic capacitive behavior of the MoS_x/GCNT/CP electrode, electrochemical impedance spectroscopy was performed at –0.1 V. The EIS Nyquist plot is shown in Figure 6-3. EIS spectrum of the MoS_x/GCNT/CP electrode shows a nearly vertical plot, which suggests a nearly idealistic capacitive behavior of the electrode.

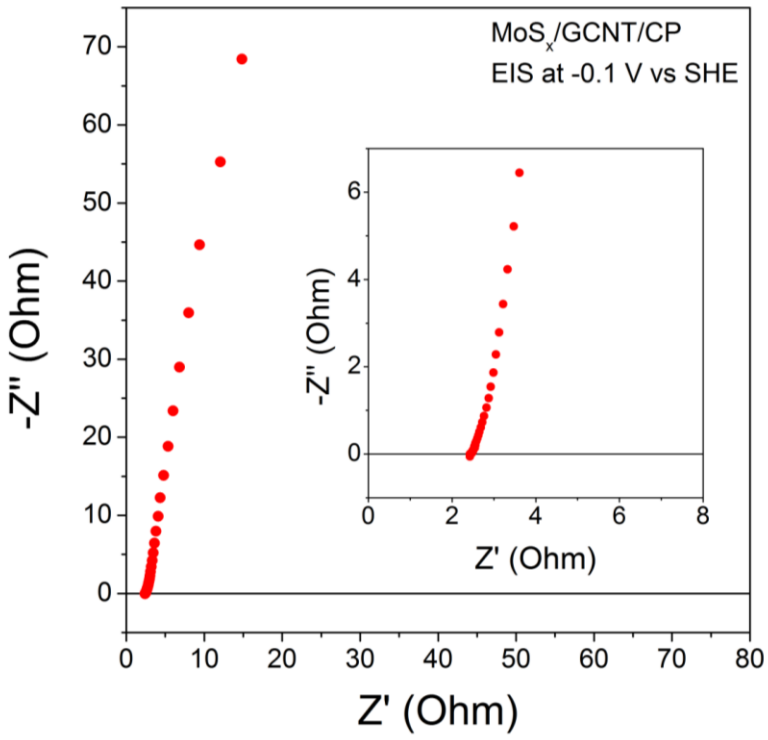


Figure 6-3. Electrochemical impedance spectrum of the MoS_x/GCNT/CP electrode measured at –0.1 V, and (inset) the closed up view of the spectrum at high frequency region.

6.2.4. Electrochemical stability evaluation

The electrochemical stability of the MoS_x/GCNT/CP electrode was assessed by a degradation test performed with 500 galvanostatic charge/discharge cycles at a high charge/discharge current density of 5 A g^{-1}. The degradation of the electrode's discharge capacitance during the degradation test is reported in Figure 6-4.

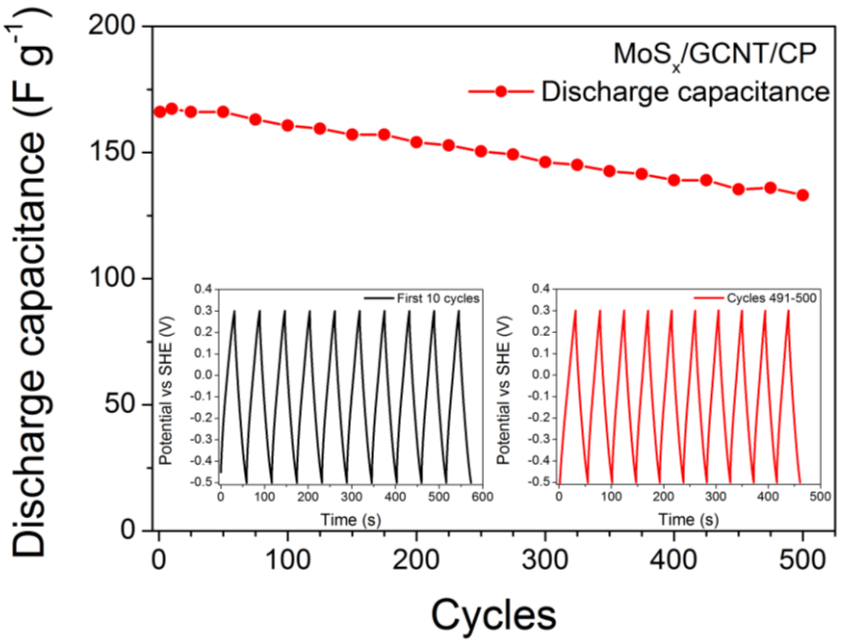


Figure 6-4. Degradation test of the MoS_x/GCNT/CP electrode performed by 500 charge/discharge cycles at 5 A g^{-1}, showing the degradation of electrode specific capacitance during the test, with (insets) plots of the first and last 10 charge/discharge cycles (time axes are referenced to the beginning of each 10-cycle set).

Figure 6-4 shows that the discharge capacitance of the electrode slowly degrades during the test with an 80% retention of capacitance after 500 charge/discharge cycles. It should be noted that the degradation test was performed at a high charge/discharge rate of 5 A g^{-1}. A high charge/discharge current can potentially degrade the electrode faster than a slow charge/discharge rate due to the quick ions insertion into and extraction from the electrode active materials. Although further optimizations of the electrode will need to be pursued, we consider an 80%

capacitance retention at a high charge/discharge rate of 5 A g^{-1} a good electrochemical stability demonstrated by the MoS_x/GCNT/CP electrode.

6.3. Electrochemical evaluations of the MoS_x/CNT/CP electrode

To have an additional comparison of another high surface area conductive substrate, MoS_x was deposited on ordinary carbon nanotubes grown on carbon paper (without a PECVD growth of graphene) with the same MoS_x loading of 3 mg cm^{-2}. The deposition and electrochemical evaluation processes for the MoS_x/CNT/CP electrode followed the same procedure as for the MoS_x/GCNT/CP and MoS_x/Carbon paper electrodes, including specific capacitance evaluations with cyclic voltammetry and galvanostatic charge/discharge, EIS, and electrochemical stability evaluation.

6.3.1. Specific capacitance evaluation with cyclic voltammetry

Figure 6-5 shows the specific capacitance evaluation for the MoS_x/CNT/CP electrode using the cyclic voltammetry method. Figure 6-5a shows the cyclic voltammograms of MoS_x/CNT/CP electrode performed at scan rates of 10, 20, 50 and 100 mV s^{-1}. Similar to the evaluation for MoS_x/GCNT/CP electrode, the cyclic voltammograms at a scan rate of 20 mV s^{-1} of bare CNT/CP support and of MoS_x/Carbon paper were also included for reference purposes. Similar to the MoS_x/GCNT/CP electrode, the MoS_x/CNT/CP electrode demonstrates *pseudo*-rectangular shaped cyclic voltammograms, even at a high scan rate of 100 mV s^{-1}. The MoS_x/CNT/CP electrode shows much higher current densities than those of the CNT/CP support and of the MoS_x/Carbon paper electrode.

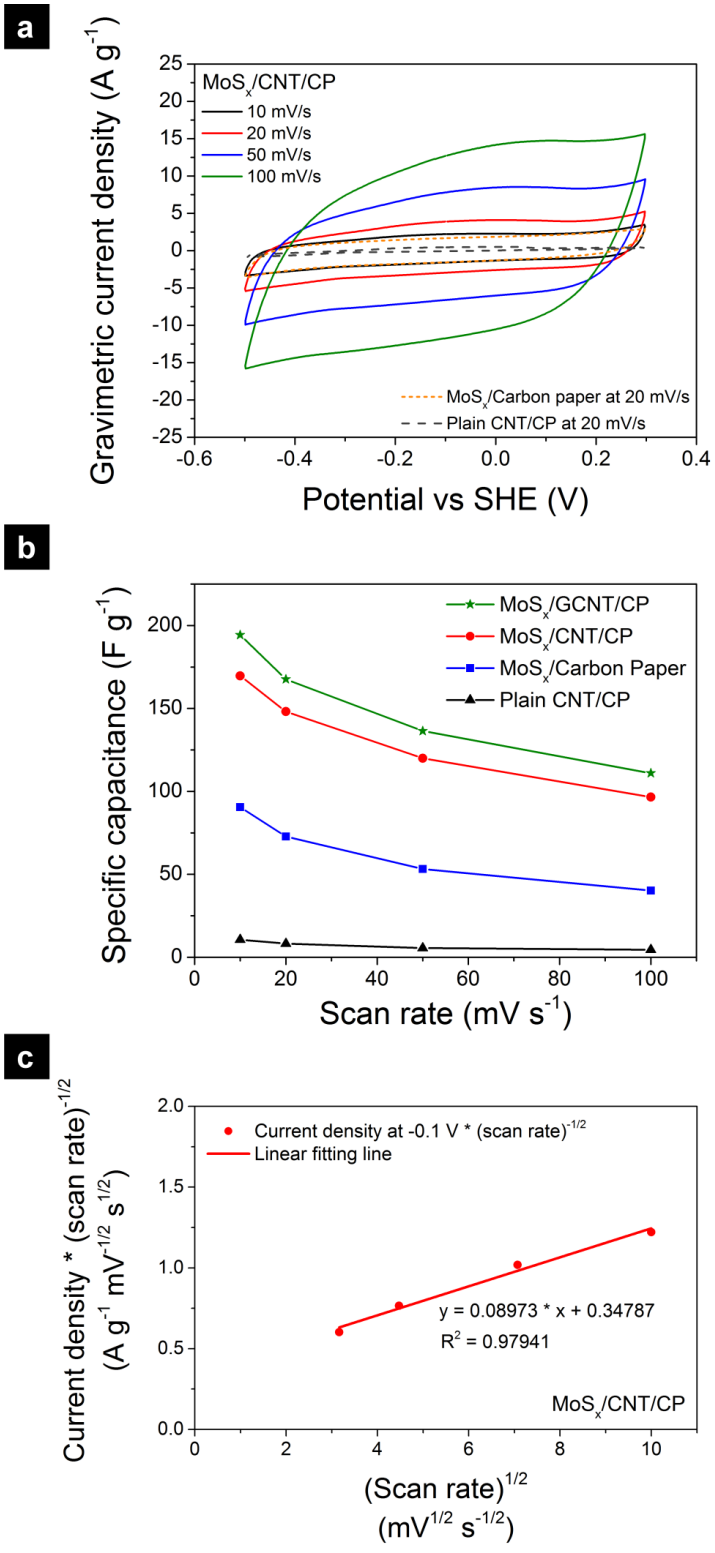


Figure 6-5. Supercapacitive performance of electrodes assessed by cyclic voltammetry. (a) Cyclic voltammograms of the MoS_x/CNT/CP electrode at different scan rates from 10 mV s^{-1} to 100 mV s^{-1}, and those of the bare CNT/CP support and MoS_x/Carbon paper electrode at a 20 mV s^{-1} scan rate. (b) The dependence of electrode specific capacitance on scan rate. (c) The deconvolution of capacitive behavior of the MoS_x/CNT/CP electrode using a linear fitting method.

The gravimetric specific capacitance of MoS_x/CNT/CP electrode is calculated from the cyclic voltammograms, as described in section 6.2.1, and compared to the MoS_x/GCNT/CP, MoS_x/Carbon paper, and bare CNT/CP electrodes as shown in Figure 6-5b. The MoS_x/CNT/CP electrode shows a gravimetric specific capacitance of 170 F g^{-1} at a scan rate of 10 mV s^{-1} and retains a gravimetric specific capacitance of 97 F g^{-1} at a high scan rate of 100 mV s^{-1}. The demonstrated specific capacitance of MoS_x/CNT/CP is ~2-3 times higher than that of the MoS_x/Carbon paper. Similar to the MoS_x/GCNT/CP electrode, the deposition of MoS_x on a high surface area conductive support of CNT/CP effectively enhances the specific capacitance of MoS_x compared to the MoS_x deposited on low surface area support of simple carbon paper. The specific capacitance demonstrated by MoS_x/CNT/CP is ~12.5% lower than that of the MoS_x/GCNT/CP electrode. The slightly lower specific capacitance of the MoS_x/CNT/CP electrode is probably due to sample variations, such as the sample variation in specific surface area of the carbon support.

The supercapacitive behavior of the MoS_x/CNT/CP is deconvoluted for Faradaic and non-Faradaic capacitances using the linear fitting method, as described in section 6.2.1. The linear fitting is shown in Figure 6-5c. From the linear fitting, at the potential of –0.1 V, the MoS_x/CNT/CP electrode has a non-Faradaic capacitance of 90 F g^{-1} and a scan-rate dependent Faradaic capacitance of $348 \times v^{-1/2}$ F g^{-1} (e.g. 110 F g^{-1} at a scan rate of 10 mV s^{-1} and 35 F g^{-1} at a scan rate of 100 mV s^{-1}). The Faradaic capacitance contribution in the MoS_x/CNT/CP electrode is significant at slow scan rates.

6.3.2. Specific capacitance evaluation with galvanostatic charge/discharge

The specific capacitance of MoS_x/CNT/CP electrode is also characterized by the galvanostatic charge/discharge test, as shown in Figure 6-6. Figure 6-6a shows the galvanostatic charge/discharge curves at different charge/discharge rates, from 1.67 A g^{-1} to 16.7 A g^{-1}. Similar to the characteristics demonstrated by the MoS_x/GCNT/CP electrode, the charge/discharge curves are *pseudo*-triangular at a low charge/discharge rate of 1.67 A g^{-1} and become more symmetric and triangular at higher charge/discharge rates. The gravimetric specific discharge capacitance of the MoS_x/CNT/CP electrode is calculated from the galvanostatic charge/discharge curves, following the method described in section 6.2.2. The calculated gravimetric specific discharge capacitance of the MoS_x/CNT/CP electrode is compared to that of the MoS_x/GCNT/CP and MoS_x/Carbon paper electrodes, and shown in Figure 6-6b. The MoS_x/CNT/CP electrode demonstrates a discharge capacitance of 237 F g^{-1} at a constant discharge rate of 1.67 A g^{-1}. The MoS_x/CNT/CP electrode retains a discharge capacitance of 96 F g^{-1} at a high discharge rate of 16.7 A g^{-1}. The reported capacitances of MoS_x/CNT/CP are much higher than those of the MoS_x/Carbon paper electrode (98 F g^{-1} and 26 F g^{-1} at discharge rates of 1.67 A g^{-1} and 16.7 A g^{-1}, respectively). The demonstrated specific capacitance of the MoS_x/CNT/CP is comparable to that of the MoS_x/GCNT/CP electrode, although with slightly lower high-discharge-rate capacitance. The lower capacitance is again probably caused by the specific surface area variation among samples. On the other hand, both the MoS_x/CNT/CP and MoS_x/GCNT/CP electrodes consistently show enhanced specific capacitance compared to the MoS_x deposited on low surface area support of simple

porous carbon paper. The deposition of MoS_x on high specific surface area conductive supports of CNT/CP and GCNT/CP proves to be an effective approach to enhance the specific capacitance of MoS_x.

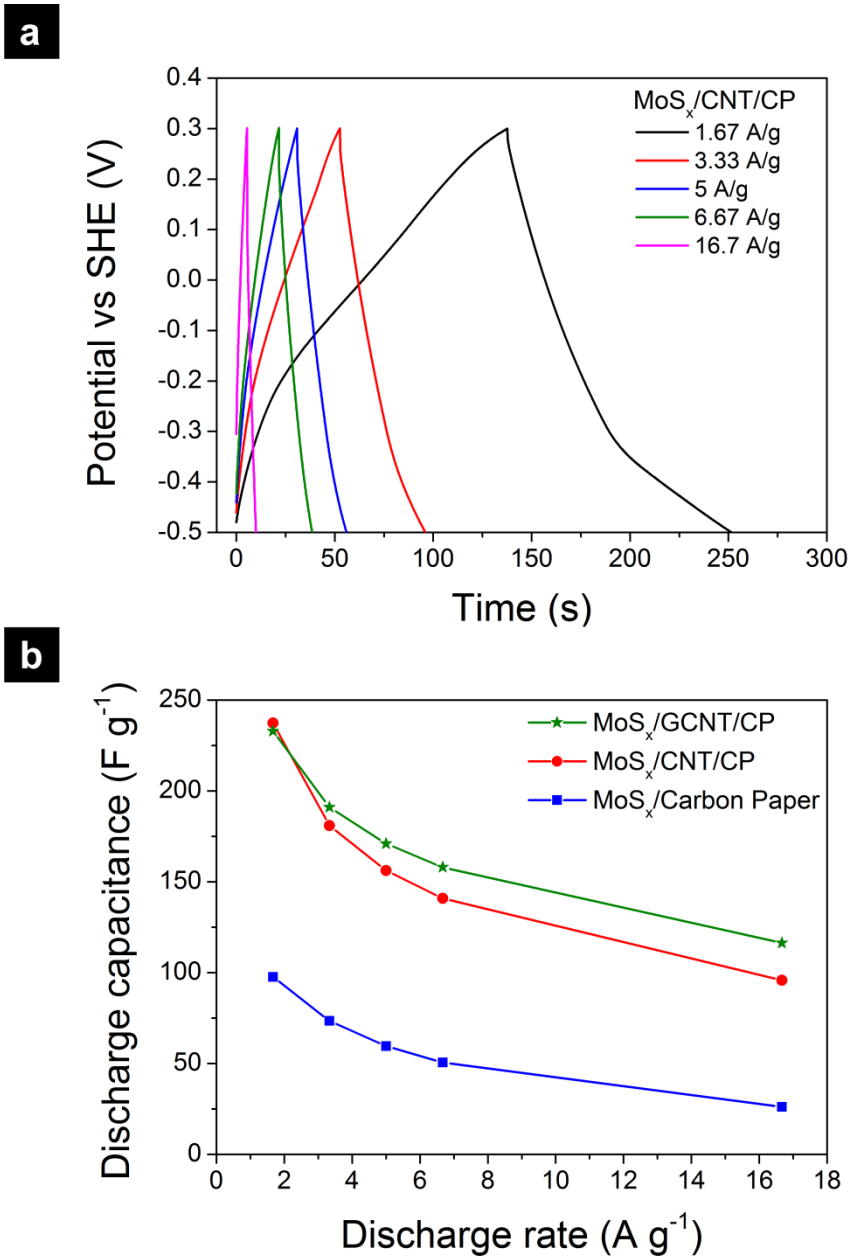


Figure 6-6. Supercapacitive performance of electrodes assessed by galvanostatic charge/discharge test. (a) Charge/discharge curves of the MoS_x/CNT/CP electrode performed at different charge/discharge rates from 1.67 A g^{-1} to 16.7 A g^{-1}. (b) The dependence of electrode specific capacitance on charge/discharge rate.

6.3.3. Electrochemical Impedance Spectroscopy measurement

The idealistic capacitive behavior of the MoS_x/CNT/CP electrode is examined with EIS, measured at –0.1 V. The EIS Nyquist plot is shown in Figure 6-7. EIS spectrum of the MoS_x/CNT/CP electrode shows a nearly vertical plot, which suggests a nearly idealistic capacitive behavior of the electrode.

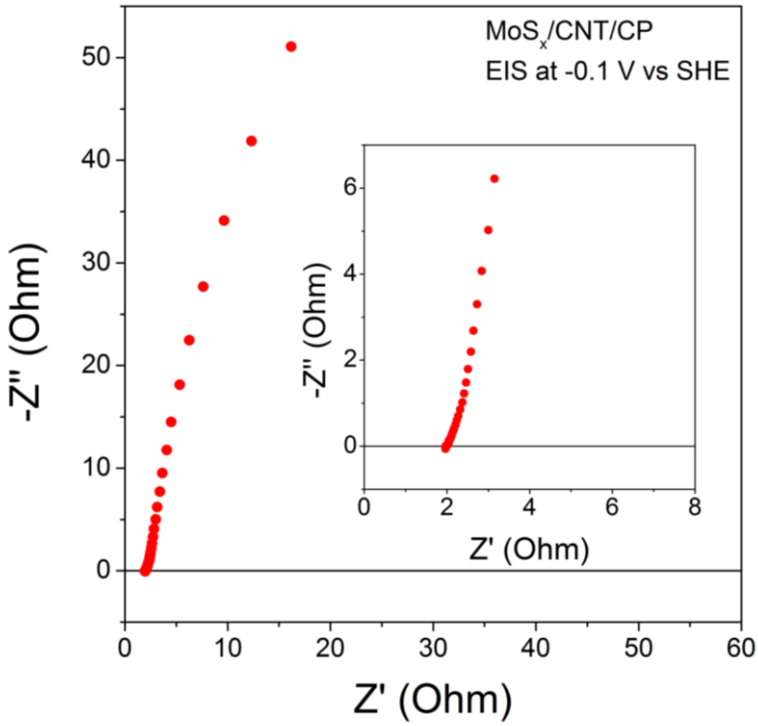


Figure 6-7. Electrochemical impedance spectrum of the MoS_x/CNT/CP electrode measured at –0.1 V, and (inset) the closed up view of the spectrum at high frequency region.

For a better understanding of the electrode interfacial properties, EIS spectra of the MoS_x/GCNT/CP, MoS_x/CNT/CP, and MoS_x/CP electrodes are analyzed with equivalent circuit fitting. The EIS spectra and fitting curves of the electrodes are shown in Figure 6-8. Figure 6-8a-b show the EIS spectra and fitting curves presented in Nyquist plot and Bode plots, respectively. The equivalent circuit used for all

fittings is presented in Figure 6-8c. In this circuit, L_{cab} represents a parasitic inductance caused by connecting cables or instruments. A minor inductive response is observed at the high frequency of ~ 10^4 Hz. R_{ohm} represents the ohmic resistance contributed by the uncompensated electrolyte resistance and internal resistance of electrode. R_{con} and C_{con} represent contact resistance and contact capacitance, respectively. The contact resistance and contact capacitance account for the small arc at high frequency range of ~ 10^3 Hz. R_{ct}, W, and CPE_{dl} represent the charge transfer resistance, Warburg diffusion impedance, and electrical double layer capacitance constant phase element, respectively. R_L and CPE_{ps} are leak resistance and *pseudo*-capacitance constant phase element, respectively. The fitting parameters are summarized in Table 6-2.

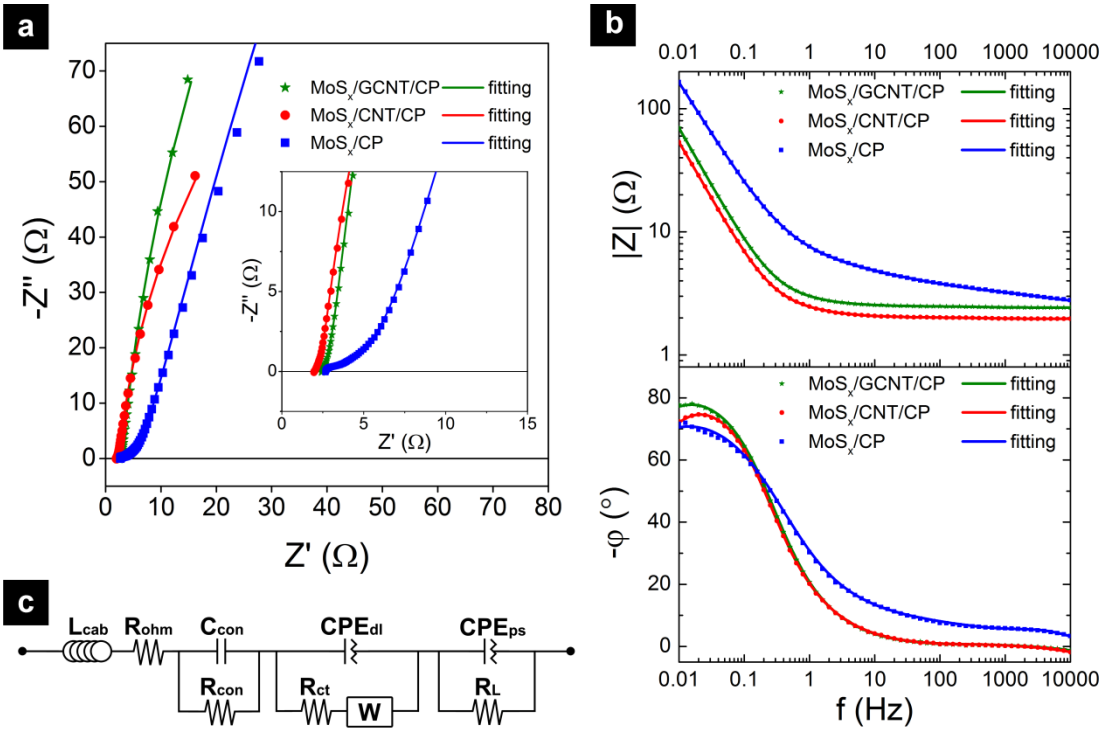


Figure 6-8. EIS spectra and equivalent circuit fittings of the MoS_x/GCNT/CP, MoS_x/CNT/CP, and MoS_x/CP electrodes presented in (a) Nyquist plot and (b) Bode plots. (c) Equivalent circuit used for all fittings in (a, b).

Table 6-2. Equivalent circuit fitting parameters for EIS spectra of the MoS_x/GCNT/CP, MoS_x/CNT/CP, and MoS_x/CP electrodes.

	L_{cab}	R_{ohm}	R_{con}	C_{con}	R_{ct}		W	CPE_{dl}		R_L		CPE_{ps}				
							Y_0	Y_0	n			Y_0	n	equiv. capacitance		
	μH	Ω	mΩ	mF	Ω	Ω cm²	S	mS		Ω	Ω cm²	mS		mF	mF cm⁻²	F g⁻¹
MoS_x/GCNT/CP	0.898	2.43	39.5	6.95	0.647	**0.352**	1.96	**478**	**0.680**	652	355	208	0.959	256	**471**	**157**
MoS_x/CNT/CP	1.021	1.97	34.8	8.60	0.545	**0.371**	19.4	**589**	**0.669**	287	195	253	0.948	321	**472**	**157**
MoS_x/CP	0.861	2.44	181	0.232	8.11	**4.850**	0.366	**102**	**0.299**	1849	1106	70.8	0.874	143	**239**	**80**

Table 6-2 shows that MoS_x deposited on high surface area conductive supports of GCNT/CP and CNT/CP demonstrates a much faster charge transfer kinetic (R_{ct} = 0.352 and 0.371 Ω cm²) compared to MoS_x deposited on carbon paper (R_{ct} = 4.850 Ω cm²). The enhancement of charge transfer kinetic (13.1–13.8 times smaller R_{ct}) is most likely attributed to the effective material dispersion and efficient electron transport towards active sites of MoS_x provided by GCNT/CP and CNT/CP. Similar enhancement in kinetics was also demonstrated in the HER application of these materials. The fast charge transfer is important for the high charge–discharge rate performance of materials. The charge transfer kinetic of MoS_x/GCNT/CP is slightly faster than that of MoS_x/CNT/CP. The order of charge transfer kinetic MoS_x/GCNT/CP > MoS_x/CNT/CP ≫ MoS_x/CP is consistent with the high charge–discharge rate relative performance of these materials, as shown in Figure 6-6b. The equivalent *pseudo*-capacitances of MoS_x/GCNT/CP and MoS_x/CNT/CP are found equal at 157 F g^{-1}, which is almost twice that of the MoS_x/CP. The result is in agreement with the relative capacitances measured by cyclic voltammetry and galvanostatic charge/discharge tests.

6.3.4. Electrochemical stability evaluation

The electrochemical stability of the MoS_x/CNT/CP electrode was assessed by a degradation test performed with 500 galvanostatic charge/discharge cycles at a high charge/discharge current density of 5 A g^{-1}. The degradation of the electrode's discharge capacitance during the degradation test is reported in Figure 6-9. The discharge capacitance of the electrode slowly degrades during the test, with an 86% retention of capacitance after 500 charge/discharge cycles. The degradation behavior is similar to that of the MoS_x/GCNT/CP electrode reported in section 6.2.4.

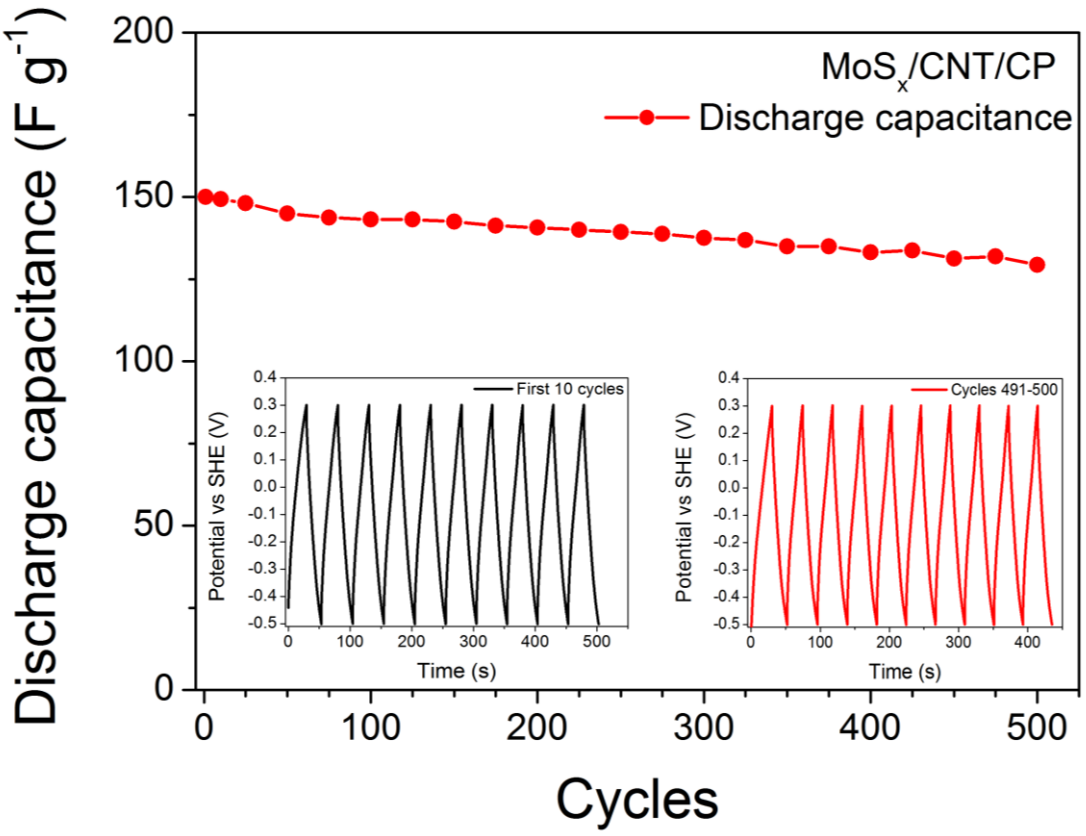


Figure 6-9. Degradation test of the MoS_x/CNT/CP electrode performed by 500 charge/discharge cycles at 5 A g^{-1}, showing the degradation of electrode specific capacitance during the test, with (insets) plots of the first and last 10 charge/discharge cycles (time axes are referenced to the beginning of each 10-cycle set).

6.4. Summary

In this study, we report on the application of amorphous molybdenum sulfide (MoS_x) as the main active material for supercapacitor electrodes. Amorphous MoS_x is easily electrodeposited onto high specific surface area conductive supports of CNT/CP and GCNT/CP at room temperature. The MoS_x/GCNT/CP and MoS_x/CNT/CP electrodes show high specific capacitances even at high discharge rates. The MoS_x/GCNT/CP electrode demonstrates a high discharge capacitance of 414 F g^{-1} at a constant discharge rate of 0.67 A g^{-1} and retains a discharge capacitance of 116 F g^{-1} even at a high discharge rate of 16.7 A g^{-1}. Similarly, the MoS_x/CNT/CP electrode demonstrates a discharge capacitance of 237 F g^{-1} at a constant discharge rate of 1.67 A g^{-1} and retains a discharge capacitance of 96 F g^{-1} at a high discharge rate of 16.7 A g^{-1}. The deposition of MoS_x on high specific surface area conductive supports demonstrates this to be an effective method to enhance the supercapacitive performance of MoS_x. At various discharge rates, 2.4–4.5 fold enhancement in specific capacitance over MoS_x/Carbon paper is demonstrated by the MoS_x/GCNT/CP and MoS_x/CNT/CP electrodes. The MoS_x/GCNT/CP and MoS_x/CNT/CP electrodes also demonstrate good electrochemical stability with ~ 80% retention of capacitance after 500 charge/discharge cycles at a high charge/discharge rate of 5 A g^{-1}. With high specific capacitance and good electrochemical stability, the amorphous MoS_x-deposited GCNT/CP and CNT/CP electrodes are demonstrated to be promising electrode material candidates for supercapacitor applications.

Chapter 7 : 3D reconstruction of porous carbon electrode nanostructures using a FIB-SEM dual beam technique

7.1. Introduction

The electrodes of electrochemical devices, such as PEMFCs, supercapacitors, HER electrodes and lithium ion batteries anodes, are commonly constructed from porous and high surface area carbon nanostructures. The electrodes of these electrochemical devices have complex three dimensional nanostructures with intertwining phases of carbon materials, porous channels, and other active phases, in order to have an extended interfacial area to maximize the device performance. The electrochemical performance of these devices crucially depends on the three dimensional characteristics of the constituent phases. For example, the continuity of the carbon material and the porous channel networks are essential for the electron transports and mass transports inside the electrode, respectively. Besides the continuity, the interconnecting configurations of the porous channels (e.g. a network of narrow and tortuous channels *vs.* a network of wide and straight channels) may also determine the mass transport efficiency of the electrodes. The three dimensional distribution of the active materials and their connections to the conductive carbon supports are deterministic to the active material properties (such as catalytic activity and capacitance).

Whilst these important characteristics of the electrode structures are strictly three dimensional (3D) in essence, currently the most commonly used electron microscopy characterization techniques are two dimensional projections of the structure. Whilst they are very useful in many aspects, the 3D structural information is lost in the process. It is therefore in need of a new experimental method to obtain the full three-dimensional information of the structures.

X-ray computed tomography [180-182] and TEM tomography [183-185] are two example experimental techniques to reconstruct the 3D structures of materials. X-ray computed tomography is, however, more suitable for relatively large microstructures, due to the relatively low resolution limit (e.g. spatial resolutions of 1–10 μm and ≤ 100 nm (or ~ 50 nm [180,182]) are commonly provided by X-ray Micro-computed tomography and X-ray Nano-computed tomography, respectively [181,186]). With these low spatial resolutions, many of the nanostructured details are lost (e.g. ~40 nm carbon black nanoparticles are smaller than the 50 nm resolution limit of X-ray Nano-computed tomography [182]). TEM tomography, on the other hand, can provide very high resolution images, with ~1 nm spatial resolutions. [183,185] Imaging volume examined by TEM tomography is, however, limited by the TEM lamellar thickness in the order of 100 nm. The 100-nm-thick TEM lamellae are not statistically representative for many applications. [182] For example, in PEMFCs, carbon black materials have primary particle diameters of ~ 40 nm and aggregate sizes of 150-200 nm. [187] For electrochemical electrodes, such as in PEMFCs, a spatial resolution of a few nm and an imaging volume of several μm each dimension are therefore a more reasonable compromise between a high resolution imaging and a representative imaging volume.

Recently, the development of high precision focused ion beam (FIB) column and its integration into the SEM instruments provide a versatile platform where both precise sample manipulation and high resolution imaging can be conveniently performed *in vacuo*. The FIB-SEM dual beam tomography method has been used to reconstruct three dimensional structures of materials such as solid oxide fuel cell (SOFC) electrodes [100-103] and PEMFC electrodes. [104-109] The FIB-SEM dual beam tomography method provides a versatility of high resolution imaging by SEM and potentially large imaging volumes, virtually limited only by the practical imaging time available. The FIB-SEM dual beam technique is therefore suitable for the 3D reconstruction of electrode structures in electrochemical applications, such as PEMFCs, supercapacitors and HER electrodes.

As a requirement for a successful reconstruction of 3D structures by the dual beam technique, the phases present in the materials have to be unambiguously distinguishable in the SEM images. In the case of porous samples, the SEM images of the sample cross-section generally show both the front surface features and sub-surface features behind the void areas. Whilst the sub-surface features may be distinguishable from the front surface by human eyes, they are frequently not unambiguously recognizable by image processing software. This in turn makes the assignment of image areas to porous channels ambiguous. To overcome this challenge, researchers investigating SOFC electrodes normally infiltrate the porous channels in the SOFC electrode with epoxy. Epoxy replaces the porous phase and prevents the subsurface features from complicating the image processing task. SOFC electrodes have multiphase porous structures of ceramic, nickel and pore channels.

Unfortunately, the above strategy is not directly applicable for the porous carbon electrodes. There is no perceivable contrast between epoxy and carbon materials. Instead, several research groups attempted to image the PEMFC electrodes without any infiltration of epoxy and implemented various strategies to minimize the effect of the subsurface features. [105-109] Nevertheless, the image processing was still arguably challenging and not fully unambiguous.

To overcome this challenge, we infiltrated the porous channels with silicone resin using a vacuum infiltration technique. As silicon resin fills the porous channels inside the electrode, the obtained SEM images represent solely the front surface of the imaging area, and are free from the complications arisen from the sub-surface features. In contrast to epoxy, silicone resin presents perceivable mass contrast to the carbon support. The available mass contrast assists the assignment of the porous channels and carbon phase from the acquired SEM images. To improve the SEM contrast while retaining high imaging resolution, Energy Selective Backscattered (EsB) electron detection mode and a low primary electron beam energy of 2 keV were employed. The EsB electron SEM imaging mode uses backscattered electrons to form SEM images with compositional contrast. The EsB imaging mode is, however, different from the conventional backscattered electron detection mode that, in the EsB mode, low energy electrons are filtered out and only high energy backscattered electrons with low energy loss are used to form SEM images. As the low energy electrons (including secondary electrons and low energy backscattered electrons) are filtered out, the EsB SEM images present almost purely compositional contrast and are insensitive to surface topological information. In addition, high energy (or low

loss) backscattered electrons are the electrons backscattered from low penetration depths on the surface of sample. As these electrons originate close to the sample surface, the backscattered electron images formed from these electrons have much higher resolution than the conventional backscattered electron SEM images. The high resolution of EsB SEM images can be enhanced with low primary electron beam energy. The low primary electron beam energy of 2 keV was used to minimize charging effect on the sample and to enhance imaging resolution by minimizing the interaction volume of primary electrons with sample materials. By combining these strategies, the carbon support, silicone-filled porous channels and other active materials can be distinguished with compositional contrast at high resolutions.

7.2. 3D reconstruction of PEMFC cathode catalyst layer nanostructures using the FIB-SEM dual beam technique

As a proof of concept, in this chapter, the FIB-SEM method was developed for the imaging of PEMFC cathode catalyst layers, although we believe that the method can be easily applicable for other similar carbon electrodes in supercapacitor and HER applications. PEMFC cathode catalyst layers have intertwining porous nanostructures of carbon phase (carbon support and Nafion ionomer), porous channels, and platinum catalyst. The Pt/VXC72 (0.2 mg_{Pt} cm^{-2}) and Pt/GCNT (0.04 mg_{Pt} cm^{-2}) PEMFC cathodes were infiltrated with silicone resin, imaged and reconstructed nanostructures using the FIB-SEM dual beam method. The detailed experimental procedure is provided in section 2.2.7.

7.2.1. Effect of silicone resin infiltration and EsB imaging mode on the acquired SEM image quality

In order to study the effect of silicone resin infiltration and EsB imaging mode on the acquired SEM image quality, SEM images were obtained for the Pt/VXC72 cathode catalyst layer at various experimental conditions. Specifically, silicone resin infiltration conditions and SEM imaging modes of secondary electron and EsB electron were studied.

Figure 7-1a shows a secondary electron SEM image of the freshly FIB-milled surface of Pt/VXC72 catalyst layer without silicone resin infiltration. This is the commonly used experimental condition in conventional 2D SEM imaging of the electrode and in previous studies on the 3D reconstruction of electrode nanostructure using FIB-SEM dual beam method. [105-109] As evidenced from the SEM image, the Pt/VXC72 cathode catalyst layer has a highly porous nanostructure of solid phases (including carbon phase and Pt catalyst) and porous channels. Whilst this experimental method is sufficiently informative in conventional 2D SEM imaging to generally reveal the porous nanostructure of the electrode, there are major shortcomings of this method when being used for 3D reconstruction of nanostructures. Firstly and most importantly, the method presents difficulties in identifying solid phases and porous channels from the SEM image. For a clearer representation of the SEM image, a higher resolution SEM image is included in the inset of Figure 7-1a. As the SEM imaging technique has large depths of field, the SEM image clearly shows both front surface features on the FIB-milled surface of solid phase and subsurface features inside the void spaces of the porous channels. The

front surface features are identified as the solid features appearing flat and smooth, as a result of the FIB-milling process. The subsurface features are not yet milled by the FIB, and therefore appear in their original morphology (near spherical, in the case of VXC72 carbon nanoparticles). The subsurface features are located behind the void spaces of the porous channels. In the 3D reconstruction of nanostructures, these void spaces should be identified and assigned to the porous channels. However, due to the presence of the subsurface solid features with similar contrast to the front surface solid features, these void spaces are incorrectly identified as the solid phase. The incorrect identification and assignment of the porous channels as solid phases result in an overestimation of solid phase content and an underestimation of the porous channel volumes. Unambiguous and accurate identification of the porous channels is critical for the 3D reconstruction of nanostructures. The second shortcoming of this method is the use of secondary electron imaging mode. As seen in Figure 7-1a and the inset, there is a lack of contrast between the carbon phase and Pt nanoparticles. Pt nanoparticles are not clearly observed and identified from the secondary electron SEM image.

To address the first challenge, the porous channels are commonly filled with liquid resin. Upon a full solidification of the resin, the electrode is fully solid, with the porous channels replaced by solid resin. As the solid resin obscures the subsurface solid features, the subsurface features are not observed in the SEM image. The resin-filled porous channels therefore can be unambiguously and accurately distinguished from the solid phase of electrode. This strategy was successfully used in SOFC electrode 3D reconstruction studies, [101,102] in which the porous channels

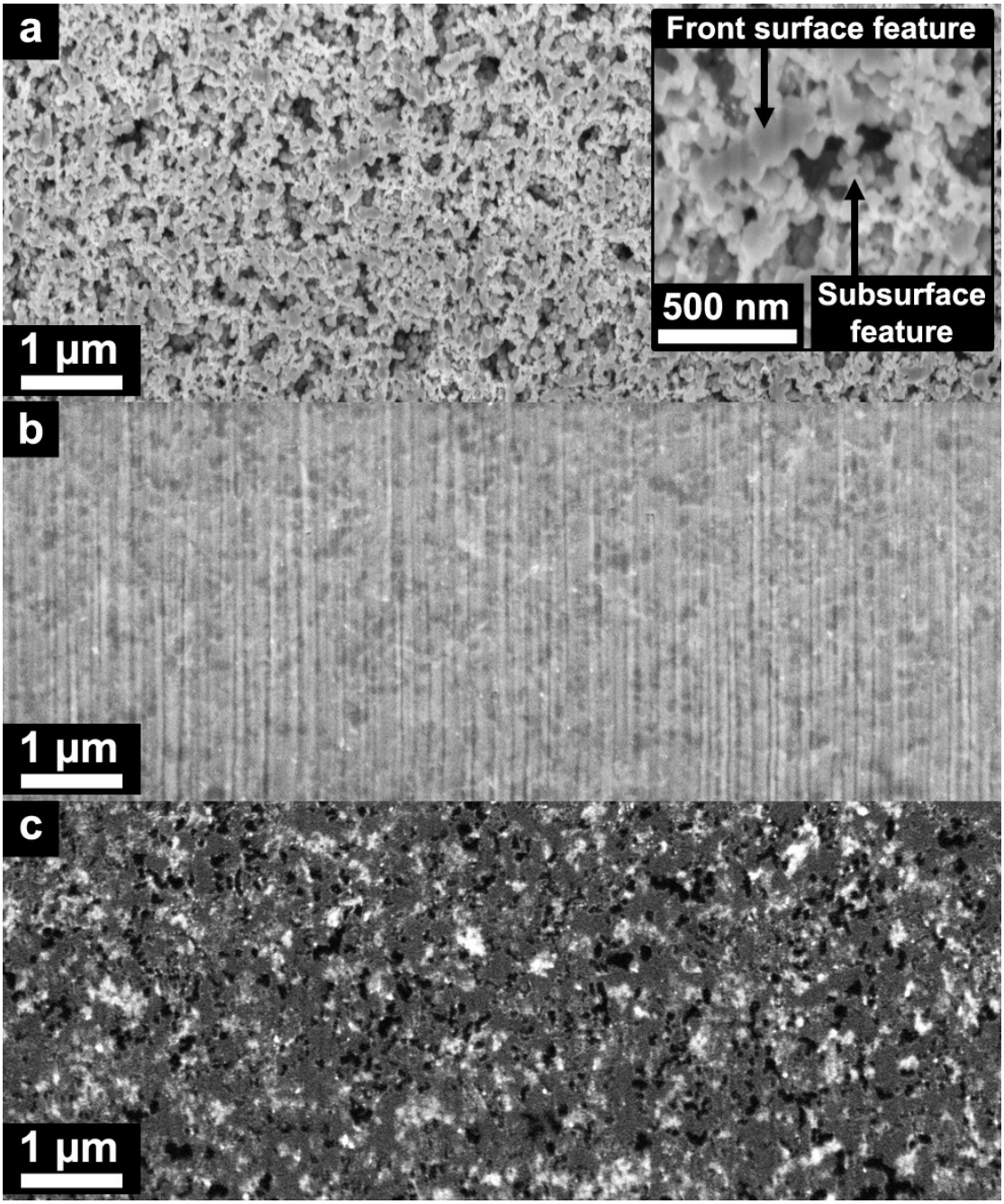


Figure 7-1. Effect of silicone resin infiltration and EsB imaging mode on the acquired SEM image quality. Secondary electron SEM images of the Pt/VXC72 PEMFC cathode catalyst layer (a) without and (b) with silicone resin infiltration. (c) EsB SEM image of the Pt/VXC72 PEMFC cathode catalyst layer with silicone resin infiltration.

were replaced with epoxy. The epoxy infiltration technique is, however, not directly applicable for the 3D reconstruction of carbon electrodes, due to the lack of contrast

between epoxy and carbon materials in SEM images. In this study, silicone resin was used to infiltrate the porous channels of carbon electrodes. Due to the differences in density and atomic mass, there is sufficient contrast between silicone-filled porous channels and carbon materials.

Figure 7-1b shows a secondary electron SEM image of the silicone-infiltrated Pt/VXC72 cathode catalyst layer. As evidenced, with the infiltration of silicone resin, the porous channels are fully replaced by solidified silicone resin. The solid silicone resin obscures the subsurface carbon solid features and effectively allows an unambiguous and accurate identification of porous channels in the electrode. The secondary electron SEM image of silicone-filled electrode is, however, still lack of contrast between carbon materials and Pt catalyst nanoparticles. In addition, there is some curtaining effect present on the FIB-milled surface of the electrode (i.e. striped surface morphology caused by uneven FIB-milling). The curtaining effect may complicate the phase assignments during image processing.

To enhance the contrast among carbon materials, silicone-filled porous channels and Pt catalysts, the EsB SEM imaging mode is used, combined with the low primary electron beam energy of 2 keV. The EsB SEM image of the silicone-infiltrated Pt/VXC72 cathode catalyst layer is shown in Figure 7-1c. As discussed in section 7.1, the EsB SEM imaging mode provides nearly purely composition contrast and is insensitive to surface topological characteristics. Two notable enhancements are observed in the EsB SEM image. Firstly, the carbon materials, silicone-filled porous channels, and Pt catalysts are clearly distinguishable with strongly enhanced compositional contrast in the EsB SEM image. In this image, carbon phase, silicone-

filled porous channels, and Pt catalysts are identified as the low brightness (black), medium brightness (gray), and high brightness (white) areas in the image, respectively. Secondly, the curtaining effect is not observed, due to the insensitivity of the EsB mode to surface topological information. The absence of curtaining artifact simplifies the image processing task. The EsB SEM image retains high resolutions when combined with the low primary electron beam energy. In this specific case, a spatial resolution of 9.83 nm was used, in consideration of a large imaging volume, although higher spatial resolutions are possible. The combination of silicone resin infiltration, EsB imaging mode and low primary electron beam energy proves to be highly effective in unambiguously and accurately identifying carbon phase, porous channels, and Pt catalyst in the electrode. This combination of experimental conditions was therefore used in this study to reconstruct the 3D nanostructure of carbon electrodes.

7.2.2. Image processing

In principle, after a series of SEM images of equally spaced cross-sections of the electrode are acquired, the SEM images can be stacked to reconstruct a 3D image of the electrode nanostructure. In practice, several image processing steps are involved. In the first step, the acquired SEM images are aligned. Due to the unavoidable instability of the sample stage and electron beam, SEM images are in general slightly shifted in relative to each other. The acquired SEM images are manually aligned by referencing to the markers created on the platinum protective mask, as described in section 2.2.7. The set of aligned SEM images is then cropped to the region of interest for further processing. In this study, a sample volume of 7.5 μm

× 3 μm × 3 μm is cropped from the original data set, corresponding to 306 consecutive cross-sectional SEM images that are equally spaced at 9.83 nm apart. A cubic voxel (i.e. a volumetric equivalent of pixel) size of 9.83 nm × 9.83 nm × 9.83 nm is used in this study. The aligned and cropped SEM images are then "segmented". The segmentation is the process of assigning various areas of the SEM images to predefined phases according to brightness level. The segmentation is performed semi-automatically using the Avizo 8.0 software with the 2D-Histogram Segmentation script module. An example of the original EsB SEM image and the corresponding segmented image is shown in Figure 7-2. In the segmented image, the assigned phases are carbon materials (black), silicone-filled porous channels (gray), and Pt-containing phase (white).

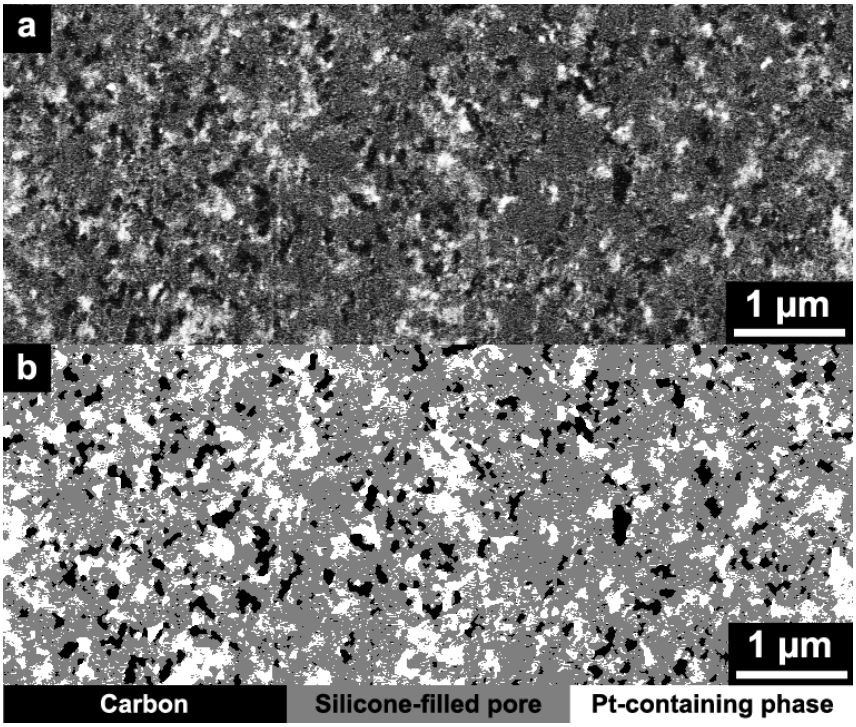


Figure 7-2. The SEM image segmentation of the Pt/VXC72 cathode catalyst layer. (a) Original EsB SEM image of the cathode catalyst layer and (b) the corresponding segmented image, with identified phases of carbon materials (black), silicone-filled porous channels (gray), and Pt-containing phase (white).

7.2.3. Reconstructed nanostructures of PEMFC cathodes

After the image segmentation step, the segmented images are stacked. A 3D reconstructed image is generated from the label fields corresponding to assigned phases. In this study, the Pt/VXC72 (0.2 mg_{Pt} cm^{-2}) and Pt/GCNT (0.04 mg_{Pt} cm^{-2}) cathode catalyst layers are reconstructed. Figure 7-3 and Figure 7-4 show the 3D reconstructed nanostructures of the Pt/VXC72 and Pt/GCNT cathode catalyst layer, respectively. In these figures, carbon phase, Pt-containing phase and porous channels are presented in green, red, and transparent, respectively. It should be noted that, however, the Pt catalyst nanoparticles are generally smaller than the voxel size, and therefore not resolved in the image. The Pt phase is therefore better understood as Pt-containing region (including Pt catalyst and surrounding materials), instead of solid Pt metallic phase. Although individual Pt catalyst nanoparticles are not resolved, the reconstructed spatial distribution of the Pt-containing phase is still valid and gives valuable information.

The 3D reconstructed image of the Pt/VXC72 cathode catalyst layer in Figure 7-3 shows the porous nanostructure of the electrode, with carbon phase, Pt–containing phase and porous channels distributed uniformly within the catalyst layer. The center of mass of each and every one of the three phases is located within 100 nm from the center of the imaging volume. The structure of the electrode is in the form of three-dimensionally interconnected networks of nanoparticle clusters. The porous channels are also in the form of interconnected networks of tortuous channels.

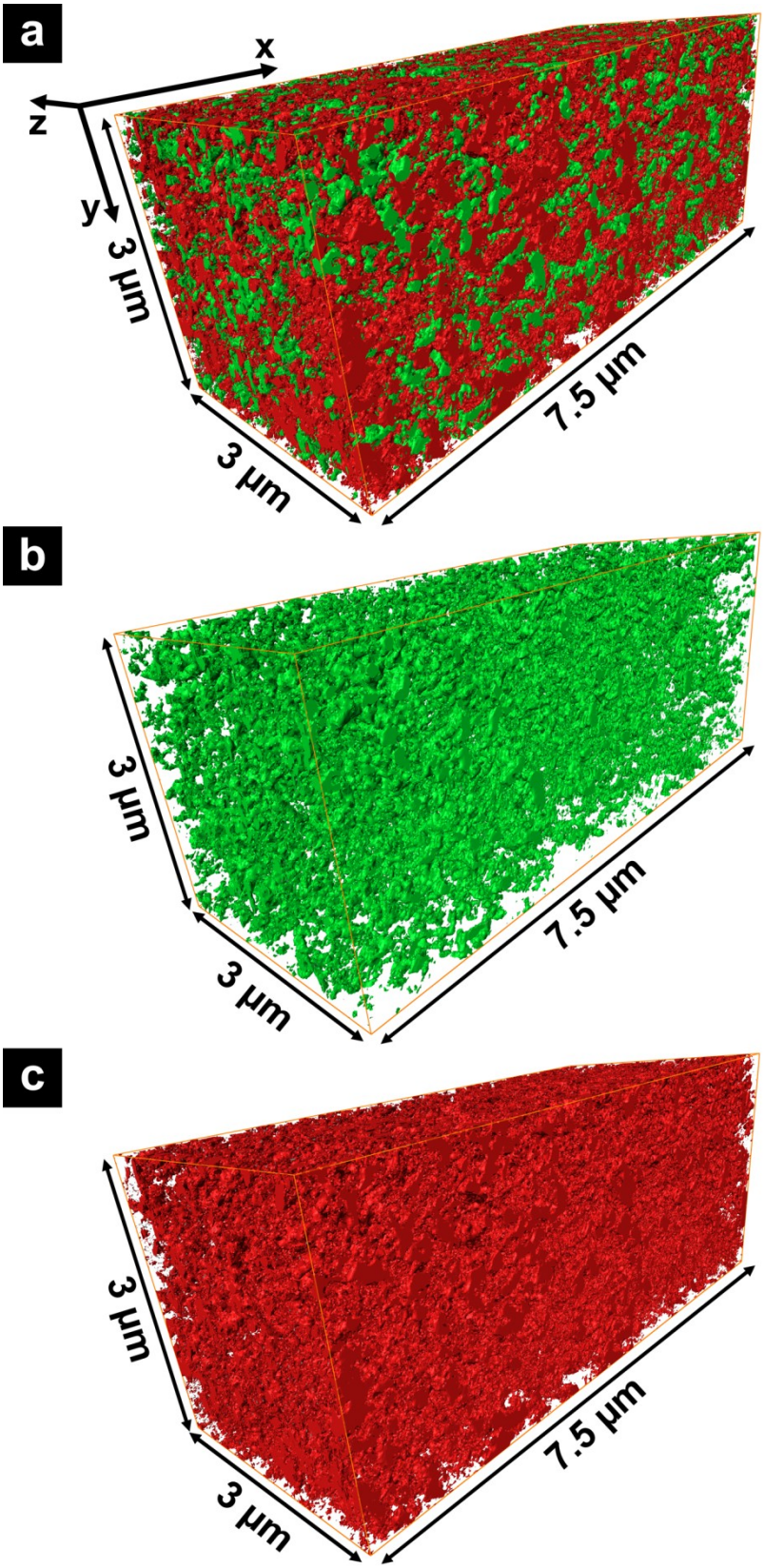


Figure 7-3. 3D reconstructed nanostructure of the Pt/VXC72 PEMFC cathode catalyst layer, presenting (a) both carbon phase (green) and Pt-containing phase (red), (b) carbon phase only, and (c) Pt-containing phase only.

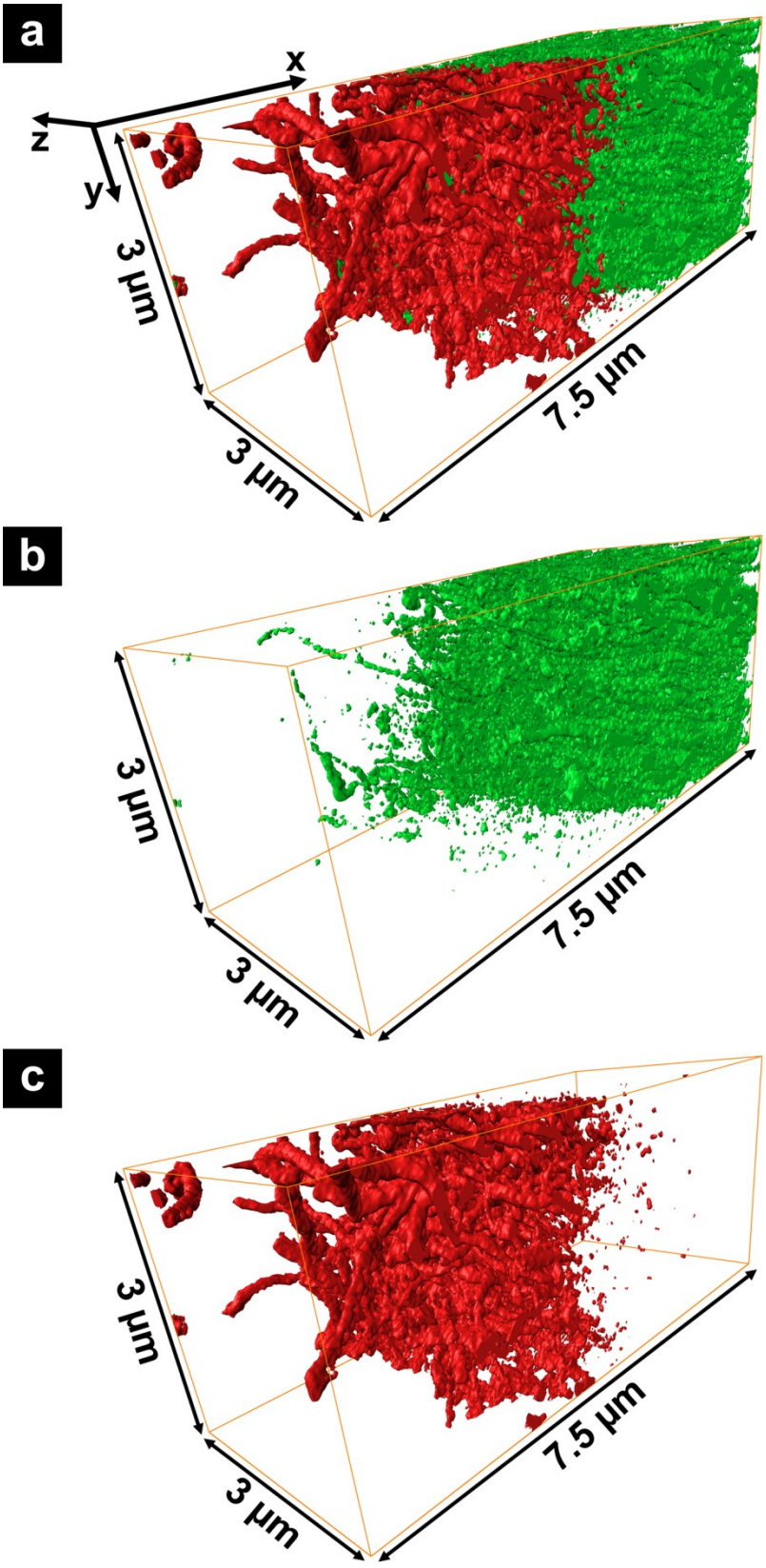


Figure 7-4. 3D reconstructed nanostructure of the Pt/GCNT PEMFC cathode catalyst layer, presenting (a) both carbon phase (green) and Pt-containing phase (red), (b) carbon phase only, and (c) Pt-containing phase only.

In contrast to the Pt/VXC72 nanostructure shown in Figure 7-3, the reconstructed nanostructure of Pt/GCNT catalyst layer in Figure 7-4 shows distinctively different characteristics. The electrode has fibrous nanostructure of both carbon phase and Pt-containing phase. The fibrous nanostructure is expected from the GCNT morphology. The Pt-containing region is distributed exclusively at one side of the imaging volume. This side of the imaging volume is in fact the top surface of the Pt/GCNT/CP electrode. The localized distribution of the Pt catalyst is a result of the magnetron sputtering electrocatalyst deposition technique used in the preparation of the Pt/GCNT/CP electrode.

7.2.4. Quantification of electrode nanostructures using 3D reconstructed images

The reconstructed 3D images of the nanostructures can be further quantified to extract structural parameters of the electrodes. Two parameters can be directly quantified from the reconstructed 3D images are volume fraction of present phases and surface-to-volume ratio of present phases. The volume fractions and surface-to-volume ratios of present phases in the two cathodes are summarized in Table 7-1.

Table 7-1. Quantification of the 3D reconstructed nanostructures.

	Pt/VXC72		**Pt/GCNT**	
	Volume fraction	**Surface-to-volume ratio**	**Volume fraction**	**Surface-to-volume ratio**
		$\mu m^2\ \mu m^{-3}$		$\mu m^2\ \mu m^{-3}$
Carbon materials	0.082	73.7	0.102	82.8
Porous channels	0.669	32.6	0.862	13.6
Pt-containing phase	0.249	64.3	0.036	61.0

Volume fraction of present phases is the most primary parameter extracted from the reconstructed 3D image. The volume fraction of each phase is calculated as the ratio between the number of voxels corresponding to the interested phase and the total number of voxels enclosed by the imaging volume. The volume fraction provides the insight on structural characteristics such as porosity. As presented in Table 7-1, the Pt/VXC72 catalyst layer has a porosity of 66.9%. The volume fractions of carbon materials and Pt-containing phase are also provided. It is noted that, however, the volume fraction of Pt-containing phase is unrealistically higher than that of the carbon materials. The overestimation of the Pt-containing phase volume fraction is most likely due to the fact that, as acknowledged previously, the Pt phase contains not only Pt catalyst nanoparticles but also the surrounding carbon materials. This is currently unavoidable, due to the sub-voxel size and extreme brightness of dispersed Pt nanoparticles. The volume fraction of phases in Pt/GCNT catalyst layer is also provided. However, due to the localized distribution of Pt catalyst in the Pt/GCNT cathode, the estimated parameters are dependent on the selected imaging volume (i.e. amount of GCNT carbon support included in the imaging volume). Nevertheless, the porosity of the Pt/GCNT cathode is generally estimated above 80%.

Surface-to-volume ratio is the ratio between the surface area and the volume occupied by the interested phase. [188] The surface-to-volume ratio is inversely dependent on the feature size of the phase. According to Table 7-1, the Pt/GCNT catalyst layer has slightly higher specific surface area carbon materials and slightly lower specific surface are Pt catalyst, compared to the Pt/VXC72 catalyst layer.

Besides the volume fraction and surface-to-volume ratio, the reconstructed images can be used as the basis for additional quantified structural parameters, such as percolation probability and tortuosity factor. [188] Percolation probability is the parameter characterizing the connectivity of each phase within the imaging volume. The connectivity of the phase is important for the performance of devices. For example, the connectivity within carbon materials and Pt catalyst phases is critical for the electron transport inside the electrode. The connectivity of the porous channels is important for the mass transport process of the electrode. Besides the connectivity, the geometry of the connected porous channels (e.g. a network of tortuous and narrow channels or a network of straight and wide channels) is an important parameter for the efficient mass transport. This geometry-dependent parameter is characterized by the tortuosity factor. In the present stage, these two parameters are not quantified in this study. The quantification of these parameters is suggested for future work.

7.3. Summary

In this study, we report a method for 3D reconstruction of porous carbon electrode nanostructures based on a FIB-SEM dual beam technique. In this method, silicone resin infiltration is used to eliminate the ambiguity in phase assignment process caused by the presence of subsurface solid features in the SEM images, and at the same time to provide compositional contrast between the carbon materials and silicone-filled porous channels. The EsB imaging mode and low primary electron

energy are used to further enhance the compositional contrast of the SEM images while retaining high imaging resolutions. The combination of silicone resin infiltration, EsB SEM imaging mode and low primary electron beam energy proves to be highly effective in unambiguously and accurately distinguishing carbon materials, porous channels, and other active phases present in the electrode structure. The imaging procedure is successfully applied for the 3D reconstruction of PEMFC cathode catalyst layer nanostructures. We believe that the same approach can be easily applied for other carbon-based nanostructures commonly used in electrochemical applications, such as supercapacitors, HER electrodes, and lithium ion battery anode. The reconstructed 3D nanostructures can be used as the basis for further quantifications to better understand the electrode nanostructures and their effects on electrochemical processes present in the electrodes.

Chapter 8 : Conclusions & Future work

8.1. Conclusions

In this thesis, we studied the development of a novel nano-structured carbon material referred to as Graphene-Carbon Nanotube hybrid (GCNT) and its applications in electrochemical energy conversion and storage devices. The hybrid was obtained by directly growing free-standing graphene onto CNT scaffolds via a two-step growth procedure. In the first step, CNTs were grown directly onto a porous carbon paper using the thermal CVD method. In the second step, free-standing graphene was grown directly onto the CNT scaffolds using the radio frequency PECVD method. Through systematic optimization of the carbon nanostructure growth conditions, including catalyst composition, deposition temperature, deposition time, and precursor gas composition, a desirable nanostructure of GCNT hybrid with numerous advantageous properties was achieved. The resulting hybrid material combines the advantageous properties of constituent materials, including an ultra-high density of graphitic edges of graphene and a porous structure of CNTs. The GCNT hybrid on carbon paper possesses an integrated all-carbon hierarchical structure where CNTs are grown directly onto carbon fibers and graphene is densely grafted onto the CNTs. Such a hierarchical structure offers direct electrical conducting pathways from graphene to the carbon paper. The hybrid possesses high chemical purity, high crystallinity and high specific surface area. These characteristics of the GCNT hybrids were well supported by the

comprehensive physical characterization using SEM, TEM, Raman spectroscopy, XPS, and BET surface area analysis. The GCNT hybrid was subsequently investigated for its applications in electrochemical devices. The GCNT hybrid was applied as the carbon support for Pt catalysts in PEMFC cathodes and as the carbon support for amorphous molybdenum sulfide in HER catalyst and supercapacitor electrode material applications.

When the GCNT hybrid is applied as the carbon support for Pt catalysts in PEMFC cathodes, the Pt/GCNT catalyst exhibits high intrinsic catalytic activity and superior electrochemical stability compared to a commercial carbon black supported Pt catalyst. The Pt/GCNT cathode shows approximately a 20% improvement in power density compared to the Pt/VXC72 cathode and a 2–3 fold improvement over the Pt/CNT cathode. The Pt/GCNT cathode retains ≈ 90% active Pt surface area after the degradation test, as opposed to only 39% Pt surface area retention demonstrated by the Pt/VXC72 catalyst. The enhanced intrinsic catalytic activity of the Pt/GCNT catalyst is attributed to the high density of graphitic edges present in the hybrid. The superior electrochemical stability of the Pt/GCNT catalyst is attributed to the high crystallinity of the GCNT support. The superior stability is expressed by a lower loss in polarization performance, a smaller increase in charge transfer resistance, a lower loss in the active platinum electrochemical surface area, a lower rate of carbon corrosion, and a more stable catalyst microstructure. With both high catalytic activity and superior electrochemical stability, the GCNT hybrid is demonstrated to be an excellent candidate for an advanced catalyst support in Proton Exchange Membrane Fuel Cells.

When the GCNT hybrid is applied as the carbon support for amorphous molybdenum sulfide in HER catalyst and supercapacitor electrode material applications, the integrated, porous, high surface area and conductive nanostructure of GCNT/carbon paper electrode provides efficient electron transport and mass transport pathways towards the active sites of MoS_x.

In the HER catalyst application, the deposition of MoS_x on high specific surface area GCNT hybrid demonstrates this to be an efficient method to increase the active loading of MoS_x while keeping the Tafel slope close to 40 mV dec^{-1}. The good electronic conductivity inside the electrode plays a crucial role in the enhancement of the MoS_x catalytic activity. With this strategy, we report one of the most active molybdenum sulfide-based HER catalysts to date. The high catalytic activity of MoS_x/GCNT is demonstrated by an overpotential of as low as 138 mV to obtain a current density of 10 mA cm^{-2}. Tafel slopes of between 39.3 and 41.8 mV dec^{-1} are demonstrated. The catalyst also demonstrates good stability with less than 10% decrease in current density obtained at –0.5 V *vs.* SHE after the degradation test. In addition, we also investigated the changes of MoS_x chemical states after the three main steps of the electrochemical evaluation process. We find that the S 2p XPS spectrum may not be a reliable prediction of the catalytic activity of MoS_x. We suggest that cautions should be made when one correlates the XPS spectrum to the HER catalytic activity of MoS_x.

In the supercapacitor electrode material application, the deposition of MoS_x on high specific surface area conductive supports demonstrates this to be an effective method to enhance the supercapacitive performance of MoS_x. The MoS_x/GCNT/CP

electrode shows high specific capacitances even at high discharge rates. The MoS_x/GCNT/CP electrode demonstrates a high discharge capacitance of 414 F g^{-1} at a constant discharge rate of 0.67 A g^{-1} and retains a discharge capacitance of 116 F g^{-1} even at a high discharge rate of 16.7 A g^{-1}. At various discharge rates, 3–4.5 fold enhancement in specific capacitance over MoS_x/Carbon paper is demonstrated by the MoS_x/GCNT/CP electrode. The MoS_x/GCNT/CP electrode also demonstrates good electrochemical stability with ≈ 80% retention of capacitance after 500 charge/discharge cycles at a high charge/discharge rate of 5 A g^{-1}. With high specific capacitance and good electrochemical stability, the MoS_x/GCNT/CP electrode is demonstrated to be promising electrode material candidates for supercapacitor applications.

An FIB-SEM dual-beam method was also developed to visually reconstruct the porous 3D nanostructure of carbon electrodes commonly used in various electrochemical devices. In our method, silicone resin infiltration was used to eliminate the ambiguity in phase assignment process caused by the presence of subsurface solid features in the SEM images, and at the same time to provide compositional contrast between the carbon materials and silicone-filled porous channels. The EsB imaging mode and low primary electron energy of 2 keV were used to further enhance the compositional contrast of the SEM images while retaining high imaging resolutions. The combination of silicone resin infiltration, EsB SEM imaging mode and low primary electron beam energy proves to be highly effective in unambiguously and accurately distinguishing carbon materials, porous channels, and other active phases present in the electrode structures. The imaging

procedure was successfully applied for the 3D reconstruction of PEMFC cathode catalyst layer nanostructures. We believe that the same approach can be easily applied for other carbon-based nanostructures commonly used in electrochemical applications, such as supercapacitors, HER electrodes, and lithium ion battery anode. The reconstructed 3D nanostructures can be used as the basis for further quantifications to better understand the electrode nanostructures and their effects on electrochemical processes present in the electrodes.

The main contribution of this work is the development of the unique all-carbon hierarchical nanostructure of graphene-carbon nanotube hybrid grown directly on carbon paper. The hybrid material possesses valuable properties, including: integrated nanostructure, high electrical conductivity, high porosity, high density of graphitic edge, high crystallinity, high purity, high specific surface area, and a flow-through electrode structure. The hybrid nanostructure serves as a highly versatile platform for various electrochemical applications. The hybrid nanostructure was successfully demonstrated to effectively enhance the electrochemical properties of supported active materials and therefore enhance the electrochemical device performances. The demonstrated examples include PEMFC cathode, HER catalyst and supercapacitor electrode materials.

The concept of combining the advantageous properties of graphene and CNTs in one single hybrid material opens up the possibility to further optimize the catalyst support in PEMFCs. Further exploration of hybrid support structures being highly crystalline, porous, and abundant of graphitic edges could lead to more active and stable catalysts for PEMFCs. Further enhancement of catalytic activity and

electrochemical stability of PEMFC catalysts are still major challenges of this technology.

Regarding the use of GCNT/CP and CNT/CP as the support materials for MoS_x in HER and supercapacitor applications, MoS_x by its own merits is an excellent material as both an HER catalyst and a supercapacitor electrode material. However, the major take-away lesson demonstrated in this thesis is the enhancement of electrochemical properties of active material (i.e. MoS_x) through the strategic coupling with GCNT/CP or CNT/CP. The integrated, conductive, high surface area and porous structures of GCNT/CP and CNT/CP enhance both electron transport and mass transport towards the deposited active materials. Whilst the thesis successfully uses MoS_x as an example for this approach, the coupling strategy is transferable to future research, where new active materials arise but experience similar limitations to MoS_x (such as low electrical conductivity). In such cases, GCNT/CP and CNT/CP can be a good platform for consideration.

8.2. Recommendations for future work

Whilst every effort has been made in this work to study as comprehensively as possible the properties and applications of the Graphene-Carbon Nanotube hybrid as well as to address all raised scientific questions, there are a few scientific questions remain unanswered and some envisaged applications remain unexplored, due to the lack of resources. These remaining questions and applications are recommended for further study in future work.

In chapter 3, it was demonstrated that the addition of an aluminum buffer layer beneath the iron catalyst layer in the growth process of CNTs tremendously enhances the growth of CNTs on carbon paper. Effects of the Al buffer layer thickness on the enhancement were demonstrated. Attempts to understand the enhancement mechanism were made by imaging the annealed Fe catalyst nanoparticles on the carbon paper. It was evidenced that the Al buffer layer effectively protects the Fe catalyst from the apparent reaction between Fe catalyst and carbon fiber. A hypothesis was raised that the Al buffer layer acts as a sacrificial layer to react with carbon fiber materials at high temperature and form a stable Al_4C_3 thin film, and effectively prevent the formation of iron carbide. To verify this hypothesis, we suggest to perform the catalyst annealing process in the Ar/H_2 carrier gas and to perform *in situ* XPS measurements using an environmental XPS instrument. In this experiment, the catalyzed carbon papers are annealed (together with required carrier gas) within the environmental XPS chamber. The *in situ* XPS measurements are performed throughout the annealing process to monitor the possible changes in the chemical states of Al and Fe catalysts. Comparisons should be made for carbon papers with and without an Al buffer layer.

In chapter 4, the Pt/GCNT catalyst demonstrates the enhanced catalytic activity and electrochemical stability compared to the carbon black supported Pt catalyst. Thanks to the versatility of the GCNT support and the magnetron sputtering electrocatalyst deposition technique, further studies on this catalyst nanostructure are possible. For example, using the magnetron sputtering method, a study of different Pt alloys supported on the GCNT hybrid as PEMFC catalysts can

be carried out. Pt alloys such as $Pt_3Ni(111)$ [137] were reported to be highly active towards oxygen reduction reaction in PEMFCs. Nitrogen-doped graphene [189-192] and nitrogen-doped carbon nanotubes [193-195] were also reported to possess catalytic activity towards oxygen reduction reaction in PEMFCs. A study on the modification of the GCNT hybrid by nitrogen doping as non-metal catalysts in PEMFCs may be carried out. Lastly, due to the similarities in electrode structures, functions and material requirements between the PEMFC cathode and the air cathode in Lithium-Air batteries, we envisage that the developed Pt/GCNT/CP electrode may also be suitable as an air cathode in Li-air batteries.

In chapter 5 and 6, the GCNT/CP electrode effectively enhances the electrochemical properties of MoS_x as HER catalyst and supercapacitor electrode materials by enhancing electron transport and mass transport towards the MoS_x active material. As reported in the literature, MoS_x can also be used as an electrode material in lithium ion batteries. [95] We suggest that, when being used as an electrode material in lithium ion batteries, the electrochemical properties of MoS_x may also benefit from the enhanced electron transport and mass transport provided by the GCNT hybrid. The MoS_x/GCNT hybrid therefore may be investigated in future study as an electrode material for lithium ion batteries.

In chapter 7, we developed the FIB-SEM dual beam method with the combination of silicone resin infiltration, EsB imaging mode, and low primary electron energy, to successfully reconstruct the 3D nanostructures of porous carbon electrodes. For the method to reach its full potential, further quantifications and numerical simulations of physical transport processes within the electrode are

desirable to fully reveal the three-dimensional properties of the electrode and the effects of electrode nanostructures on the physical processes. These studies are, however, beyond the scope of the current work. These studies are suggested for future research.

From the broader perspective of the hydrogen economy, beside material issues and system cost considerations, one major hurdle that prevents a quick adoption of the technology is the lack of an extensive hydrogen distribution infrastructure. For a successful adoption of the technology, a well distributed hydrogen network will be required. Such an infrastructure system requires support from both enterprises and governments through encouraging policies. The development concept of the hydrogen economy has been well supported by multiple countries, notably Japan, US, Germany, European Union, South Korea and China. Japan has been at the forefront in the transition to hydrogen as a fuel and energy carrier. Hydrogen has been given "the central role" in the low carbon energy future by the Japanese government, with more than $500 million has committed for research and infrastructure deployment in 2015. [196] More than 100,000 residential fuel cell systems have been installed in Japan within 2014. [196] Japan has planned for 2 million fuel cell vehicles and 1000 hydrogen refueling stations by 2025, and about 100 stations by 2015. Similarly, California plans to build 100 stations across the state. [196] In Europe, the European Union has committed more than $800 million for the research and development of fuel cell and hydrogen research, through the H_2Mobility program. [196] The fuel cell technology is also supported by various automobile manufacturers, notably Toyota with its newly released commercial fuel

cell car model Mirai or Honda with the FCV Clarity, both achieving a notable ~700 km range. Although the adoption of hydrogen economy is still in a relatively early stage, with the efforts from governments and enterprises, the future of hydrogen economy remains promising.

Bibliography

[1] World Population Prospects: The 2008 Revision. *United Nations, Department of Economic and Social Affairs, Population Division*, (2009).

[2] Stambouli, A. B. & Traversa, E. Solid oxide fuel cells (SOFCs): a review of an environmentally clean and efficient source of energy. *Renewable and Sustainable Energy Reviews* **6**, 433-455, (2002).

[3] Zhang, L. L. & Zhao, X. S. Carbon-based materials as supercapacitor electrodes. *Chemical Society Reviews* **38**, 2520-2531, (2009).

[4] Winter, M. & Brodd, R. J. What Are Batteries, Fuel Cells, and Supercapacitors? *Chemical Reviews* **104**, 4245-4270, (2004).

[5] Wang, Y., Chen, K. S., Mishler, J., Cho, S. C. & Adroher, X. C. A review of polymer electrolyte membrane fuel cells: Technology, applications, and needs on fundamental research. *Applied Energy* **88**, 981-1007, (2011).

[6] Yu, G., Xie, X., Pan, L., Bao, Z. & Cui, Y. Hybrid nanostructured materials for high-performance electrochemical capacitors. *Nano Energy* **2**, 213-234, (2013).

[7] Barreto, L., Makihira, A. & Riahi, K. The hydrogen economy in the 21st century: a sustainable development scenario. *International Journal of Hydrogen Energy* **28**, 267-284, (2003).

[8] Marbán, G. & Valdés-Solís, T. Towards the hydrogen economy? *International Journal of Hydrogen Energy* **32**, 1625-1637, (2007).

[9] Walter, M. G., Warren, E. L., McKone, J. R., Boettcher, S. W., Mi, Q., Santori, E. A. *et al*. Solar Water Splitting Cells. *Chemical Reviews* **110**, 6446-6473, (2010).

[10] Abbasi, T. & Abbasi, S. A. 'Renewable' hydrogen: Prospects and challenges. *Renewable and Sustainable Energy Reviews* **15**, 3034-3040, (2011).

[11] Muradov, N. Z. & Veziroğlu, T. N. From hydrocarbon to hydrogen–carbon to hydrogen economy. *International Journal of Hydrogen Energy* **30**, 225-237, (2005).

[12] Morales-Guio, C. G. & Hu, X. Amorphous Molybdenum Sulfides as Hydrogen Evolution Catalysts. *Accounts of Chemical Research* **47**, 2671-2681, (2014).

[13] Ellis, M. W., von Spakovsky, M. R. & Nelson, D. J. Fuel cell systems: efficient, flexible energy conversion for the 21st century. *Proceedings of the IEEE* **89**, 1808-1818, (2001).

[14] Larminie, J. & Dicks, A. *Fuel Cell Systems Explained*. 2nd Edition edn, (John Wiley & Sons Ltd, 2003).

[15] Kirubakaran, A., Jain, S. & Nema, R. K. A review on fuel cell technologies and power electronic interface. *Renewable and Sustainable Energy Reviews* **13**, 2430-2440, (2009).

[16] Mehta, V. & Cooper, J. S. Review and analysis of PEM fuel cell design and manufacturing. *Journal of Power Sources* **114**, 32-53, (2003).

[17] NIST. PEM Fuel Cells. (2006).

[18] Baker, R. & Zhang, J. Proton Exchange Membrane or Polymer Electrolyte Membrane (PEM) Fuel Cells. *Electrochemistry Encyclopedia*, (2011).

[19] Toyota Motor Sales, U. S. A., Inc. Toyota Mirai - The Turning Point. (2015).

[20] Zhang, J. *PEM Fuel Cell Electrocatalysts and Catalyst Layers*. 1 edn, (Springer-Verlag London, 2008).

[21] Ferreira, P. J., la O', G. J., Shao-Horn, Y., Morgan, D., Makharia, R., Kocha, S. *et al.* Instability of Pt/C Electrocatalysts in Proton Exchange Membrane Fuel Cells: A Mechanistic Investigation. *Journal of The Electrochemical Society* **152**, A2256-A2271, (2005).

[22] Shao, Y., Kou, R., Wang, J., Viswanathan, V. V., Kwak, J. H., Liu, J. *et al.* The influence of the electrochemical stressing (potential step and potential-static holding) on the degradation of polymer electrolyte membrane fuel cell electrocatalysts. *Journal of Power Sources* **185**, 280-286, (2008).

[23] Zhang, S., Yuan, X., Wang, H., Mérida, W., Zhu, H., Shen, J. *et al.* A review of accelerated stress tests of MEA durability in PEM fuel cells. *International Journal of Hydrogen Energy* **34**, 388-404, (2009).

[24] Bi, W., Gray, G. E. & Fuller, T. F. PEM Fuel Cell Pt/C Dissolution and Deposition in Nafion Electrolyte. *Electrochemical and Solid-State Letters* **10**, B101-B104, (2007).

[25] Yasuda, K., Taniguchi, A., Akita, T., Ioroi, T. & Siroma, Z. Platinum dissolution and deposition in the polymer electrolyte membrane of a PEM fuel cell as studied by potential cycling. *Physical Chemistry Chemical Physics* **8**, 746-752, (2006).

[26] Akita, T., Taniguchi, A., Maekawa, J., Siroma, Z., Tanaka, K., Kohyama, M. *et al.* Analytical TEM study of Pt particle deposition in the proton-exchange membrane of a membrane-electrode-assembly. *Journal of Power Sources* **159**, 461-467, (2006).

[27] Tang, Z., Ng, H. Y., Lin, J., Wee, A. T. S. & Chua, D. H. C. Pt/CNT-Based Electrodes with High Electrochemical Activity and Stability for Proton Exchange Membrane Fuel Cells. *Journal of The Electrochemical Society* **157**, B245-B250, (2010).

[28] Knights, S. D., Colbow, K. M., St-Pierre, J. & Wilkinson, D. P. Aging mechanisms and lifetime of PEFC and DMFC. *Journal of Power Sources* **127**, 127-134, (2004).

[29] Park, S., Shao, Y., Wan, H., Viswanathan, V. V., Towne, S. A., Rieke, P. C. *et al.* Degradation of the Ionic Pathway in a PEM Fuel Cell Cathode. *The Journal of Physical Chemistry C* **115**, 22633-22639, (2011).

[30] Antolini, E. Carbon supports for low-temperature fuel cell catalysts. *Applied Catalysis B: Environmental* **88**, 1-24, (2009).

[31] Roen, L. M., Paik, C. H. & Jarvi, T. D. Electrocatalytic Corrosion of Carbon Support in PEMFC Cathodes. *Electrochemical and Solid-State Letters* **7**, A19-A22, (2004).

[32] Tang, Z., Poh, C. K., Tian, Z., Lin, J., Ng, H. Y. & Chua, D. H. C. In situ grown carbon nanotubes on carbon paper as integrated gas diffusion and catalyst layer for proton exchange membrane fuel cells. *Electrochimica Acta* **56**, 4327-4334, (2011).

[33] Wang, C., Waje, M., Wang, X., Tang, J. M., Haddon, R. C. & Yan, Y. Proton exchange membrane fuel cells with carbon nanotube based electrodes. *Nano letters* **4**, 345-348, (2004).

[34] Sharma, S. & Pollet, B. G. Support materials for PEMFC and DMFC electrocatalysts—A review. *Journal of Power Sources* **208**, 96-119, (2012).

[35] Meyyappan, M., Lance, D., Alan, C. & David, H. Carbon nanotube growth by PECVD: a review. *Plasma Sources Science and Technology* **12**, 205, (2003).

[36] Thostenson, E. T., Ren, Z. & Chou, T.-W. Advances in the science and technology of carbon nanotubes and their composites: a review. *Composites Science and Technology* **61**, 1899-1912, (2001).

[37] Hata, K., Futaba, D. N., Mizuno, K., Namai, T., Yumura, M. & Iijima, S. Water-Assisted Highly Efficient Synthesis of Impurity-Free Single-Walled Carbon Nanotubes. *Science* **306**, 1362-1364, (2004).

[38] Saha, M. S., Li, R. & Sun, X. High loading and monodispersed Pt nanoparticles on multiwalled carbon nanotubes for high performance proton exchange membrane fuel cells. *Journal of Power Sources* **177**, 314-322, (2008).

[39] Qu, L., Zhao, Y. & Dai, L. Carbon Microfibers Sheathed with Aligned Carbon Nanotubes: Towards Multidimensional, Multicomponent, and Multifunctional Nanomaterials. *Small* **2**, 1052-1059, (2006).

[40] Wu, Y., Qiao, P., Chong, T. & Shen, Z. Carbon Nanowalls Grown by Microwave Plasma Enhanced Chemical Vapor Deposition. *Advanced materials* **14**, 64-67, (2002).

[41] Shang, N. G., Papakonstantinou, P., McMullan, M., Chu, M., Stamboulis, A., Potenza, A. *et al.* Catalyst-Free Efficient Growth, Orientation and Biosensing Properties of Multilayer Graphene Nanoflake Films with Sharp Edge Planes. *Advanced Functional Materials* **18**, 3506-3514, (2008).

[42] Teii, K., Shimada, S., Nakashima, M. & Chuang, A. T. H. Synthesis and electrical characterization of n-type carbon nanowalls. *Journal of Applied Physics* **106**, 084303-084306, (2009).

[43] Malesevic, A., Vitchev, R., Schouteden, K., Volodin, A., Zhang, L., Tendeloo, G. V. *et al.* Synthesis of few-layer graphene via microwave plasma-enhanced chemical vapour deposition. *Nanotechnology* **19**, 305604, (2008).

[44] Wang, J., Zhu, M., Outlaw, R. A., Zhao, X., Manos, D. M. & Holloway, B. C. Synthesis of carbon nanosheets by inductively coupled radio-frequency plasma enhanced chemical vapor deposition. *Carbon* **42**, 2867-2872, (2004).

[45] Hiramatsu, M., Shiji, K., Amano, H. & Hori, M. Fabrication of vertically aligned carbon nanowalls using capacitively coupled plasma-enhanced chemical vapor deposition assisted by hydrogen radical injection. *Applied Physics Letters* **84**, 4708-4710, (2004).

[46] Takeuchi, W., Ura, M., Hiramatsu, M., Tokuda, Y., Kano, H. & Hori, M. Electrical conduction control of carbon nanowalls. *Applied Physics Letters* **92**, 213103-213103-213103, (2008).

[47] Kondo, S., Hori, M., Yamakawa, K., Den, S., Kano, H. & Hiramatsu, M. Highly reliable growth process of carbon nanowalls using radical injection plasma-enhanced chemical vapor deposition. *Journal of Vacuum Science & Technology B: Microelectronics and Nanometer Structures* **26**, 1294-1300, (2008).

[48] Lisi, N., Giorgi, R., Re, M., Dikonimos, T., Giorgi, L., Salernitano, E. *et al.* Carbon nanowall growth on carbon paper by hot filament chemical vapour deposition and its microstructure. *Carbon* **49**, 2134-2140, (2011).

[49] Vizireanu, S., Stoica, S. D., Luculescu, C., Nistor, L. C., Mitu, B. & Dinescu, G. Plasma techniques for nanostructured carbon materials synthesis. A case study: carbon nanowall growth by low pressure expanding RF plasma. *Plasma Sources Science and Technology* **19**, 034016, (2010).

[50] Saito, T., Chiba, H., Ito, T. & Ogino, T. Growth of carbon hybrid materials by grafting on pre-grown carbon nanotube surfaces. *Carbon* **48**, 1305-1311, (2010).

[51] Parker, C. B., Raut, A. S., Brown, B., Stoner, B. R. & Glass, J. T. Three-dimensional arrays of graphenated carbon nanotubes. *Journal of Materials Research* **27**, 1046-1053, (2012).

[52] Rout, C. S., Kumar, A., Fisher, T. S., Gautam, U. K., Bando, Y. & Golberg, D. Synthesis of chemically bonded CNT-graphene heterostructure arrays. *RSC Advances* **2**, 8250-8253, (2012).

[53] Feng, J.-M. & Dai, Y.-J. Water-assisted growth of graphene on carbon nanotubes by the chemical vapor deposition method. *Nanoscale* **5**, 4422-4426, (2013).

[54] Yu, K., Lu, G., Bo, Z., Mao, S. & Chen, J. Carbon Nanotube with Chemically Bonded Graphene Leaves for Electronic and Optoelectronic Applications. *The Journal of Physical Chemistry Letters* **2**, 1556-1562, (2011).

[55] Stoner, B. R., Raut, A. S., Brown, B., Parker, C. B. & Glass, J. T. Graphenated carbon nanotubes for enhanced electrochemical double layer capacitor performance. *Applied Physics Letters* **99**, 183104, (2011).

[56] Hsu, H.-C., Wang, C.-H., Nataraj, S. K., Huang, H.-C., Du, H.-Y., Chang, S.-T. *et al.* Stand-up structure of graphene-like carbon nanowalls on CNT directly grown on polyacrylonitrile-based carbon fiber paper as supercapacitor. *Diamond and Related Materials* **25**, 176-179, (2012).

[57] Okamoto, A., Tanaka, K., Yoshimura, M., Ueda, K., Ghosh, P. & Tanemura, M. Synthesis of Vertically Aligned Carbon Nanofibers-Carbon Nanowalls by Plasma-Enhanced Chemical Vapor Deposition. *Journal of Nanoscience and Nanotechnology* **13**, 1956-1960, (2013).

[58] Chen, C.-C., Chen, C.-F., Lee, I. H. & Lin, C.-L. Fabrication of high surface area graphitic nanoflakes on carbon nanotubes templates. *Diamond and Related Materials* **14**, 1897-1900, (2005).

[59] Du, H.-Y., Wang, C.-H., Hsu, H.-C., Chang, S.-T., Huang, H.-C., Chen, L.-C. *et al.* Graphene nanosheet–CNT hybrid nanostructure electrode for a proton exchange membrane fuel cell. *International Journal of Hydrogen Energy* **37**, 18989-18995, (2012).

[60] Benck, J. D., Hellstern, T. R., Kibsgaard, J., Chakthranont, P. & Jaramillo, T. F. Catalyzing the Hydrogen Evolution Reaction (HER) with Molybdenum Sulfide Nanomaterials. *ACS Catalysis* **4**, 3957-3971, (2014).

[61] Zou, X. & Zhang, Y. Noble metal-free hydrogen evolution catalysts for water splitting. *Chemical Society Reviews* **44**, 5148-5180, (2015).

[62] Jaramillo, T. F., Jørgensen, K. P., Bonde, J., Nielsen, J. H., Horch, S. & Chorkendorff, I. Identification of Active Edge Sites for Electrochemical H2 Evolution from MoS2 Nanocatalysts. *Science* **317**, 100-102, (2007).

[63] Hinnemann, B., Moses, P. G., Bonde, J., Jørgensen, K. P., Nielsen, J. H., Horch, S. *et al.* Biomimetic Hydrogen Evolution: MoS2 Nanoparticles as Catalyst for Hydrogen Evolution. *Journal of the American Chemical Society* **127**, 5308-5309, (2005).

[64] Chen, Z., Cummins, D., Reinecke, B. N., Clark, E., Sunkara, M. K. & Jaramillo, T. F. Core–shell MoO3–MoS2 Nanowires for Hydrogen Evolution: A Functional Design for Electrocatalytic Materials. *Nano letters* **11**, 4168-4175, (2011).

[65] Kong, D., Wang, H., Cha, J. J., Pasta, M., Koski, K. J., Yao, J. *et al.* Synthesis of MoS2 and MoSe2 Films with Vertically Aligned Layers. *Nano letters* **13**, 1341-1347, (2013).

[66] Xie, J., Zhang, H., Li, S., Wang, R., Sun, X., Zhou, M. *et al.* Defect-Rich MoS2 Ultrathin Nanosheets with Additional Active Edge Sites for Enhanced Electrocatalytic Hydrogen Evolution. *Advanced materials* **25**, 5807-5813, (2013).

[67] Li, Y., Wang, H., Xie, L., Liang, Y., Hong, G. & Dai, H. MoS2 Nanoparticles Grown on Graphene: An Advanced Catalyst for the Hydrogen Evolution Reaction. *Journal of the American Chemical Society* **133**, 7296-7299, (2011).

[68] Kibsgaard, J., Chen, Z., Reinecke, B. N. & Jaramillo, T. F. Engineering the surface structure of MoS2 to preferentially expose active edge sites for electrocatalysis. *Nat Mater* **11**, 963-969, (2012).

[69] Merki, D., Fierro, S., Vrubel, H. & Hu, X. Amorphous molybdenum sulfide films as catalysts for electrochemical hydrogen production in water. *Chemical Science* **2**, 1262-1267, (2011).

[70] Vrubel, H. & Hu, X. Growth and Activation of an Amorphous Molybdenum Sulfide Hydrogen Evolving Catalyst. *ACS Catalysis* **3**, 2002-2011, (2013).

[71] Li, D. J., Maiti, U. N., Lim, J., Choi, D. S., Lee, W. J., Oh, Y. *et al.* Molybdenum Sulfide/N-Doped CNT Forest Hybrid Catalysts for High-Performance Hydrogen Evolution Reaction. *Nano letters* **14**, 1228-1233, (2014).

[72] Chang, Y.-H., Lin, C.-T., Chen, T.-Y., Hsu, C.-L., Lee, Y.-H., Zhang, W. *et al.* Highly Efficient Electrocatalytic Hydrogen Production by MoSx Grown on Graphene-Protected 3D Ni Foams. *Advanced materials* **25**, 756-760, (2013).

[73] Laursen, A. B., Vesborg, P. C. K. & Chorkendorff, I. A high-porosity carbon molybdenum sulphide composite with enhanced electrochemical hydrogen evolution and stability. *Chemical Communications* **49**, 4965-4967, (2013).

[74] Benck, J. D., Chen, Z., Kuritzky, L. Y., Forman, A. J. & Jaramillo, T. F. Amorphous Molybdenum Sulfide Catalysts for Electrochemical Hydrogen Production: Insights into the Origin of their Catalytic Activity. *ACS Catalysis* **2**, 1916-1923, (2012).

[75] Huang, K.-J., Wang, L., Zhang, J.-Z., Wang, L.-L. & Mo, Y.-P. One-step preparation of layered molybdenum disulfide/multi-walled carbon nanotube composites for enhanced performance supercapacitor. *Energy* **67**, 234-240, (2014).

[76] Wang, G., Zhang, L. & Zhang, J. A review of electrode materials for electrochemical supercapacitors. *Chemical Society Reviews* **41**, 797-828, (2012).

[77] Wang, Y., Shi, Z., Huang, Y., Ma, Y., Wang, C., Chen, M. *et al.* Supercapacitor Devices Based on Graphene Materials. *The Journal of Physical Chemistry C* **113**, 13103-13107, (2009).

[78] Hu, C.-C., Chang, K.-H., Lin, M.-C. & Wu, Y.-T. Design and Tailoring of the Nanotubular Arrayed Architecture of Hydrous RuO2 for Next Generation Supercapacitors. *Nano letters* **6**, 2690-2695, (2006).

[79] Long, J. W., Bélanger, D., Brousse, T., Sugimoto, W., Sassin, M. B. & Crosnier, O. Asymmetric electrochemical capacitors—Stretching the limits of aqueous electrolytes. *MRS Bulletin* **36**, 513-522, (2011).

[80] Hou, Y., Cheng, Y., Hobson, T. & Liu, J. Design and Synthesis of Hierarchical MnO2 Nanospheres/Carbon Nanotubes/Conducting Polymer Ternary Composite for High Performance Electrochemical Electrodes. *Nano letters* **10**, 2727-2733, (2010).

[81] Jiang, H., Ma, J. & Li, C. Mesoporous Carbon Incorporated Metal Oxide Nanomaterials as Supercapacitor Electrodes. *Advanced materials* **24**, 4197-4202, (2012).

[82] Salunkhe, R. R., Jang, K., Lee, S.-w., Yu, S. & Ahn, H. Binary metal hydroxide nanorods and multi-walled carbon nanotube composites for electrochemical energy storage applications. *Journal of Materials Chemistry* **22**, 21630-21635, (2012).

[83] Jiang, H., Zhao, T., Li, C. & Ma, J. Hierarchical self-assembly of ultrathin nickel hydroxide nanoflakes for high-performance supercapacitors. *Journal of Materials Chemistry* **21**, 3818-3823, (2011).

[84] Ratha, S. & Rout, C. S. Supercapacitor Electrodes Based on Layered Tungsten Disulfide-Reduced Graphene Oxide Hybrids Synthesized by a Facile Hydrothermal Method. *ACS Applied Materials & Interfaces* **5**, 11427-11433, (2013).

[85] Acerce, M., Voiry, D. & Chhowalla, M. Metallic 1T phase MoS2 nanosheets as supercapacitor electrode materials. *Nature Nanotechnology* **10**, 313-318, (2015).

[86] Hu, B., Qin, X., Asiri, A. M., Alamry, K. A., Al-Youbi, A. O. & Sun, X. Synthesis of porous tubular C/MoS2 nanocomposites and their application as a novel electrode material for supercapacitors with excellent cycling stability. *Electrochimica Acta* **100**, 24-28, (2013).

[87] Soon, J. M. & Loh, K. P. Electrochemical Double-Layer Capacitance of MoS2 Nanowall Films. *Electrochemical and Solid-State Letters* **10**, A250-A254, (2007).

[88] da Silveira Firmiano, E. G., Rabelo, A. C., Dalmaschio, C. J., Pinheiro, A. N., Pereira, E. C., Schreiner, W. H. *et al.* Supercapacitor Electrodes Obtained by Directly Bonding 2D MoS2 on Reduced Graphene Oxide. *Advanced Energy Materials* **4**, n/a-n/a, (2014).

[89] Sun, G., Zhang, X., Lin, R., Yang, J., Zhang, H. & Chen, P. Hybrid Fibers Made of Molybdenum Disulfide, Reduced Graphene Oxide, and Multi-Walled Carbon Nanotubes for Solid-State, Flexible, Asymmetric Supercapacitors. *Angewandte Chemie International Edition* **54**, 4651-4656, (2015).

[90] Huang, K.-J., Wang, L., Liu, Y.-J., Liu, Y.-M., Wang, H.-B., Gan, T. *et al.* Layered MoS2–graphene composites for supercapacitor applications with enhanced capacitive performance. *International Journal of Hydrogen Energy* **38**, 14027-14034, (2013).

[91] Ramadoss, A., Kim, T., Kim, G.-S. & Kim, S. J. Enhanced activity of a hydrothermally synthesized mesoporous MoS2 nanostructure for high performance supercapacitor applications. *New Journal of Chemistry* **38**, 2379-2385, (2014).

[92] Zhang, Y., Sun, W., Rui, X., Li, B., Tan, H. T., Guo, G. *et al.* One-Pot Synthesis of Tunable Crystalline Ni3S4@Amorphous MoS2 Core/Shell Nanospheres for High-Performance Supercapacitors. *Small*, n/a-n/a, (2015).

[93] Xiao, J., Choi, D., Cosimbescu, L., Koech, P., Liu, J. & Lemmon, J. P. Exfoliated MoS2 Nanocomposite as an Anode Material for Lithium Ion Batteries. *Chemistry of Materials* **22**, 4522-4524, (2010).

[94] Cao, X., Shi, Y., Shi, W., Rui, X., Yan, Q., Kong, J. *et al.* Preparation of MoS2-Coated Three-Dimensional Graphene Networks for High-Performance Anode Material in Lithium-Ion Batteries. *Small* **9**, 3433-3438, (2013).

[95] Miki, Y., Nakazato, D., Ikuta, H., Uchida, T. & Wakihara, M. Amorphous MoS2 as the cathode of lithium secondary batteries. *Journal of Power Sources* **54**, 508-510, (1995).

[96] Bouroushian, M. *Electrochemistry of Metal Chalcogenides*. 1 edn, (Springer-Verlag Berlin Heidelberg, 2010).

[97] Pumera, M., Sofer, Z. & Ambrosi, A. Layered transition metal dichalcogenides for electrochemical energy generation and storage. *Journal of Materials Chemistry A* **2**, 8981-8987, (2014).

[98] Gardiner, D. J. & Graves, P. R. *Practical Raman Spectroscopy*. (Springer Berlin Heidelberg, 1989).

[99] Brunauer, S., Emmett, P. H. & Teller, E. Adsorption of Gases in Multimolecular Layers. *Journal of the American Chemical Society* **60**, 309-319, (1938).

[100] Wilson, J. R., Kobsiriphat, W., Mendoza, R., Chen, H.-Y., Hiller, J. M., Miller, D. J. *et al.* Three-dimensional reconstruction of a solid-oxide fuel-cell anode. *Nature Materials* **5**, 541-544, (2006).

[101] Wilson, J. R., Duong, A. T., Gameiro, M., Chen, H.-Y., Thornton, K., Mumm, D. R. *et al.* Quantitative three-dimensional microstructure of a solid oxide fuel cell cathode. *Electrochemistry Communications* **11**, 1052-1056, (2009).

[102] Iwai, H., Shikazono, N., Matsui, T., Teshima, H., Kishimoto, M., Kishida, R. *et al.* Quantification of SOFC anode microstructure based on dual beam FIB-SEM technique. *Journal of Power Sources* **195**, 955-961, (2010).

[103] Shearing, P. R., Cai, Q., Golbert, J. I., Yufit, V., Adjiman, C. S. & Brandon, N. P. Microstructural analysis of a solid oxide fuel cell anode using focused ion beam techniques coupled with electrochemical simulation. *Journal of Power Sources* **195**, 4804-4810, (2010).

[104] Zils, S., Timpel, M., Arlt, T., Wolz, A., Manke, I. & Roth, C. 3D Visualisation of PEMFC Electrode Structures Using FIB Nanotomography. *Fuel Cells* **10**, 966-972, (2010).

[105] Ostadi, H., Rama, P., Liu, Y., Chen, R., Zhang, X. X. & Jiang, K. 3D reconstruction of a gas diffusion layer and a microporous layer. *Journal of Membrane Science* **351**, 69-74, (2010).

[106] Ziegler, C., Thiele, S. & Zengerle, R. Direct three-dimensional reconstruction of a nanoporous catalyst layer for a polymer electrolyte fuel cell. *Journal of Power Sources* **196**, 2094-2097, (2011).

[107] Thiele, S., Zengerle, R. & Ziegler, C. Nano-morphology of a polymer electrolyte fuel cell catalyst layer—imaging, reconstruction and analysis. *Nano Res.* **4**, 849-860, (2011).

[108] Singh, R., Akhgar, A. R., Sui, P. C., Lange, K. J. & Djilali, N. Dual-Beam FIB/SEM Characterization, Statistical Reconstruction, and Pore Scale Modeling of a PEMFC Catalyst Layer. *Journal of The Electrochemical Society* **161**, F415-F424, (2014).

[109] Schulenburg, H., Schwanitz, B., Linse, N., Scherer, G. G., Wokaun, A., Krbanjevic, J. *et al.* 3D Imaging of Catalyst Support Corrosion in Polymer Electrolyte Fuel Cells. *The Journal of Physical Chemistry C* **115**, 14236-14243, (2011).

[110] Kim, B., Chung, H. & Kim, W. Supergrowth of Aligned Carbon Nanotubes Directly on Carbon Papers and Their Properties as Supercapacitors. *The Journal of Physical Chemistry C* **114**, 15223-15227, (2010).

[111] Tang, Z., Poh, C. K., Lee, K. K., Tian, Z., Chua, D. H. C. & Lin, J. Enhanced catalytic properties from platinum nanodots covered carbon nanotubes for proton-exchange membrane fuel cells. *Journal of Power Sources* **195**, 155-159, (2010).

[112] Futaba, D. N., Goto, J., Yasuda, S., Yamada, T., Yumura, M. & Hata, K. General Rules Governing the Highly Efficient Growth of Carbon Nanotubes. *Advanced materials* **21**, 4811-4815, (2009).

[113] He, C. N., Zhao, N. Q., Shi, C. S. & Song, S. Z. Fabrication of aluminum carbide nanowires by a nano-template reaction. *Carbon* **48**, 931-938, (2010).

[114] Tuinstra, F. & Koenig, J. L. Raman Spectrum of Graphite. *The Journal of Chemical Physics* **53**, 1126-1130, (1970).

[115] Ni, Z. H., Fan, H. M., Feng, Y. P., Shen, Z. X., Yang, B. J. & Wu, Y. H. Raman spectroscopic investigation of carbon nanowalls. *The Journal of Chemical Physics* **124**, 204703, (2006).

[116] Pimenta, M. A., Dresselhaus, G., Dresselhaus, M. S., Cancado, L. G., Jorio, A. & Saito, R. Studying disorder in graphite-based systems by Raman spectroscopy. *Physical Chemistry Chemical Physics* **9**, 1276-1290, (2007).

[117] nanocyl. NC7000 Technical Data Sheet. (2014).

[118] Wu, Y., Yang, B., Zong, B., Sun, H., Shen, Z. & Feng, Y. Carbon nanowalls and related materials. *Journal of Materials Chemistry* **14**, 469-477, (2004).

[119] Hiramatsu, M. & Hori, M. *Carbon Nanowalls: Synthesis and Emerging Applications*. (Springer-Verlag Wien, 2010).

[120] Zeng, L., Lei, D., Wang, W., Liang, J., Wang, Z., Yao, N. *et al.* Preparation of carbon nanosheets deposited on carbon nanotubes by microwave plasma-enhanced chemical vapor deposition method. *Applied Surface Science* **254**, 1700-1704, (2008).

[121] Mineo, H., Yuki, N., Hiroki, K. & Masaru, H. Nucleation Control of Carbon Nanowalls Using Inductively Coupled Plasma-Enhanced Chemical Vapor Deposition. *Japanese Journal of Applied Physics* **52**, 01AK05, (2013).

[122] Zhu, M., Wang, J., Holloway, B. C., Outlaw, R. A., Zhao, X., Hou, K. *et al.* A mechanism for carbon nanosheet formation. *Carbon* **45**, 2229-2234, (2007).

[123] Wu, Y. & Yang, B. Effects of Localized Electric Field on the Growth of Carbon Nanowalls. *Nano letters* **2**, 355-359, (2002).

[124] Aricò, A. S., Shukla, A. K., Kim, H., Park, S., Min, M. & Antonucci, V. An XPS study on oxidation states of Pt and its alloys with Co and Cr and its relevance to electroreduction of oxygen. *Applied Surface Science* **172**, 33-40, (2001).

[125] Lewera, A., Timperman, L., Roguska, A. & Alonso-Vante, N. Metal–Support Interactions between Nanosized Pt and Metal Oxides (WO3 and TiO2) Studied Using X-ray Photoelectron Spectroscopy. *The Journal of Physical Chemistry C* **115**, 20153-20159, (2011).

[126] Fuggle, J. C. & Mårtensson, N. Core-level binding energies in metals. *Journal of Electron Spectroscopy and Related Phenomena* **21**, 275-281, (1980).

[127] Litster, S. & McLean, G. PEM fuel cell electrodes. *Journal of Power Sources* **130**, 61-76, (2004).

[128] Huang, S.-Y., Ganesan, P. & Popov, B. N. Titania supported platinum catalyst with high electrocatalytic activity and stability for polymer electrolyte membrane fuel cell. *Applied Catalysis B: Environmental* **102**, 71-77, (2011).

[129] Cruz-Manzo, S., Chen, R. & Rama, P. Inductive Effect on the Fuel Cell Cathode Impedance Spectrum at High Frequencies. *Journal of Fuel Cell Science and Technology* **9**, 051002-051002, (2012).

[130] Antoine, O., Bultel, Y. & Durand, R. Oxygen reduction reaction kinetics and mechanism on platinum nanoparticles inside Nafion®. *Journal of Electroanalytical Chemistry* **499**, 85-94, (2001).

[131] Roy, S. K., Orazem, M. E. & Tribollet, B. Interpretation of Low-Frequency Inductive Loops in PEM Fuel Cells. *Journal of The Electrochemical Society* **154**, B1378-B1388, (2007).

[132] Jeon, M. K., Won, J. Y., Oh, K. S., Lee, K. R. & Woo, S. I. Performance degradation study of a direct methanol fuel cell by electrochemical impedance spectroscopy. *Electrochimica Acta* **53**, 447-452, (2007).

[133] Chang, Y., Han, G., Li, M. & Gao, F. Graphene-modified carbon fiber mats used to improve the activity and stability of Pt catalyst for methanol electrochemical oxidation. *Carbon* **49**, 5158-5165, (2011).

[134] Roy, S. K. & Orazem, M. E. Error Analysis of the Impedance Response of PEM Fuel Cells. *Journal of The Electrochemical Society* **154**, B883-B891, (2007).

[135] Franco, A. A. *Polymer Electrolyte Fuel Cells: Science, Applications, and Challenges*. (Pan Stanford, 2013).

[136] Henry, P. A., Raut, A. S., Ubnoske, S. M., Parker, C. B. & Glass, J. T. Enhanced electron transfer kinetics through hybrid graphene-carbon nanotube films. *Electrochemistry Communications* **48**, 103-106, (2014).

[137] Stamenkovic, V. R., Fowler, B., Mun, B. S., Wang, G., Ross, P. N., Lucas, C. A. *et al.* Improved Oxygen Reduction Activity on Pt3Ni(111) via Increased Surface Site Availability. *Science* **315**, 493-497, (2007).

[138] Li, C., Wang, D., Wang, X. & Liang, J. Controlled electrochemical oxidation for enhancing the capacitance of carbon nanotube composites. *Carbon* **43**, 1557-1560, (2005).

[139] Negro, E., Latsuzbaia, R., Dieci, M., Boshuizen, I. & Koper, G. J. M. Pt electrodeposited over carbon nano-networks grown on carbon paper as durable catalyst for PEM fuel cells. *Applied Catalysis B: Environmental* **166–167**, 155-165, (2015).

[140] Lee, W. J., Maiti, U. N., Lee, J. M., Lim, J., Han, T. H. & Kim, S. O. Nitrogen-doped carbon nanotubes and graphene composite structures for energy and catalytic applications. *Chemical Communications* **50**, 6818-6830, (2014).

[141] Ghosh, D. & Kim, S. Chemically modified graphene based supercapacitors for flexible and miniature devices. *Electron. Mater. Lett.* **11**, 719-734, (2015).

[142] Weber, T., Muijsers, J. C. & Niemantsverdriet, J. W. Structure of Amorphous MoS3. *The Journal of Physical Chemistry* **99**, 9194-9200, (1995).

[143] Chang, C. H. & Chan, S. S. Infrared and Raman studies of amorphous MoS3 and poorly crystalline MoS2. *Journal of Catalysis* **72**, 139-148, (1981).

[144] Voiry, D., Salehi, M., Silva, R., Fujita, T., Chen, M., Asefa, T. *et al.* Conducting MoS2 Nanosheets as Catalysts for Hydrogen Evolution Reaction. *Nano letters* **13**, 6222-6227, (2013).

[145] Kibsgaard, J., Jaramillo, T. F. & Besenbacher, F. Building an appropriate active-site motif into a hydrogen-evolution catalyst with thiomolybdate [Mo3S13]2− clusters. *Nat Chem* **6**, 248-253, (2014).

[146] Wang, H., Lu, Z., Xu, S., Kong, D., Cha, J. J., Zheng, G. *et al.* Electrochemical tuning of vertically aligned MoS2 nanofilms and its application in improving hydrogen evolution reaction. *Proceedings of the National Academy of Sciences* **110**, 19701-19706, (2013).

[147] Wang, H., Lu, Z., Kong, D., Sun, J., Hymel, T. M. & Cui, Y. Electrochemical Tuning of MoS2 Nanoparticles on Three-Dimensional Substrate for Efficient Hydrogen Evolution. *ACS Nano* **8**, 4940-4947, (2014).

[148] Vrubel, H., Merki, D. & Hu, X. Hydrogen evolution catalyzed by MoS3 and MoS2 particles. *Energy & Environmental Science* **5**, 6136-6144, (2012).

[149] Liao, L., Zhu, J., Bian, X., Zhu, L., Scanlon, M. D., Girault, H. H. *et al.* MoS2 Formed on Mesoporous Graphene as a Highly Active Catalyst for Hydrogen Evolution. *Advanced Functional Materials* **23**, 5326-5333, (2013).

[150] Lasia, A. in *Electrochemical Impedance Spectroscopy and its Applications* Ch. 7, 155-175 (Springer New York, 2014).

[151] Conway, B. E., Birss, V. & Wojtowicz, J. The role and utilization of pseudocapacitance for energy storage by supercapacitors. *Journal of Power Sources* **66**, 1-14, (1997).

[152] León-Reyes, Á., Epifani, M., Chávez-Capilla, T., Palma, J. & Díaz, R. Analysis of the Different Mechanisms of Electrochemical Energy Storage in Magnetite Nanoparticles. *International Journal of Electrochemical Science* **9**, 3837-3845, (2014).

[153] Hsu, C.-L., Chang, Y.-H., Chen, T.-Y., Tseng, C.-C., Wei, K.-H. & Li, L.-J. Enhancing the electrocatalytic water splitting efficiency for amorphous MoSx. *International Journal of Hydrogen Energy* **39**, 4788-4793, (2014).

[154] Wu, X., Tang, J., Duan, Y., Yu, A., Berry, R. M. & Tam, K. C. Conductive cellulose nanocrystals with high cycling stability for supercapacitor applications. *Journal of Materials Chemistry A* **2**, 19268-19274, (2014).

[155] Zhao, G., Zhao, F.-G., Sun, J., Lu, Y., Wang, W., Li, W.-S. *et al.* Improving supercapacitor performance of alkylated graphene nanosheets via partial fluorination on their alkyl chains. *RSC Advances* **5**, 92159-92164, (2015).

[156] Zhang, L. L., Zhou, R. & Zhao, X. S. Graphene-based materials as supercapacitor electrodes. *Journal of Materials Chemistry* **20**, 5983-5992, (2010).

[157] Das, R. K., Liu, B., Reynolds, J. R. & Rinzler, A. G. Engineered Macroporosity in Single-Wall Carbon Nanotube Films. *Nano letters* **9**, 677-683, (2009).

[158] Fan, L.-Q., Liu, G.-J., Zhang, C.-Y., Wu, J.-H. & Wei, Y.-L. Facile one-step hydrothermal preparation of molybdenum disulfide/carbon composite for use in supercapacitor. *International Journal of Hydrogen Energy* **40**, 10150-10157, (2015).

[159] Zhou, X., Xu, B., Lin, Z., Shu, D. & Ma, L. Hydrothermal Synthesis of Flower-Like MoS2 Nanospheres for Electrochemical Supercapacitors. *Journal of Nanoscience and Nanotechnology* **14**, 7250-7254, (2014).

[160] González, A., Goikolea, E., Barrena, J. A. & Mysyk, R. Review on supercapacitors: Technologies and materials. *Renewable and Sustainable Energy Reviews* **58**, 1189-1206, (2016).

[161] Jiang, J., Zhang, L., Wang, X., Holm, N., Rajagopalan, K., Chen, F. *et al.* Highly ordered macroporous woody biochar with ultra-high carbon content as supercapacitor electrodes. *Electrochimica Acta* **113**, 481-489, (2013).

[162] Du, X., Zhao, W., Wang, Y., Wang, C., Chen, M., Qi, T. *et al.* Preparation of activated carbon hollow fibers from ramie at low temperature for electric double-layer capacitor applications. *Bioresource Technology* **149**, 31-37, (2013).

[163] Thambidurai, A., Lourdusamy, J. K., John, J. V. & Ganesan, S. Preparation and electrochemical behaviour of biomass based porous carbons as electrodes for supercapacitors — a comparative investigation. *Korean Journal of Chemical Engineering* **31**, 268-275, (2014).

[164] Pandolfo, A. G. & Hollenkamp, A. F. Carbon properties and their role in supercapacitors. *Journal of Power Sources* **157**, 11-27, (2006).

[165] TalapatraS, KarS, Pal, S. K., VajtaiR, CiL, VictorP *et al.* Direct growth of aligned carbon nanotubes on bulk metals. *Nat Nano* **1**, 112-116, (2006).

[166] Stoller, M. D., Park, S., Zhu, Y., An, J. & Ruoff, R. S. Graphene-Based Ultracapacitors. *Nano letters* **8**, 3498-3502, (2008).

[167] Zheng, J. P., Cygan, P. J. & Jow, T. R. Hydrous Ruthenium Oxide as an Electrode Material for Electrochemical Capacitors. *Journal of The Electrochemical Society* **142**, 2699-2703, (1995).

[168] Zheng, Y.-Z., Ding, H.-Y. & Zhang, M.-L. Hydrous–ruthenium–oxide thin film electrodes prepared by cathodic electrodeposition for supercapacitors. *Thin Solid Films* **516**, 7381-7385, (2008).

[169] Zheng, J. P. & Jow, T. R. A New Charge Storage Mechanism for Electrochemical Capacitors. *Journal of The Electrochemical Society* **142**, L6-L8, (1995).

[170] Hu, C.-C. & Tsou, T.-W. Ideal capacitive behavior of hydrous manganese oxide prepared by anodic deposition. *Electrochemistry Communications* **4**, 105-109, (2002).

[171] Zolfaghari, A., Ataherian, F., Ghaemi, M. & Gholami, A. Capacitive behavior of nanostructured MnO2 prepared by sonochemistry method. *Electrochimica Acta* **52**, 2806-2814, (2007).

[172] Ghaemi, M., Ataherian, F., Zolfaghari, A. & Jafari, S. M. Charge storage mechanism of sonochemically prepared MnO2 as supercapacitor electrode: Effects of physisorbed water and proton conduction. *Electrochimica Acta* **53**, 4607-4614, (2008).

[173] Khomenko, V., Frackowiak, E. & Béguin, F. Determination of the specific capacitance of conducting polymer/nanotubes composite electrodes using different cell configurations. *Electrochimica Acta* **50**, 2499-2506, (2005).

[174] Wang, J., Xu, Y., Chen, X. & Du, X. Electrochemical supercapacitor electrode material based on poly(3,4-ethylenedioxythiophene)/polypyrrole composite. *Journal of Power Sources* **163**, 1120-1125, (2007).

[175] An, H., Wang, Y., Wang, X., Zheng, L., Wang, X., Yi, L. *et al.* Polypyrrole/carbon aerogel composite materials for supercapacitor. *Journal of Power Sources* **195**, 6964-6969, (2010).

[176] Fang, Y., Liu, J., Yu, D. J., Wicksted, J. P., Kalkan, K., Topal, C. O. *et al.* Self-supported supercapacitor membranes: Polypyrrole-coated carbon nanotube networks enabled by pulsed electrodeposition. *Journal of Power Sources* **195**, 674-679, (2010).

[177] Mujawar, S. H., Ambade, S. B., Battumur, T., Ambade, R. B. & Lee, S.-H. Electropolymerization of polyaniline on titanium oxide nanotubes for supercapacitor application. *Electrochimica Acta* **56**, 4462-4466, (2011).

[178] Zhang, H., Cao, G., Wang, Z., Yang, Y., Shi, Z. & Gu, Z. Tube-covering-tube nanostructured polyaniline/carbon nanotube array composite electrode with high capacitance and superior rate performance as well as good cycling stability. *Electrochemistry Communications* **10**, 1056-1059, (2008).

[179] Acerce, M., Voiry, D. & Chhowalla, M. Metallic 1T phase MoS2 nanosheets as supercapacitor electrode materials. *Nat Nano* **10**, 313-318, (2015).

[180] Izzo, J. R., Joshi, A. S., Grew, K. N., Chiu, W. K. S., Tkachuk, A., Wang, S. H. *et al.* Nondestructive Reconstruction and Analysis of SOFC Anodes Using X-ray Computed Tomography at Sub-50 nm Resolution. *Journal of The Electrochemical Society* **155**, B504-B508, (2008).

[181] Jhong, H.-R., Brushett, F. R., Yin, L., Stevenson, D. M. & Kenis, P. J. A. Combining Structural and Electrochemical Analysis of Electrodes Using Micro-Computed Tomography and a Microfluidic Fuel Cell. *Journal of The Electrochemical Society* **159**, B292-B298, (2012).

[182] Epting, W. K., Gelb, J. & Litster, S. Resolving the Three-Dimensional Microstructure of Polymer Electrolyte Fuel Cell Electrodes using Nanometer-Scale X-ray Computed Tomography. *Advanced Functional Materials* **22**, 555-560, (2012).

[183] Yu, Y., Xin, H. L., Hovden, R., Wang, D., Rus, E. D., Mundy, J. A. *et al.* Three-Dimensional Tracking and Visualization of Hundreds of Pt–Co Fuel Cell Nanocatalysts During Electrochemical Aging. *Nano letters* **12**, 4417-4423, (2012).

[184] Uchida, H., Song, J. M., Suzuki, S., Nakazawa, E., Baba, N. & Watanabe, M. Electron Tomography of Nafion Ionomer Coated on Pt/Carbon Black in High Utilization Electrode for PEFCs. *The Journal of Physical Chemistry B* **110**, 13319-13321, (2006).

[185] Kübel, C., Voigt, A., Schoenmakers, R., Otten, M., Su, D., Lee, T.-C. *et al.* Recent Advances in Electron Tomography: TEM and HAADF-STEM Tomography for Materials Science and Semiconductor Applications. *Microscopy and Microanalysis* **11**, 378-400, (2005).

[186] Ostadi, H., Rama, P., Liu, Y., Chen, R., Zhang, X. X. & Jiang, K. Influence of threshold variation on determining the properties of a polymer electrolyte fuel cell gas diffusion layer in X-ray nano-tomography. *Chemical Engineering Science* **65**, 2213-2217, (2010).

[187] Beguin, F. & Frackowiak, E. *Carbons for Electrochemical Energy Storage and Conversion Systems*. (CRC Press, 2009).

[188] Kishimoto, M., Iwai, H., Saito, M. & Yoshida, H. Quantitative evaluation of solid oxide fuel cell porous anode microstructure based on focused ion beam and scanning electron microscope technique and prediction of anode overpotentials. *Journal of Power Sources* **196**, 4555-4563, (2011).

[189] Zhang, L. & Xia, Z. Mechanisms of Oxygen Reduction Reaction on Nitrogen-Doped Graphene for Fuel Cells. *The Journal of Physical Chemistry C* **115**, 11170-11176, (2011).

[190] Qu, L., Liu, Y., Baek, J. B. & Dai, L. Nitrogen-doped graphene as efficient metal-free electrocatalyst for oxygen reduction in fuel cells. *ACS Nano* **4**, 1321-1326, (2010).

[191] Li, Y., Zhou, W., Wang, H., Xie, L., Liang, Y., Wei, F. *et al.* An oxygen reduction electrocatalyst based on carbon nanotube-graphene complexes. *Nat Nanotechnol* **7**, 394-400, (2012).

[192] Liang, Y., Li, Y., Wang, H., Zhou, J., Wang, J., Regier, T. *et al.* Co3O4 nanocrystals on graphene as a synergistic catalyst for oxygen reduction reaction. *Nat Mater* **10**, 780-786, (2011).

[193] Gong, K., Du, F., Xia, Z., Durstock, M. & Dai, L. Nitrogen-doped carbon nanotube arrays with high electrocatalytic activity for oxygen reduction. *Science* **323**, 760-764, (2009).

[194] Yu, D., Zhang, Q. & Dai, L. Highly efficient metal-free growth of nitrogen-doped single-walled carbon nanotubes on plasma-etched substrates for oxygen reduction. *J Am Chem Soc* **132**, 15127-15129, (2010).

[195] Xiong, W., Du, F., Liu, Y., Perez, A., Jr., Supp, M., Ramakrishnan, T. S. *et al.* 3-D carbon nanotube structures used as high performance catalyst for oxygen reduction reaction. *J Am Chem Soc* **132**, 15839-15841, (2010).

[196] 2014 Annual Report of The Hydrogen and Fuel Cell Technical Advisory Committee. *U.S. Department of Energy*, (2015).